KU LEUVEN

ARENBERG DOCTORAL SCHOOL
Faculty of Engineering Science

Dynamic Spectrum Management Algorithms for Interference Mitigation in DSL Networks

Jeroen Verdyck

Supervisors:
Prof. dr. ir. M. Moonen
Prof. dr. C. Blondia
(University of Antwerp)

Dissertation presented in partial fulfillment of the requirements for the degree of Doctor of Engineering Science (PhD): Electrical Engineering

June 2021

Dynamic Spectrum Management Algorithms for Interference Mitigation in DSL Networks

Jeroen VERDYCK

Examination committee:
Prof. dr. ir. P. Verbaeten, chair
Prof. dr. ir. M. Moonen, supervisor
Prof. dr. C. Blondia, supervisor
(University of Antwerp)
Prof. dr. ir. S. Pollin
Prof. dr. ir. P. Patrinos
Prof. dr. ir. G. Leus
(TU Delft)
Prof. dr. ir. S. McLaughlin
(Heriot-Watt University)

Dissertation presented in partial fulfillment of the requirements for the degree of Doctor of Engineering Science (PhD): Electrical Engineering

June 2021

© 2021 KU Leuven – Faculty of Engineering Science
Uitgegeven in eigen beheer, Jeroen Verdyck, Kasteelpark Arenberg 10 box 2446, B-3001 Leuven (Belgium)

Alle rechten voorbehouden. Niets uit deze uitgave mag worden vermenigvuldigd en/of openbaar gemaakt worden door middel van druk, fotokopie, microfilm, elektronisch of op welke andere wijze ook zonder voorafgaande schriftelijke toestemming van de uitgever.

All rights reserved. No part of the publication may be reproduced in any form by print, photoprint, microfilm, electronic or any other means without written permission from the publisher.

Preface

Over the past six years, the goal of obtaining a Ph.D. degree has seemed so distant that it is hard to believe I have almost reached it. I never imagined that—one day—I would actually wrap up a dissertation by writing its preface. Yet here I am. Had I known that the path here would be long and contain numerous obstacles and some painful dead-ends, I may have never embarked on the journey. I am grateful for my (former) ignorance. In all respects, the journey here was much more rewarding than it was challenging. My success is due in no small part to those who accompanied me and I must now thank.

First and foremost, I wish to thank Prof. Marc Moonen. His scientific contributions to my thesis were significant, of course. The chapters that I regard as the best ones in this dissertation have always come about after a masterful "assist" by Marc. As a supervisor, Marc strikes the perfect balance between leaving room to grow and explore when his students want it, while providing detailed feedback and new ideas when they need it. Even more than for his scientific contributions, I have to thank Marc for his unwavering trust. His belief in me—especially when my belief in myself wavered—was essential for my success.

I would also like to thank my external co-supervisor, Prof. Chris Blondia. Apart from being quite fruitful—as proven by the best paper award at ICC 2017—our collaboration with Chris has been delightful on a personal level as well.

I am grateful to the members of the supervisory and examination committee for carefully reading my dissertation and for the interesting discussions. Thank you Prof. Ingrid Moerman, Prof. Sofie Pollin, Prof. Geert Leus, Prof. Stephen McLaughlin, Prof. Panagiotis Patrinos, and Prof. Pierre Verbaeten.

With everyone working individually on their own research topic, the academic environment can sometimes induce feelings of "professional isolation". Fortunately for me, I have often been able to combat these feelings by collaborating with talented people, both from KU Leuven and from other

universities. Thank you Adriaan, Jeremy, Mohit, Pourya, Rich, and Wouter, for taking an interest in my work and for allowing me to take part in yours.

In the final years of my Ph.D. project, I have also been able to collaborate with the researchers of the Fixed Networks Department of Nokia Bell Labs in Antwerp. During our monthly meetings, their ability to immediately put their finger on the weaknesses in our ideas has often astounded me, and has significantly improved the quality of the work in this dissertation. I hereby want to thank everyone in the team.

I also want to thank all of my colleagues, past and present, from the STADIUS group, particularly, the DSP team. Conducting research can be an emotional roller coaster, with peaks after every achievement and a valley after each setback. Having so many awesome companions, who are all going through the same cycles,[1] places the valleys in perspective and—more importantly—has resulted in more reasons to celebrate over the last six years than I am able to remember. All of you have influenced who I am today and I feel privileged to count so many of you among my friends. Special thanks goes to Jasper, for "leading by example".[2]

I thank my friends and family for being a constant source of pleasant yet vital distractions. Nothing takes my mind off work more than having you around to celebrate birthdays/Christmas/Easter/new years, to go on relaxing holidays and to exhausting festivals, to practice sports, or to simply spend time together. I feel fortunate for being surrounded by so many people who care for me. I want to especially thank my parents, for being my biggest supporters.[3] Without them, none of this would have been possible. I also want to explicitly thank Gerrit and Nele for their ever open door, regardless of the circumstances.

Finally, I want to thank Heleen. For her patience during a Ph.D. project that took longer than anticipated. For keeping me focussed on what really matters in life. For being my rock when it felt like I was drowning. Heleen, your "take the bull by the horns"-mentality and your love give me the courage to take on any challenge. I aspire to mean as much to you as you mean to me, and there is nothing I look forward to more than continuing to build our life together in Turnhout.

Jeroen Verdyck

Turnhout, June 2021

[1] Maybe not *all* of them. Some are rumored to experience no setbacks.

[2] Jasper, if you want to join me at GN in a couple of years and show me how its done again, you would be more than welcome!

[3] In this sentence, *supporters* can be correctly interpreted both in English and in Dutch.

Abstract

This thesis considers digital subscriber line (DSL) networks that provide fixed broadband access over copper twisted-pair lines. In order to cost-effectively achieve ever higher data rates on these twisted-pair lines, the adopted strategy over the last two decades has been to gradually replace them with fiber optic cables, thereby reducing the copper loop length and enabling signal transmission over a higher frequency bandwidth. An important disadvantage of using a higher bandwidth however, is the resulting increase in interference between the different signals in the DSL network. This thesis studies novel and advanced strategies to reduce the impact of interference in DSL networks. Two general strategies will be pursued, each corresponding to a different Part of this thesis.

The strategy in Part I consists of dynamically changing the interference mitigation configuration—also referred to as the dynamic spectrum management (DSM) configuration—in real time. Such a real-time adaptive DSM design, which dynamically adapts the DSM configuration to user requirements in real time, mitigates competition between different users in the network by capitalizing on the elastic, time dependent nature of the traffic the network is carrying. The two keys to implementing real-time adaptive DSM are 1) extending the DSM design to a cross-layer design, thereby allowing users or applications to express their requirements regarding the DSM configuration, and 2) fast optimization algorithms able to adapt the DSM configuration to user or application requirements in real time.

The first contribution of this thesis is a new real-time DSM algorithm which, contrary to the state-of-the-art algorithms, provably converges to a stationary point of the considered optimization problem. Simulation results additionally demonstrate that the proposed algorithm outperforms state-of-the-art real-time DSM algorithms in practice as well.

To enable users or applications to express their requirements regarding the DSM configuration, cross-layer DSM design by means of network utility maximization

(NUM) is considered. A fast DSM algorithm is proposed, which finds a local solution to the considered NUM problem. The proposed algorithm is applicable in many DSL deployment scenarios, and regardless of the utility function's properties. Empirical evidence shows that the proposed algorithm needs only few iterations to find a satisfactory solution.

The strategy in Part II consists of reducing the impact of interference in DSL networks by accounting for the interplay between the DSM design and new features of the upcoming DSL standard—G.mgfast. These new features affect the optimality of the state-of-the-art DSM approaches and may—if they are accounted for in the DSM design rather than be treated as separate features—yield increased performance by adding new degrees of freedom to the DSM design space. Three new physical layer features are considered in this thesis, namely QoS classes, full duplex transmission, and channel shortening.

In order to support QoS classes, this thesis considers providing for unequal error protection (UEP). Four new algorithms are presented for joint DSM and UEP design: two optimal spectrum balancing (OSB) algorithms—one for upstream and one for downstream transmission—and two low-complexity adaptations of the OSB algorithms, referred to as distributed spectrum balancing (DSB) algorithms. In addition, an algorithm is presented which selects an optimal modulation and coding scheme to be used for each QoS class. Results show the benefit of UEP, as it is able to achieve modest performance gains.

DSM design for DSL networks implementing full duplex transmission is considered as well. A new MAC-BC duality theory for multi-user FDX networks is developed, from which an OSB algorithm is derived that determines the globally optimal DSM design. The developed OSB algorithm is—to the best of the authors' knowledge—the first to establish the globally optimal solution to the considered full-duplex DSM problem. In addition to the OSB algorithm, two low-complexity DSB algorithms are proposed. Simulations show that FDX transmission indeed leads to significant performance gains in MU DSL networks.

As a final feature, channel shortening algorithms are considered, which apply an FIR filter to the transmitted or received signals to reduce the apparent channel impulse response length, thereby increasing the achievable data rates. New algorithms for joint channel shortening filter and DSM design are presented. Moreover, a duality result is presented, demonstrating a theoretical equivalence between DSL systems with either transmitter and or receiver-side channel shortening filters. Finally, it is shown that the received signals in systems using channel shortening filters can be improper. A new signal constellation design is proposed that takes this impropriety explicitly into account. Simulations demonstrate that the proposed methods and designs can achieve significant performance gains on highly dispersive long twisted-pair lines.

Beknopte Samenvatting

Deze thesis beschouwt DSL-netwerken (Digital Subscriber Line), dewelke internettoegang bieden via een getorst of getwist koperpaar. Om steeds hogere datasnelheden op deze koperparen te realiseren, is de afgelopen twee decennia een strategie gehanteerd waarbij de koperparen gradueel vervangen worden door glasvezelkabels, waardoor de koperparen korter worden en bijgevolg signaaloverdracht over een hogere frequentiebandbreedte mogelijk wordt. Een belangrijk nadeel van het gebruik van een hogere bandbreedte is echter de resulterende toename van interferentie tussen de verschillende signalen in het DSL-netwerk. Dit proefschrift bestudeert nieuwe en geavanceerde strategieën om de impact van interferentie in DSL-netwerken te verminderen. Twee algemene strategieën zullen worden nagestreefd, elk corresponderend met een ander deel van dit proefschrift.

De strategie in Deel I bestaat uit het dynamisch wijzigen van de configuratie voor het beperken van interferentie – ook wel de configuratie van het dynamisch spectrumbeheer (DSM) genoemd – in realtime. Een dergelijk real-time adaptief DSM-ontwerp, dat de DSM-configuratie dynamisch in real-time aanpast aan de gebruikersvereisten, vermindert de concurrentie tussen verschillende gebruikers in het netwerk door te profiteren van de elastische, tijdsafhankelijke aard van het verkeer dat het netwerk vervoert. De twee sleutels tot het implementeren van real-time adaptieve DSM zijn 1) het DSM-ontwerp uitbreiden naar een cross-layer-ontwerp, wat gebruikers of applicaties de mogelijkheid geeft hun vereisten met betrekking tot de DSM-configuratie kenbaar te maken, en 2) snelle optimalisatie-algoritmen die de DSM-configuratie in real-time kunnen aanpassen aan de vereisten van gebruikers of applicaties.

De eerste bijdrage van dit proefschrift is een nieuw real-time DSM-algoritme dat, in tegenstelling tot de state-of-the-art algoritmen, aantoonbaar convergeert naar een stationair punt van het beschouwde optimalisatieprobleem. Simulatieresultaten tonen bovendien aan dat het voorgestelde algoritme ook in de praktijk de state-of-the-art real-time DSM-algoritmen overtreft.

Om gebruikers of applicaties in staat te stellen hun eisen met betrekking tot de DSM-configuratie kenbaar te maken, wordt een cross-layer DSM-ontwerp door middel van netwerk-utiliteit-maximalisatie (NUM) beschouwd. Er wordt een DSM-algoritme met een lage complexiteit voorgesteld dat een lokale oplossing vindt voor het beschouwde NUM-probleem. Het voorgestelde algoritme is toepasbaar in diverse DSL netwerken en ongeacht de eigenschappen van de beschouwde utiliteit-functie. Empirisch bewijs toont verder aan dat het voorgestelde algoritme slechts enkele iteraties nodig heeft om een bevredigende oplossing te vinden.

De strategie in Deel II bestaat uit het verminderen van de impact van interferentie in DSL-netwerken door rekening te houden met het samenspel tussen het DSM-ontwerp en nieuwe functies van de volgende DSL-standaard – G.mgfast. Deze nieuwe functies beïnvloeden de optimaliteit van de state-of-the-art DSM-benaderingen en kunnen – als ze in het DSM-ontwerp worden opgenomen in plaats van als afzonderlijke functies te worden behandeld – betere prestaties opleveren door nieuwe vrijheidsgraden toe te voegen aan de DSM-ontwerpruimte. Drie nieuwe functies worden die in dit proefschrift besproken, namelijk QoS-klassen, full-duplex transmissie en kanaalverkorting.

Om QoS-klassen te ondersteunen, beschouwt dit proefschrift het bieden van ongelijke foutbescherming (UEP). Vier nieuwe algoritmen worden gepresenteerd voor gezamenlijk DSM- en UEP-ontwerp: twee optimale OSB-algoritmen – één voor transmissie van signalen vanuit het netwerk naar de gebruiker, en één voor transmissie in de omgekeerde richting – en twee DSB-algoritmen, aangepaste versies van de OSB-algoritmen met een lagere complexiteit. Bovendien wordt een algoritme gepresenteerd dat een optimaal modulatie- en coderingsschema selecteert dat voor elke QoS-klasse gebruikt dient te worden. Resultaten tonen het voordeel van UEP aan, aangezien het in staat is om bescheiden prestatieverbeteringen te behalen.

DSM-ontwerp voor DSL-netwerken die FDX-transmissie (full-duplex) implementeren, wordt eveneens beschouwd. Een nieuwe dualiteitstheorie voor FDX-netwerken met meerdere gebruikers wordt ontwikkeld, waaruit een OSB-algoritme wordt afgeleid dat in staat is de globaal optimale DSM-configuratie te bepalen. Het ontwikkelde OSB-algoritme is het eerste dat de globaal optimale oplossing van het beschouwde full-duplex DSM-probleem kan vinden. Naast het OSB-algoritme worden twee DSB-algoritmen met lage complexiteit voorgesteld. Simulaties tonen aan dat FDX-transmissie inderdaad leidt tot aanzienlijke prestatieverbeteringen in DSL-netwerken met meerdere gebruikers.

Als laatste nieuwe functie worden verkortingsalgoritmen beschouwd, die een FIR-filter (finite impulse response) toepassen op de verzonden of ontvangen signalen om de lengte van de impulsresponsie schijnbaar te verkleinen, waardoor

de haalbare gegevenssnelheden toenemen. Nieuwe algoritmen voor het gezamenlijk ontwerp van de kanaalverkortingsfilter en de DSM-configuratie worden gepresenteerd. Bovendien wordt een dualiteitstheorie gepresenteerd, die een theoretische equivalentie aantoont tussen DSL-systemen met een kanaalverkortingsfilter aan de zend- of de ontvangst-zijde van het koperpaar. Ten slotte wordt aangetoond dat de ontvangen signalen in systemen die kanaalverkortingsfilters gebruiken, “improper” kunnen zijn. Er wordt een nieuw constellatieontwerp voorgesteld dat expliciet rekening houdt met deze “impropriety”. Simulaties tonen aan dat de voorgestelde methoden en ontwerpen aanzienlijke prestatieverbeteringen kunnen behalen op koperparen met een lange impulsresponsie.

Glossary

Abbreviations

a.k.a.	also known as
cf.	*conferre*, compare with, see also
e.g.	*exempli gratia*, for example
i.e.	*id est*, that is
i.i.d.	independent and identically distributed
w.l.o.g.	without loss of generality
w.r.t.	with respect to

Acronyms

3GPP	3-rd generation partnership project
A-RoC	analog radio-over-copper
ADSL	asymmetric digital subscriber line
AMC	adaptive modulation and coding
AN	access node
ANN	artificial neural network

ARA	adaptive resource allocation
ATP	aggregate transmit power
AWG	American wire gauge
BBU	base band unit
BC	broadcast channel
BER	bit error rate
BSUM	block successive upper bound minimization
CG	conditional gradient
CIR	channel impulse response
CO	central office
CO-ASB	constant offset autonomous spectrum balancing
CP	cyclic prefix
CPE	customer premises equipment
CPRI	common public radio interface
CWDD	column-wise diagonal dominant
DAS	distributed antenna system
DB	derivative based
DFE	decision-feedback equalization
DFT	discrete Fourier transform
DMT	discrete multi-tone
DoV	difference of variables
DP	distribution point
DPC	dirty paper coding
DPU	distribution point unit
DS	downstream
DSB	distributed spectrum balancing
DSL	digital subscriber line
DSLAM	digital subscriber line access multiplexer
DSM	dynamic spectrum management
EC	echo cancellation
EEP	equal error protection

F-DB-IPDB	fast derivative-based iterative power difference balancing
F-IPDB	fast iterative power difference balancing
FDD	frequency division duplex
FDMA	frequency-division multiple access
FDX	full-duplex
FEC	forward error correction
FEQ	frequency-domain equalization
FEXT	far-end crosstalk
FIR	finite impulse response
FLEXA	inexact flexible parallel algorithm
FTTB	fiber to the building
FTTC	fiber-to-the-curb, fiber-to-the-cabinet
FTTdp	fiber-to-the-distribution-point
FTTH	fiber-to-the-home
FTTx	fiber-to-the-X
G.fast	G series of recommendations; fast access to subscriber terminals
G.mgfast	G series of recommendations; multi-gigabit fast access to subscriber terminals
GDFE	generalized decision-feedback equalization
GS	Gauss-Seidel
GV	grouped vectoring
HDSL	high-bit-rate digital subscriber line
HDTV	high-definition television
IC	interference channel
ICI	inter-carrier interference
IDFT	inverse discrete Fourier transform
IEEE	Institute of Electrical and Electronics Engineers
IP	Internet protocol
IPDB	iterative power difference balancing
IQ	in-phase quadrature
ISI	inter-symbol interference

ISP	Internet service provider
ITU	International Telecommunication Union
ITU-T	International Telecommunication Union - Telecommunications sector
IWF	iterative water filling
KKT	Karush-Kuhn-Tucker
L-BFGS-B	limited-memory Broyden-Fletcher-Goldfarb-Shano with box constraints
LR	long-reach
LTE	long-term evolution
MAC	multiple access channel
MC	modulation and coding
MDV	minimal delay violation
MIMO	multiple-input multiple-output
MISO	multiple-input single-output
MM	minorize-maximization
MMC	multiple modulation and coding schemes
MMCR	multiple modulation and coding schemes relaxation
MMCR-RS	multiple modulation and coding schemes relaxation-based rate selection
MMSE	minimum mean square error
MO	monotonic optimization
MPEG	moving pictures experts group
MU	multi-user
NEXT	near-end crosstalk
NP-hard	non-deterministic polynomial-time hard
NT	network termination
NUM	network utility maximization
OFDMA	orthogonal frequency division multiple access
OLA	overlap-add
OLT	optical line terminal
OMC	one modulation and coding scheme
OSB	optimal spectrum balancing
OSI	open systems interconnection

P/S	parallel-to-serial
PAM	pulse amplitude modulation
POTS	plain old telephone system
PTEQ	per-tone equalization
PTPC	per-tone precoding
QAM	quadrature amplitude modulation
QoS	quality of service
QRD	QR-decomposition
RF	radio frequency
RRH	remote radio head
RRU	remote radio unit
RS	Reed-Solomon
RT	remote terminal
RT-DSM	real-time dynamic spectrum management
S/P	serial-to-parallel
SCA	successive convex approximation
SIC	successive interference cancellation
SINR	signal-to-interference-plus-noise ratio
SISO	single-input single-output
SNR	signal-to-noise ratio
TCM	trellis coded modulation
TDD	time division duplex
TEQ	time-domain equalization
THP	Tomlinson-Harashima precoding
TPC	time-domain precoding
UEP	unequal error protection
ULLS	ultra low-latency service
URLLS	ultra reliable low-latency service
US	upstream
VDSL	very high bit rate digital subscriber line
VDSL2	very high bit rate digital subscriber line 2

VoIP	voice over IP
WL	widely linear
WMMSE	weighted minimum mean square error
WSR	weighted sum rate
ZF	zero forcing
ZP	zero pad

Mathematical notation

$\mathcal{A}$	set
$\mathbf{A}$	matrix
$\boldsymbol{a}$, $\boldsymbol{A}$	vector
a, A	scalar
$\mathbb{C}$	set of complex numbers
$\mathbb{R}$	set of real numbers
$\mathbb{R}_{+}$	set of non-negative real numbers
$\mathbb{R}_{++}$	set of strictly positive real numbers
$\mathbf{I}_n$	$n \times n$ identity matrix
$\mathbf{1}_{n\times m}$	$n \times m$ all-one matrix
$\mathbf{0}_{n\times m}$	$n \times m$ all-zero matrix
$\mathcal{A} \setminus \mathcal{B}$	set subtraction
$\mathbf{A} \circ \mathbf{B}$	Hadamard product of matrices $\mathbf{A}$ and $\mathbf{B}$
$\mathcal{A} \subseteq \mathcal{B}$	$\mathcal{A}$ is a subset of $\mathcal{B}$
$\mathcal{A} \subset \mathcal{B}$	$\mathcal{A}$ is a strict subset of $\mathcal{B}$
$\mathbf{A} \succeq \mathbf{B}$	$\mathbf{A} - \mathbf{B}$ is positive semidefinite
$\mathbf{A} \succ \mathbf{B}$	$\mathbf{A} - \mathbf{B}$ is positive definite
$\mathbf{A} \geq \mathbf{B}$	$\mathbf{A} - \mathbf{B} \in \mathbb{R}_{+}^{m\times n}$
$\mathbf{A} > \mathbf{B}$	$\mathbf{A} - \mathbf{B} \in \mathbb{R}_{++}^{m\times n}$
$\mathbf{A}^{\mathrm{T}}$	transpose of $\mathbf{A}$

$\mathbf{A}^{\mathcal{H}}$	conjugate transpose of $\mathbf{A}$
$\mathbf{A}^{*}$	complex conjugate of $\mathbf{A}$
$\Re(\mathbf{A})$	real part of $\mathbf{A}$
$\Im(\mathbf{A})$	imaginary part of $\mathbf{A}$
$\mathbf{A}^{\mathbb{R}}$	composite real representation of $\mathbf{A}$
$\text{diag}(\mathbf{A})$	vector containing $\mathbf{A}$'s main diagonal
$\text{diag}(\boldsymbol{a})$	diagonal matrix with $\boldsymbol{a} = \text{diag}(\text{diag}(\boldsymbol{a}))$
$\text{tr}(\mathbf{A})$	trace of $\mathbf{A}$
$\text{null}(\mathbf{A})$	null space of $\mathbf{A}$
$\text{col}_n(\mathbf{A})$	n-th column of $\mathbf{A}$
$\text{row}_n(\mathbf{A})$	n-th row of $\mathbf{A}$
$[\mathbf{A}]_{m,n}$	$\text{row}_m(\text{col}_n(\mathbf{A}))$
$\det(\mathbf{A})$	determinant of $\mathbf{A}$
$\lvert \cdot \rvert$	modulus, 2-norm, Frobenius norm, set cardinality
$\mathbb{E}\{\cdot\}$	expected value
$\log(\cdot)$	natural logarithm
$\log_2(\cdot)$	binary logarithm
$\mathcal{O}(\cdot)$	big O

Contents

Abstract iii

Beknopte Samenvatting v

Glossary ix

Contents xvii

List of Figures xxiii

List of Tables xxv

1 Introduction 1

1.1 Interference in DSL networks 4

1.1.1 Inter-symbol interference 4

1.1.2 Far-end crosstalk 9

1.1.3 Echo and near-end crosstalk 19

1.2 Novel interference mitigation strategies 23

1.2.1 Cross-layer DSM 23

1.2.2 New DSM degrees of freedom 25

1.3 Contributions and thesis outline 28

I Cross-Layer DSM **33**

2 Real-time DSM **35**

2.1 Introduction 36
2.2 Spectrum coordination 37
2.3 Real-time spectrum coordination and bi-coordinate ascent methods 39
2.4 Derivative based real-time spectrum coordination 41
2.5 Fast derivative based iterative power difference balancing . . . 43
2.6 Simulation results 45
2.7 Conclusion 46

3 Network Utility Maximization-based DSM **49**

3.1 Introduction 50
3.2 DSB as a minorize-maximization algorithm 51
3.3 NUM-DSB 53
3.4 Application: downstream grouped vectoring 55
3.5 Simulation results 58
3.6 Conclusion 59

II New DSM Degrees of Freedom **61**

4 DSM and QoS Classes **63**

4.1 Introduction 64
4.2 System model 66
4.2.1 Multiple access channel 67
4.2.2 Broadcast channel 68
4.2.3 Bitloading and error control 69
4.2.4 Unequal error protection 70

4.3 Rate-adaptive DSM with unequal error protection 71
4.4 Upstream DSM with unequal error protection 73
4.4.1 Globally optimal solution: MAC-OSB-UEP 73
4.4.2 Locally optimal solution: MAC-DSB-UEP 76
4.5 Downstream DSM with unequal error protection 78
4.5.1 MAC-BC duality 80
4.5.2 Globally optimal solution: BC-OSB-UEP 81
4.5.3 Locally optimal solution: BC-DSB-UEP 82
4.6 Joint resource allocation and Reed-Solomon code rate optimization 84
4.7 Simulation results 87
4.7.1 Performance comparison OSB and DSB algorithms . . . 87
4.7.2 MMCR-RS performance analysis 88
4.8 Conclusion 90

5 Full-Duplex DSM 93

5.1 Introduction 94
5.2 System model 97
5.2.1 Upstream channel 97
5.2.2 Downstream channel 99
5.2.3 Performance metrics 100
5.3 Full-duplex dynamic spectrum management 101
5.4 Optimal spectrum balancing 101
5.4.1 Dual decomposition 102
5.4.2 MAC-BC duality for FDX DSL 103
5.4.3 Exhaustive grid search 105
5.5 Distributed spectrum balancing 107
5.5.1 DSB algorithm 107

5.5.2 FDX dual domain DSB algorithm (FDX-DD-DSB) . . . 109
5.5.3 FDX primal domain DSB algorithm (FDX-PD-DSB) . . 112
5.6 Simulation results . . . 117
5.6.1 DSB optimality gap . . . 117
5.6.2 Convergence of the DSB algorithms . . . 119
5.6.3 Performance of MU FDX DSL networks . . . 122
5.7 Conclusion . . . 123

6 DSM and Channel Shortening **125**

6.1 Introduction . . . 126
6.2 System model . . . 129
6.2.1 Cyclic prefix OFDM (CP-OFDM) . . . 130
6.2.2 Zero-padded OFDM (ZP-OFDM) . . . 131
6.2.3 Per-tone equalization . . . 131
6.2.4 Per-tone precoding . . . 135
6.2.5 Performance metrics . . . 138
6.3 PTEQ filter optimization & resource allocation . . . 139
6.3.1 Problem reformulation . . . 140
6.3.2 Successive convex approximation algorithm . . . 141
6.3.3 Solving the surrogate problem . . . 143
6.4 PTPC filter optimization & resource allocation . . . 144
6.4.1 Dual system with PTEQ . . . 145
6.4.2 PTEQ-PTPC duality . . . 147
6.4.3 PTPC filter optimization & resource allocation based on PTEQ-PTPC duality . . . 150
6.5 Simulation results . . . 151
6.5.1 PTEQ and PTPC performance . . . 153
6.5.2 SCA convergence . . . 156

6.6 Conclusion & future work 158

7 DSM and Widely Linear Channel Shortening 161

7.1 Introduction 162

7.2 DMT system model & per-tone equalization 166

7.2.1 DMT transceiver 167

7.2.2 Channel shortening - TEQ & PTEQ 169

7.2.3 Signal-to-interference-plus-noise ratio 171

7.2.4 Bit loading 173

7.3 Problem statement 173

7.4 Composite real channel model 177

7.4.1 Signal-to-interference-plus-noise ratio 177

7.4.2 Bit loading 179

7.5 Optimizing performance: widely linear PTEQ & symbol rotation 180

7.5.1 Widely linear per-tone equalization 180

7.5.2 Transmitter-side symbol rotation 182

7.5.3 Symbol rotation optimality 185

7.6 Simulation results 187

7.6.1 Examples Figure 7.2 and Table 7.2 189

7.6.2 PTEQ output impropriety 191

7.6.3 SINR and achievable bit loading 191

7.6.4 Achievable data rate 193

7.7 Conclusion 196

8 Conclusions 199

8.1 Conclusions and suggestions for future work 199

8.1.1 Cross-layer DSM 199

8.1.2 New DSM degrees of freedom 201

8.2 Future DSL technologies 205
8.2.1 Terabit digital subscriber lines 205
8.2.2 Cellular subscriber lines 206

A Appendix to Chapter 2 **209**

B Appendix to Chapter 5 **213**

C Appendix to Chapter 6 **217**

D Appendix to Chapter 7 **223**

Bibliography **225**

Curriculum Vitae **247**

List of publications **249**

List of Figures

1.1 Schematic overview of fiber-to-the-X network topologies. 4

1.2 Far-end crosstalk in downstream DSL. 9

1.3 FEXT channels. 11

1.4 Example rate region of a 2-user G.Fast DSL system. 13

1.5 Near-end crosstalk and echo received by the 2-nd CPE in the downstream channel. 20

2.1 Bit loading and transmit spectrum of a three user G.fast system, obtained through F-IPDB and F-DB-IPDB. 46

2.2 Convergence result for F-IPDB and F-DB-IPDB. 47

3.1 Utility function value after convergence of NUM-DSB. 60

4.1 Information bit rate and transmit spectrum for two user US and DS G.fast systems, respectively obtained through MAC-OSB-UEP and BC-OSB-UEP, and through MAC-DSB-UEP and BC-DSB-UEP. 89

4.2 Achievable rate region of 10 user US and DS G.fast systems using RS codewords either of length $\nu = 64$, or of length $\nu = 255$. . . . 91

5.1 Multi-user full-duplex DSL network topology. 97

5.2 A DSL network in a 10-user fiber-to-the-building scenario, which is considered to be the main use case for G.mgfast. 118

5.3 Illustration of the optimality of DSB algorithms. It is seen that the solution obtained by DSB algorithms closely resembles the one obtained by the OSB algorithm. 119

5.4 Number of iterations required for convergence and final weighted sum rate value, obtained by executing FDX-DD-DSB and FDX-PD-DSB for the network of Figure 5.2a. 123

5.5 Convergence of the WMMSE and FDX-PD-DSB algorithms. . 124

5.6 Average achievable US and DS rates of FDX transmission in the DSL networks of Figure 5.2, relative to maximum achievable TDD rates. 124

6.1 A general OFDM/DMT transceiver model. 129

6.2 Synthesis filter bank representation of an OFDM transmitter (including P/S converter), concatenated with a Time-domain PreCoding (TPC) filter $W(z)$. 136

6.3 Channel impulse responses considered in simulations. 152

6.4 Achieved data rate for different values of the delay δ. 154

6.5 Achieved maximum data rate for different values of the CP/ZP length ν. 155

6.6 Convergence of the SCA algorithm: distance to optimal rate . . 157

6.7 Convergence of the SCA algorithm: relative KKT error 158

7.1 Signal flow graph of a general DMT system. 167

7.2 Example of a received signal after DMT demodulation in a G.fast system with a 600 m loop length and $\nu_{\mathrm{p}} = 128$. 174

7.3 The three CIRs that are considered in the simulations. 187

7.4 Circularity coefficients of the received direct signal and the received interference-plus-noise in a DMT receiver using PTEQ. 190

7.5 Achieved SINR and achievable bit loading. 192

7.6 Achievable data rate as a function of the delay δ for G.fast systems using WL PTEQ with impulse responses given by Figure 7.3. . 194

7.7 Maximum data rate achieved for different CP lengths. 195

List of Tables

1.1 DSL generations as defined by the ITU-T. 3

2.1 G.fast parameter settings. 45

3.1 G.fast parameter settings. 59

3.2 Number of iterations of NUM-DSB before convergence. 59

4.1 Data rates for two user US and DS systems, in Mbit/s. 88

5.1 Data rate and WSR for a three user FDX DSL network (Gbit/s). 120

6.1 Simulation parameters. 152

7.1 Number of floating point operations required by channel shortening and equalization a DMT receiver. 171

7.2 Achieved SINR and maximum bit loading for the received signals in Figure 7.2. 175

7.3 Number of floating point operations required by channel shortening and equalization a DMT receiver (continued). 182

7.4 Simulation parameters. 188

Chapter 1

Introduction

"Communications services represent a vital resource in our modern society. There is, accordingly, a major public interest in assuring the adequacy and efficiency of these services." These words are as true today, as when they were first spoken by Harry S. Truman in 1950 [70]; communications networks form the backbone of the digital economy, play a central role in in-home entertainment, shape our social interactions, and have revolutionized our access to and our interaction with information.

This thesis considers digital subscriber line (DSL) networks that provide fixed broadband access over copper twisted-pair lines. Unlike what is the case for the telephone, it is undisputed that Alexander Graham Bell invented the copper twisted-pair line in 1881 [43, 112]. Ever since, the number of twisted-pair telephone connections has steadily grown to roughly 1.3 billion worldwide by 2011 [43].[1] It is precisely this wide-spread availability of twisted-pair lines that makes DSL networks relevant to this day.

From a technological point of view, communication over copper twisted-pairs has long been overshadowed by communication over fiber optic cables [43], as the latter is able to achieve higher data rates over longer distances without suffering from electromagnetic interference. Fiber optic cables have therefore become the *de facto* standard for connecting (equipment in) Internet service providers' (ISPs') core networks. In the last-mile—the final leg of the network that physically reaches the end-users' premises, a.k.a. the local loop—however, non-fiber-optic-based access technologies are still in use. While fiber optic cables

[1] This success of the twisted-pair line was not even anticipated by Bell himself, who—upon being asked what the future of the telephone was—allegedly said: "I truly believe that one day, there will be a telephone in every town in America."

have become the dominant access medium in Asia, the most commonly used access technologies in the rest of the world are still based on already available cable types such as twisted-pair lines and coaxial cables [152]. The reason for the relatively low fiber penetration outside of Asia is economical rather than technological: it is often more cost-effective to re-use the available copper cables than to install new fiber optic cables. The roll-out of fiber-to-the-home (FTTH) is both cost-intensive and time-consuming [106, 222] due to the significant cost of "trenching" [64, 89], as well as due to the often lengthy bureaucratic processes associated with obtaining the necessary permissions [157, 158].

Rather than exclusively using fiber optic cables in the last-mile, many ISPs' strategy has therefore been to gradually extend the fiber network to a final distribution point that lies ever closer to the user premises. This strategy counteracts the dominant performance impairment of twisted-pair lines: their attenuation per unit distance, which increases with signal frequency f [5]. To illustrate this attenuation, the following equation expresses the magnitude of the transfer function of an idealized perfectly terminated and homogeneous twisted-pair cable [5].

$$|H(f)| = e^{-d\,\alpha(f)} \tag{1.1}$$

In (1.1), d is the cable length and $\alpha(f)$ is the frequency-dependent attenuation constant which can in turn be approximated as

$$\alpha(f) = k_1\sqrt{|f|} + k_2|f|, \tag{1.2}$$

for some positive real constants k_1 and k_2 [5]. Eq. (1.1) illustrates that, by extending the fiber network to a distribution point which lies closer to the user—i.e. by decreasing the twisted-pair cable length d—attenuation can be reduced across all frequencies. At higher frequencies, where attenuation may previously have been prohibitively high, communication can thus be enabled by reducing the cable length d. In turn, the increased frequency bandwidth that becomes available for communication enables higher data rates to be achieved.

The adopted strategy of gradually decreasing the distance between the optical network termination point and the user premises has lead to multiple generations of standards for communication over twisted-pair lines. According to the international telecommunications union (ITU), there are five such generations of DSL technologies: HDSL (ITU-T G.991.x series), ADSL (ITU-T G.992.x series), VDSL (ITU-T G.993.x series), G.fast (ITU-T G.970x series), and—most recently—G.mgfast (ITU-T G.971x series). An overview of these DSL generations is given in Table 1.1.[2]

[2]Note that the data in Table 1.1 constitutes a simplified summarization of the existing DSL standards. In reality, each series of recommendations contains multiple standards and many of these standards define multiple profiles. Each of these profiles employs a different bandwidth and is therefore able to achieve a different aggregate data rate $R_{\max}$.

Table 1.1: DSL generations as defined by the ITU-T, source: [120, 185].

	ITU-T	$d_{\max}$	Bandwidth	$R_{\max}$ (aggregated)
HDSL	G.991.x	3.7 km	350 - 485 kHz	1.6 - 4 Mbit/s
ADSL	G.992.x	6 km	1.1 - 2.2 MHz	6.6 - 25 Mbit/s
VDSL	G.993.x	2.5 km	8.8 - 35.2 MHz	54 - 400 Mbit/s
G.fast	G.970x	400 m	106 - 212 MHz	1 - 2 Gbit/s
G.mgfast	G.971x	100 m	424 - 848 MHz	5 - 10 Gbit/s

Each of the DSL generations has been designed with a target network topology in mind. An overview of these network topologies and their associated nomenclature can be found in Figure 1.1. HDSL and ADSL were designed to be operated directly on twisted-pair lines as they were used in the plain old telephone system (POTS) network. These twisted-pair lines connect the digital subscriber line access multiplexer (DSLAM, pronounced "dee-slam") in the central office (CO) to the customer premises equipment (CPE). In the target network topology of VDSL, the first part of the twisted pair cable is replaced with a fiber optic cable. This fiber optic cable connects the optical line terminal (OLT) in the CO to an access node (AN) in the remote terminal (RT). The AN is in turn connected to the CPE using a twisted-pair line. This network topology is commonly referred to as fiber-to-the-curb or fiber-to-the-cabinet (FTTC). In the target network topology of G.fast—which is commonly referred to as fiber-to-the-distribution-point (FTTdp)—the fiber optic cable is extended even further, and is terminated in the distribution point unit (DPU). Finally, G.mgfast will mostly be used to connect apartments in larger multi-dwelling units. Its target network topology is therefore referred to as fiber-to-the-building (FTTB).

Each DSL generation's increase in data rate is thus enabled by reducing the length of the twisted-pair lines, which in turn leads to higher bandwidths becoming available for data transmission. An important disadvantage of using a higher bandwidth however, is that it increases interference between the different signals in the DSL network. With each new generation of DSL networks, the resulting interference problems have become more severe. Accordingly, with each generation of DSL technology, new solutions have been proposed to deal with the increasingly problematic interference. The following section gives a detailed overview of different types of interference in DSL networks, as well as an overview of state-of-the-art strategies that have been developed to deal with each type of interference.

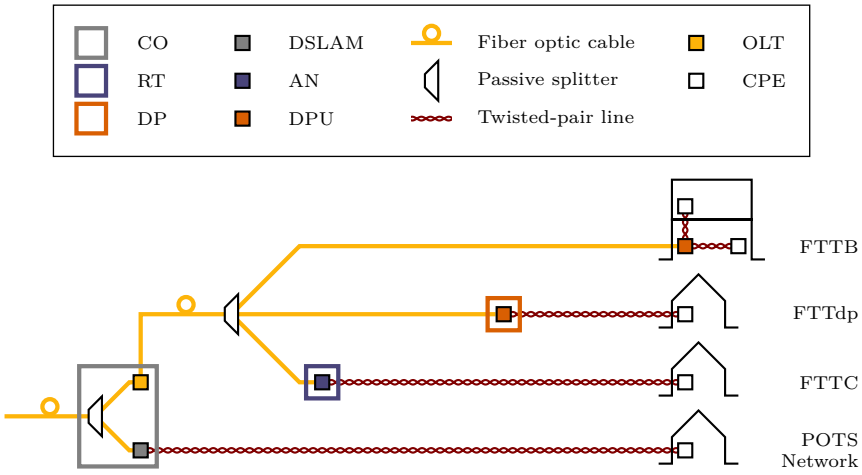


Figure 1.1: Schematic overview of fiber-to-the-X (FTTx) network topologies.

1.1 Interference in DSL networks

This section provides a detailed overview of three prominent types of interference, and presents strategies to deal with each type of interference that are currently being—or have previously been—employed in DSL networks.

1.1.1 Inter-symbol interference

As was illustrated by (1.1), twisted-pair lines are characterized by a frequency-selective attenuation. In the time-domain, this frequency selectivity corresponds to the channel being characterized by long channel impulse responses (CIRs). To make the problem description more concrete, consider the following DSL channel model

$$y[t'] = (h * x)[t'] + z[t'], \tag{1.3}$$

where $y[t']$ is the received signal and $z[t']$ is the noise. It is noted that t' does not represent time, but the discretized time index. Moreover, $(h * x)[t']$ denotes the convolution of the transmitted signal $x[t']$ and the CIR $h[t']$, i.e.

$$(h * x)[t'] = \sum_{\tau=0}^{L} h[\tau]\, x[t' - \tau] \tag{1.4}$$

with L the channel order. In single-carrier systems—such as HDSL—each sample in the transmitted signal $x[t']$ contains a real symbol that is to be

transmitted.[3] Each sample of the received signal $y[t']$ then contains a linear combination of $L+1$ transmitted symbols $x[t']$. The interference term in the DSL channel model can be exposed by rewriting (1.3) as

$$y[t'] = x[t']\,h[0] + \sum_{\tau=1}^{L} h[\tau]\,x[t'-\tau] + z[t']. \tag{1.5}$$

The second term in the right-hand side of (1.5) is referred to as inter-symbol interference (ISI). Even without a detailed mathematical description, it is intuitively clear that increasing the bandwidth—i.e. decreasing the sampling period between subsequent samples of the signals $x[t']$, $y[t']$ and $z[t']$—results in a longer impulse response $h[t']$ for the same twisted-pair line, thus aggravating the effect of ISI.

A first interference management technique one could consider to reduce the ISI consists of linear filtering or linear equalization. Linear equalization is however known to result in significant noise enhancement [19], and is therefore considered to be inferior when compared to its two main competitors: decision-feedback equalization (DFE) and discrete multi-tone (DMT) modulation. Assuming the CIR is known, a DFE receiver would estimate the transmitted signals as

$$\hat{x}[t'] = (f_{\mathrm{FFF}} * y)[t'] - (f_{\mathrm{DFF}} * \dot{x})[t'-1], \tag{1.6}$$

$$\dot{x}[t'] = \mathrm{decide}(\hat{x}[t']), \tag{1.7}$$

where $f_{\mathrm{FFF}}[t']$ and $f_{\mathrm{DFF}}[t']$ are respectively referred to as the feedforward filter and the decision feedback filter, and where it has been assumed that $f_{\mathrm{FFF}}[t'] = 0$ and $f_{\mathrm{DFF}}[t'] = 0$ for $t' < 0$. DMT modulation, on the other hand, is a multi-carrier modulation technique that is based on the fast Fourier transform (FFT).[4] The choice between DFE and DMT modulation for DSL systems was the subject of heated debates in the early 1990's [43]. DMT modulation came out as the superior choice due to its greater immunity to impulse noise [19], due to multiple DFEs being required to guarantee performance in the presence of deep fades [43], and—perhaps most importantly—due to DMT's ability to leave some frequency-bands unused, enabling the simultaneous transmission of voice and data signals. DMT modulation has been employed in all DSL technologies since ADSL, and it is DMT modulation that enabled the simultaneous reach, data rate, and bandwidth increase in ADSL as compared to HDSL [43].

[3] The transmitted symbols in HDSL were drawn from an uncoded 4-PAM modulation, which was referred to as "two-binary, one quaternary" (2B1Q) [43].

[4] A mathematical description of DMT modulation is given in the next subsection.

Discrete multi-tone modulation

DMT is a multi-carrier modulation technique. The DMT transmitter first groups κ complex QAM symbols $X_k[t]$ together into frequency-domain DMT symbols $\boldsymbol{X}[t] \triangleq [X_0[t], X_1[t], \ldots, X_{\kappa-1}[t]]^{\mathrm{T}}$,[5] with κ the employed DFT/IDFT size (see below). The frequency-domain DMT symbols are then transformed to the time domain by application of a discrete Fourier transform (DFT). After adding a cyclic prefix (CP) of length ν to the result, the time-domain DMT symbols $\boldsymbol{x}[t]$ are obtained. Summarizing, the time-domain DMT symbols are obtained from the frequency-domain DMT symbols as

$$\boldsymbol{x}[t] = \begin{bmatrix} \mathbf{0}_{(\kappa-\nu)\times\nu} & \mathbf{I}_{\nu} \\ & \mathbf{I}_{\kappa} \end{bmatrix} \mathcal{F}_{\kappa}^{-1}\left(\boldsymbol{X}[t]\right), \tag{1.8}$$

where $\mathcal{F}_{\kappa}^{-1}(\cdot)$ is the inverse discrete Fourier transform (IDFT) operator. Finally, the time-domain DMT signal is obtained by concatenating the elements of $\boldsymbol{x}[t]$.

$$x[t(\kappa+\nu)+k] = [\boldsymbol{x}[t]]_k \tag{1.9}$$

In (1.9), $[\boldsymbol{a}]_k$ denotes the element in vector $\boldsymbol{a}$ with index k, where—as in the remainder of this chapter—zero-based indexing is used.

DMT systems operate in baseband, resulting in the requirement that the time-domain DMT symbols $\boldsymbol{x}[t]$ be real-valued. In (1.8), this requirement is satisfied if and only if $\boldsymbol{X}[t]$ admits the following Hermitian symmetric structure:

$$X_{k^*}[t] = X_k^*[t], \forall k, \tag{1.10}$$

where—with a slight abuse of notation—k^* is the index of the subcarrier that is the Hermitian symmetric of subcarrier k, i.e. where $k^* \triangleq (\kappa - k) \mod \kappa$. The DC and Nyquist subcarriers should contain real PAM symbols in order to satisfy (1.10), while all other subcarriers can be modulated with complex QAM symbols. As DSL systems typically do not use the DC and Nyquist subcarriers, it will be assumed in Chapter 1 that $X_0[t] = 0$ and $X_{\kappa/2}[t] = 0$. The DFT size κ is assumed to be even, such that the number of complex subcarriers is given by $K = \kappa/2 - 1$.

The DMT receiver estimates the transmitted symbols based on the $\kappa \times 1$ received signal vector $\boldsymbol{y}[t]$, the elements of which are given as

$$[\boldsymbol{y}[t]]_k = y\left[t(\kappa+\nu)+\nu+k\right]. \tag{1.11}$$

[5] Note that 0-based indexing is used to address rows, columns, and elements of matrices in Chapter 1.

If $\nu \geq L$, then combining (1.3) and (1.11) yields

$$\boldsymbol{y}[t] = \left[\begin{array}{c|cccccc} & h[L] & \cdots & h[1] & h[0] & 0 & \cdots & 0 \\ & 0 & \ddots & & \ddots & \ddots & \ddots & \vdots \\ \mathbf{0}_{(\nu-L)\times N} & \vdots & \ddots & h[L] & \cdots & h[1] & h[0] & 0 \\ & 0 & \cdots & 0 & h[L] & \cdots & h[1] & h[0] \end{array}\right] \boldsymbol{x}[t] + \boldsymbol{z}[t]. \tag{1.12}$$

Equation (1.12) illustrates the first role of the CP: if $\nu \geq L$, then $\boldsymbol{y}[t]$ is only affected by the t-th DMT symbol $\boldsymbol{x}[t]$. In other words, if $\nu \geq L$, then $\boldsymbol{y}[t]$ is free of ISI from neighboring DMT symbols.

The CP serves a second purpose, which can be illustrated by substituting (1.8) into (1.12).

$$\boldsymbol{y}[t] = \left[\begin{array}{cccccccc} h[0] & 0 & \cdots & 0 & h[L] & \cdots & h[2] & h[1] \\ h[1] & h[0] & 0 & \cdots & 0 & h[L] & \cdots & h[2] \\ \vdots & \ddots & \ddots & \ddots & & \ddots & \ddots & \vdots \\ \vdots & & \ddots & \ddots & \ddots & & \ddots & h[L] \\ h[L] & \cdots & \cdots & h[1] & h[0] & 0 & \cdots & 0 \\ 0 & \ddots & & & \ddots & \ddots & \ddots & \vdots \\ \vdots & \ddots & h[L] & \cdots & \cdots & h[1] & h[0] & 0 \\ 0 & \cdots & 0 & h[L] & \cdots & \cdots & h[1] & h[0] \end{array}\right] \mathcal{F}_\kappa^{-1}\left(\boldsymbol{X}[t]\right) + \boldsymbol{z}[t] \tag{1.13}$$

The large matrix in (1.13) is a *circulant matrix*, the multiplication with which executes a circular convolution between its first column and the vector it is multiplied with. Eq. (1.13) can thus be rewritten as

$$\boldsymbol{y}[t] = \boldsymbol{h} \circledast \mathcal{F}_\kappa^{-1}\left(\boldsymbol{X}[t]\right) + \boldsymbol{z}[t] \tag{1.14}$$

where $[\boldsymbol{h}]_k = h[k]$,[6] and where the circular convolution operator $\circledast$ is defined as

$$[\boldsymbol{a} \circledast \boldsymbol{b}]_k \triangleq \sum_{l=0}^{\kappa-1} [\boldsymbol{a}]_l \, [\boldsymbol{b}]_{k-l \mod \kappa}. \tag{1.15}$$

Applying the circular convolution theorem—which states that

$$\boldsymbol{c} = \boldsymbol{a} \circledast \boldsymbol{b} \iff \mathcal{F}_\kappa\left(\boldsymbol{c}\right) = \mathcal{F}_\kappa\left(\boldsymbol{a}\right) \circ \mathcal{F}_\kappa\left(\boldsymbol{b}\right) \tag{1.16}$$

with $\circ$ the Hadamard product operator—to (1.14), and taking the DFT of both sides yields

$$\boldsymbol{Y}[t] \triangleq \mathcal{F}_\kappa\left(\boldsymbol{y}[t]\right) = \mathcal{F}_\kappa\left(\boldsymbol{h}\right) \circ \boldsymbol{X}[t] + \mathcal{F}_\kappa\left(\boldsymbol{z}[t]\right). \tag{1.17}$$

[6] It is assumed that $h[k] = 0$ for $k > L$.

Finally, after defining $H_k \triangleq [\mathcal{F}_\kappa(\boldsymbol{h})]_k$ and $Z_k[t] \triangleq [\mathcal{F}_N(\boldsymbol{z}[t])]_k$, (1.17) can be rewritten as

$$Y_k[t] = H_k\, X_k[t] + Z_k[t]. \tag{1.18}$$

Assuming the CIR is known, a DMT receiver thus estimates the transmitted QAM symbols as

$$\dot{X}_k[t] = \text{decide}\left(Y_k[t]/H_k\right). \tag{1.19}$$

Equation (1.14) has revealed the second role of the CP: it turns the linear convolution with the CIR into a circular convolution. As a result, the circular convolution theorem dictates that there is no interference between subcarriers of the same DMT symbol, as is illustrated by (1.18). Put differently, the CP prevents inter-carrier interference (ICI).

An important advantage of DMT modulation is that it enables adapting the constellation size on each subcarrier k to the achieved signal-to-noise ratio (SNR). From (1.18), it is immediately seen that the SNR on subcarrier k can be calculated as

$$\gamma_k = \frac{S_k\,|H_k|^2}{\sigma_k^2}, \tag{1.20}$$

where $S_k = \mathbb{E}\left\{|X_k[t]|^2\right\}$ is the transmitted symbol power and $\sigma_k^2 = \mathbb{E}\left\{|Z_k[t]|^2\right\}$ is the noise power. If a given target bit error rate (BER) is to be achieved on all subcarriers, then the maximum constellation size—expressed in number of bits per QAM symbol—can be calculated as[7]

$$b_k = \log_2\left(1 + \frac{\gamma_k}{\Gamma}\right). \tag{1.21}$$

The quantity b_k is commonly referred to as the *bit loading*. In deriving (1.21), it is usually assumed that $Z_k[t]$ has a Gaussian circularly symmetric distribution. Moreover, Γ represents the signal-to-noise ratio gap-to-capacity or SNR gap, the value of which depends on the target BER and on the employed (possibly coded) modulation [19, 182]. For example, if uncoded QAM symbols are transmitted and a target BER of 10^{-5} is to be achieved, then the value of the SNR gap that should be employed in (1.21) is 8.4 dB [2]. The SNR gap in DSL systems often also includes an additional noise margin, which serves as protection against impulse noise. Finally, the achieved data rate can be calculated as

$$R = \frac{f_\text{s}}{\kappa + \nu} \sum_{k=1}^{K} b_k, \tag{1.22}$$

with f_s the employed sample frequency.

[7] The expression (1.21) is not valid for PAM symbols. It has however been assumed that the real subcarriers are not used, i.e. that $X_0[t] = 0$ and $X_{\kappa/2}[t] = 0$.

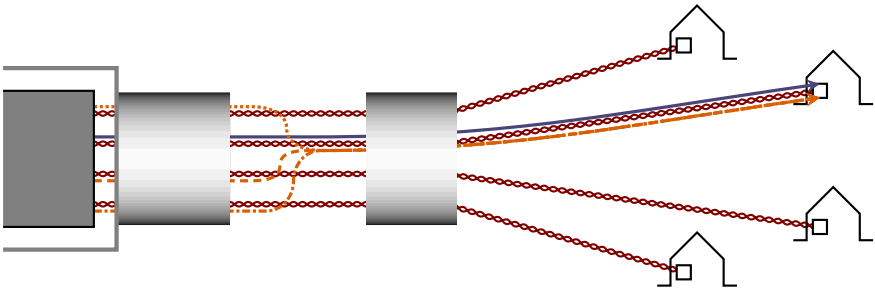


Figure 1.2: Far-end crosstalk in downstream DSL. The solid blue arrow represents the direct signal, the dashed or dotted red arrows represent the FEXT signals.

1.1.2 Far-end crosstalk

The schematic representation in Figure 1.1 has ignored one important aspect of DSL network topologies, namely that each DPU is typically connected to multiple CPEs.[8] This aspect is better represented in Figure 1.2, which depicts a single DPU with four CPEs connected to it. At the DPU, the twisted-pair lines are typically bundled together in a single cable binder which, after a certain distance, branches out towards the different CPEs. The dense packing of twisted-pair lines inside the cable binder results in capacitive and inductive coupling, in turn leading to signal leakage—i.e. to signals transmitted by the DPU on one twisted-pair line being received by all CPEs. Conversely, each CPE will receive a mixture of the signals that have been transmitted by the DPU on the different twisted-pair lines—see Figure 1.2 for a graphical representation of this phenomenon.

The time-domain channel model of (1.3) is readily extended to the multi-user setting. This extension yields the following expression for $y_n[t']$, the received signal on line n:

$$y_n[t'] = (h_{nn} * x_n)[t'] + \sum_{\substack{m=1 \\ m \neq n}}^{N} (h_{nm} * x_m)[t'] + z_n[t'], \tag{1.23}$$

where N is the number CPEs connected to the DPU, $z_n[t']$ is the noise on line n, $x_m[t']$ is the signal transmitted on line m, and $h_{nm}[t']$ is the impulse response of the channel between transmitter m and receiver n. CIRs $h_{nn}[t']$ correspond to the direct channels, and CIRs $h_{nm}[t']$ with $m \neq n$ correspond to

[8] From here on, "DPU" will be used as a catch-all term that applies to any hardware terminating the fiber optic network and to which CPEs are connected using twisted-pair lines.

the so-called far-end crosstalk (FEXT) channels. In general, the second term in the right-hand-side of (1.23) is referred to as FEXT.

If the CP length is higher than the CIR order of all direct and FEXT channels, then the single user model in (1.18) can be straightforwardly extended to the following multi-user channel model:

$$Y_{k,n}[t] = H_{k,nn}\, X_{k,n}[t] + \sum_{\substack{m=1 \\ m \neq n}}^{N} H_{k,nm}\, X_{k,m}[t] + Z_{k,n}[t], \tag{1.24}$$

where $H_{k,nm} = \left[\mathcal{F}_\kappa \left([h_{nm}[0], h_{nm}[1], \ldots, h_{nm}[\kappa]]^{\mathrm{T}}\right)\right]_k$ is the frequency response between transmitter m and receiver n evaluated on subcarrier k, $X_{k,m}[t]$ is the symbol transmitted on line m and on subcarrier k, and $Z_{k,n}[t]$ is the noise at the DMT receiver's DFT output on line n and on subcarrier k. Respectively grouping the signals and the frequency response values together in vectors and matrices, the multi-user channel model as in (1.24) becomes

$$\boldsymbol{Y}_k[t] = \mathbf{H}_k\, \boldsymbol{X}_k[t] + \boldsymbol{Z}_k[t], \tag{1.25}$$

with $[\boldsymbol{X}_k[t]]_m = X_{k,m}[t]$, $[\boldsymbol{Y}_k[t]]_n = Y_{k,n}[t]$, $[\boldsymbol{Z}_k[t]]_n = Z_{k,n}[t]$, and $[\mathbf{H}_k]_{nm} = H_{k,nm}$.

In DSL systems, it is quite common to treat the (residual) interference as noise. If the FEXT-terms in (1.25) are indeed interpreted as additional noise terms, then the achievable bit loading should not be calculated based on the SNR, but rather based on the signal-to-interference-plus-noise ratio (SINR). The SINR on line n and on subcarrier k can be calculated as

$$\gamma_{k,n} = \frac{S_{k,n}\, |H_{k,nn}|^2}{\sum_{m \neq n} S_{k,m}\, |H_{k,nm}|^2 + \sigma^2_{k,n}}, \tag{1.26}$$

where, similar to before, $S_{k,n} = \mathbb{E}\left\{|X_{k,n}[t]|^2\right\}$ and $\sigma^2_{k,n} = \mathbb{E}\left\{|Z_{k,n}[t]|^2\right\}$. If the interference-plus-noise is Gaussian, then the SNR-gap approximation of (1.21) is still valid and the maximum achievable bit loading on line n and on subcarrier k can be calculated as

$$b_{k,n} = \log_2\left(1 + \frac{\gamma_{k,n}}{\Gamma}\right). \tag{1.27}$$

In literature, it is often argued that the FEXT is Gaussian—i.e. that the approximation in (1.27) is valid—under the assumption that N is large [32, 85, 113, 136, 188]. Finally, the achieved data rate on line n can be calculated as

$$R_n = \frac{f_{\mathrm{s}}}{\kappa + \nu} \sum_{k=1}^{K} b_{k,n}. \tag{1.28}$$

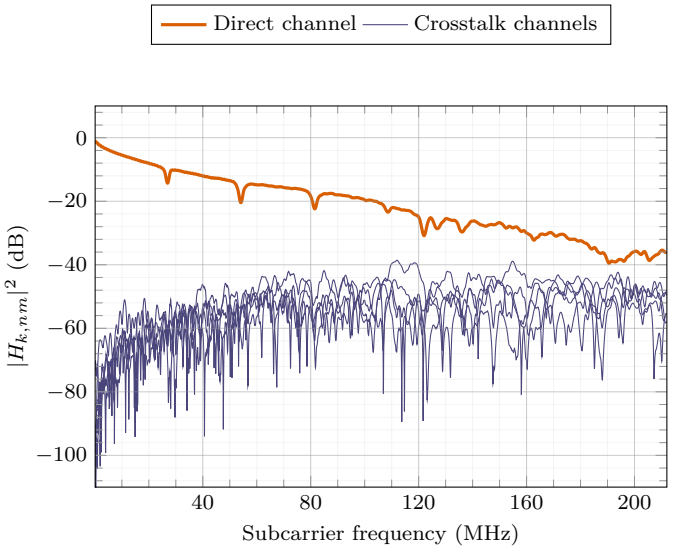


Figure 1.3: FEXT channels.

To illustrate the severity of the FEXT problem, Figure 1.3 plots the squared magnitude of the direct and the FEXT channels as seen by a single CPE in a 100 m-long twisted-pair line across the frequency range employed in the 212 MHz-profile of G.fast. From (1.26) and (1.27), it is known that the extent of the FEXT's impact depends on the squared magnitude of the FEXT channels relative to the squared magnitude of the direct channels. Figure 1.3 thus demonstrates that the impact of FEXT is typically more severe at higher frequencies, where the direct channel is attenuated strongly and the FEXT channels achieve their highest values.

The ensemble of techniques that deal with FEXT is commonly referred to as dynamic spectrum management (DSM). Three tiers of DSM are distinguished. Level 1 DSM manages each line individually, and at most introduces some politeness in order to mitigate the effects of FEXT. Level 2 DSM manages the transmit powers $S_{k,n}$ of different lines jointly, in order to cooperatively mitigate the effects of FEXT. This technique is also referred to as spectrum coordination. Finally, level 3 DSM consists of coordinating multiple lines on a signal-level, and is commonly referred to as signal coordination or vectoring. The following subsections will elaborate further on Level 2 and Level 3 DSM.

Level 2 DSM—spectrum coordination

Spectrum coordination methods—also often referred to as power or resource allocation methods—reduce the FEXT impact by choosing the transmit powers $S_{k,n}$ such that a good data rate is achieved by all CPEs. The transmit powers $S_{k,n}$ are often determined by solving an optimization problem of the following form:

$$\underset{S_{k,n}\in\mathbb{R}_+,\forall k,n}{\text{maximize}} \quad \sum_{n=1}^{N} \omega_n R_n \tag{1.29a}$$

$$\text{s.t.} \quad \sum_{k=1}^{K} S_{k,n} \leq P_{\text{tot}},\ \forall n \tag{1.29b}$$

$$S_{k,n} \leq S_k^{\text{mask}},\ \forall k, n \tag{1.29c}$$

where ω_n is the weight associated with user n, and where the relation between R_n and each $S_{k,m}$ is determined by (1.26), (1.27), and (1.28). Moreover, (1.29b) represents the aggregate transmit power constraint—where the value of P_{tot} depends on the DSL generation under consideration—and (1.29c) is the spectral mask constraint, which is put in place to limit both crosstalk and RFI egress. The optimization problem in (1.29) is referred to as the weighted sum rate (WSR) maximization problem.

The WSR problem in (1.29) is non-convex and NP-hard [118]. As a result, many power allocation algorithms have been developed over the years. WSR-based power allocation algorithms range from globally optimal [32, 137, 194]—with an asymptotic complexity that is exponential in the number of CPEs— over locally optimal [31, 147, 149, 188, 213]—i.e. converging to a stationary point of the WSR maximization problem—to heuristics that achieve a Nash equilibrium between different competing users [37, 163] or that mimic the solutions obtained by (locally) optimal algorithms [30, 84, 113].

Another relevant concept in the context of spectrum coordination—as well as in the context of dynamic spectrum management in general—is the rate region. The rate region is the set of all rate-vectors that can be achieved with a feasible power allocation. To define the rate region a bit more rigorously, first define the set $\mathcal{S}$ containing all feasible power allocations:

$$\mathcal{S} \triangleq \prod_{n=1}^{N} \left\{ \boldsymbol{S} \in \mathbb{R}_+^K \mid \boldsymbol{S} \leq \boldsymbol{S}_{\text{mask}} \text{ and } \mathbf{1}_{K\times 1}^{\text{T}} \boldsymbol{S} \leq P_{\text{tot}} \right\} \tag{1.30}$$

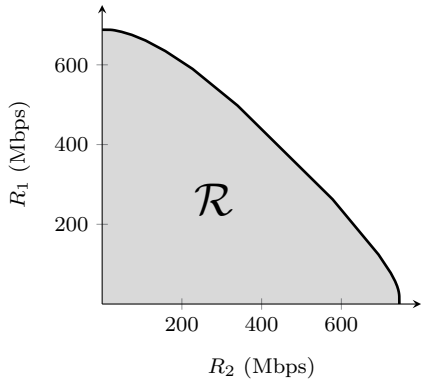


Figure 1.4: Example rate region of a 2-CPE G.fast system. This figure was originally published in [200] (©IEEE 2017).

with $\boldsymbol{S}_{\text{mask}} = \left[S_1^{\text{mask}}, \ldots, S_K^{\text{mask}}\right]^{\text{T}}$. Moreover, let $R_n(\boldsymbol{S})$ be the achievable data rate on line n given some feasible power vector $\boldsymbol{S} \in \mathcal{S}$.[9] The rate region $\mathcal{R}$ can then be defined as

$$\mathcal{R} \triangleq \left\{\boldsymbol{r} \in \mathbb{R}_+^N \mid \exists \boldsymbol{S} \in \mathcal{S} : \boldsymbol{r} \leq \boldsymbol{R}(\boldsymbol{S})\right\} \tag{1.31}$$

with $\boldsymbol{R}(\boldsymbol{S}) = [R_1(\boldsymbol{S}), \ldots, R_N(\boldsymbol{S})]^{\text{T}}$. As an example, Figure 1.4 plots the rate region of a 2-CPE G.fast system.

It should be noted that many spectrum coordination approaches determine the transmit powers $S_{k,n}$ by solving an optimization problem that is different from the WSR maximization problem in (1.29). Most notably, these alternative optimization problems include fairness-based formulations—with objective functions targeting, e.g., (weighted) max-min fairness [116], proportional fairness [118], harmonic-rate fairness [118], or generalized α-fair fairness [109]—and formulations that add QoS constraints of the form $R_n^{\min} \leq R_n$ [32, 85]. The main difference between these alternative formulations is that they will select a different Pareto-optimal operating point on the rate region. The Pareto set, i.e. the set of Pareto-optimal operating points, can be defined as

$$\mathcal{P} \triangleq \left\{\boldsymbol{r} \in \mathcal{R} \mid \nexists \boldsymbol{r}' \in \mathcal{R} : \boldsymbol{r} < \boldsymbol{r}'\right\}. \tag{1.32}$$

Using the same argument as is used in [118] to show that the duality gap between the optimization problem in (1.29) and its Lagrange dual is zero, it can also be shown that rate region $\mathcal{R}$ of a DMT system is convex if the number of subcarriers $K \to \infty$. As a result, it can be concluded that—for large enough

[9] Note that $R_n(\boldsymbol{S})$ can be calculated using (1.26), (1.27), and (1.28).

values of K—each Pareto-optimal point $\boldsymbol{R} \in \mathcal{P}$ is a solution to the WSR maximization problem for some $\boldsymbol{\omega}$ [32].

Spectrum coordination is able to yield significant performance improvements if the FEXT is not too severe. It has therefore been considered in ADSL, which—as it only uses frequencies below 2.2 MHz—suffered from levels of FEXT that were still manageable using spectrum coordination techniques. When the FEXT channels are stronger, it can however be shown that the optimization problem in (1.29)—with P_{tot} large and all weights ω_n being equal—has many frequency-division-multiple-access-type (FDMA-type) stationary points [71]. Stronger FEXT thus makes the optimization problem in (1.29) "more non-convex", and may result in locally optimal algorithms getting stuck in suboptimal FDMA-type stationary points.

Level 3 DSM—vectoring

When the FEXT channels are strong, additional performance gains can be obtained by employing vectoring techniques, i.e. by jointly pre-processing (or post-processing) signals intended for (or coming from) the different CPEs to remove FEXT. Vectoring has been introduced as an optional part of VDSL, and has become a mandatory part of G.fast and G.mgfast. A distinction is made between receiver-side vectoring and transmitter-side vectoring.

In receiver-side vectoring, the received signals in $\boldsymbol{Y}_k[t]$ are jointly processed to obtain a received signal $\hat{\boldsymbol{X}}_k[t]$ containing little or no interference. More concretely, the received signal is obtained as

$$\hat{\boldsymbol{X}}_k[t] = \mathbf{R}_k^{\mathrm{H}} \boldsymbol{Y}_k[t] = \mathbf{R}_k^{\mathrm{H}} \mathbf{H}_k \boldsymbol{X}_k[t] + \mathbf{R}_k^{\mathrm{H}} \boldsymbol{Z}_k[t], \tag{1.33}$$

where $\mathbf{R}_k$ is referred to as the receive matrix of subcarrier k. This joint processing of the signals in $\boldsymbol{Y}_k[t]$ can only be implemented if the considered signals are all available to the receiver, such that receiver-side vectoring can only be applied in the upstream (US) channel—i.e. the channel in which the CPEs are the transmitters and the DPU is the receiver. When receiver-side vectoring is applied, it is immediately seen that the SINR can be calculated as

$$\gamma_{k,n}^{\text{US}} = \frac{S_{k,n} \left| \boldsymbol{r}_{k,n}^{\mathrm{H}} \boldsymbol{h}_{k,n} \right|^2}{\sum_{m \neq n} S_{k,m} \left| \boldsymbol{r}_{k,n}^{\mathrm{H}} \boldsymbol{h}_{k,m} \right|^2 + \boldsymbol{r}_{k,n}^{\mathrm{H}} \boldsymbol{\Sigma}_k \boldsymbol{r}_{k,n}} \tag{1.34}$$

where $\mathbf{R}_k = [\boldsymbol{r}_{k,1}, \ldots, \boldsymbol{r}_{k,N}]$ and $\mathbf{H}_k = [\boldsymbol{h}_{k,1}, \ldots, \boldsymbol{h}_{k,N}]$. Moreover, $\boldsymbol{\Sigma}_k = \mathbb{E}\{\boldsymbol{Z}_k[t](\boldsymbol{Z}_k[t])^{\mathrm{H}}\}$ is the noise covariance matrix on subcarrier k. A seemingly obvious choice for $\mathbf{R}_k$, is to let it eliminate all FEXT by setting

$$\mathbf{R}_k^{\mathrm{H}} = \operatorname{diag}(\operatorname{diag}(\mathbf{H}_k))\mathbf{H}_k^{-1}. \tag{1.35}$$

This particular choice of $\mathbf{R}_k$ (1.35) is referred to as the zero-forcing (ZF) receive matrix. Finally, substituting (1.35) into (1.34) yields the following simplified SINR expression for ZF receivers.

$$\gamma_{k,n}^{\mathrm{US}} = \frac{S_{k,n} \left| H_{k,nn} \right|^2}{\boldsymbol{r}_{k,n}^{\mathrm{H}} \boldsymbol{\Sigma}_k \boldsymbol{r}_{k,n}} \tag{1.36}$$

In transmitter-side vectoring, the signals-to-be-transmitted $\boldsymbol{X}_k[t]$ are jointly processed prior to transmission such that, at the receiver, $\boldsymbol{Y}_k[t]$ contains little or no interference. More concretely, the transmitted signal is generated as

$$\tilde{\boldsymbol{X}}_k[t] = \mathbf{T}_k \boldsymbol{X}_k[t], \tag{1.37}$$

resulting in the following channel equation.

$$\boldsymbol{Y}_k[t] = \mathbf{H}_k^{\mathrm{H}} \mathbf{T}_k \boldsymbol{X}_k[t] + \boldsymbol{Z}_k[t] \tag{1.38}$$

In (1.38), $\mathbf{T}_k$ is referred to as the precoding matrix—transmitter-side vectoring is also commonly referred to as precoding. It is noted that, w.l.o.g., $\mathbf{H}_k^{\mathrm{H}}$ is used instead of $\mathbf{H}_k$ in the context of transmitter-side vectoring to simplify notation. This joint processing of the signals $\boldsymbol{X}_k[t]$ can only be implemented if the considered signals are all available to the transmitter, such that precoding can only be applied in the downstream (DS) channel—i.e. the channel in which the DPU is the transmitter and the CPEs are the receivers. When precoding is applied, it is immediately seen that the SINR can be calculated as

$$\gamma_{k,n}^{\mathrm{DS}} = \frac{S_{k,n} \left| \boldsymbol{h}_{k,n}^{\mathrm{H}} \boldsymbol{t}_{k,n} \right|^2}{\sum_{m \neq n} S_{k,m} \left| \boldsymbol{h}_{k,n}^{\mathrm{H}} \boldsymbol{t}_{k,m} \right|^2 + \sigma_{k,n}^2}, \tag{1.39}$$

where $\mathbf{T}_k = [\boldsymbol{t}_{k,1}, \ldots, \boldsymbol{t}_{k,N}]$. As before, a seemingly obvious choice for $\mathbf{T}_k$, is to let it eliminate all FEXT by setting

$$\mathbf{T}_k^{\mathrm{H}} = \mathrm{diag}(\mathrm{diag}(\mathbf{H}_k)) \mathbf{H}_k^{-1}. \tag{1.40}$$

This particular choice of $\mathbf{T}_k$ is referred to as the diagonalizing or zero-forcing precoding matrix. Substituting (1.40) into (1.39) yields the following simplified expression for the SINR.

$$\gamma_{k,n}^{\mathrm{DS}} = \frac{S_{k,n} \left| H_{k,nn} \right|^2}{\sigma_{k,n}^2} \tag{1.41}$$

When vectoring is used, spectrum coordination can be employed to further improve the data rate. Moreover, as the SINR expressions in (1.36) and (1.41)

are linear functions of the transmit powers, it is readily seen that the ZF precoder and ZF receiver yield a concave objective function in the WSR maximization problem. For the upstream channel, this immediately implies that the resulting WSR maximization problem is convex. In the downstream channel however, it should be taken into account that the transmitter-side vectoring affects the power constraints as follows.

$$\sum_{k=1}^{K} \operatorname{diag}\left(\mathbf{T}_k \operatorname{diag}\left([S_{k,1},\ldots,S_{k,N}]^{\mathrm{T}}\right)\mathbf{T}_k^{\mathrm{H}}\right) \leq \mathbf{1}_{N\times 1} P_{\mathrm{tot}} \tag{1.42a}$$

$$\operatorname{diag}\left(\mathbf{T}_k \operatorname{diag}\left([S_{k,1},\ldots,S_{k,N}]^{\mathrm{T}}\right)\mathbf{T}_k^{\mathrm{H}}\right) \leq \mathbf{1}_{N\times 1} S_k^{\mathrm{mask}} \tag{1.42b}$$

As the power constraints in (1.42) are linear functions of $S_{k,n}$, it is seen that the DS WSR maximization problem with ZF precoding matrices is convex as well.

Even though the ZF vectoring matrices seem an obvious choice, they have important disadvantages associated with them. In the upstream channel, the linear ZF receiver is known to cause noise enhancement if the channel matrix $\mathbf{H}_k$ is ill-conditioned. In the downstream channel, on the other hand, use of the linear ZF precoder leads to an undesired power scaling of the transmitted signals if the $\mathbf{H}_k$ is ill-conditioned [67]. One possible strategy to counteract these noise enhancement and power scaling effects, is the use of optimal MMSE-based vectoring matrices [60, 61, 108, 111, 193, 195]. Achieving channel capacity however requires non-linear vectoring techniques such as successive interference cancellation (SIC) in the upstream channel, and decision-feedback transmit structures based on dirty paper coding (DPC) in the downstream channel [50,67].

In the upstream channel, noise enhancement can be prevented with the use of a non-linear SIC-based receiver, such as the generalized decision feedback equalizer (GDFE). The GDFE can be seen as a multiple-input multiple-output (MIMO) extension of the DFE, which was described in (1.6). The GDFE successively estimates the signals coming from the different CPEs as

$$\hat{X}_{k,n}[t] = \boldsymbol{r}_{k,n}^{\mathrm{H}}\big(\boldsymbol{Y}[t] - \sum_{m>n}^{N} \boldsymbol{h}_{k,m}\dot{X}_{k,m}[t]\big), \tag{1.43}$$

$$\dot{X}_{k,n}[t] = \operatorname{decide}(\hat{X}_{k,n}[t]), \tag{1.44}$$

where the signal decoding order is, w.l.o.g., chosen as the reverse CPE index order. Assuming no wrong decisions are made, the SINR of a GDFE receiver

can be calculated as

$$\gamma_{k,n}^{\text{GDFE}} = \frac{S_{k,n}\left|\boldsymbol{r}_{k,n}^{\mathcal{H}}\boldsymbol{h}_{k,n}\right|^2}{\sum_{m<n} S_{k,m}\left|\boldsymbol{r}_{k,n}^{\mathcal{H}}\boldsymbol{h}_{k,m}\right|^2 + \boldsymbol{r}_{k,n}^{\mathcal{H}}\boldsymbol{\Sigma}_k\boldsymbol{r}_{k,n}}. \tag{1.45}$$

If all FEXT is to be eliminated, one can choose the receive matrix based on the QR-decomposition of the channel matrix $\mathbf{H}_k = \mathbf{Q}_k\mathbf{U}_k$.[10]

$$\mathbf{R}_k = \mathbf{Q}_k \tag{1.46}$$

This particular choice of receive structure is referred to as ZF-GDFE. Assuming that the noise covariance matrix $\boldsymbol{\Sigma}_k$ is of the form $\sigma_k^2\mathbf{I}_N$, substituting (1.46) into (1.45) yields the following expression for the SINR of a ZF-GDFE receiver.

$$\gamma_{k,n}^{\text{GDFE}} = \frac{S_{k,n}\left|U_{k,nn}\right|^2}{\sigma_k^2} \tag{1.47}$$

In the above equation, $U_{k,nn}$ is defined by $[U_{k,11},\ldots,U_{k,NN}]^{\text{T}} = \text{diag}\,(\mathbf{U}_k)$. It can be seen from (1.47) that the ZF-GDFE receive matrix can no longer lead to noise enhancement, as the noise term in the denominator is no longer affected by the receive matrix.

In the downstream channel, power scaling can be prevented with the use of a non-linear DPC-based transmitter, such as the Tomlinson-Harashima precoder (THP) [69, 187]. DPC-based transmitters successively encode the signals intended for different CPEs, treating interference generated by previously encoded CPEs as side information [207]. More specifically, the THP precoder encodes the signals $X_{k,n}$ as

$$\tilde{X}_{k,n} = \mod_{A_{n,k}}\left[X_{k,n} - \sum_{m<n}\frac{\boldsymbol{h}_{k,n}^{\mathcal{H}}\boldsymbol{t}_{k,m}}{\boldsymbol{h}_{k,n}^{\mathcal{H}}\boldsymbol{t}_{k,n}}\tilde{X}_{k,n}\right], \tag{1.48}$$

where the signal encoding order is, w.l.o.g., chosen to be the same as the CPE index order. The modulo-operation in (1.48) is defined as

$$\mod_A[X] = X - A\,\text{sgn}(X)\left\lfloor\frac{|X|}{A}\right\rfloor \tag{1.49}$$

for $X \in \mathbb{R}$, with $\lfloor\cdot\rfloor$ the floor operator. If $X \in \mathbb{C}$, then the modulo-operation is defined as $\mod_A[X] = \mod_A[\Re(X)] + j\ \mod_A[\Im(X)]$. It is important that $A_{k,n}$ is chosen large enough, such that $X_{k,n} = \mod_{A_{k,n}}[X_{k,n}]$. In what

[10] As $\mathbf{R}_k$ already denotes the receive matrix, $\mathbf{U}_k$ is used instead to denote the upper triangular matrix in the QR-decomposition of $\mathbf{H}_k$.

follows, the significance of this lower bound on $A_{k,n}$ is that it implies the following.

$$X_{k,n} = \mod_{A_{k,n}} \left[\tilde{X}_{k,n} + \sum_{m<n} \frac{\boldsymbol{h}_{k,n}^{\mathcal{H}} \boldsymbol{t}_{k,m}}{\boldsymbol{h}_{k,n}^{\mathcal{H}} \boldsymbol{t}_{k,n}} \tilde{X}_{k,m} \right] \tag{1.50}$$

On the other hand, $A_{k,n}$ should not be chosen too large, as a large value for $A_{k,n}$ will result in a more significant power increase in $\tilde{X}_{k,n}$ due to the side-information-terms in (1.48). An appropriate choice for QAM constellations is $A_{k,n} = X_{k,n}^{\max} + d/2$, with d the distance between constellation points, and with $X_{k,n}^{\max}$ the maximum absolute value of any real or imaginary component achieved by any point in the constellation that $X_{k,n}$ is drawn from [67]. In M^2-QAM constellations, this choice for $A_{k,n}$ results in the transmit power increasing by a factor of $\frac{M}{M-1}$ [66]. The resulting power increase is thus not excessive, and becomes negligible for large constellations [66]. In what follows, the power increase factor will be ignored, i.e. it is assumed that $\mathbb{E}\{|\tilde{X}_{k,n}|^2\} = \tilde{S}_{k,n} = S_{k,n}$. After THP encoding, the transmitted signal is generated by multiplying $\tilde{\boldsymbol{X}}_k$ with the precoding matrix $\mathbf{T}_k$. The received signal after FEQ in CPE n can then be decomposed as follows.

$$\hat{X}_{k,n} = \frac{1}{\boldsymbol{h}_{k,n}^{\mathcal{H}} \boldsymbol{t}_{k,n}} \boldsymbol{h}_{k,n}^{\mathcal{H}} \mathbf{T}_k \tilde{\boldsymbol{X}}_k + \frac{1}{\boldsymbol{h}_{k,n}^{\mathcal{H}} \boldsymbol{t}_{k,n}} \boldsymbol{Z}_k \tag{1.51a}$$

$$= \tilde{X}_{k,n} + \sum_{m<n} \frac{\boldsymbol{h}_{k,n}^{\mathcal{H}} \boldsymbol{t}_{k,m}}{\boldsymbol{h}_{k,n}^{\mathcal{H}} \boldsymbol{t}_{k,n}} \tilde{X}_{k,m} + \sum_{m>n} \frac{\boldsymbol{h}_{k,n}^{\mathcal{H}} \boldsymbol{t}_{k,m}}{\boldsymbol{h}_{k,n}^{\mathcal{H}} \boldsymbol{t}_{k,n}} \tilde{X}_{k,m} + \frac{1}{\boldsymbol{h}_{k,n}^{\mathcal{H}} \boldsymbol{t}_{k,n}} \boldsymbol{Z}_k \tag{1.51b}$$

Assuming that the last two terms in (1.51b) are sufficiently small—specifically too small to trigger the modulo-operation when added to $X_{k,n}$—applying a second modulo operation to the FEQ output and considering (1.50) yields

$$\mod_{A_{k,n}} \left[\hat{X}_{k,n} \right] = X_{k,n} + \sum_{m>n} \frac{\boldsymbol{h}_{k,n}^{\mathcal{H}} \boldsymbol{t}_{k,m}}{\boldsymbol{h}_{k,n}^{\mathcal{H}} \boldsymbol{t}_{k,n}} \tilde{X}_{k,m} + \frac{1}{\boldsymbol{h}_{k,n}^{\mathcal{H}} \boldsymbol{t}_{k,n}} \boldsymbol{Z}_k. \tag{1.52}$$

As it has been assumed that $\tilde{S}_{k,n} = S_{k,n}$, the following expression for the SINR is thus obtained when THP is employed.

$$\gamma_{k,n}^{\text{THP}} = \frac{S_{k,n} \left| \boldsymbol{h}_{k,n}^{\mathcal{H}} \boldsymbol{t}_{k,n} \right|^2}{\sum_{m>n} S_{k,m} \left| \boldsymbol{h}_{k,n}^{\mathcal{H}} \boldsymbol{t}_{k,m} \right|^2 + \sigma_{k,n}^2} \tag{1.53}$$

If all FEXT is to be eliminated, one can choose the precoding matrix $\mathbf{T}_k$ based on the QR-decomposition of the channel matrix $\mathbf{H}_k = \mathbf{Q}_k \mathbf{U}_k$.

$$\mathbf{T}_k = \mathbf{Q}_k \tag{1.54}$$

This particular choice of precoding structure is referred to as ZF-THP, and has the following expression for the SINR associated with it—which can be obtained by substituting (1.54) into (1.53).

$$\gamma_{k,n}^{\mathrm{THP}} = \frac{S_{k,n} \left| U_{k,nn} \right|^2}{\sigma_{k,n}^2} \tag{1.55}$$

It is readily seen that the ZF-THP transmit matrix can no longer lead to a transmit power increase: as the precoding matrix is orthogonal, precoding with $\mathbf{Q}_k$ merely leads to redistributing the power in $\tilde{\boldsymbol{X}}_k$ over the different lines. The sum power of $\tilde{\boldsymbol{X}}_k$ is however the same as the sum power of $\mathbf{Q}_k \tilde{\boldsymbol{X}}_k$.

Non-linear vectoring thus performs better than linear vectoring when the channels are ill-conditioned. However, it also results in a significant computational complexity increase. Moreover, non-linear vectoring techniques are sensitive to channel estimation errors, the effect of which tends to be aggravated when channels are ill-conditioned [67]. This fact was empirically verified for THP in [122] by demonstrating that optimized linear precoding outperforms THP under a wide range of channel estimation errors, even when the channel is ill-conditioned. If the channel matrix is well conditioned however—more specifically if the matrix $\mathbf{H}_k$ is column-wise diagonal dominant (CWDD)—then the linear ZF transmitter and receiver are known to achieve close-to-capacity performance [28, 29]. In VDSL channels, where it can safely be assumed that $\mathbf{H}_k$ is CWDD [28, 29], ZF vectoring matrices have been successfully deployed to achieve near-capacity performance. The more severe crosstalk levels in G.fast and G.mgfast have however resulted in a renewed interest in non-linear vectoring techniques for FEXT cancellation.

1.1.3 Echo and near-end crosstalk

So far, two types of interference have been introduced: inter-symbol interference, and far-end crosstalk. This leaves two types of interference, namely near-end crosstalk (NEXT) and echo, both of which are illustrated in Figure 1.5. Contrary to FEXT, NEXT and echo induce interference in receivers which are located at the same side of the network as the transmitters. In Figure 1.5, the echo is represented by the solid blue arrow and the NEXT is represented by the by the dashed or dotted red arrows. The echo is thus induced in the receiver that is connected to the same line as the interfering transmitter, whereas NEXT is induced in receivers that are connected to different lines than the transmitter. One of the reasons that a distinction is often made between echo and NEXT, is that they are caused by different mechanisms.

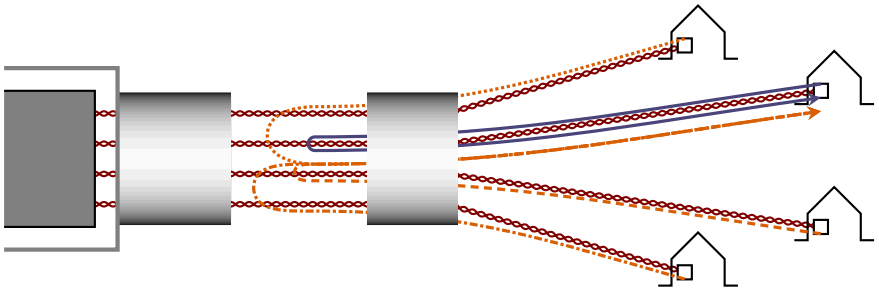


Figure 1.5: Near-end crosstalk and echo received by the 2-nd CPE in the downstream channel. The solid blue arrow represents the echo signal, the dashed or dotted red arrows represent the NEXT signals.

Echo occurs when the transmitter and receiver connected to the same end of a twisted-pair line are simultaneously active. To avoid echo, the transmitter and receiver are typically connected to twisted-pair line via a *hybrid*, a circuit which—when its internal reference impedance is perfectly matched to the twisted-pair line—prevents signal leakage from the transmitter to the collocated receiver [53, 54, 175, 216]. In practice however, perfect matching of the hybrid's reference impedance to the line impedance is not possible due to the large variations between twisted-pair lines [216], such that there is always signal leakage from the transmitter into the collocated receiver [54]. The maximum isolation yielded by an analog hybrid is therefore typically $15 - 20\,\mathrm{dB}$ [53]. Moreover, additional echo can be caused by a receiver-side impedance mismatch [53]. In a DSL network with a single twisted-pair, taking the echo into account yields the following channel model.

$$y[t'] = (h * x_{\mathrm{DS}})[t'] + (h_{\mathrm{echo}} * x_{\mathrm{US}})[t'] + z[t'], \tag{1.56}$$

Unlike echo, NEXT is caused by the same mechanisms as FEXT: by the close proximity of twisted-pair lines to one-another in the cable binder resulting in capacitive and inductive coupling, in turn leading to signal leakage. Each CPE thus receives a mixture of the signals that have been transmitted by all other CPEs on the different twisted-pair lines—see Figure 1.2 for a graphical representation of this phenomenon. Conversely, in the upstream channel, the received signal on each line connected to the DPU will contain a linear combination of the signals transmitted on all other lines connected to the same DPU. The NEXT in multi-user DSL networks can be taken into account in the channel model by extending (1.56) to a multi-user model, similar to how (1.3) was extended to obtain (1.23).

Echo and NEXT cancellation

In order to enable simultaneously transmitting and receiving data, echo or NEXT cancellation techniques should be used to reduce the interference. Echo cancellation (EC) techniques will be addressed first.

Broadly speaking, digital EC—which further reduces the echo after the analog cancellation by the hybrid—can be implemented in the time domain or in the frequency domain [178]. Regardless of which domain the EC is applied in, the basic approach remains the same: estimate the echo, and cancel it from received signal. In time-domain EC, $h_{\text{echo}}[t']$ is estimated and the echo is reconstructed by convolving the estimate with the known signal $x_{\text{US}}[t']$. Frequency-domain EC, on the other hand, is performed after DMT demodulation. Assuming the CP is sufficiently long, the channel model after DMT demodulation is given as

$$Y_k[t] = H_k X_k^{\text{DS}}[t] + H_k^{\text{echo}} X_k^{\text{US}}[t] + Z_k[t]. \tag{1.57}$$

The echo is then reconstructed by estimating H_k^{echo} and multiplying the estimate with the known signal $X_k^{\text{US}}[t]$. The main advantage of frequency-domain EC over time-domain EC is its lower computational complexity [178]. However, frequency-domain EC requires good synchronization between transmitted and received signals, and a long cyclic prefix that accounts for both CIR orders, as well as for the relative delay between the direct and echo signals [178].[11]

Contrary to echo cancellation, the topic of NEXT cancellation has not been considered much in DSL literature. Time-domain NEXT cancellation was studied in [79, 144], where the strategy has been to estimate all NEXT channel CIRs, and subsequently calculating and canceling the received NEXT signals from the received signals. Frequency-domain NEXT cancellation has been proposed as well, which is based on the multi-user extension of the channel model in (1.57). As these techniques are straightforward extensions from the echo-cancellation techniques in the previous paragraph, no further mathematical details are given here. It is important to note, however, that NEXT cancellation requires collocation of all transmitters and receivers. As such, NEXT cancellation is only possible at the DPU side [226]. NEXT cancellation in the downstream channel is not possible, and one needs to resort to avoidance strategies if all NEXT is to be eliminated.

[11] This short overview of EC constitutes a severe oversimplification of a diverse field of research. Only a brief introduction is given here as echo cancellation is not the focus of this thesis. For more information on digital echo cancellation in DSL systems, the reader is referred to [7, 54, 151, 216] and references therein.

Echo and NEXT avoidance

The first DSL standard, HDSL, used echo cancellation to enable simultaneous upstream and downstream data transmission [43]. The three subsequent standards, ADSL, VDSL and G.fast, have however employed interference avoidance techniques that separate NEXT sources and victims in the time or frequency domain by means of multiple access techniques.

ADSL and VDSL separated upstream and downstream transmission by means of frequency division duplexing (FDD),[12] which divides the frequency spectrum into non-overlapping bands used either for upstream or downstream transmission. Good separation in FDD can be achieved using analog upstream-downstream separation filters, the use of which is allowed—but not enforced—by the ADSL standard [91]. Such filters require a sharp cutoff, making them expensive to implement in practice [53]. Not only are sharp analog filters costly, they will also cut away valuable spectrum to allow for guard bands and prohibit the use of a flexible band plan [133]. FDD can also be enabled by increasing the CP length—or, equivalently, adding a cyclic suffix—such that it accommodates for all upstream and downstream CIRs, as well as for the delay difference between direct/FEXT and echo/NEXT signals. This increased CP length forces orthogonality between different subcarriers of the direct and echo/NEXT channels, thus eliminating echo/NEXT if subcarriers are assigned to either upstream or downstream transmission. The resulting FDD strategy is also referred to as Zipper duplexing, and is used in VDSL [53, 170].

G.fast separates upstream and downstream transmission by means of time division duplexing (TDD), which divides time into non-overlapping slots used either for upstream or downstream transmission. The main advantages of TDD over FDD are that it allows for a simplified analog front-end—as no hybrid is required—and that it enables a simple yet flexible tuning of the ratio between US and DS rates [121, 123, 186]. It is noted that TDD requires good synchronization between all transmitters, as well as guard time interval between upstream and downstream transmission [123]. Moreover, systems using TDD have a longer round trip time than systems using FDD [123]. In G.fast however, the round trip time was suppressed by employing TDD frames with a duration of no more than 1 ms [186].

[12] It should be noted that ADSL and ADSL2 did also offer an echo canceling mode [91, 92].

1.2 Novel interference mitigation strategies

This thesis studies novel and advanced strategies to reduce the impact of interference in DSL networks. Two general strategies to enhance existing interference mitigation methods will be pursued, each corresponding to a different Part of this thesis. The first strategy consists of dynamically changing the DSM configuration based on instantaneous user requirements. The second strategy consists of expanding the DSM design space to improve achievable interference rejection performance. Before describing the contributions and giving the thesis outline, this section will give a general introduction to each of these advanced interference mitigation strategies.

1.2.1 Cross-layer DSM

Vectoring is often able to fully eliminate the detrimental effects of crosstalk in DSL networks, and has therefore become the industry standard as of VDSL2 [93]. In many practical deployment scenarios however, the elimination of all crosstalk through vectoring is inhibited, and one has to rely on spectrum coordination to tone down the effects of the residual crosstalk. Examples of such scenarios include FTTB deployments implementing multi-user full-duplex signaling [110, 177], VDSL networks implementing dynamic band planning to divide the available spectrum over US and DS transmission [63], or deployments where multiple DPUs are active on a single cable binder [209]. When optimizing the performance in such a network, it is often seen that the competition for data rate between different vectoring groups can be fierce [110, 209]. Moreover, it was recently reported in [13] that competition for data rate can even occur between different users of the same vectoring group.

Optimizing the performance of a DSL network that exhibits a competition for data rate corresponds to solving a multi-objective optimization problem lacking a solution that simultaneously maximizes the performance for all users. Instead, there is a collection of Pareto optimal DSM configurations, from which one has to choose a single configuration for transmission—see Figure 1.4. As has been discussed in Section 1.1.2, a conservative approach is usually followed where the physical layer is configured statically over time using a single Pareto optimal DSM configuration that satisfies some minimal rate requirements, achieves fairness, or results in the highest possible sum rate. However, this static configuration of the physical layer does not capitalize on the elastic, time dependent nature of the traffic it is carrying [13, 41, 80, 164, 196].

In order to profit from the time dependency of traffic, cross-layer DSM can be employed. The idea is to adapt the DSM configuration to instantaneous

traffic demands, such as to properly exploit the time dimension. There are two keys to implementing cross-layer DSM. First, higher layers in the Open Systems Interconnect (OSI) model should be enabled to communicate preference information that will be used by the physical layer to select an appropriate DSM configuration. By dynamically selecting Pareto optimal DSM configurations, whilst making an informed decision on which configuration to select using information from upper layers, significant performance gains can be achieved [41, 80, 164, 196]. Second, fast optimization algorithms should be designed that are able to adapt the DSM configuration to upper layer requirements in real time. The following two subsections will elaborate a bit further on the interface through which the upper layers will communicate preference information, and will more rigorously define the concept of "real time DSM algorithms" considered in this thesis.

Real-time DSM

Real-time DSM algorithms will be employed to dynamically select new DSM configurations. In [190], real-time DSM algorithms are given the defining property of satisfying all constraints after each 'calculation'. This way, after every calculation a new and (hopefully) better feasible DSM configuration becomes available. This definition is however very broad, as the granularity of a calculation remains undefined. Nonetheless, the concept of real-time DSM algorithms from [190] has additionally been studied in [15, 189], and will be adopted in this thesis as well.

Network utility maximization

The observations in the previous paragraphs signal the demand for an interface through which the upper layers or the ISP can communicate their preferences to the resource allocation algorithms of the physical layer. One such interface is provided through the framework of network utility maximization (NUM) [36,100], in which preferences are expressed by means of a utility function $U(\boldsymbol{R})$. The operating point $\boldsymbol{R}$ for the physical layer is then chosen such that the utility function is maximized, i.e. it is chosen as the solution to

$$\underset{\boldsymbol{R}\in\mathcal{R}}{\text{maximize}}\ U(\boldsymbol{R}), \tag{1.58}$$

where $\mathcal{R}$ is the rate region, which was defined for DSL networks employing spectrum coordination methods in Section 1.1.2.

Which approach should be taken to solve the NUM problem depends on the utility function. When U is concave, one can obtain the solution to the NUM

problem by solving its Lagrange dual. Due to the time-sharing property of multi-carrier systems, and due to the rate region of a DSL network being convex [32], the duality gap between the NUM problem and its Lagrange dual will then be zero. When U is non-concave, the NUM problem can be solved using the polyblock algorithm, which in turn solves a sequence of NUM problems with a concave utility function [22]. Convergence of these Lagrange dual-based NUM algorithms requires an exact evaluation of the Lagrange dual function. Algorithms that perform this exact evaluation are available [32, 111, 118, 174, 194, 202], but exhibit a computational complexity that is exponential in the number of users connected to the network.[13] As such, directly applying a Lagrange dual-based NUM algorithm to problem (1.58) would result in an exceedingly high computational complexity. In the context of scheduling algorithms, where a vast amount of NUM problems is to be solved in a limited amount of time [41, 200], or in the context of non-concave utility functions, where finding the optimal solution requires solving many intersection problems [22], this high computational complexity is especially problematic.

1.2.2 New DSM degrees of freedom

Aside from expanding the usable frequency bandwidth to 848 MHz, the following features, among others, have been proposed to improve the performance of G.mgfast as compared to G.fast: advanced low-density parity-check-based (LDPC-based) coding schemes, the use of disparate quality of service (QoS) classes for different types of traffic, full-duplex (FDX) transmission, and channel shortening [123, 145]. These new features affect the optimality of the state-of-the-art DSM approaches and may—if they are accounted for in the DSM optimization problems rather than be treated as separate features—yield increased performance by adding new degrees of freedom to the DSM design space. In order to assess the potential performance gains of these new degrees of freedom, integrated DSM optimization problems, which explicitly account for these new features, should be formulated and solved. In what follows, a short description of the new physical layer features considered in this thesis—QoS classes, FDX transmission, and channel shortening—is given, as well as a description of how they can be integrated into existing DSM approaches.

[13] This is especially true for those deployment scenarios where signal coordination is not possible across all users.

QoS classes

In HDSL, ADSL, VDSL, and G.fast, all the data carried by the DSL network is treated equal. The fact that all data is treated equal is at odds with the fact that multiple applications transmit data over the DSL physical layer, many with very different QoS requirements. G.mgfast will therefore support multiple QoS classes, which may mutually differ in aspects such as data rate, priority, transmission delay, and packet error rate [145]. Supported QoS classes will include an ultra-low-latency service (ULLS) class and an ultra-reliable low-latency service (URLLS) class, both of which will be supported by fifth generation (5G) wireless networks as well [145].

The QoS differentiating aspect of focus in this thesis will be the achieved error rate. In the DSL generations between HDSL and G.mgfast, data has always been protected with the same error correction scheme: an outer Reed-Solomon (RS) code supplemented with interleaving, and an inner trellis-coded modulation (TCM) [96, 140, 165]. Additionally, ARQ has been employed to counteract the effects of impulse noise [140]. Together with the employed SNR gap Γ in (1.21) and (1.27), these error correction schemes thus determine the achieved bit error rate (BER).

In DSM algorithms, the appropriate value for Γ thus depends on the target BER, as well as on the error correction scheme in use. Not only will the supported QoS classes have a different target BER, satisfying their delay requirements may additionally necessitate to the use of low latency error correction schemes. As such, different values of Γ may be appropriate for the different QoS classes. However, each subcarrier can only employ a single value for Γ, such that using a different Γ for different QoS classes requires assigning each subcarrier to a specific QoS class—the resulting problem is referred to as the subcarrier assignment problem. Combining the use of multiple QoS classes with existing DSM approaches will thus be achieved by integrating the spectrum coordination problem, the vectoring matrix design problem and the subcarrier assignment problem into a single integrated DSM optimization problem.

Full-duplex transmission

As discussed in Section 1.1.3, the DSL generations between HDSL and G.mgfast mostly avoided the influence of NEXT by dividing resources between US and DS transmission using either FDD [91–94] or TDD [96]. G.mgfast will however use FDX transmission, in which US and DS transmissions occur at the same time and in the same frequency band. In this FDX setting, NEXT is no longer avoided, but will be dealt with using DSM techniques.

At the DPU, interfering DS transmitters and victim US receivers are co-located. Therefore, the effects of NEXT can be reduced with the NEXT cancellation techniques discussed in Section 1.1.3. In DSL, the DPU-side NEXT is typically not much stronger than the received signal, such that it is reasonable to assume perfect NEXT cancellation at the DPU, yielding a NEXT-free US channel. At the CPEs however, interfering US transmitters and victim DS receivers are not co-located, such that only spectrum coordination techniques are available to mitigate the NEXT impact. Fortunately, CPE-side NEXT is known to be consistently lower than DPU side NEXT [178, 226]. It is therefore likely that significant performance improvements can still be achieved by implementing FDX transmission, even without canceling the CPE-side NEXT.

The considered FDX DSL networks thus use joint vectoring and spectrum coordination to deal with FEXT, spectrum coordination to deal with CPE-side NEXT, and echo/NEXT cancellation to deal with DPU-side NEXT. The resulting integrated optimization algorithm will jointly determine the optimal US and DS transmit powers for all users, as well as optimal receive and precoding vectoring matrices.

Channel shortening

The final physical layer feature that will be considered in this thesis, is channel shortening. Channel shortening methods reduce the impact of interference in DSL networks by reducing the impact of the CP overhead without incurring too much inter-symbol interference. The idea of channel shortening is to apply an FIR filter to the received time-domain signal $y[t']$ prior to DMT demodulation. This FIR filter $f_{\mathrm{CS}}[t']$ is then designed such that it reduces the length of the apparent CIR $(f_{\mathrm{CS}} * h)[t']$, thereby lowering the required CP length for ISI-free transmission.

Channel shortening techniques were originally considered for legacy DSL generations, e.g. for ADSL2+ [123]. These legacy DSL generations allowed loop lengths of up to 6 km—see Table 1.1—and were therefore affected by very long CIRs [166]. Even though new DSL generations operate on far shorter loop lengths, there has recently been a renewed interest in the subject of channel shortening. This renewed interest has multiple origins, most notably the fact that extending the reach makes new DSL technologies more economically viable, and the fact that converging to single technology may yield performance gains by eliminating co-existence problems.

The number of homes covered per DPU is one of the factors that determines the capital expenditure of rolling out any DSL technology, and is proportional to the area covered per DPU. Given a minimum data rate that is to be achieved,

the area covered per DPU depends quadratically on the maximum range over which this data rate can be achieved. As channel shortening techniques can aid in achieving the better performance on long loops [123], they may be used to increase the maximum reach of—and by extension the economic viability of—any DSL generation.

In addition to strengthening the economic viability of future DSL generations, channel shortening techniques may also help addressing coexistence issues between different DSL generations—which are described in more detail in [222, 226]—by enabling convergence to a single DSL standard that can operate on a broad range of loop lengths [123]. It should however be noted that G.fast DMT symbols are shorter than VDSL DMT symbols: the G.fast symbol rate is 48 kHz, while the VDSL symbol rate is 4 kHz. Operating G.fast on lines that are currently operated with VDSL may therefore result in a significantly increased CP overhead [222], which can however be prevented if the apparent CIR length can be reduced using a channel shortening method.

In literature, channel shortening filter design and DSM are mostly considered as separate problems. However, properly combining channel shortening with DSM approaches requires simultaneously optimizing the channel shortening filters and the DSM configuration. Such joint optimization has been considered in [146], but the developed algorithm can not be shown to converge to a stationary point of the optimization problem it considers.

1.3 Contributions and thesis outline

Part I: Cross-layer DSM

Part I of this thesis contains contributions in the context of cross-layer DSM. A new network utility maximization algorithm will be proposed, as well as a new real-time DSM algorithm. It is noted that one key aspect of cross-layer DSM will not be considered in this thesis, namely the upper layer scheduling algorithms that specify preference information for the physical layer by means of utility functions. The candidate has contributed to the design of such upper layer scheduling algorithms as well—see e.g. [199, 200]. These works will however not be included in this thesis.

Chapter 2: Real-time DSM

This chapter presents a simple and powerful framework for real-time spectrum coordination based on bi-coordinate ascent methods. This framework is then used to define a novel derivative based real-time spectrum coordination algorithm which provably converges to a stationary point of the considered WSR problem, referred to as fast derivative-based iterative power difference balancing (F-DB-IPDB). This convergence property of the proposed algorithms, as well as its faster convergence in practice, form important improvements over the state-of-the-art real-time DSM algorithms in [189, 190]. The contents of this chapter have previously been published in the following conference paper.

> Jeroen Verdyck, Chris Blondia, and Marc Moonen, "Derivative Based Real-Time Spectrum Coordination for DSL," *Proc. 24th European Signal Processing Conference (EUSIPCO)*, pp. 305 - 309, September 2016.

Chapter 3: Network utility maximization-based DSM

This chapter presents a fast algorithm for finding a local solution to the NUM problem, which is referred to as NUM-DSB. The algorithm is able to handle many DSL deployment scenarios, and is applicable regardless of the utility function's properties. The contents of this chapter have previously been published in the following conference paper.

> Jeroen Verdyck, Chris Blondia, and Marc Moonen, "Network Utility Maximization for Adaptive Resource Allocation in DSL Systems," *Proc. 26th European Signal Processing Conference (EUSIPCO)*, pp. 787 - 791, September 2018.

Part II: New DSM degrees of freedom

Part II of this thesis contains contributions that exploit new DSM degrees of freedom to improve DSL network performance. The considered new DSM degrees of freedom are QoS classes, FDX transmission, and channel shortening. The candidate has also contributed to adapting existing DSM approaches to the newly considered LDPC-based coding schemes. The results of this effort have been published in [182], but will not be included in this thesis.

Chapter 4: DSM and QoS classes

This Chapter considers DSM for DSL networks that provide unequal error protection by assigning each subcarrier to a single QoS class, and using a different value for the SNR gap Γ depending on the considered QoS class' employed coding scheme and target error rate. Four joint signal and spectrum coordination algorithms are presented. These algorithms are modified versions of existing optimal spectrum balancing (OSB) and distributed spectrum balancing (DSB) algorithms for joint signal and spectrum coordination in upstream as well as downstream DSL channels. In addition, an algorithm is presented which, for each QoS class, selects a suitable modulation and coding (MC) scheme from a set of admissible MC schemes. Through simulations, it is shown that DSM with unequal error protection can indeed lead to moderate performance gains. The contents of this chapter have previously been published in the following journal article.

> Jeroen Verdyck, and Marc Moonen, "Dynamic Spectrum Management in Digital Subscriber Line Networks with Unequal Error Protection Requirements," *IEEE Access*, Vol. 5, pp. 18107 - 18120, September 2017.

Chapter 5: Full-duplex DSM

This chapter proposes three novel DSM algorithms for multi-user (MU) FDX DSL networks. First, an OSB algorithm is derived which calculates the globally optimal DSM solution, but does so at an exceedingly high computational cost. Key in this algorithm is the use of a novel MAC-BC duality for the specific case of perfect DPU-side NEXT cancellation. Two low-complexity DSB algorithms are then proposed, for which simulations show that their performance is very close to what is achieved by the OSB algorithm. Therefore, these DSB algorithms can be used to estimate the achievable performance of an MU FDX DSL network. Such performance estimations show that FDX transmission can indeed lead to significant gains in MU DSL networks. The contents of this chapter have previously been published in the following journal article.

> Jeroen Verdyck, Wouter Lanneer, Paschalis Tsiaflakis, Werner Coomans, Panagiotis Patrinos, and Marc Moonen, "Optimal Dynamic Spectrum Management Algorithms for Multi-User Full-Duplex DSL," *IEEE Access*, Vol. 7, pp. 106600 - 106616, July 2019.

Chapter 6: DSM and channel shortening

This chapter proposes a new algorithm to simultaneously optimize channel shortening per-tone equalization (PTEQ) filters and the DSM configuration. In addition, transmitter-side channel shortening filters are considered, more specifically so-called per-tone precoding (PTPC) filters. At first glance, the FIR filter optimization for PTPC seems much more involved than the relatively straightforward FIR filter optimization for PTEQ. However, it will be demonstrated that any DMT system with PTPC is—after time-reversing the CIR—equivalent to a DMT system employing PTEQ. With this result in hand, systems with PTPC can take full advantage of the straightforward FIR filter optimization in systems with PTEQ, as well as of the aforementioned resource allocation algorithm. Simulation results show that the performance obtained for systems with PTPC is nearly indistinguishable from that obtained for systems with PTEQ, making PTPC an interesting alternative channel shortening strategy. The contents of this chapter have previously been published in the following journal article.

> Jeroen Verdyck, Yannick Lefevre, Paschalis Tsiaflakis, and Marc Moonen, "Per-Tone Precoding and Per-Tone Equalization for OFDM and DMT Transmission Systems: Duality, Filter Optimization, and Resource Allocation," *IEEE Open Journal of Signal Processing*, Vol. 1, pp. 257-273, November 2020.

The developed theory and presented results in this chapter have been obtained for single-user DSL systems. It should however be noted that these can, and have been, extended to multi-user DSL systems as well. Even though these extensions have not been published in isolation, the efforts in obtaining them have contributed to the work in [167]. The considered work will however not be included in this thesis.

Chapter 7: DSM and widely linear channel shortening

When channel shortening techniques are analyzed, it is often overlooked that the received signals after DMT demodulation are generally *improper* when the CP is too short. Hence, the state-of-the-art signal-to-interference-plus-noise ratio (SINR) and bit loading expressions employed to assess system performance, which implicitly assume the received signals to be proper, misrepresent the true achievable performance. New expressions for the SINR and bit loading are therefore presented that explicitly take signal impropriety into account. Based on these expressions, it is then observed that—if the received signals are

improper—the PTEQ FIR filters are no longer optimal, and that the achievable bit loading depends on a particular phase shift experienced by the transmitted signals. This chapter therefore introduces a novel widely linear PTEQ—which is again optimal when the received signals are improper—and additionally proposes to optimally rotate signals in the complex plane prior to transmission. Finally, this chapter assesses the performance increase obtainable by explicitly accounting for signal impropriety. The contents of this chapter have previously been published in the following journal article.

Jeroen Verdyck, Yannick Lefevre, Paschalis Tsiaflakis, and Marc Moonen, "Signal Impropriety in Discrete Multi-Tone Systems and Widely Linear Per-Tone Equalization," *IEEE Open Journal of the Communications Society*, Vol. 2, pp. 367-383, February 2021.

Part I

Cross-Layer DSM

Chapter 2

Real-time DSM

Derivative Based Real-Time Spectrum Coordination for DSL

Jeroen Verdyck, Chris Blondia, and Marc Moonen

Published in *Proc. 24th European Signal Processing Conference (EUSIPCO)*, pp. 305 - 309, September 2016, DOI: 10.1109/EUSIPCO.2016.7760259.

© 2016 IEEE.
Jeroen Verdyck, Chris Blondia, and Marc Moonen, "Derivative Based Real-Time Spectrum Coordination for DSL," *Proc. 24th European Signal Processing Conference (EUSIPCO)*, pp. 305 - 309, September 2016.
Changes include layout, representation, and minor editing aspects. In addition, a convergence proof for Algorithm 1 has been added in Appendix A. The iteration indexing in Algorithm 1 has been altered in order to simplify notation in Appendix A. Finally, improved definitions are now employed for the sets $\mathcal{A}_n^\epsilon$ and $\mathcal{D}_n^\epsilon$.

The candidate's contributions as first author include: all performed research and writing of the article under guidance of the co-authors.

Abstract

In digital subscriber line systems, spectrum coordination is a powerful technique to improve performance. A typical spectrum coordination algorithm employs an iterative procedure to solve the rate adaptive spectrum management problem. These iterative procedures deliver a feasible result only after convergence, and are therefore mostly unable to deal with real-time computational constraints. Recently, the new paradigm of so-called real-time dynamic spectrum management has been defined. This chapter presents a simple and powerful framework for real-time spectrum coordination based on bi-coordinate ascent methods. This framework is then used to define a novel derivative based real-time spectrum coordination algorithm with provable convergence properties, referred to as fast derivative-based iterative power difference balancing (F-DB-IPDB). Simulation results show a significant improvement in performance compared to the state of the art.

2.1 Introduction

Crosstalk, i.e. interference among different users, is the main source of performance degradation in digital subscriber line (DSL) systems. The ensemble of techniques that deal with the crosstalk problem is commonly referred to as dynamic spectrum management (DSM). Three tiers of DSM are distinguished. Level 1 DSM manages each line individually, and at most introduces some politeness in order to mitigate the effects of crosstalk. Level 2 DSM manages the transmit powers of different lines jointly, in order to cooperatively mitigate the effects of crosstalk. This technique is also referred to as spectrum coordination, and will be considered in this chapter. Many examples of spectrum coordination algorithms can be found in [85] and references therein. Finally, level 3 DSM consists of coordinating multiple lines on a signal-level, and is commonly referred to as signal coordination or vectoring.

A typical spectrum coordination algorithm employs an iterative procedure to solve the rate adaptive spectrum management problem. These iterative procedures deliver a feasible result only after convergence, and are therefore mostly unable to deal with real-time computational constraints. In order to take into account constraints on computation time and compute power, the new paradigm of real-time dynamic spectrum management (RT-DSM) has been proposed [190]. Two RT-DSM algorithms, iterative power difference balancing (IPDB) [190] and fast iterative power difference balancing (F-IPDB) [189], have been proposed, which employ difference of variables (DoV) transformations.

This chapter introduces the similar framework of bi-coordinate ascent methods [14] as a simpler and more powerful alternative for DoV transformations. This framework is then used to define a derivative based real-time spectrum coordination algorithm that employs a simple heuristic to improve performance. Bi-coordinate ascent methods were first introduced for training support vector machines [99], but have not been considered much outside of this context. A very comprehensive selection from the available literature on bi-coordinate ascent algorithms can be found in [14]. Bi-coordinate ascent methods also strongly resemble the method of bi-coordinate variations in [104], which is used to solve the variational inequality problem.

2.2 Spectrum coordination

DSL systems employ discrete multi-tone (DMT) modulation, which splits the available spectrum into a large number of sub carriers or tones. The transmission in an N-user cable bundle is, on each tone, modeled as

$$\boldsymbol{y}_k = \mathbf{H}_k \boldsymbol{x}_k + \boldsymbol{z}_k, \quad \forall k \in \mathcal{K}, \tag{2.1}$$

where $\mathcal{K}$ denotes the set of K tones, $\boldsymbol{x}_k = [x_{1,k}, x_{2,k}, \ldots, x_{N,k}]^{\mathrm{T}}$ contains the transmitted symbols of all N users on tone k, and $\mathbf{H}_k$ is the $N \times N$ channel matrix where $[\mathbf{H}_k]_{n,m} = h_k^{n,m}$ is the transfer function between transmitter m and receiver n, evaluated on tone k. Furthermore, $\boldsymbol{z}_k$ is a vector of additive zero-mean Gaussian noise on tone k and $\boldsymbol{y}_k$ contains the received signal for all N users on tone k. Also, let $\mathcal{N}$ denote the set of users that are connected to the same cable bundle. The transmit power and received noise power of user n on tone k are given as $s_{k,n} = \Delta_f \, \mathbb{E}\{|x_{k,n}|^2\}$ and $\sigma_{k,n} = \Delta_f \, \mathbb{E}\{|z_{k,n}|^2\}$, with $\mathbb{E}\{\cdot\}$ the expected value operator and Δ_f the tone spacing. The total power consumption of user n is $P_n = \sum_k s_{k,n}$.

As crosstalk is treated as noise, the achievable bit loading for user n on tone k, given $\boldsymbol{s}_k = [s_{1,k}, s_{2,k}, \ldots, s_{N,k}]^{\mathrm{T}}$, can be calculated as

$$b_{k,n}(\boldsymbol{s}_k) = \log_2 \left(1 + \frac{1}{\Gamma} \frac{s_{k,n}}{\sum_{m \neq n} \alpha_k^{n,m} s_{k,m} + \tilde{\sigma}_{k,n}} \right), \tag{2.2}$$

where Γ is the signal-to-noise ratio (SNR) gap to capacity, where $\alpha_k^{m,n} = |h_k^{n,m}|^2 / |h_k^{n,n}|^2$, and where $\tilde{\sigma}_{k,n} = \sigma_{k,n} / |h_k^{n,n}|^2$. The signal-to-noise ratio gap to capacity, or SNR gap for short, is a function of the coding gain, noise margin and target average BER. The achievable bit loading is considered to be a continuous variable.

This chapter considers spectrum coordination through rate adaptive spectrum management. The objective of rate adaptive spectrum management is to determine a transmit spectrum $\boldsymbol{s}_n = [s_{1,n}, \ldots, s_{K,n}]^{\mathrm{T}}$ for each user n, subject to spectral mask constraints and per user total power constraints, such that the weighted sum of the per user data rates is maximized. The corresponding optimization problem is given by

$$\begin{aligned} \arg\max_{\boldsymbol{s}} \quad & \sum_{k\in\mathcal{K}} \sum_{n\in\mathcal{N}} \omega_n b_{k,n}(\boldsymbol{s}_k) \\ \text{s.t.} \quad & 0 \leq s_{k,n} \leq s_{k,n}^{\text{mask}}, \quad \forall n, k \\ & P_n = P_n^{\text{tot}}, \quad \forall n \end{aligned} \tag{2.3}$$

where ω_n is the weight that is associated with the data rate of user n, and where $\boldsymbol{s} = [\boldsymbol{s}_1{}^{\mathrm{T}}, \ldots, \boldsymbol{s}_N{}^{\mathrm{T}}]^{\mathrm{T}}$. The objective function of problem (2.3) is commonly referred to as the weighted sum rate (WSR).

It is noted that in (2.3), the total power constraints are expressed as equality constraints, which is unusual for rate adaptive spectrum management where total power constraints are typically expressed as $P_n \leq P_n^{\text{tot}}$. The requirement to satisfy these constraints with equality does not have a large influence on the obtained solutions, as total power constraints are generally met with equality, yet greatly simplifies the formulation of real-time algorithms [190].

Except for the total power constraints, every constituent of problem (2.3) can be separated per tone. The optimization problem is said to be coupled through the per user total power constraints. This coupling complicates the formulation of a solution, and is therefore typically eliminated by applying a dual decomposition method. Dual decomposition methods solve the Lagrange dual problem of (2.3), i.e.

$$\begin{aligned} \arg\min_{\boldsymbol{\lambda}} \quad & g(\boldsymbol{\lambda}) = \sum_{k\in\mathcal{K}} \left[\max_{\boldsymbol{s}_k} \mathcal{L}_k(\boldsymbol{s}_k, \boldsymbol{\lambda}) \right] + \sum_{n\in\mathcal{N}} \lambda_n P_n^{\text{tot}} \\ \text{with} \quad & \mathcal{L}_k(\boldsymbol{s}_k, \boldsymbol{\lambda}) = \sum_{n\in\mathcal{N}} \omega_n b_{k,n}(\boldsymbol{s}_k) - \sum_{n\in\mathcal{N}} \lambda_n s_{k,n}. \end{aligned} \tag{2.4}$$

Provided that the duality gap between the primal problem (2.3) and the Lagrange dual problem (2.4) is equal to 0, the solution to the primal problem (2.3) can be found through solving the dual problem (2.4) [220]. A dual decomposition algorithm iteratively updates the Lagrange dual variable $\boldsymbol{\lambda}$, and calculates the corresponding optimal transmit spectra by maximizing the per tone Lagrangian functions $\mathcal{L}_k(\boldsymbol{s}_k, \boldsymbol{\lambda})$, $\forall k \in \mathcal{K}$. This iterative procedure stops when the optimal Lagrange dual variables are determined. A large number of

update strategies for $\boldsymbol{\lambda}$ have been developed, as well as various techniques to solve the per tone maximization of $\mathcal{L}_k(\boldsymbol{s}_k, \boldsymbol{\lambda})$.

2.3 Real-time spectrum coordination and bi-coordinate ascent methods

In [190], an RT-DSM algorithm is defined as a DSM algorithm that iteratively updates the transmit spectra $\boldsymbol{s}$, such that all constraints continue to be satisfied after each update. Traditional dual decomposition methods do not fit this definition, as the total power constraints are only guaranteed to be satisfied after the Lagrange dual variables have converged to their optimal values. The challenge in defining RT-DSM algorithms thus lies in finding alternative techniques that eliminate the coupling through the per user total power constraints.

This chapter considers a decomposition framework which is based on bi-coordinate ascent methods [14]. In each iteration ℓ of a bi-coordinate ascent method, two tones i and j of user n exchange power.

$$s_{i,n}^{(\ell+1)} \leftarrow s_{i,n}^{(\ell)} + t, \quad s_{j,n}^{(\ell)} \leftarrow s_{j,n}^{(\ell)} - t \tag{2.5}$$

It is clear that if $\boldsymbol{s}^{(\ell)}$ satisfies the per user total power constraints, these constraints continue to be satisfied for $\boldsymbol{s}^{(\ell+1)}$. The amount of power that is exchanged, is calculated as the solution to

$$\begin{aligned} \arg\max_{t} \quad & \phi_n^{i,j}(t; \boldsymbol{s}) = f_{i,n}(t; \boldsymbol{s}_i) + f_{j,n}(-t; \boldsymbol{s}_j) \\ \text{s.t.} \quad & t_{\min} \leq t \leq t_{\max} \end{aligned} \tag{2.6}$$

where

$$t_{\min} = \max\{-s_{i,n}, s_{j,n} - s_{j,n}^{\text{mask}}\} \tag{2.7}$$

$$t_{\max} = \min\{s_{i,n}^{\text{mask}} - s_{i,n}, s_{j,n}\} \tag{2.8}$$

$$f_{k,n}(t; \boldsymbol{s}_k) = \sum_{m \in \mathcal{N}} \omega_m b_{k,m}(\boldsymbol{s}_k + t\boldsymbol{e}_n), \tag{2.9}$$

with $\boldsymbol{e}_n$ the n^{th} vector in the standard basis of $\mathbb{R}^N$.

Another decomposition framework, which is based on difference of variables (DoV) transformations, is proposed in [190]. The main idea of DoV

transformations is to construct a parameterization of all feasible transmit spectra. An example of such a parametrization is

$$\begin{aligned} & s_{k,n} = t_{k,n} - t_{\pi_n(k),n} + \gamma_{k,n} P_n^{\text{tot}}, \quad \forall k \in \mathcal{K}, \forall n \in \mathcal{N} \\ \text{with} \quad & 0 \leq \gamma_{k,n}, \quad \forall k \in \mathcal{K}, \forall n \in \mathcal{N} \\ & \sum_{k \in \mathcal{K}} \gamma_{k,n} = 1, \quad \forall n \in \mathcal{N} \end{aligned} \tag{2.10}$$

where π_n is a cyclic permutation of vector $[1, \ldots, K]$, $\pi_n(k)$ represents its k-th element, and $\gamma_{k,n}$ are constants. The new variables $t_{k,n}$ that appear through the DoV transformation are called difference variables. In (2.5), t resembles the difference variable of the DoV transformation. DoV based RT-DSM algorithms solve problem (2.3) by substituting the power variables with the parametrization of the DoV transformation, and applying a coordinate ascent method to the difference variables.

In general, DoV transformations are characterized by the number of tones that are affected when the value of a difference variable changes. For example, the parametrization in (2.10) is said to describe a general 2-tone DoV transformation, as each of the difference variables $t_{k,n}$ affects the power loading of two tones. If a bi-coordinate ascent method imposes restrictions on which tones are able to mutually exchange power, i.e. when j is restricted to $j = \pi_n(i)$, then it is equivalent to a coordinate ascent method applied after a 2-tone DoV transformation. Bi-coordinate ascent methods are thus a simpler and more general alternative to 2-tone DoV methods.

Two DoV based RT-DSM algorithms, referred to as IPDB [190] and F-IPDB [189], are now introduced using the framework of bi-coordinate ascent methods. The DoV based RT-DSM algorithms first initialize $\gamma_{k,n}$, $\forall k \in \mathcal{K}, \forall n \in \mathcal{N}$. In the context of bi-coordinate ascent methods, this corresponds to initializing the transmit spectra $\boldsymbol{s}$ such that all constraints are satisfied. Then, in each coordinate ascent step, IPDB and F-IPDB exchange power between tones i and $j = \pi_n(i)$. IPDB and F-IPDB differ only in their approach to solving (2.6). IPDB employs an exhaustive line search over a discrete grid of points between the $t_{\min}$ and $t_{\max}$. Alternatively, F-IPDB solves a sequence of convex approximations of (2.6), which are defined as

$$\begin{aligned} \arg\max_{t} \quad & \phi_n^{i,j}{}_{\text{cvx}}(t; \boldsymbol{s}) = f_{i,n_{\text{cvx}}}(t; \boldsymbol{s}_i) + f_{j,n_{\text{cvx}}}(-t; \boldsymbol{s}_j) \\ \text{s.t.} \quad & t_{\min} \leq t \leq t_{\max} \\ \text{where} \quad & f_{k,n_{\text{cvx}}}(t; \boldsymbol{s}_k) = \omega_n b_{k,n}(\boldsymbol{s}_k + t\boldsymbol{e}_n) + t \sum_{m \neq n} \omega_m b_{k,m}{}'(\boldsymbol{s}_k), \end{aligned} \tag{2.11}$$

with $b_{k,m}{}'(\boldsymbol{s}_k)$ the directional derivative of $b_{k,m}(\cdot)$ along $\boldsymbol{e}_n$ at $\boldsymbol{s}_k$. F-IPDB iteratively solves new instances of (2.11) for the same i and j, updating $s_{i,n}$ and $s_{j,n}$ using (2.5) every time a solution to (2.11) is calculated. This iterative procedure converges to a stationary point of (2.6) [189]. As (2.11) corresponds to a one-dimensional convex problem, its solution $t^\star$ either satisfies the optimality condition

$$\phi_n^{i,j}{}'_{\text{cvx}}(t^\star; \boldsymbol{s}_k) = 0 \tag{2.12}$$

with $\phi_n^{i,j}{}'_{\text{cvx}}(t^\star; \boldsymbol{s}_k) \triangleq \frac{d}{dt}\phi_{ij\,\text{cvx}}(t; \boldsymbol{s}_k)\big|_{t=t^\star}$, or lies on the boundary of the feasible interval $[t_{\min}, t_{\max}]$. Equation (2.12) can be reformulated as a quadratic equation, hence with two roots $\tilde{t}_1$ and $\tilde{t}_2$. To solve (2.11), F-IPDB calculates $\tilde{t}_1$ and $\tilde{t}_2$, and evaluates the objective function of (2.11) at $t = \tilde{t}_1, \tilde{t}_2, t_{\min}, t_{\max}$.

2.4 Derivative based real-time spectrum coordination

In [190], several possibilities have been examined for the tone permutation π_n of IPDB and F-IPDB, including a predetermined permutation such as $[K, 1, 2, \ldots, K-1]$, or random permutations of $[1, \ldots, K]$. Using bi-coordinate ascent methods, it is possible to choose tones i and j such that the expected WSR increase is large. First, define sets $\mathcal{A}_n^\epsilon$ and $\mathcal{D}_n^\epsilon$ for user n, which constitute the sets of tones that are able to accept and donate a given amount of power ϵ, respectively.

$$\mathcal{A}_n^\epsilon(\boldsymbol{s}_n) = \{k : s_{k,n} \leq s_{k,n}^{\text{mask}} - \epsilon\}, \quad \mathcal{D}_n^\epsilon(\boldsymbol{s}_n) = \{k : s_{k,n} \geq \epsilon\} \tag{2.13}$$

In each iteration of the bi-coordinate ascent algorithm, a donor i and an acceptor j will be selected using the following rule.

$$i = \underset{k \in \mathcal{A}_n^\epsilon(\boldsymbol{s}_n)}{\arg\max}\ f_{k,n}{}'(0; \boldsymbol{s}_k), \quad j = \underset{k \in \mathcal{D}_n^\epsilon(\boldsymbol{s}_n)}{\arg\min}\ f_{k,n}{}'(0; \boldsymbol{s}_k) \tag{2.14}$$

It is easily seen that when i and j are chosen using rule (2.14), for small positive t, the largest possible WSR increase is achieved. The resulting algorithm framework for derivative based (DB) real-time spectrum coordination is given in Algorithm 1. Algorithm 1 allows multiple algorithms to be defined, depending on how the step size t is calculated in line 7. One possibility, inspired by F-IPDB is examined in Section 2.5. First, however, the stop criterion in line 4 is explained.

It is well known that $\boldsymbol{s}^{(\ell)}$ is a stationary point if and only if it satisfies the Karush-Kuhn-Tucker (KKT) conditions. The per user version of problem (2.3)

Algorithm 1. derivative based spectrum coordination.

1: Initialize $\tau > 0$, $\epsilon > 0$ $\ell = 0$, and $\boldsymbol{s}^{(1)}$
2: **while** no global convergence **do**
3: **for** $n \in \mathcal{N}$ **do**
4: **while** $f_{i,n}{}'(0; \boldsymbol{s}_i^{(\ell)}) - f_{j,n}{}'(0; \boldsymbol{s}_j^{(\ell)}) \geq \tau$ **do**
5: $\ell \leftarrow \ell + 1$
6: Determine i and j using (2.14)
7: Calculate t
8: Update $s_{i,n}^{(\ell+1)}$ and $s_{j,n}^{(\ell+1)}$ using (2.5)

is considered, which has the same objective function as (2.3), but limits its set of decision variables to $\boldsymbol{s}_n$, the transmit spectrum of a single user n. For the per user version of problem (2.3), the KKT conditions can be stated as

$$\exists \lambda_n : \quad f_{k,n}{}'(0; \boldsymbol{s}_k) \begin{cases} = \lambda_n & 0 < s_{k,n} < s_{k,n}^{\text{mask}} \\ \geq \lambda_n & s_{k,n} = s_{k,n}^{\text{mask}} \\ \leq \lambda_n & s_{k,n} = 0 \end{cases} \quad \forall k \in \mathcal{K}.$$

The KKT conditions can alternatively be formulated in the primal domain, without employing the dual variable λ_n.

$$\max_{k \in \mathcal{A}_n^{\epsilon}(\boldsymbol{s})} f_{k,n}{}'(0; \boldsymbol{s}) \leq \min_{k \in \mathcal{D}_n^{\epsilon}(\boldsymbol{s})} f_{k,n}{}'(0; \boldsymbol{s}), \quad \forall \epsilon \in \mathbb{R}_+ \tag{2.15}$$

Consider $\boldsymbol{s}_n^{(\ell)}$, the power spectrum of user n that is obtained after the stop criterion in line 4 of Algorithm 1 is satisfied. Clearly, $\boldsymbol{s}_n^{(\ell)}$ satisfies stationarity condition (2.15) up to tolerances of τ and ϵ, i.e.

$$\max_{k \in \mathcal{A}_n^{\epsilon}(\boldsymbol{s}_n^{(\ell)})} f_{k,n}{}'(0; \boldsymbol{s}_n^{(\ell)}) < \min_{k \in \mathcal{D}_n^{\epsilon}(\boldsymbol{s}_n^{(\ell)})} f_{k,n}{}'(0; \boldsymbol{s}_n^{(\ell)}) + \tau. \tag{2.16}$$

In accordance with the terminology defined in [99], $\boldsymbol{s}_n^{(\ell)}$ is referred to as an ϵ-τ-stationary point of the per user version of problem (2.3). By choosing ϵ and τ small, the result from the inner iteration of Algorithm 1 can be made to lie arbitrarily close to a stationary point. Assuming this stationary point is uniquely attained [17], the iteration over different users converges to stationary point of (2.3).

2.5 Fast derivative based iterative power difference balancing

The framework of Algorithm 1 allows multiple algorithms to be defined, which differ solely in their approach to calculating t. Here, an algorithm is formulated that takes a similar approach to calculating t as F-IPDB. The algorithm, referred to as fast derivative-based iterative power difference balancing (F-DB-IPDB), calculates the step size as the solution to (2.11). This solution is henceforth denoted as $t^\star$. Note that this is different from the calculation of the step size t for F-IPDB, which involves iteratively solving (2.11). F-DB-IPDB applies no such iterations, but solves (2.11) only once, updates $s_{i,n}$ and $s_{j,n}$, and then selects new tones i and j.

It can be shown that for F-DB-IPDB, the inner loop of Algorithm 1 will stop in a finite number of iterations. The proof of this convergence result can be found in Appendix A. Note however that this convergence result is significant in that for the 2-tone DoV based coordinate ascent methods, convergence to a stationary point could not be established [190].

As (2.11) is a convex one-dimensional problem, the following statement holds. If $\exists \tilde{t} \in [t_{\min}, t_{\max}]$ that satisfies (2.12), then $t^\star = \tilde{t}$. Otherwise, $t^\star$ is one of the boundary points of $[t_{\min}, t_{\max}]$. Equation (2.12) can be written more explicitly as

$$\frac{\omega_n / \log(2)}{A_{i,n} + t} + B_{i,n} = \frac{\omega_n / \log(2)}{A_{j,n} - t} + B_{j,n}, \tag{2.17}$$

where $A_{k,n} = s_{k,n} + \Gamma(\sigma_{k,n} + \sum_{m \neq n} \alpha_k^{n,m} s_{k,m})$, and $B_{k,n} = \sum_{m \neq n} \omega_m {b_{k,m}}'(\boldsymbol{s}_k)$. It is easily verified that equation (2.17) has two solutions $\tilde{t}_+$ and $\tilde{t}_-$, which are given as

$$\tilde{t}_{+,-} = \frac{A_{j,n} - A_{i,n}}{2} + \frac{1}{B} \pm \frac{\sqrt{(A_{i,n} + A_{j,n})^2 B^2 + 4}}{2B}, \tag{2.18}$$

where $B = \log(2)(B_{j,n} - B_{i,n})/\omega_n$. In case $B = 0$, there is only one solution to (2.17), which is $\tilde{t} = (A_{j,n} - A_{i,n})/2$. Four candidate solutions are thus available: $t_{\min}$, $t_{\max}$, $\tilde{t}_+$, and $\tilde{t}_-$. It will now be shown that this set can be reduced, as both $t_{\min}$ and $\tilde{t}_+$ cannot be optimal. Consequently, the complexity of solving (2.11) can be reduced.

First, it is shown that $t_+^\star$ cannot be a solution to (2.11). It is easily verified that the following inequality holds.

$$\frac{A_{i,n} + A_{j,n}}{2} < \operatorname{sgn}(B) \frac{\sqrt{(A_{i,n} + A_{j,n})^2 B^2 + 4}}{2B} \tag{2.19}$$

where $\mathrm{sgn}(\cdot)$ represents the signum function. For $B > 0$, combining (2.18) and (2.19), and using the definition of $t_{\max}$ from (2.8), leads to the conclusion that

$$\tilde{t}_+ > A_{j,n} + \frac{1}{B} > t_{\max}. \tag{2.20}$$

Similarly, for $B < 0$ it can be shown that

$$\tilde{t}_+ < -A_{i,n} + \frac{1}{B} < t_{\min}. \tag{2.21}$$

From (2.20) and (2.21), it immediately follows that $\tilde{t}_+ \notin [t_{\min}, t_{\max}]$. Therefore, $\tilde{t}_+$ cannot be a solution to (2.11). The fact that $\tilde{t}_+ \notin [t_{\min}, t_{\max}]$ can also be used to speed up the calculations of the original F-IPDB algorithm.

Secondly, it is shown that $t_{\min}$ cannot be a solution to (2.11). Due to rule (2.14) that is used in choosing i and j, ${\phi_n^{i,j}}'_{\mathrm{cvx}}(t; \boldsymbol{s})$ is positive for $t = 0$. Also, ${\phi_n^{i,j}}_{\mathrm{cvx}}(t; \boldsymbol{s})$ is known to be concave. Combining these facts, it is easily seen that

$$\forall t \in [t_{\min}, 0): \quad {\phi_n^{i,j}}_{\mathrm{cvx}}(t; \boldsymbol{s}) < {\phi_n^{i,j}}_{\mathrm{cvx}}(0; \boldsymbol{s}), \tag{2.22}$$

which excludes $t_{\min}$ as a possible solution to (2.11).

Two possible solutions remain, i.e. $t^\star = \tilde{t}_-$ or $t^\star = t_{\max}$. The calculation of $t^\star$ can be further simplified by making the following observations. First, recall that if $\tilde{t}_- \in [t_{\min}, t_{\max}]$, then $t^\star = \tilde{t}_-$. Examining (2.17), it is seen that $\exists t \in [0, A_{j,n})$ that satisfies (2.17), which is given by either $\tilde{t}_+$ or $\tilde{t}_-$. Due to (2.20) and (2.21), this cannot be $\tilde{t}_+$, which implies $\tilde{t}_- \in [0, A_{j,n})$. It can therefore be concluded that $\tilde{t}_- \in [t_{\min}, t_{\max}]$ if and only if $\tilde{t}_- < t_{\max}$. Keeping in mind the definition of $t_{\max}$, the optimal solution to (2.11) can thus be calculated as

$$t^\star = \min\{\tilde{t}_-, s_{i,n}^{\mathrm{mask}} - s_{i,n}, s_{j,n}\}. \tag{2.23}$$

The resulting F-DB-IPDB algorithm is given as Algorithm 1 with line 7 replaced by equations (2.18) and (2.23).

It could be argued that F-DB-IPDB has a higher complexity than F-IPDB due to the calculation of ${f_{k,n}}'(0; \boldsymbol{s}_k)$, and applying rule (2.14). Note however that ${f_{k,n}}'(0; \boldsymbol{s}_k)$ is computed as $1/A_{k,n} + B_{k,n}$, where terms $A_{k,n}$ and $B_{k,n}$ are also used to determine $\tilde{t}_-$. The calculation of ${f_{k,n}}'(0; \boldsymbol{s}_k)$ thus adds small additional computational complexity. The tone selection rule (2.14) can be efficiently implemented by storing an ordered list of derivatives ${f_{k,n}}'(0; \boldsymbol{s}_k)$. Tones i and j are then simply chosen as the first and last entries of this list, that are also elements of $\mathcal{A}_n^\epsilon$ and $\mathcal{D}_n^\epsilon$, respectively. In each iteration, updating this list requires searching the new derivative's position, which introduces a complexity of order $\log(K)$. Overall, the complexity of a single calculation of

Table 2.1: G.fast parameter settings.

Parameter	Value	Parameter	Value
P_n^{tot}	4 dBm	K	2047
f_{s}	48 kHz	Δ_f	51.75 kHz
Γ	12.6 dB	ω_n	1 $\quad \forall n \in \mathcal{N}$

F-DB-IPDB thus certainly increases w.r.t. F-IPDB. Simulations however show that F-DB-IPDB requires less time to converge than F-IPDB. This is explained by the larger per iteration WSR increase of F-DB-IPDB, which is a consequence of the greedy tone selection strategy, and the non-iterative nature of the step size selection.

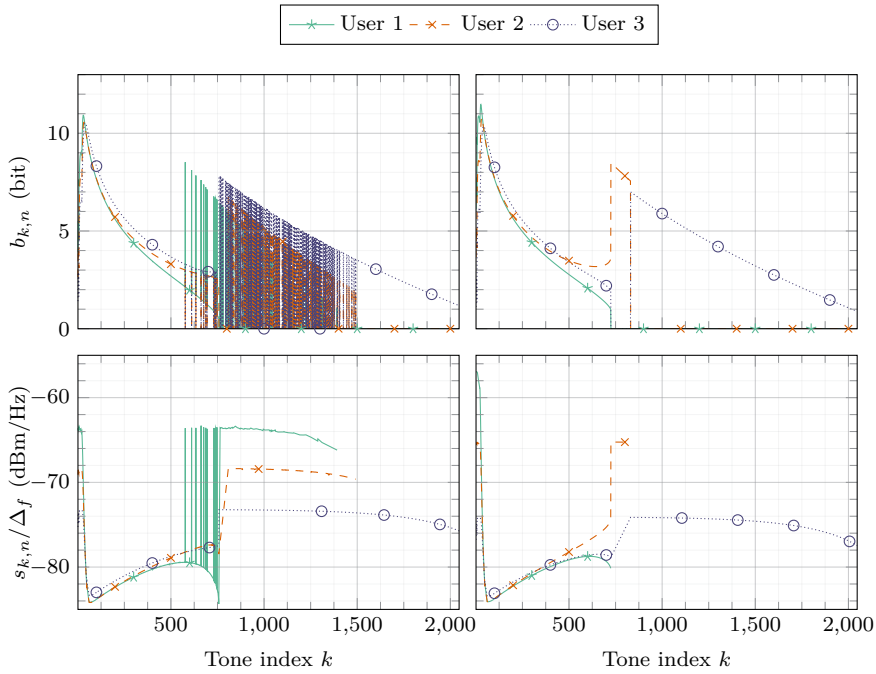
2.6 Simulation results

The performance of F-DB-IPDB is compared to F-IPDB for a three user G.fast scenario, the settings of which are described by Table 2.1. The line lengths of the three users are 200m for user 1, 160m for user 2, and 120m for user 3. No spectral mask is applied throughout the simulations.

To allow for a fair comparison between F-IPDB and F-DB-IPDB, the parameters of both algorithms are chosen similarly. The initial transmit spectrum is $s_{k,n} = P_n^{\text{tot}}/K$. Both algorithms iterate 50 times over all users. Within these outer iterations, the algorithm selects each user in random order. Then F-IPDB generates two random permutations π of $[1, \ldots, K]$, and loops over all i for both of these permutations. For each combination of tones i and $j = \pi(i)$, F-IPDB iteratively calculates a stationary point of (2.6). Alternatively, F-DB-IPDB executes lines 5 to 8 of Algorithm 1.

The resulting power spectrum and bit loading for F-IPDB are shown in Figure 2.1a. At high frequencies, where crosstalk is strong, the power spectrum and bit loading are non-smooth functions. For F-IPDB, an equalization procedure has been proposed to suppress this phenomena and boost performance [190]. Equalization is a heuristic procedure which is based on the assumption that the transmit spectrum should not vary much from one tone to the next. It is however not included in these simulations, to allow for a more fair comparison.

Figure 2.1b displays the transmit spectrum and bit loading that result from F-DB-IPDB. It is readily seen that the power spectrum and bit loading are smooth functions. The equalization procedure from F-IPDB is, in this specific case,



(a) F-IPDB (b) F-DB-IPDB

Figure 2.1: Bit loading and transmit spectrum of a three user G.fast system, obtained through F-IPDB and F-DB-IPDB.

not required. Figure 2.2 gives some indication on the convergence of F-IPDB and F-DB-IPDB. It displays the sequence of values of the objective function of (2.3) that are obtained after each iteration of both F-IPDB and F-DB-IPDB. Note again that each iteration of F-IPDB itself features an iterative procedure to select a step size, while F-DB-IPDB calculates the step size analytically. Figure 2.2 clearly indicates that F-DB-IPDB converges both faster and to a better solution, a result which has been observed in most simulations and regardless of whether a spectral mask is applied.

2.7 Conclusion

We have proposed the framework of bi-coordinate ascent methods for real-time spectrum coordination. The new framework gives rise to F-DB-IPDB, an RT-DSM algorithm with provable convergence properties. Using simulations,

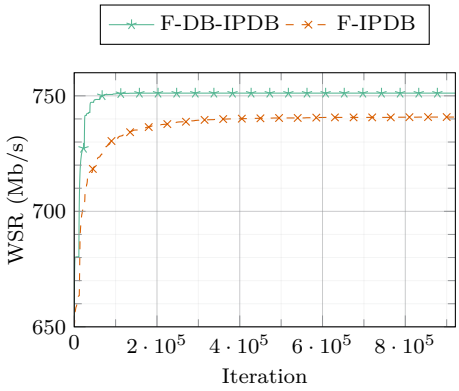


Figure 2.2: Convergence result for F-IPDB and F-DB-IPDB.

F-DB-IPDB has been shown to outperform state of the art real-time spectrum coordination algorithms. Further improvements to F-DB-IPDB encompass including inequality constraints by the means of 'slack tones', and deriving tone selection rules that allow for parallel execution.

Chapter 3

Network Utility Maximization-based DSM

Network Utility Maximization for Adaptive Resource Allocation in DSL Systems

Jeroen Verdyck, Chris Blondia, and Marc Moonen

Published in *Proc. 26th European Signal Processing Conference (EUSIPCO)*, pp. 787 - 791, September 2018, DOI: 10.23919/EUSIPCO.2018.8553357.

© 2018 IEEE. Reprinted, with permission, from:
Jeroen Verdyck, Chris Blondia, and Marc Moonen, "Network Utility Maximization for Adaptive Resource Allocation in DSL Systems," *Proc. 26th European Signal Processing Conference (EUSIPCO)*, pp. 787 - 791, September 2018.
Changes include layout, representation, and minor editing aspects.

The candidate's contributions as first author include: all performed research and writing of the article under guidance of the co-authors.

Abstract

When signal coordination techniques can not eliminate all crosstalk in a digital subscriber line (DSL) system, competition for data rate among different users is strong. In such scenarios, employing a static resource allocation fails to capitalize on the time dependent nature of the traffic carried by the DSL network. An alternative approach is adaptive resource allocation, consisting of dividing time into slots of short duration and using a different resource allocation in each slot. A cross-layer scheduler then decides on the resource allocation for each time slot by solving a network utility maximization (NUM) problem. For many DSL systems however, this NUM problem is non-convex and NP-hard. This chapter presents a fast algorithm for finding a local solution to the NUM problem, which is referred to as NUM-DSB. The algorithm is able to handle many DSL deployment scenarios, and is applicable regardless of the utility function's properties.

3.1 Introduction

Dynamic spectrum management (DSM) techniques, which are used in digital subscriber line (DSL) systems to fight crosstalk, are often divided into two categories: spectrum coordination and vectoring. Spectrum coordination reduces crosstalk by jointly managing the transmit power spectra of all users, whereas vectoring encompasses jointly coordinating multiple lines on a signal level. As vectoring techniques are often able to fully eliminate the effects of crosstalk, they have become the industry standard as of VDSL2 [94].

In many practical deployment scenarios however, the elimination of all crosstalk through vectoring is inhibited, such that one has to rely on spectrum coordination to tone down the effects of the residual crosstalk. Examples include fiber to the frontage deployments implementing multi-user full-duplex signaling [110, 177], and deployments where multiple DSL access multiplexers (DSLAMs) are active on a single cable binder [209]. Optimizing the performance in such a system corresponds to solving a multi-objective optimization problem, yielding a collection of Pareto optimal resource allocation configurations from which one has to choose a single configuration for transmission. Often, a conservative approach is followed where the physical layer is configured statically over time using a single Pareto optimal resource allocation.

An alternative to this static resource allocation is adaptive resource allocation (ARA), which consists of dividing time into slots of short duration, and changing the resource allocation from one time slot to the next. A cross-layer scheduler

Algorithm 2. Sequential WSR maximization for NUM

1: Initialize $\boldsymbol{\omega} \in \mathbb{R}_+^N$
2: **for** i = 0, 1, ... **do**
3: Solve maximize$_{\boldsymbol{x}\in\mathcal{X}}$ $\boldsymbol{\omega}^{\mathrm{T}}\boldsymbol{r}(\boldsymbol{x})$
4: Update $\boldsymbol{\omega}$

then chooses one setting for each time slot in accordance with upper layer requirements. To this end, the cross-layer scheduler defines a utility function U, and solves the resulting network utility maximization (NUM) problem, i.e.

$$\underset{\boldsymbol{x}\in\mathcal{X}}{\text{maximize}}\ U([r_1(\boldsymbol{x}), ..., r_N(\boldsymbol{x})]^{\mathrm{T}}), \tag{3.1}$$

where $\boldsymbol{x}$ is the physical layer resource allocation, and $r_n(\boldsymbol{x})$ denotes the resulting data rate for user n. Algorithms finding the global optimum of problem (3.1) are available in [22, 131]. It has been shown that adaptive resource allocation can lead to significantly improved throughput and delay performance [171, 200], as well as to a reduced power consumption [196].

As the rate region of a DSL system is a convex set [32], the solution to any NUM problem can be found by solving a sequence of weighted sum rate (WSR) maximization subproblems [22], as in Algorithm 2. Convergence of such WSR based NUM algorithms however requires finding the global optimum of each WSR maximization subproblem. As finding the globally optimal solution to the WSR maximization subproblem yielded by many DSM techniques, including the techniques considered in this chapter, is itself NP-hard [228], directly applying Algorithm 2 to problem (3.1) results in an exceedingly high computational complexity. This is especially problematic in the context of ARA, where a large number of NUM problems is to be solved.

This chapter therefore proposes an new algorithm for the NUM problem (3.1), which will be referred to as NUM-DSB. The algorithm is highly generic—both in the sense of being able to handle many deployment scenarios, and of being applicable regardless of the utility function's properties. NUM-DSB is based on distributed spectrum balancing (DSB) [188] for WSR maximization in systems that only employ spectrum coordination.

3.2 DSB as a minorize-maximization algorithm

DSB [188, 193] is a low-complexity algorithm for finding a local solution of the WSR maximization problem in DSL systems that do not employ any signal

coordination. Initially, DSB has been introduced as a fixed point algorithm aimed at finding a solution to the KKT stationarity conditions [188]. In this section, a generalized version of DSB is described, encompassing coupling constraints between users. In the exposition, DSB is interpreted as a minorize-maximization (MM) algorithm [183]. This interpretation is in line with recent optimization literature [56, 154, 162], and more easily lends itself to be extended to NUM problems.

DSB can be applied to optimization problems of the form

$$\underset{\boldsymbol{x}}{\text{maximize}} \quad \sum_{i\in\mathcal{I}} \sum_{n\in\mathcal{N}_i} \omega_{i,n} r_{i,n}(\boldsymbol{x}) \tag{3.2a}$$

$$\text{subject to} \quad \boldsymbol{x}_i \in \mathcal{X}_i, \, \forall i \in \mathcal{I}, \tag{3.2b}$$

where $\mathcal{I} \triangleq \{1, ..., I\}$ is a set of group indices, and where $\mathcal{N}_i \triangleq \{1, \ldots, N_i\}$ denotes the set of users that are in group i. The decision variable $\boldsymbol{x}$ consists of multiple coordinate blocks, i.e. $\boldsymbol{x}^{\mathrm{T}} = [\boldsymbol{x}_1^{\mathrm{T}}, ..., \boldsymbol{x}_I^{\mathrm{T}}]$, where coordinate block $\boldsymbol{x}_i$ corresponds to the resource allocation variables of the users in group i. Moreover, each rate function $r_{i,n}$ is assumed to be concave in the coordinate block associated with its group $\boldsymbol{x}_i$, and convex in all other coordinate blocks $\boldsymbol{x}_j$, where $j \in \mathcal{I} \setminus i$.

Many DSM techniques yield resource allocation problems that fit problem (3.2). Examples include the power allocation problem in DSL systems employing only spectrum coordination [188], the joint transmit power allocation and receive filter design problem in upstream DSL systems [193], the power allocation problem in multi-user full-duplex DSL systems employing zero-forcing precoders and receive filters [177], and the power allocation problem in downstream grouped vectoring (GV) scenarios with zero-forcing precoders [209]. This last problem will be studied more extensively in Section 3.4.

In each iteration, DSB solves a set of surrogate problems, one for each group $i \in \mathcal{I}$, which are much easier to solve than the original WSR maximization problem (3.2). The surrogate problem of group i is obtained from (3.2) by restricting the maximization to $\boldsymbol{x}_i$—i.e. by considering all variables $\boldsymbol{x}_j$ with $j \in \mathcal{I} \setminus i$ to be constant—and approximating the rate of the users not in $\mathcal{N}_i$ with a first order Taylor expansion, i.e.

$$\underset{\boldsymbol{x}_i}{\text{maximize}} \quad \sum_{j\in\mathcal{I}} \sum_{n\in\mathcal{N}_j} \omega_{j,n} \tilde{r}_{j,n}^{(i)}(\boldsymbol{x}_i; \bar{\boldsymbol{x}}) \tag{3.3a}$$

$$\text{subject to} \quad \boldsymbol{x}_i \in \mathcal{X}_i. \tag{3.3b}$$

In (3.3), $\bar{\boldsymbol{x}}$ is the current value of $\boldsymbol{x}$, and $\tilde{r}_{j,n}^{(i)}$ is defined as

$$\tilde{r}_{j,n}^{(i)}(\boldsymbol{x}_i;\bar{\boldsymbol{x}}) \triangleq \begin{cases} r_{j,n}([\bar{\boldsymbol{x}}_1^{\mathrm{T}},...,\boldsymbol{x}_i^{\mathrm{T}},...,\bar{\boldsymbol{x}}_I^{\mathrm{T}}]^{\mathrm{T}}) & \text{if } j=i \\ \bar{r}_{j,n}+(\boldsymbol{x}_i-\bar{\boldsymbol{x}}_i)^{\mathrm{T}}\nabla_{\boldsymbol{x}_i} r_{j,n}\big|_{\boldsymbol{x}=\bar{\boldsymbol{x}}} & \text{if } j\neq i \end{cases} \tag{3.4}$$

where $\bar{r}_{j,n} \triangleq r_{j,n}(\bar{\boldsymbol{x}})$. After solving a set of surrogate problems, either a single or all coordinate blocks of $\bar{\boldsymbol{x}}$ are updated (these modes of operation are respectively referred to as 'Gauss-Seidel' (GS) and 'Jacobi' updating), and a new set of surrogate problems is constructed. The resulting sequence of values for $\bar{\boldsymbol{x}}$ *can* converge to a stationary point of the original optimization problem (3.2). Moreover, each iterate $\bar{\boldsymbol{x}}$ generated by the algorithm is feasible, such that DSB complies with the definition of a real-time DSM algorithm [190].

Due to its convexity in $\boldsymbol{x}_i$ for $j \neq i$, $\tilde{r}_{j,n}^{(i)}$ constitutes a lower bound approximation on $r_{j,n}$ which is exact in $\bar{\boldsymbol{x}}$, i.e.

$$r_{j,n}([\bar{\boldsymbol{x}}_1^{\mathrm{T}},...,\boldsymbol{x}_i^{\mathrm{T}},...,\bar{\boldsymbol{x}}_I^{\mathrm{T}}]^{\mathrm{T}}) \geq \tilde{r}_{j,n}^{(i)}(\boldsymbol{x}_i;\bar{\boldsymbol{x}}) \tag{3.5a}$$

$$r_{j,n}(\bar{\boldsymbol{x}}) = \tilde{r}_{j,n}^{(i)}(\bar{\boldsymbol{x}}_i;\bar{\boldsymbol{x}}). \tag{3.5b}$$

Similarly, the objective in (3.3a) is a lower bound on the objective in (3.2a). When employing GS updating, DSB can thus be interpreted as a block-wise (MM) algorithm which is guaranteed to converge when as the objective of (3.3a) is bounded from above. As the surrogate functions (3.4) also satisfy [154, Assumption 2], it can additionally be proven that DSB with GS updating indeed converges to a stationary point of problem (3.2).

It is noted that in this section, DSL nomenclature has been adopted by referring to the algorithm as 'DSB'. The general algorithmic structure is however known as 'successive convex approximation' (SCA). SCA algorithms with proven convergence that include DSB as a special case, are BSUM [154], SJBR [162] and FLEXA [56].

3.3 NUM-DSB

This section shows how the DSB algorithm can be extended such that it can be applied to NUM problems. The resulting algorithm will be referred to as DSB for network utility maximization (NUM-DSB), and can be applied to NUM problems of the following form.

$$\underset{\boldsymbol{x}}{\text{maximize}} \quad U\left(\boldsymbol{r}(\boldsymbol{x})\right) \tag{3.6a}$$

$$\text{subject to} \quad \boldsymbol{x}_i \in \mathcal{X}_i,\ \forall i \in \mathcal{I} \tag{3.6b}$$

In (3.6), $\boldsymbol{r}(\boldsymbol{x})$ contains the rate vectors of all groups, i.e. $\boldsymbol{r}(\boldsymbol{x})^{\mathrm{T}} = [\boldsymbol{r}_1(\boldsymbol{x})^{\mathrm{T}}, ..., \boldsymbol{r}_I(\boldsymbol{x})^{\mathrm{T}}]$. In turn, $\boldsymbol{r}_i$ contains the rate of all users in group i, i.e. $\boldsymbol{r}_i(\boldsymbol{x})^{\mathrm{T}} = [r_{i,1}(\boldsymbol{x}), ..., r_{i,N_i}(\boldsymbol{x})]$. As before, each rate function $r_{i,n}(\boldsymbol{x})$ is assumed to be concave in its associated coordinate block $\boldsymbol{x}_i$, and convex in all other coordinate blocks $\boldsymbol{x}_j$, where $j \in \mathcal{I} \setminus i$. It should be noted that the same DSM techniques that yield WSR maximization problems fitting (3.2), will also yield NUM problems that fit (3.6).

In each iteration, NUM-DSB solves a set of surrogate problems, one for each group $i \in \mathcal{I}$. The surrogate problem of group i is obtained from problem (3.1) by, again, restricting the maximization to $\boldsymbol{x}_i$, and approximating the rate of all users not in $\mathcal{N}_i$ with a first order Taylor expansion.

$$\underset{\boldsymbol{x}_i}{\text{maximize}} \quad U\left(\tilde{\boldsymbol{r}}^{(i)}(\boldsymbol{x}_i; \bar{\boldsymbol{x}})\right) \tag{3.7a}$$

$$\text{subject to} \quad \boldsymbol{x}_i \in \mathcal{X}_i \tag{3.7b}$$

$$\tilde{r}^{(i)}_{j,n}(\boldsymbol{x}_i; \bar{\boldsymbol{x}}) \geq 0, \, \forall j \in \mathcal{I} \setminus \{i\} \tag{3.7c}$$

In (3.7), $\tilde{\boldsymbol{r}}^{(i)}_{j,n}$ is defined as in (3.4). As the utility function U might be undefined for negative rates, the NUM-DSB surrogate problem enforces positivity of U's arguments by including a positivity constraint on the approximate rates (3.7c). After solving (3.7), $\bar{\boldsymbol{x}}$ is updated and a new set of surrogate problems is constructed. As before, each iterate $\bar{\boldsymbol{x}}$ that is generated by NUM-DSB is feasible, such that NUM-DSB complies with the definition of a real-time DSM algorithm [190].

Each NUM-DSB surrogate problem (3.7) is solved using Algorithm 2. In turn, each iteration of Algorithm 2 requires solving a problem that is, apart from positivity constraint (3.7c), identical to the DSB surrogate problem (3.3). Assuming that the DSB surrogate problem can be solved efficiently, it is likely that each WSR maximization subproblem obtained by applying Algorithm 2 to problem (3.7) can be as well.

Combining the lower bounding property of (3.5a)-(3.5b) with the assumption that U is monotonically increasing in all its components, NUM-DSB with GS updating can still be interpreted as a block-wise MM algorithm. Moreover, as the objective of (3.6a) is bounded from above, NUM-DSB is guaranteed to converge regardless of the utility function's properties. No such convergence guarantees can be given when Jacobi updating is employed. However, NUM-DSB with Jacobi updating has been seen to converge in all numerical experiments that have been executed.

3.4 Application: downstream grouped vectoring

This section considers a downstream grouped vectoring scenario. Each index $i \in \mathcal{I}$ now corresponds to a single vectoring group that contains users $\mathcal{N}_i$. After introducing the system model for such DSL systems, the exposition will focus on showing that the WSR problems yielded by applying Algorithm 2 to problem (3.7) can be solved efficiently.

DSL systems employ discrete multi-tone (DMT) modulation to split the available spectrum into a set of K tones, which is denoted as $\mathcal{K} = \{1, ..., K\}$. It is assumed that there is no so-called inter-carrier interference and hence transmission can be modeled on each tone k independently as

$$\begin{bmatrix} \boldsymbol{y}_{k,1} \\ \vdots \\ \boldsymbol{y}_{k,I} \end{bmatrix} = \begin{bmatrix} \mathbf{H}_{k,11} & \cdots & \mathbf{H}_{k,1I} \\ \vdots & \ddots & \vdots \\ \mathbf{H}_{k,I1} & \cdots & \mathbf{H}_{k,II} \end{bmatrix} \begin{bmatrix} \hat{\boldsymbol{x}}_{k,1} \\ \vdots \\ \hat{\boldsymbol{x}}_{k,I} \end{bmatrix} + \begin{bmatrix} \boldsymbol{z}_{k,1} \\ \vdots \\ \boldsymbol{z}_{k,I} \end{bmatrix}, \tag{3.8}$$

where $\hat{\boldsymbol{x}}_{k,i}$ is an $N_i \times 1$ vector containing the signals transmitted by the i-th vectoring group on tone k. Similarly, $\boldsymbol{y}_{k,i}$ and $\boldsymbol{z}_{k,i}$ respectively contain the received signals and additive Gaussian noise of the i-th vectoring group on tone k. Moreover, $\mathbf{H}_{k,ij}$ is an $N_i \times N_j$ channel matrix with $[\mathbf{H}_{k,ij}]_{nm} = h_{k,ij}^{nm}$ the transfer function between transmitter m of group j and receiver n of group i, evaluated on tone k.

Signal coordination among users in the same group is possible at the transmitter side. Transmitted signals are generated as

$$\hat{\boldsymbol{x}}_{k,i} = \mathbf{T}_{k,i} \boldsymbol{x}_{k,i} \tag{3.9}$$

in group i, where $\mathbf{T}_{k,i}$ is the precoding matrix of group i on tone k, and where $\boldsymbol{x}_{k,i}^{\mathrm{T}} = [x_{k,i,1}, ..., x_{k,i,N_i}]$ contains the transmitted symbols of all users n in group i on tone k. Furthermore, the symbol power of user n in group i on tone k is defined as $s_{k,i,n} = \Delta_f \, \mathbb{E}[|x_{k,i,n}|^2]$, with Δ_f the tone spacing. The aggregate transmit power (ATP) on the n-th line of group i is then calculated as

$$P_{i,n} = \sum_{k \in \mathcal{K}} [\mathbf{T}_{k,i} \operatorname{diag}(\boldsymbol{s}_{k,i}) \mathbf{T}_{k,i}^{\mathrm{H}}]_{nn}, \tag{3.10}$$

with $\boldsymbol{s}_{k,i}^{\mathrm{T}} = [s_{k,i,1}, ..., s_{k,i,N_i}]$. In G.fast, the ATP of each line is limited to $P_{\mathrm{tot}} = 4\,\mathrm{dBm}$.

It is assumed that each vectoring group $i \in \mathcal{I}$ uses a zero-forcing precoder, i.e.

$$\mathbf{T}_{k,i} = \mathbf{H}_{k,ii}^{-1}. \tag{3.11}$$

In order to simplify notation, the effective channel matrix $\hat{\mathbf{H}}_{k,ji} = \mathbf{H}_{k,ji}\mathbf{T}_{k,i}$ is introduced. The resulting SINR of user n in group i on tone k is then

$$\gamma_{k,i,n} = \frac{s_{k,i,n}}{\sigma_{k,i,n} + \sum_{j\in\mathcal{I}\setminus\{i\}} \sum_{m=1}^{N_j} |\hat{h}_{k,ij}^{nm}|^2 s_{k,j,m}}, \tag{3.12}$$

with $\sigma_{k,i,n} = \Delta_f \, \mathbb{E}[|z_{k,i,n}|]$ the received noise power of user n in group i on tone k. When the number of interferers $\sum_{j\in\mathcal{I}\setminus\{i\}} N_j$ is large, then the interference-plus-noise received by the users of group i is well approximated by a Gaussian distribution. Under this assumption, bitloading of user n in group i on tone k is accurately modeled by

$$b_{k,i,n} = \log_2(1 + \Gamma^{-1}\gamma_{k,i,n}), \tag{3.13}$$

where Γ denotes the SNR gap to capacity. The rate of user n in group i is then

$$r_{i,n} = f_{\mathrm{s}} \sum_{k\in\mathcal{K}} b_{k,i,n}, \tag{3.14}$$

with f_{s} the DMT symbol rate.

The above DSL system fits problem (3.6), regardless of the considered utility function. The different groups in (3.6) are given by the vectoring groups in $\mathcal{I}$, and where the feasible sets are defined as

$$\mathcal{X}_i = \{\boldsymbol{s}_i \in \mathbb{R}_+^{KN_i} \mid P_{i,n} \leq P_{\mathrm{tot}}, \, \forall n \in \mathcal{N}_i\}, \tag{3.15}$$

with $\boldsymbol{s}_i = [s_{1,i,1}, ..., s_{K,i,1}, s_{1,i,2}, ..., s_{K,i,N_i}]^{\mathrm{T}}$. It is now shown that the WSR subproblem, obtained by applying Algorithm 2 to the NUM problem in (3.7), can be solved efficiently for the considered DSL system.

First, Lagrange dual decomposition is applied to decouple the WSR problem over users and tones. The Lagrangian $\mathcal{L}_i$ is obtained by dualizing the ATP and rate positivity constraints, i.e.

$$\begin{aligned}\mathcal{L}_i = &\sum_{j\in\mathcal{I}} \sum_{n\in\mathcal{N}_j} \omega_{j,n} \tilde{r}_{j,n}^{(i)}(\boldsymbol{s}_i; \bar{\boldsymbol{s}}) + \sum_{j\in\mathcal{I}\setminus\{i\}} \sum_{n\in\mathcal{N}_j} \lambda_{j,n}^{\mathrm{r}} \tilde{r}_{j,n}^{(i)}(\boldsymbol{s}_i; \bar{\boldsymbol{s}}) \\ &+ \sum_{n\in\mathcal{N}_i} \lambda_{i,n}^{\mathrm{p}} P_{\mathrm{tot}} - \sum_{n\in\mathcal{N}_i} \sum_{k\in\mathcal{K}} \boldsymbol{t}_{k,i,n}^{\mathcal{H}} \boldsymbol{\Lambda}^{\mathrm{p}} \boldsymbol{t}_{k,i,n} s_{k,i,n},\end{aligned} \tag{3.16}$$

with $\boldsymbol{t}_{k,i,n}$ the n-th column of $\mathbf{T}_{k,i}$, and where $\boldsymbol{\lambda}^{\mathrm{p}}$ and $\boldsymbol{\lambda}^{\mathrm{r}}$ respectively contain the Lagrange multipliers associated with the ATP and rate positivity constraints. The resulting Lagrange dual function is then given by

$$g_i(\boldsymbol{\lambda}^{\mathrm{p}}, \boldsymbol{\lambda}^{\mathrm{r}}) = \sup_{\boldsymbol{s}_i \in \mathbb{R}_+^{K\times N_i}} \{\mathcal{L}_i\}. \tag{3.17}$$

As the considered WSR subproblem is convex, the duality gap with problem (3.17) is zero. The maximization in (3.17) is separable per user and per tone, and has a unique maximizer that is given by

$$s^{\star}_{k,i,n} = \Bigg[\frac{f_{\mathrm{s}} \omega_{i,n} / \log(2)}{\boldsymbol{t}_{k,i,n} \boldsymbol{\Lambda}^{\mathrm{p}} \boldsymbol{t}_{k,i,n} - f_{\mathrm{s}} \sum_{j \in \mathcal{I} \setminus \{i\}} \sum_{m \in \mathcal{N}_j} (\omega_{j,m} + \lambda^{\mathrm{r}}_{j,m}) \frac{\partial b_{k,j,m}}{\partial s_{k,i,n}} \big|_{\boldsymbol{x} = \bar{\boldsymbol{x}}}} - \Gamma \Bigg(\sigma_{k,i,n} + \sum_{j \in \mathcal{I} \setminus \{i\}} \sum_{m \in \mathcal{N}_j} |\hat{h}^{nm}_{k,ij}|^2 \bar{s}_{k,j,m} \Bigg) \Bigg]^{+}. \quad (3.18)$$

It can be proven that the dual function as defined in (3.17) is continuously differentiable on its domain, with its partial derivatives given by

$$\frac{\partial g(\boldsymbol{\lambda}^{\mathrm{p}}, \boldsymbol{\lambda}^{\mathrm{r}})}{\partial \lambda^{\mathrm{p}}_{i,n}} = P_{\mathrm{tot}} \mathbf{1} - \sum_{k \in \mathcal{K}} [\mathbf{T}_{k,i} \operatorname{diag}(\boldsymbol{s}^{\star}_{k,i}) \mathbf{T}^{\mathcal{H}}_{k,i}]_{n,n}, \quad (3.19)$$

$$\frac{\partial g(\boldsymbol{\lambda}^{\mathrm{p}}, \boldsymbol{\lambda}^{\mathrm{r}})}{\partial \lambda^{\mathrm{r}}_{j,n}} = \tilde{r}^{(i)}_{j,n}(\boldsymbol{s}^{\star}_{i}; \bar{\boldsymbol{s}}). \quad (3.20)$$

As the dual function is differentiable, one can employ gradient descent methods to solve the Lagrange dual problem, which is given by

$$\underset{\boldsymbol{\lambda}^{\mathrm{p}} \geq 0, \boldsymbol{\lambda}^{\mathrm{r}} \geq 0}{\text{minimize}} \quad g_i(\boldsymbol{\lambda}^{\mathrm{p}}, \boldsymbol{\lambda}^{\mathrm{r}}). \quad (3.21)$$

Differentiability of g_i can be established using results from [155]. First, define function $F_{i,n}$ and its convex conjugate $F^{*}_{i,n}$ as in [155, Chapter 11], i.e.

$$F_{i,n}(\boldsymbol{s}_{i,n}) = \begin{cases} -\tilde{r}^{(i)}_{i,n}([\mathbf{0}^{\mathrm{T}}, ..., \boldsymbol{s}^{\mathrm{T}}_{i,n}, ..., \mathbf{0}^{\mathrm{T}}]^{\mathrm{T}}; \bar{\boldsymbol{s}}) & \text{if } \boldsymbol{s}_{i,n} \geq \mathbf{0} \\ +\infty & \text{if } \boldsymbol{s}_{i,n} \ngeq \mathbf{0} \end{cases}$$

$$F^{*}_{i,n}(\boldsymbol{y}) \triangleq \sup_{\boldsymbol{s}_{i,n}} \{ \boldsymbol{y}^{\mathrm{T}} \boldsymbol{s}_{i,n} - F_{i,n}(\boldsymbol{s}_{i,n}) \}, \quad (3.22)$$

where $\boldsymbol{s}_{i,n} \geq \mathbf{0}$ denotes the element wise inequality, and where $\mathbf{0}$ is an all-zeros vector. Function $F^{*}_{i,n}$ is bounded from above if and only if all elements in $\boldsymbol{y}$ are strictly negative, such that its domain is given by $\operatorname{dom} F^{*}_{i,n} = \{ \boldsymbol{y} \in \mathbb{R}^{N_i \times K} \mid \boldsymbol{y}_{k,n} < 0 \}$. Moreover, for each $\boldsymbol{y} \in \operatorname{dom} F^{*}_{i,n}$, the solution set of the optimization problem defining $F^{*}_{i,n}$ is a singleton. Continuous differentiability of $F^{*}_{i,n}$ then immediately follows from [155, Theorem 11.8] and [155, Corollary 9.19]. As it is possible to equivalently define the dual function from (3.17) as

$$g_i(\boldsymbol{\lambda}^{\mathrm{p}}, \boldsymbol{\lambda}^{\mathrm{r}}) = \sum_{n \in \mathcal{N}_i} F^{*}_{i,n}(\boldsymbol{y}_n) + \boldsymbol{y}_0, \quad (3.23)$$

where each $\boldsymbol{y}_n$, $n \in \{0\} \cup \mathcal{N}_i$ is some affine vector function of the Lagrange multipliers $\boldsymbol{\lambda}^{\mathrm{p}}$ and $\boldsymbol{\lambda}^{\mathrm{r}}$, it follows that the dual function itself is continuously differentiable.

As the weights in the WSR problem are determined by the NUM algorithm that is chosen to update $\boldsymbol{\omega}$ in Algorithm 2, they may often be very different from one another. These large differences result in the curvature of the dual problem being strongly anisotropic, in the sense that the dual function's Hessian has a fairly high condition number. When applying a gradient descent method, this often leads to slow convergence in practice. It is therefore advised to solve problem (3.21) with a variable metric method such as L-BFGS-B [25].

3.5 Simulation results

In this section, simulation results are provided that illustrate the convergence behavior of NUM-DSB. Two versions of NUM-DSB are evaluated: one employing Jacobi updating, which for the original DSB often leads to faster convergence and solutions that achieve a higher WSR value, and one that employs GS updating, which enjoys stronger convergence guarantees.

The DSL systems under consideration contain 2, 3, or 4 vectoring groups. The DSLAM of each vectoring group connects to a maximum of 10 users, where the distance to the DSLAM ranges from 110 m for user 1 up to 200 m for user 10, increasing with 10 m for each consecutive user. The DSL systems with $N_i \leq 10$ contain, for each DSLAM, the first N_i users of their 10-user systems. The utility function of the minimal delay violation (MDV) scheduler [200] is considered, which is of the form $U(\boldsymbol{r}) = \sum_{i\in\mathcal{I}} \sum_{n\in\mathcal{N}_i} -a_{i,n}/r_{i,n}$ and represents an prediction of the number of delay violations as a function of the assigned rates. Note that $a_{i,n}$ is a constant that is determined by the cross-layer scheduler. Parameter settings for the DSL system are summarized in Table 3.1.

The number of iterations required by NUM-DSB to converge is given in Table 3.2, and the utility function value after convergence is displayed in Figure 3.1. The algorithm is terminated when the relative decrease of the utility function between two iterations drops below 10^{-6}. From Table 3.2, it is seen that the required number of iterations often decreases when more groups or users are added to the system. This can be explained by the increased interference in the system, rendering frequency division multiple access solutions optimal. In these cases, NUM-DSB on many tones switches off all but one vectoring group early on, and does not reactivate these in subsequent iterations, leading to fast convergence.

Overall, it is seen that GS updating leads to faster convergence than Jacobi

Table 3.1: G.fast parameter settings.

Parameter	Value	Parameter	Value
P_{tot}	4 dBm	K	2047
f_s	48 kHz	Δ_f	51.75 kHz
Γ	10 dB	a_n	$10^8 \quad \forall n \in \mathcal{N}$

Table 3.2: Number of iterations of NUM-DSB before convergence.

	Gauss-Seidel			**Jacobi**		
N_i	$I = 2$	$I = 3$	$I = 4$	$I = 2$	$I = 3$	$I = 4$
1	53	5	8	59	8	7
2	49	22	38	52	6	14
3	19	29	29	53	18	17
4	17	36	29	52	19	20
5	19	24	9	55	20	21
6	23	9	10	53	21	15
7	22	39	7	60	20	15
8	23	36	8	62	7	16
9	31	47	9	91	8	23
10	49	46	10	70	9	22

updating. Moreover, Figure 3.1 illustrates that GS updating also outperforms Jacobi updating in the sense that it achieves equal or higher utility function values. Contrary to the original DSB, it is no longer true that Jacobi updating mostly outperforms GS updating. In general, NUM-DSB requires only few iterations to obtain a local solution.

3.6 Conclusion

In this chapter, a fast algorithm has been presented for finding a local solution to the NUM problem, which is referred to as NUM-DSB, and which consists of iteratively solving sets of surrogate problems. The algorithm has been shown to be applicable in many DSL deployment scenarios, and regardless of the utility function's properties. In the context of grouped vectoring deployment scenarios, NUM-DSB leads to surrogate problems that are straightforward to solve. Moreover, using empirical evidence it has been shown that NUM-DSB needs only few iterations to find a satisfactory solution.

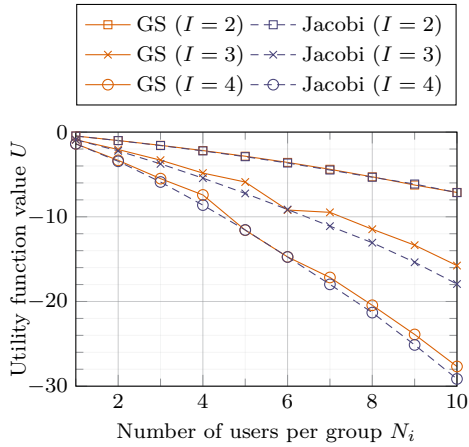


Figure 3.1: Utility function value after convergence of NUM-DSB.

Part II

New DSM Degrees of Freedom

Chapter 4

DSM and QoS Classes

Dynamic Spectrum Management in Digital Subscriber Line Networks with Unequal Error Protection Requirements

Jeroen Verdyck, and Marc Moonen

Published in *IEEE Access*, Vol. 5, pp. 18107 - 18120, September 2017, DOI: 10.1109/ACCESS.2017.2748359.

© 2017 IEEE. Reprinted, with permission, from:
Jeroen Verdyck, and Marc Moonen, "Dynamic Spectrum Management in Digital Subscriber Line Networks with Unequal Error Protection Requirements," *IEEE Access*, Vol. 5, pp. 18107 - 18120, September 2017.
Changes include layout, representation, and minor editing aspects.

The candidate's contributions as first author include: all performed research and writing of the article under guidance of the co-author.

Abstract

Digital subscriber line (DSL) technology remains the most popular broadband access technology. A variety of algorithms has been developed to improve performance in DSL networks, which are commonly referred to as dynamic spectrum management (DSM) algorithms. The main goal of these algorithms is to fight crosstalk between different lines in a cable bundle. Current DSM algorithms provide an equal level of error protection for each serviced application and each user. However, different applications may have unequal error protection (UEP) requirements. The equal level of error protection usually provided by DSM algorithms may then be excessive for some applications, which leads to a waste of valuable resources. This chapter therefore considers DSM for DSL networks providing UEP. Four joint signal and spectrum coordination algorithms are presented, enabling a different level of error protection for different applications. These algorithms are modified versions of existing optimal spectrum balancing (OSB) and distributed spectrum balancing (DSB) algorithms for joint signal and spectrum coordination in upstream as well as downstream DSL. In addition, an algorithm is presented which, for each application, selects a suitable modulation and coding (MC) scheme from a set of admissible MC schemes. Through simulations, it is shown that DSM with UEP can indeed lead to moderate performance gains.

4.1 Introduction

From the vantage point of other layers in the OSI model, the digital subscriber line (DSL) physical layer can be modeled as a single connection per user, through which it can send data at a certain data rate and with a particular level of error protection. The DSL physical layer uses discrete multitone (DMT) modulation, and hence effectively consists of many parallel connections, corresponding to the individual tones. Usually, the same bit error rate (BER) is achieved across tones, as otherwise the BER of the entire system would be dominated by the tone with the highest error rate. However, when a collection of different applications is serviced, there will be differences in the level of error protection that is appropriate for each application. Such differences can even exist within one application, e.g. when a source encoder yields data with different levels of importance. Unequal error protection (UEP) takes advantage of these differences by dividing the one connection per user into a set of subconnections, each with its own data rate, BER, collection of tones, and channel coding. By accommodating for UEP, further performance gains can indeed be achieved.

In general, the BER is governed by two mechanisms. First, modulation based error control consists of choosing the amount of signal power allocated for different constellations. Second, forward error correction (FEC) based error control consists of selecting a certain channel coding scheme. Current DSL networks implement FEC through Reed-Solomon (RS) error correcting codes and trellis coded modulation (TCM) [94,96]. A particular combination of modulation based and FEC based error control will be referred to as a modulation and coding (MC) scheme. Note that different MC schemes can often achieve the same BER. However, these MC schemes do not necessarily result in equal delay or throughput performance. Therefore, care should be taken in choosing an appropriate MC scheme to achieve a specific target BER.

Analogous to error control mechanisms, UEP techniques are classified into two major categories [88]. Transceiver or modulation based UEP schemes constitute the first category, and consist of allocating an unequal amount of transmit power to the constellations of different subconnections. Most modulation based UEP schemes implement either hierarchical modulation [74] or UEP bitloading [23, 74, 129, 205, 227], the latter of which will be considered in this chapter. The second category consists of FEC based UEP schemes, where FEC codes with different rates are used for different subconnections.

Apart from UEP, a variety of algorithms has been developed to improve performance in DSL networks, commonly referred to as dynamic spectrum management (DSM) algorithms [42]. The main goal of these algorithms is to fight crosstalk between different lines in a cable bundle. DSM mainly addresses the problem of interference between different lines in a cable bundle—called crosstalk in the DSL context—which is *the* major source of DSL performance degradation. Increasing demand for higher data rates forces telcos to operate at higher frequencies, at which the crosstalk problem is even more severe.

Three DSM levels are distinguished [42]. Level 1 DSM manages each line individually, at most introducing some politeness in order to mitigate the effects of crosstalk. Higher DSM levels assume some cooperation between lines. In level 2 DSM, the transmit powers of different lines are managed jointly, in order to cooperatively mitigate the effects of crosstalk [32, 47, 147, 176, 192, 218]. This technique is also referred to as spectrum coordination. Finally, level 3 DSM consists of coordinating multiple lines on the signal level [28, 29, 67], and is commonly referred to as signal coordination or vectoring. Signal coordination requires the modems of different lines to be co-located, thus introducing a difference between upstream (US) and downstream (DS) transmission. In US transmission, signal coordination is possible at the receiver side only, such that the US system corresponds to a multiple access channel (MAC). Conversely, DS transmission allows signal coordination only at the transmitter, such that the DS system corresponds to a broadcast channel (BC). Combinations of different

DSM levels are also possible, and exceedingly high data rates can be achieved by combining signal and spectrum coordination [107, 111, 134, 193, 195].

Current DSM algorithms consider DSL networks with a single connection per user, and are incompatible with UEP. This chapter shows how these DSM algorithms can be adapted in order to support UEP. While previous work focused on UEP adaptations of spectrum coordination algorithms [205], this chapter extends the joint signal and spectrum coordination algorithms from [107, 111, 193, 195] to support UEP. Moreover, the problem of joint DSM and per subconnection MC scheme selection, commonly referred to as adaptive modulation and coding (AMC), is tackled. This chapter develops a heuristic algorithm that selects an MC scheme for each subconnection from a set of candidate MC schemes. Furthermore, an upper bound is established which, in simulations, is used to demonstrate that the proposed heuristic algorithm performs very well.

The chapter is organized as follows. In Section 4.2, the system model for the MAC and BC is presented, and a description of how UEP is achieved is given. The general problem statement is provided in Section 4.3. Four algorithms for joint signal and spectrum coordination with UEP are derived in Sections 4.4 and 4.5. These algorithms are adaptations of existing optimal spectrum balancing (OSB) and distributed spectrum balancing (DSB) algorithms for joint signal and spectrum coordination in US and DS DSL. AMC is considered in Section 4.6, where a heuristic algorithm is developed selecting an MC scheme for each subconnection. The performance of the five proposed algorithms is assessed in Section 4.7.

4.2 System model

The DSL physical layer uses DMT to split the available spectrum into a set of orthogonal carriers or tones that experience flat fading. Assuming no inter-carrier interference occurs, transmission can be modeled for each tone independently. For each tone, the channel is modeled as a multiple access channel (MAC) or a broadcast channel (BC), depending on whether US or DS transmission is considered, where signals are jointly coordinated at the receiver or transmitter side. In case coordination is possible neither at the transmitter nor at the receiver side, such as in CO/RT deployments, the channel is modeled as an interference channel for which UEP spectrum coordination algorithms have been developed in [205].

4.2.1 Multiple access channel

US transmission in an N-user DSL network can be modeled for each tone independently as

$$\boldsymbol{y}_k = \mathbf{H}_k \boldsymbol{x}_k + \boldsymbol{z}_k, \quad \forall k \in \mathcal{K}, \tag{4.1}$$

where $\mathcal{K}$ denotes the set of K tones. The vector $\boldsymbol{x}_k = [x_{k,1}, x_{k,2}, \ldots, x_{k,N}]^{\mathrm{T}}$ contains the data symbol of all users on tone k, with $\cdot^{\mathrm{T}}$ denoting the transpose operator. $[\mathbf{H}_k]_{n,m} = h_k^{n,m}$ is the $N \times N$ channel matrix containing the transfer function between the transmitter of user m and receiver of user n, evaluated on tone k. Moreover, $\boldsymbol{z}_k$ is a vector of additive Gaussian noise, and $\boldsymbol{y}_k$ contains the received signal for all users on tone k. Also, define $\mathcal{N}$ as the set of N users.

The transmitted symbol power and received noise power of user n on tone k are respectively denoted as $s_{k,n} = \Delta_f \, \mathbb{E}\{|x_{k,n}|^2\}$ and $\sigma_{k,n} = \Delta_f \, \mathbb{E}\{|z_{k,n}|^2\}$, where Δ_f is the tone spacing and $\mathbb{E}\{\cdot\}$ is the expected value operator. Also define $\boldsymbol{s}_k = [s_{k,1}, s_{k,2}, \ldots, s_{k,N}]^{\mathrm{T}}$ as the symbol power vector of tone k. Likewise, define $\boldsymbol{s}_n = [s_{1,n}, s_{2,n}, \ldots, s_{K,n}]^{\mathrm{T}}$ as the symbol power vector of user n and $\boldsymbol{s} = [\boldsymbol{s}_1^{\mathrm{T}}, \boldsymbol{s}_2^{\mathrm{T}}, \ldots, \boldsymbol{s}_K^{\mathrm{T}}]^{\mathrm{T}}$ as the vector containing the symbol power vectors of all users. Similar vector notation will be used for other power variables, as well as for the SINR, bit rate and Lagrange dual variables. Also, define $p_{k,n}$ as the line power of user n on tone k, which in the MAC is equal to $s_{k,n}$. The total line power of user n is given by

$$P_n = \sum_{k \in \mathcal{K}} p_{k,n}. \tag{4.2}$$

In a MAC, signal coordination is possible at the receiver side. Linear receiver structures are assumed, i.e. transmitted symbols are estimated from the received signal as

$$\hat{\boldsymbol{x}}_k = \mathbf{R}_k^{\mathrm{H}} \boldsymbol{y}_k, \tag{4.3}$$

where $\mathbf{R}_k = [\boldsymbol{r}_{k,1}, \boldsymbol{r}_{k,2}, \ldots, \boldsymbol{r}_{k,N}]$ is the receive matrix on tone k, containing a receive vector $\boldsymbol{r}_{k,n}$ for each transmitted symbol $x_{k,n}$, and where $(\cdot)^{\mathrm{H}}$ denotes the Hermitian transpose operator. The signal-to-interference-plus-noise ratio (SINR) for user n on tone k is given as

$$\gamma_{k,n} = \frac{s_{k,n} |\boldsymbol{r}_{k,n}^{\mathrm{H}} \boldsymbol{h}_{k,n}|^2}{\boldsymbol{r}_{k,n}^{\mathrm{H}} \boldsymbol{\Sigma}_k \boldsymbol{r}_{k,n} + \sum_{m \in \mathcal{N} \setminus \{n\}} s_{k,m} |\boldsymbol{r}_{k,n}^{\mathrm{H}} \boldsymbol{h}_{k,m}|^2}, \tag{4.4}$$

with $\boldsymbol{\Sigma}_k$ the noise covariance matrix on tone k, $\boldsymbol{h}_{k,n}$ the n^{th} column of $\mathbf{H}_k$, and $\cdot \setminus \cdot$ the set subtraction operator.

The optimal linear receiver in the MAC is the MMSE receiver, which maximizes the SINR of each user. Given the symbol power vector $\boldsymbol{s}_k$, the MMSE receive

matrix and resulting SINR for user n are calculated as

$$\mathbf{R}_k = \left(\mathbf{H}_k \mathbf{S}_k \mathbf{H}_k^{\mathcal{H}} + \mathbf{\Sigma}_k \right)^{-1} \mathbf{H}_k \mathbf{S}_k, \tag{4.5}$$

$$\gamma_{k,n} = s_{k,n} \boldsymbol{h}_{k,n}^{\mathcal{H}} \mathbf{\Psi}_{k,n}^{-1} \boldsymbol{h}_{k,n}, \tag{4.6}$$

where $\mathbf{S}_k = \mathrm{diag}\{\boldsymbol{s}_k\}$, and with $\mathbf{\Psi}_{k,n} = \sum_{m \in \mathcal{N} \setminus \{n\}} s_{k,m} \boldsymbol{h}_{k,m} \boldsymbol{h}_{k,m}^{\mathcal{H}} + \mathbf{\Sigma}_k$ the interference-plus-noise covariance matrix of user n on tone k [101, 119]. Note that (4.6) provides the SINR without explicitly determining the corresponding MMSE receive matrix $\mathbf{R}_k$.

The linear MMSE receiver may be the optimal linear receiver, but it is not capacity achieving. The receiver structure that achieves the highest possible weighted sum rate is the non-linear MMSE-GDFE receiver [44], which sequentially decodes the signals of the different users, using the previously decoded signals to remove crosstalk from signals that are decoded subsequently. Optimizing the performance of such a receiver in practice involves finding the optimal decoding order, which is a non-trivial problem [59]. However, assuming the decoding order is fixed, the resource allocation algorithms that are presented here can be readily extended to the MMSE-GDFE case.

4.2.2 Broadcast channel

DS transmission in an N-user DSL network can be modeled for each tone independently as

$$\boldsymbol{y}_k = \mathbf{H}_k^{\mathcal{H}} \mathbf{T}_k \boldsymbol{x}_k + \boldsymbol{z}_k, \quad \forall k \in \mathcal{K}, \tag{4.7}$$

where the $N \times N$ channel matrix $[\mathbf{H}_k]_{n,m} = (h_k^{m,n})^*$ contains the complex conjugate of the transfer function between the transmitter of user n and receiver of user m, evaluated on tone k. The conjugate transpose in (4.7) is introduced in order to simplify notation later on.

Prior to transmission, data symbols are precoded by means of the transmit matrix $\mathbf{T}_k = [\boldsymbol{t}_{k,1}, \boldsymbol{t}_{k,2}, \ldots, \boldsymbol{t}_{k,N}]$, containing a transmit vector $\boldsymbol{t}_{k,n}$ for each data symbol $x_{k,n}$. The line power of line n on tone k is thus calculated as

$$p_{k,n} = [\mathbf{T}_k \mathbf{S}_k \mathbf{T}_k^{\mathcal{H}}]_{nn} \,. \tag{4.8}$$

The SINR for user n on tone k is given as

$$\gamma_{k,n} = \frac{s_{k,n} |\boldsymbol{h}_{k,n}^{\mathcal{H}} \boldsymbol{t}_{k,n}|^2}{\sigma_{k,n} + \sum_{m \in \mathcal{N} \setminus \{n\}} s_{k,m} |\boldsymbol{h}_{k,n}^{\mathcal{H}} \boldsymbol{t}_{k,m}|^2}, \tag{4.9}$$

with $\boldsymbol{h}_{k,n}$ the n-th column of $\mathbf{H}_k$. The problem of finding the optimal transmit matrices $\mathbf{T}_k$ for the BC is more involved than selecting the optimal receive matrices $\mathbf{R}_k$ for the MAC, and will be addressed in Section 4.5.

Again, linear precoding is not optimal. Higher data rates are achievable with non-linear precoders implementing dirty paper coding (DPC) [50]. A DPC-based transmitter successively encodes the symbols of the different users, such that no additional interference is caused into previously encoded users. Finding the optimal DPC transmitter in practice involves finding the optimal encoding order, which is a non-trivial problem [59]. However, once the precoding order is fixed, the resource allocation algorithms that are presented here can be readily extended to the DPC case.

4.2.3 Bitloading and error control

When the number of users N is large, the interference-plus-noise is well approximated by a Gaussian distribution. Under this assumption, the relation between the achieved SINR, as in (4.3) and (4.9), and the achievable information bit rate $b_{k,n}$ of user n on tone k is given by

$$b_{k,n} = b(\gamma_{k,n}, \rho, \Gamma) = \rho \log_2 \left(1 + \frac{\gamma_{k,n}}{\Gamma}\right) \tag{4.10}$$

with ρ the code rate and Γ the signal-to-noise ratio gap to capacity or SNR gap. Throughout this chapter, the information bit rate is considered to be a continuous variable. In what follows, it is outlined how values for ρ and Γ, as well for the post-decoding byte error rate $\mathbb{P}$, are determined for a specific MC scheme.

The SNR gap Γ is determined by the target average BER, coding gain, and noise margin. In the case of zero coding gain and noise margin, assuming QAM constellations with Gray bit mapping, the SNR gap is closely approximated by

$$\Gamma_0 = -\frac{\log\left(5\,\mathrm{BER}\right)}{1.6} \tag{4.11}$$

with $\log(\cdot)$ the natural logarithm. For $\mathrm{BER} \geq 10^{-3}$ and $b \geq 2$, (4.11) results in an overestimation of the true SNR gap by no more than 1dB [40].

Current DSL FEC mechanisms consist of a Reed-Solomon (RS) code and a trellis coded modulation (TCM) [94, 96]. The performance of the TCM is aptly modeled by including a coding gain Γ_c in the SNR gap, the value of which depends on the dimensionality of the TCM code in use [139]. Moreover, the SNR gap can include a noise margin Γ_n, which acts as a protection against

non-stationary noise [198]. By including both the noise margin and the coding gain, the SNR gap becomes

$$\Gamma = \frac{\Gamma_n}{\Gamma_c}\Gamma_0. \tag{4.12}$$

RS codes employed in DSL networks are defined over the Galois field GF(256), implying that each RS symbol consists of one byte. A Reed-Solomon code RS(ν, κ) yields codewords of length ν, containing $\nu - \kappa$ parity symbols and κ information symbols. The RS code thus reduces the data rate of the system by a factor of $\rho_{\text{RS}} = \kappa/\nu$. The code rate is then given by

$$\rho = \rho_{\text{RS}}. \tag{4.13}$$

Assuming no retransmissions are possible and uncorrected errors are passed on unaltered, the post-decoding symbol (i.e. byte) error rate is given by

$$\mathbb{P} = \sum_{i=\tau+1}^{\nu} \frac{(\nu-1)!}{(\nu-i)!(i-1)!} \mathbb{P}_{\text{symb}}{}^{i} (1 - \mathbb{P}_{\text{symb}})^{\nu-i}. \tag{4.14}$$

with $\mathbb{P}_{\text{symb}}$ the pre-decoding symbol error rate calculated as $\mathbb{P}_{\text{symb}} = 1 - (1 - \text{BER})^8$ [208], and with $\tau = \lfloor \frac{\nu-\kappa}{2} \rfloor$ the maximum number of erroneous symbols per codeword that can be corrected.

Although the approximations in this section are fairly accurate, they are only approximations and might lead to flawed DSL performance numbers. Therefore, in the simulations section, we refrain from making comments on absolute performance, and limit the discussion to mutually comparing the performance of algorithms that are developed in this chapter. Moreover, it is possible to obtain more accurate estimations of the parameters ρ and Γ through extensive simulations and measurements, as in [139]. However, this chapter focuses on the interaction between DSM and UEP, not on the estimation of system model parameters such as Γ and ρ.

4.2.4 Unequal error protection

UEP is accomplished by dividing the one connection per user into a set of subconnections, and by employing a specific MC scheme for each subconnection. Each user $n \in \mathcal{N}$ has a set of subconnections $\mathcal{Q}_n$, where each subconnection $q \in \mathcal{Q}_n$ has a set of tones $\mathcal{K}_q$ associated with it. Consequently, each user decides on a tone allocation, i.e. assigns each tone $k \in \mathcal{K}$ to a single subconnection $q \in \mathcal{Q}_n$. Notice that each user transmits data over all tones $k \in \mathcal{K}$, i.e. $\mathcal{K} = \bigcup_{q \in \mathcal{Q}_n} \mathcal{K}_q$, $\forall n \in \mathcal{N}$. Furthermore, define the tone allocation of user n as $\mathcal{T}_n = \{\mathcal{K}_q | q \in \mathcal{Q}_n\}$ and the overall tone allocation as $\mathcal{T} = \{\mathcal{K}_q \mid q \in \bigcup_{n \in \mathcal{N}} \mathcal{Q}_n\}$.

Each subconnection $q \in \mathcal{Q}_n$ is offered a different level of error protection $\mathbb{P}_q$, achieved by using a specific SNR gap Γ_{0q} and resulting BER_q on each tone $k \in \mathcal{K}_q$, and by using dedicated RS and TCM codes to encode its data. Given a target $\mathbb{P}_q$ and the employed RS and TCM codes, the Γ_q required to achieve $\mathbb{P}_q$ is calculated by first inverting (4.14) to obtain the target pre-decoding symbol error rate $\mathbb{P}_{\mathrm{symb}}$ and hence BER, and then applying (4.11) and (4.12).

It is often possible to achieve a single target $\mathbb{P}_q$ using various SNR gap-RS/TCM code combinations, i.e. using various MC schemes. The set of MC schemes achieving $\mathbb{P}_q$ is referred to as the MC set of subconnection q, denoted $\mathcal{M}_q$. Although achieving the same error performance, not all MC schemes in $\mathcal{M}_q$ result in the same delay and throughput performance. Therefore, care should be taken in selecting an MC scheme $i \in \mathcal{M}_q$ for each subconnection q in the DSL network.

The data rate associated with subconnection $q \in \mathcal{Q}_n$ is finally calculated as

$$R_q = f_{\mathrm{s}} \sum_{k \in \mathcal{K}_q} b(\gamma_{k,n}, \rho_q, \Gamma_q) \tag{4.15}$$

with f_{s} the symbol rate.

4.3 Rate-adaptive DSM with unequal error protection

The problem of maximizing the data rates in a DSL network by appropriately choosing symbol powers (and transmit matrices) is commonly referred to as rate-adaptive DSM [175]. Rate adaptive DSM is usually formulated as an optimization problem, where the objective is to maximize the weighted sum of the per user data rates subject to per line power constraints P_n^{tot}. However, here the objective is to maximize the weighted sum of the *per subconnection* data rates, i.e.

$$\begin{aligned} \max_{\substack{\boldsymbol{s},\mathcal{T} \\ \text{or} \\ \boldsymbol{s},\mathbf{T},\mathcal{T}}} \quad & \sum_{n \in \mathcal{N}} \sum_{q \in \mathcal{Q}_n} \omega_q R_q \\ \text{s.t.} \quad & P_n \leq P_n^{\mathrm{tot}}, \, \forall n \in \mathcal{N} \\ & \boldsymbol{s} \in \mathbb{R}_+^{N \times K}, \end{aligned} \tag{4.16}$$

where the positive real weights ω_q are used to give a higher priority to some users or subconnections. In [129, 205], the same approach towards rate-adaptive

DSM with UEP has been considered for the interference channel. The decision variables of problem (4.16) are the symbol power vectors of all users $\boldsymbol{s}$, the overall tone allocation $\mathcal{T}$, and, whenever DS transmission is considered, the transmit matrices $\mathbf{T} = \left[\mathbf{T}_1^{\mathrm{T}}, \mathbf{T}_2^{\mathrm{T}}, \ldots, \mathbf{T}_K^{\mathrm{T}}\right]^{\mathrm{T}}$.

Note that, for now, the problem of optimally choosing an MC scheme $i \in \mathcal{M}_q$ for each $q \in \bigcup_{n\in\mathcal{N}} \mathcal{Q}_n$ is not considered in (4.16). In other words, problem (4.16) considers the case where each MC set $\mathcal{M}_q$ is a singleton. The problem of optimally choosing an MC scheme for each subconnection is addressed in Section 4.6. First, the MAC and BC version of problem (4.16) are tackled in sections 4.4 and 4.5, respectively.

The tone allocation problem can be solved through primal decomposition. Observe that when the symbol power vector $\boldsymbol{s}_k$ (and the transmit matrix $\mathbf{T}_k$) is fixed, user n's decision to allocate tone k to a particular subconnection $q \in \mathcal{Q}_n$ does not affect the achievable value for $\omega_{\bar{q}} b_{k,m}(\gamma_{k,m}, \rho_{\bar{q}}, \Gamma_{\bar{q}})$ for any $\bar{q} \in \mathcal{Q}_m$ of user m, if $m \neq n$. In optimization terms, the tone allocation variable $\mathcal{T}$ is a "local" variable, while $\boldsymbol{s}_k$ and $\mathbf{T}_k$ are "complicating" variables [21]. Therefore, primal decomposition can be applied to problem (4.16). The per user per tone slave problem in this primal decomposition is given by

$$\ddot{b}_n(\gamma_{k,n}) = \max_{q\in\mathcal{Q}_n} \omega_q f_{\mathrm{s}} b(\gamma_{k,n}, \rho_q, \Gamma_q). \tag{4.17}$$

The corresponding master problem is then

$$\begin{aligned} \max_{\substack{\boldsymbol{s} \\ \text{or} \\ \boldsymbol{s},\mathbf{T}}} \quad & \sum_{n\in\mathcal{N}} \sum_{k\in\mathcal{K}} \ddot{b}_n(\gamma_{k,n}) \\ \text{s.t.} \quad & P_n \leq P_n^{\mathrm{tot}}, \, \forall n \in \mathcal{N} \\ & \boldsymbol{s} \in \mathbb{R}_+^{N\times K}. \end{aligned} \tag{4.18}$$

Problem (4.18) will be easier to solve than the original problem, as in (4.16). Therefore, the following sections will focus on solving (4.18) rather than (4.16).

From the definition of $\ddot{b}_n(\gamma_{k,n})$, it is seen that each subconnection $q \in \mathcal{Q}_n$ has a corresponding range for $\gamma_{k,n}$ where allocating tone k to subconnection q results in the maximum weighted information bit rate value. For subconnection $q \in \mathcal{Q}_n$, this range is more formally defined as $\mathcal{G}_q = \left\{\gamma \in \mathbb{R}_+ \mid \ddot{b}_n(\gamma) = \omega_q f_{\mathrm{s}} b(\gamma, \rho_q, \Gamma_q)\right\}$. For user n, $\mathcal{G}_q$ is the same on each tone k and depends solely on the values of ω_q, ρ_q, and Γ_q of each subconnection $q \in \mathcal{Q}_n$. It is readily seen that each $\mathcal{G}_q$ corresponds to a single closed interval. Therefore, given $\gamma_{k,n}$, evaluating (4.17) is efficiently implemented by looking up $\bar{q}$ for which $\gamma_{k,n} \in \mathcal{G}_{\bar{q}}$, and subsequently calculating $\omega_{\bar{q}} f_{\mathrm{s}} b(\gamma_{k,n}, \rho_{\bar{q}}, \Gamma_{\bar{q}})$.

Enabling all subconnections $q \in \mathcal{Q}_n$ to achieve a nonzero data rate requires $\mathcal{G}_q$ to be a nonempty set for each subconnection. Consider the case where user n has two subconnections $\mathcal{Q}_n = \{q_1, q_2\}$, with $\Gamma_{q_1} > \Gamma_{q_2}$. It is readily seen that $\mathcal{G}_{q_1} = \emptyset$ if $\omega_{q_1}\rho_{q_1} < \omega_{q_2}\rho_{q_2}$. Likewise, $\mathcal{G}_{q_2} = \emptyset$ if $\frac{\omega_{q_1}\rho_{q_1}}{\omega_{q_2}\rho_{q_2}} > \frac{\Gamma_{q_1}}{\Gamma_{q_2}}$. Care thus needs to be taken when choosing the weights ω_q. In the previous example, given ω_{q_2}, a good range of values to choose ω_{q_1} from is $\left[\omega_{q_2}\frac{\rho_{q_2}}{\rho_{q_2}}, \omega_{q_2}\frac{\Gamma_{q_1}\rho_{q_2}}{\Gamma_{q_2}\rho_{q_1}}\right]$. Another possible strategy is to let each weight depend on the instantaneous queue length of the associated subconnection.

4.4 Upstream DSM with unequal error protection

In this section, two algorithms that solve the US version of the rate-adaptive DSM problem are presented: MAC-OSB-UEP achieves the global optimum of problem (4.18) at the cost of an exponential complexity in the number of users N; MAC-DSB-UEP exhibits lower complexity, but attains only a local optimum of problem (4.18). In this section, whenever problem (4.18) is referred to, the US version is considered.

4.4.1 Globally optimal solution: MAC-OSB-UEP

Optimization problem (4.18) is non-convex. Exhaustively searching for its global optimum results in an exponential complexity in NK. However, the same globally optimal solution strategy as in [205] can be employed, which is based on the optimal spectrum balancing (OSB) dual decomposition algorithm [32, 195].

The idea of dual decomposition is to solve the Lagrange dual problem associated with (4.18), given by

$$\min_{\boldsymbol{\lambda}} \quad g(\boldsymbol{\lambda}) \tag{4.19}$$

$$\text{with} \quad g(\boldsymbol{\lambda}) = \max_{\boldsymbol{s}\in\mathbb{R}_+^{N\times K}} \mathcal{L}(\boldsymbol{\lambda}, \boldsymbol{s}) \tag{4.20}$$

where $\boldsymbol{\lambda} = [\lambda_1, \lambda_2, \ldots, \lambda_N]^{\mathrm{T}}$ contains the Lagrange dual variables or Lagrange multipliers, and where the Lagrangian $\mathcal{L}(\boldsymbol{\lambda}, \boldsymbol{s})$ is defined as

$$\mathcal{L}(\boldsymbol{\lambda}, \boldsymbol{s}) = \sum_{k\in\mathcal{K}} \mathcal{L}_k(\boldsymbol{\lambda}, \boldsymbol{s}_k) + \sum_{n\in\mathcal{N}} \lambda_n P_n^{\mathrm{tot}} \tag{4.21}$$

$$\text{with} \quad \mathcal{L}_k(\boldsymbol{\lambda}, \boldsymbol{s}_k) = \sum_{n\in\mathcal{N}} \ddot{b}_n(\gamma_{k,n}) - \sum_{n\in\mathcal{N}} \lambda_n p_{k,n}.$$

A well known result from convex optimization states that, when some constraint qualification holds, a primal problem and its Lagrange dual problem have the same solution. Unfortunately, (4.18) is non-convex and the result does not apply. The primal and dual problem have different solutions, the difference being the duality gap. However, when the number of tones K is large, the time sharing property of [220] holds and the duality gap is assumed to be zero.

The Lagrange dual problem consists of a master problem (4.19) and a slave problem (4.20). Dual decomposition algorithms iteratively search for the optimal Lagrange multipliers of the master problem, solving the slave problem at every step along the way. The objective function of the master problem, i.e. the Lagrange dual function $g(\boldsymbol{\lambda})$, is convex but not differentiable. Therefore, the subgradient method [17, 220] is used to solve problem (4.19), which updates $\boldsymbol{\lambda}$ as

$$\lambda_n^{(l+1)} = \left[\lambda_n^{(l)} + \mu^{(l)}\left(\sum_{k=1}^{K} p_{k,n} - P_n^{\text{tot}}\right)\right]^+, \quad \forall n \in \mathcal{N}, \tag{4.22}$$

where l is the iteration number, $\mu^{(l)}$ is a scalar step size, and $[\cdot]^+ = \max(\cdot, 0)$. The subgradient method is guaranteed to converge to the optimal $\boldsymbol{\lambda}$ as long as $\mu^{(l)}$ is sufficiently small [194], and is known to exhibit a convergence rate of $\mathcal{O}(1/\sqrt{l})$. In practice however, sufficient convergence speeds can be achieved using step size scaling heuristics [194] which, assuming adequate algorithm parameters are chosen, typically result in an acceptable solution accuracy after 50-200 iterations.

From the way (4.21) is formulated, it is clear that the Lagrangian $\mathcal{L}(\boldsymbol{\lambda}, \boldsymbol{s})$ can be split into a sum of per tone Lagrangians $\mathcal{L}_k(\boldsymbol{\lambda}, \boldsymbol{s}_k)$, and a term $\sum_{n=1}^{N} \lambda_n P_n^{\text{tot}}$ which is independent of $\boldsymbol{s}$. The slave problem, consisting of maximizing $\mathcal{L}(\boldsymbol{\lambda}, \boldsymbol{s})$ as a function of the transmit spectra $\boldsymbol{s}$, can thus be solved for each tone independently through an exhaustive grid search over a discrete set of symbol power vectors $\boldsymbol{s}_k$. Given the desired solution accuracy ϵ, the number of points in the search grid is $\mathcal{O}(\epsilon^{-N})$. In other words, the resulting algorithm has a complexity that is exponential in N. The exhaustive grid search algorithm is readily seen to converge, as it is guaranteed to have found the optimum after examining each point in the search grid.

The algorithm is summarized in Algorithm 3 and is referred to as MAC-OSB with UEP (MAC-OSB-UEP). As both the subgradient algorithm and the exhaustive grid search can be proven to converge to the global optimum of the problems they solve, MAC-OSB-UEP is guaranteed to converge to the global optimum of problem (4.18).

The complexity difference between MAC-OSB and MAC-OSB-UEP is negligible for any reasonable value of N and $|\mathcal{Q}|$. This fact is demonstrated by the

Algorithm 3. MAC-OSB-UEP

1: Determine $\mathcal{G}_q$, $\forall q \in \bigcup_{n\in\mathcal{N}} \mathcal{Q}_n$
2: **while** distance $> \delta_P$ **do** ▷ Master Problem
3: $\mu \leftarrow 1$
4: $\boldsymbol{\lambda} \leftarrow$ best $\boldsymbol{\lambda}$ so far
5: $\Delta\boldsymbol{\lambda} \leftarrow (\boldsymbol{P}_{\boldsymbol{\lambda}} - \boldsymbol{P}_{\text{tot}})$
6: **while** distance $\leq$ previousDistance **do**
7: previousDistance $\leftarrow$ distance
8: $\mu \leftarrow \mu \times 2$
9: $\boldsymbol{s} \leftarrow$ EXHAUSTIVESEARCH$(\boldsymbol{\lambda} + \mu\Delta\boldsymbol{\lambda})$
10: $\boldsymbol{P}_{\boldsymbol{\lambda}+\mu\Delta\boldsymbol{\lambda}} \leftarrow \sum_{k\in\mathcal{K}} \boldsymbol{s}_k$
11: distance $\leftarrow |\boldsymbol{P}_{\text{tot}} - \boldsymbol{P}_{\boldsymbol{\lambda}+\mu\Delta\boldsymbol{\lambda}}|$
12: $\forall k \in \mathcal{K}$: calculate $\boldsymbol{R}_k$ with (4.5)

13: **function** EXHAUSTIVESEARCH$(\boldsymbol{\lambda})$ ▷ Slave Problem
14: **for** $k \in \mathcal{K}$ **do**
15: **for** $\boldsymbol{s}_k \in$ grid **do**
16: **for** $n \in \mathcal{N}$ **do**
17: Calculate $\gamma_{k,n}$ using (4.6)
18: Look up $\bar{q} \in \mathcal{Q}_n$ for which $\gamma_{k,n} \in \mathcal{G}_{\bar{q}}$
19: Evaluate $\omega_{\bar{q}} f_s b(\gamma_{k,n}, \rho_{\bar{q}}, \Gamma_{\bar{q}})$
20: Calculate $\mathcal{L}_k(\boldsymbol{\lambda}, \boldsymbol{s}_k)$, retain if best so far

following complexity analysis of Algorithm 3. Both MAC-OSB and MAC-OSB-UEP require $I_{\text{SG}} \in [50, \ldots, 200]$ iterations for the subgradient algorithm to achieve acceptable precision, each demanding $\mathcal{O}(K\epsilon^{-N})$ evaluations of the per tone Lagrangian. The lines of Algorithm 3 involved in evaluating the per tone Lagrangian have the following asymptotic complexity. Assuming the Sherman-Morisson relation is used in the calculation of $\gamma_{k,n}, \forall n$ as in [107], line 17 results in $\mathcal{O}(N^3)$ complexity. Furthermore, if the intervals $\mathcal{G}_q, \forall q \in \mathcal{Q}_n$ are stored in an interval tree, then the N queries on line 18 amount to a complexity of $\mathcal{O}(N \log |\mathcal{Q}|)$. Note that it has been assumed that $|\mathcal{Q}_n| = |\mathcal{Q}|, \forall n$. This assumption will be made in all subsequent convergence analyses. The complexity of lines 19 and 20 is respectively $\mathcal{O}(N)$ and $\mathcal{O}(1)$ per evaluation of the Lagrangian. The overall asymptotic complexity of MAC-OSB-UEP is therefore $\mathcal{O}(I_{\text{SG}} K\epsilon^{-N} N(N^2 + \log |\mathcal{Q}|))$. As MAC-OSB is obtained from MAC-OSB-UEP by deleting line 18, the complexity of MAC-OSB is $\mathcal{O}(I_{\text{SG}} K\epsilon^{-N} N^3)$. Therefore, it is concluded that Algorithm 3 adds UEP functionality to MAC-OSB without severely affecting its computational complexity.

4.4.2 Locally optimal solution: MAC-DSB-UEP

Due to its exhaustive grid search with exponential complexity in N, Algorithm 3 is not practical when $N > 5$. Therefore, this subsection derives an alternative to Algorithm 3, achieving a locally optimal solution to problem (4.18). In each iteration of the algorithm, an approximation of (4.18) is constructed for each user. The sequence of solutions to these approximate problems produces a monotonically increasing objective function value, and can be shown to converge to a local optimum of (4.18). The algorithm derived here is a generalization of the so-called MAC-DSB algorithm for rate-adaptive spectrum management [193], and is a type of minorize-maximization (MM) algorithm.

User n's approximation of (4.18) is obtained by fixing the symbol power vectors $\boldsymbol{s}_m$ and tone allocation $\mathcal{T}_m$ of all users $m \neq n$, and by approximating the bit rate of users $m \neq n$ with a lower bound hyperplane. The resulting problem is not convex, yet easy to solve, and is given as

$$\begin{aligned} \max_{\boldsymbol{s}_n \in \mathbb{R}_+^K} \quad & \sum_{k \in \mathcal{K}} \ddot{b}_n(\gamma_{k,n}) + \sum_{k \in \mathcal{K}} a_{k,n} s_{k,n} \\ \text{s.t.} \quad & P_n \leq P_n^{\text{tot}} \\ \text{with} \quad & a_{k,n} = \sum_{m \in \mathcal{N} \setminus \{n\}} \omega_{q_{k,m}} f_{\text{s}} \frac{\partial b(\gamma_{k,m}, \rho_{q_{k,m}}, \Gamma_{q_{k,m}})}{\partial s_{k,n}}. \end{aligned} \tag{4.23}$$

In (4.23), $q_{k,m} \in \mathcal{Q}_m$ denotes the subconnection to which user m has allocated tone k. The derivatives in (4.23) are calculated as

$$\frac{\partial b(\gamma_{k,m}, \rho_{q_{k,m}}, \Gamma_{q_{k,m}})}{\partial s_{k,n}} = \frac{-\rho_{q_{k,m}}}{\log(2)} \frac{s_{k,m} (\boldsymbol{h}_{k,n}^{\text{H}} \boldsymbol{\Psi}_{k,m}^{-1} \boldsymbol{h}_{k,m})^2}{\Gamma_{q_{k,m}} + s_{k,m} \boldsymbol{h}_{k,m}^{\text{H}} \boldsymbol{\Psi}_{k,m}^{-1} \boldsymbol{h}_{k,m}}. \tag{4.24}$$

Problem (4.23) is again solved trough dual decomposition. The Lagrange dual problem of (4.23) is

$$\min_{\lambda} \quad g_n(\lambda) \tag{4.25}$$

$$\text{with} \quad g_n(\lambda) = \max_{\boldsymbol{s}_n \in \mathbb{R}_+^K} \mathcal{L}_n(\boldsymbol{s}_n, \lambda) \tag{4.26}$$

where the Lagrangian is given by

$$\mathcal{L}_n(\boldsymbol{s}_n, \lambda) = \sum_{k \in \mathcal{K}} \mathcal{L}_{k,n}(s_{k,n}, \lambda) + \lambda P_n^{\text{tot}} \tag{4.27}$$

$$\text{with} \quad \mathcal{L}_{k,n}(s_{k,n}, \lambda) = \ddot{b}_n(\gamma_{k,n}) + s_{k,n}(a_{k,n} - \lambda).$$

The duality gap between (4.25) and (4.23) is assumed to be zero by virtue of the same argument as in the derivation of MAC-OSB-UEP. As the Lagrange dual function $g(\lambda)$ is convex and depends only on a single argument λ, problem (4.25) can be solved with a simple bisection search algorithm.

Problem (4.26) can again be solved for each tone independently. The per tone slave problem, defined as

$$\max_{s_{k,n}\geq 0} \mathcal{L}_{k,n}(s_{k,n}, \lambda), \tag{4.28}$$

is non-convex, but can be reformulated as an equivalent problem which is easier to solve.

$$\max_{q\in\mathcal{Q}_n} h(q) \tag{4.29}$$

$$h(q) = \max_{s_{k,n}\geq 0} \left[f_{\mathrm{s}}\omega_q b(\gamma_{k,n}, \rho_q, \Gamma_q) + s_{k,n}\Big(a_{k,n} - \lambda_n\Big)\right] \tag{4.30}$$

The maximization over $s_{k,n}$ will thus be executed for each $q \in \mathcal{Q}_n$, prior to selecting the subconnection q that maximizes $\mathcal{L}_k(s_{k,n}, \lambda)$. What remains is to solve (4.30). Due to the concavity of the objective function in (4.30), the Karush-Kuhn-Tucker (KKT) conditions provide a sufficient condition for optimality. From the system of KKT conditions, the solution to (4.30) is obtained as

$$s_{k,n} = \left[\omega_q\rho_q \frac{f_{\mathrm{s}}/\log(2)}{\lambda_n - a_{k,n}} - \frac{\Gamma_q}{\boldsymbol{h}_{k,n}^{\mathcal{H}}\boldsymbol{\Psi}_{k,n}^{-1}\boldsymbol{h}_{k,n}}\right]^+. \tag{4.31}$$

The resulting algorithm is summarized in Algorithm 4 and is referred to as MAC-DSB with UEP (MAC-DSB-UEP). Convergence of MAC-DSB-UEP is established by demonstrating that, up to a constant factor and for each value of $\boldsymbol{s}_n$, the objective function of (4.23) is a lower bound on the objective function of (4.18). Convergence then follows from the fact that the objective function of (4.18) is upper bounded. Note that this convergence result does not imply that Algorithm 4 converges to a stationary point of problem (4.18).

To see the lower bound property of the objective function of (4.23), first observe that each $\ddot{b}_m(\gamma_{k,m})$ is a non-smooth convex function of $s_{k,n}$. This is due to $\ddot{b}_m(\gamma_{k,m})$ being the pointwise supremum over a set of convex functions $\{\omega_q f_{\mathrm{s}} b(\gamma_{k,m}, \rho_q, \Gamma_q)\}_{q\in\mathcal{Q}_n}$ of $s_{k,n}$. Therefore, $a_{k,n}$ is a subderivative of $\sum_{m\in\mathcal{N}\setminus\{n\}} \ddot{b}_m(\gamma_{k,m})$ as a function of $s_{k,n}$. Furthermore, $a_{k,n}s_{k,n} + c_{k,n}$ is an affine lower bound on $\sum_{m\in\mathcal{N}\setminus\{n\}} \ddot{b}$, where $c_{k,n}$ is chosen such that $\sum_{m\in\mathcal{N}\setminus\{n\}} \ddot{b} = a_{k,n}s_{k,n} + c_{k,n}$ in the point of approximation. For each value

of $\boldsymbol{s}_n$, the objective function of problem (4.23) is thus a lower bound on the objective function of problem (4.18), up to a constant $\sum_{k\in\mathcal{K}} c_{k,n}$. As each iteration of Algorithm 4 updates $\boldsymbol{s}_n$ to be the solution of problem (4.23), it is readily seen that each iteration of MAC-DSB-UEP increases the objective function value of both problem (4.23) and problem (4.18).

Algorithm 4 adds UEP functionality to MAC-DSB without severely affecting its computational complexity, as is demonstrated by the following asymptotic complexity analysis. Both MAC-DSB and MAC-DSB-UEP require $I_{\mathrm{MM}} \in [10,\ldots,50]$ iterations of the outer MM algorithm to achieve acceptable precision. For each iteration of the MM algorithm, N approximating problems are constructed (line 4) and solved (lines 5 to 13). From (4.24), it can be seen that line 4 requires $\boldsymbol{h}_{k,n}^{\varkappa}{\boldsymbol{\Psi}_{k,n}}^{-1}\boldsymbol{h}_{k,n}$ to be calculated for all n. As this calculation is similar to the calculation of $\gamma_{k,n}, \forall n$ in Algorithm 3, it has complexity $\mathcal{O}(KN^3)$ which dominates the complexity of line 4. Problem (4.23) is then solved by applying a bisection search algorithm to the corresponding Lagrange dual problem, which typically requires $I_{\mathrm{BCT}} \in [2,\ldots,20]$ iterations to achieve acceptable precision. In each iteration of the bisection search algorithm, the Lagrange dual function is evaluated by lines 8 and 9. The complexity of both lines is $\mathcal{O}(K|\mathcal{Q}|)$. Therefore, the overall asymptotic complexity of MAC-DSB-UEP is $\mathcal{O}(I_{\mathrm{MM}}NK(N^3 + I_{\mathrm{BCT}}|\mathcal{Q}|))$. As MAC-DSB can be obtained from MAC-DSB-UEP by deleting line 9 and executing line 8 only once for each user, it is seen that the complexity of MAC-DSB is $\mathcal{O}(I_{\mathrm{MM}}NK(N^3 + I_{\mathrm{BCT}}))$. It is concluded that if $N^3 + I_{\mathrm{BCT}}$ is large compared to $I_{\mathrm{BCT}}|\mathcal{Q}|$, Algorithm 4 adds UEP functionality to MAC-DSB without severely affecting its complexity.

4.5 Downstream DSM with unequal error protection

In this section, two algorithms that solve the DS version of the rate-adaptive DSM problem are presented: BC-OSB-UEP achieves the global optimum of problem (4.18) at the cost of an exponential complexity in the number of users N; BC-DSB-UEP exhibits lower complexity, but attains only a local optimum of problem (4.18). In this section, whenever problem (4.18) is referred to, the DS version is considered.

Algorithm 4. MAC-DSB-UEP

repeat
  for all $n \in \mathcal{N}$ **do**
    $\lambda_n^{\min} \leftarrow 0$, $\lambda_n^{\max} \leftarrow \Lambda_{\max}$
    Calculate $a_{k,n}$ and $\boldsymbol{h}_{k,n}^{\mathcal{H}} \boldsymbol{\Psi}_{k,n}^{-1} \boldsymbol{h}_{k,n}$, $\forall k \in \mathcal{K}$.
    while $|\sum_k p_{k,n} - P_n^{\text{tot}}| > \delta_P$ & $\lambda_n > \delta_\lambda$ **do**
      $\lambda_n \leftarrow \left(\lambda_n^{\min} + \lambda_n^{\max}\right)/2$
      for all k **do**
        Calculate $(s_{k,n}, q)$ as (4.31), $\forall q \in \mathcal{Q}_n$.
        Select $(s_{k,n}, q)$ that solves (4.29).
      if $\sum_k p_{k,n} > P_n^{\text{tot}}$ **then**
        $\lambda_n^{\min} \leftarrow \lambda_n$
      else
        $\lambda_n^{\max} \leftarrow \lambda_n$
until convergence
Calculate $\mathbf{R}_k$ using (4.5), $\forall k \in \mathcal{K}$

Dual decomposition again allows problem (4.18) to be solved for each tone independently. The Lagrange dual problem of (4.18) is defined as

$$\min_{\boldsymbol{\lambda}} \quad g(\boldsymbol{\lambda}) \tag{4.32}$$

$$\text{with} \quad g(\boldsymbol{\lambda}) = \max_{\boldsymbol{s} \in \mathbb{R}_+^{N \times K}, \mathbf{T}} \mathcal{L}(\boldsymbol{s}, \mathbf{T}, \boldsymbol{\lambda}) \tag{4.33}$$

and the Lagrangian is defined as

$$\mathcal{L}(\boldsymbol{s}, \mathbf{T}, \boldsymbol{\lambda}) = \sum_{k \in \mathcal{K}} \mathcal{L}_k(\boldsymbol{s}_k, \mathbf{T}_k, \boldsymbol{\lambda}) + \sum_{n \in \mathcal{N}} \lambda_n P_n^{\text{tot}} \tag{4.34}$$

$$\text{with} \quad \mathcal{L}_k(\boldsymbol{s}_k, \mathbf{T}_k, \boldsymbol{\lambda}) = \sum_{n \in \mathcal{N}} \left[\ddot{b}_n(\gamma_{k,n}) - s_{k,n} \boldsymbol{t}_{k,n}{}^{\mathcal{H}} \boldsymbol{\Lambda} \boldsymbol{t}_{k,n} \right]$$

where $\boldsymbol{\Lambda} = \text{diag}\{\boldsymbol{\lambda}\}$. The duality gap between the primal problem (4.18) and the corresponding Lagrange dual problem (4.32) is assumed to be zero by virtue of the same argument as in Section 4.4.1.

The master problem (4.32) is convex, not differentiable, and can again be solved with the subgradient method of Section 4.4.1. What remains is to solve the slave problem (4.33). Finding the optimal transmit matrices $\mathbf{T}_k$ for the BC is not as straightforward as finding the optimal receive matrices $\mathbf{R}_k$ for the MAC [159]. It is however possible to transform the BC slave problem into

an equivalent and simpler dual MAC slave problem using MAC-BC duality theory [87, 111, 153, 206, 219].

4.5.1 MAC-BC duality

The MAC-BC duality theory used in this chapter is based on [87, 111, 219]. In [111, 219], it is shown that the per tone slave problem in (4.33), i.e.

$$\max_{\boldsymbol{s}_k \in \mathbb{R}_+^N, \mathbf{T}_k} \mathcal{L}_k(\boldsymbol{s}_k, \mathbf{T}_k, \boldsymbol{\lambda}), \tag{4.35}$$

is equivalent to the per tone slave problem of a dual MAC system. The per tone Lagrangian of this dual MAC system is defined as

$$\mathcal{L}_k(\boldsymbol{\delta}_k, \mathbf{T}_k, \boldsymbol{\lambda}) =$$

$$\sum_{n \in \mathcal{N}} \ddot{b}_n \left(\frac{\delta_{k,n} |\boldsymbol{t}_{k,n}{}^{\mathcal{H}} \boldsymbol{h}_{k,n}|^2}{\sum_{m \neq n} \delta_{k,m} |\boldsymbol{t}_{k,n}{}^{\mathcal{H}} \boldsymbol{h}_{k,m}|^2 + \boldsymbol{t}_{k,n}{}^{\mathcal{H}} \boldsymbol{\Lambda} \boldsymbol{t}_{k,n}} \right) - \sum_{n \in \mathcal{N}} \delta_{k,n} \sigma_{k,n}, \tag{4.36}$$

where $\delta_{k,n}$ is the symbol power of user n on tone k of the dual MAC system. The dual MAC system to which this Lagrangian function corresponds, is obtained from the original BC system in the following way: the channel matrix of the dual MAC system is the Hermitian transpose of the BC channel matrix, the dual MAC system uses the transmit vectors $\boldsymbol{t}_{k,n}$ from the BC system as its receive vectors, and the noise powers of the BC system $\boldsymbol{\Sigma}_k = \text{diag}\{\boldsymbol{\sigma}_k\}$ constitute the Lagrange multipliers in the dual system and vice versa.

Duality between $\mathcal{L}_k(\boldsymbol{\delta}_k, \mathbf{T}_k, \boldsymbol{\lambda})$ and $\mathcal{L}_k(\boldsymbol{s}_k, \mathbf{T}_k, \boldsymbol{\lambda})$ is established by the following two statements, which hold true for any $\mathbf{T}_k$:

1. For every symbol power vector $\boldsymbol{\delta}_k$, a corresponding feasible symbol power vector $\boldsymbol{s}_k$ exists such that, for each user, the achieved SINR in the BC system is the same as in the dual MAC system, and such that $\mathcal{L}_k(\boldsymbol{\delta}_k, \mathbf{T}_k, \boldsymbol{\lambda}) = \mathcal{L}_k(\boldsymbol{s}_k, \mathbf{T}_k, \boldsymbol{\lambda})$. This symbol power vector $\boldsymbol{s}_k$ can be obtained from $\boldsymbol{\delta}_k$ by solving the system of equations in (4.37).

2. Conversely, for every $\boldsymbol{s}_k$, it is possible to find a corresponding feasible $\boldsymbol{\delta}_k$ such that the achieved SINR is the same for each user in both systems and such that $\mathcal{L}_k(\boldsymbol{s}_k, \mathbf{T}_k, \boldsymbol{\lambda}) = \mathcal{L}_k(\boldsymbol{\delta}_k, \mathbf{T}_k, \boldsymbol{\lambda})$.

$$\mathbf{Z}_k \boldsymbol{s}_k = \boldsymbol{\Sigma}_k \boldsymbol{\delta}_k \tag{4.37}$$

$$[\mathbf{Z}_k]_{n,m} = \begin{cases} \sum_{i \neq m} \delta_{k,i} |\boldsymbol{t}_{k,m}{}^{\mathcal{H}} \boldsymbol{h}_{k,i}|^2 + \boldsymbol{t}_{k,m}{}^{\mathcal{H}} \boldsymbol{\Lambda} \boldsymbol{t}_{k,m} & \text{if } n = m \\ -\delta_{k,n} |\boldsymbol{t}_{k,m}{}^{\mathcal{H}} \boldsymbol{h}_{k,n}|^2 & \text{if } n \neq m \end{cases}$$

Both statements can be shown to be true using the same reasoning as in [87]. From this duality result, it is readily concluded that the solution of

$$\max_{\boldsymbol{\delta}_k \in \mathbb{R}_+^N, \mathbf{T}_k} \mathcal{L}_k(\boldsymbol{\delta}_k, \mathbf{T}_k, \boldsymbol{\lambda}), \tag{4.38}$$

when transformed to the BC domain using (4.37), solves the BC per tone slave problem (4.35).

So far it has been established that solving (4.38) for each tone k leads to a solution to (4.33) through applying the MAC-BC duality transformation from (4.37). As the Lagrangian in (4.38) corresponds to a MAC system (cf. (4.36)), given the symbol power vector $\boldsymbol{\delta}_k$, the optimal $\mathbf{T}_k$ and corresponding SINR for user n are calculated as

$$\mathbf{T}_k = \left(\mathbf{H}_k \boldsymbol{\Delta}_k \mathbf{H}_k^{\mathcal{H}} + \boldsymbol{\Lambda} \right)^{-1} \mathbf{H}_k \boldsymbol{\Delta}_k \tag{4.39}$$

$$\gamma_{k,n} = \delta_{k,n} \boldsymbol{h}_{k,n}^{\mathcal{H}} (\boldsymbol{\Psi}_{k,n})^{-1} \boldsymbol{h}_{k,n} \tag{4.40}$$

with $\boldsymbol{\Delta}_k = \text{diag}\{\boldsymbol{\delta}_k\}$ and $\boldsymbol{\Psi}_{k,n} = \sum_{m \in \mathcal{N} \setminus \{n\}} \delta_{k,m} \boldsymbol{h}_{k,m} \boldsymbol{h}_{k,m}^{\mathcal{H}} + \boldsymbol{\Lambda}$, which is similar to (4.5),(4.6). The SINR can thus again be calculated without explicitly evaluating $\mathbf{T}_k$. Hence, optimization over $\mathbf{T}_k$ can effectively be removed from (4.38), reducing the per tone slave problem to

$$\max_{\boldsymbol{\delta}_k \in \mathbb{R}_+^N} \mathcal{L}_k(\boldsymbol{\delta}_k, \boldsymbol{\lambda}). \tag{4.41}$$

4.5.2 Globally optimal solution: BC-OSB-UEP

To formulate a globally optimal algorithm for problem (4.18), it remains to define a procedure to solve (4.41). As before, an exhaustive search will be employed, for which a search grid is to be defined. This poses a specific problem. Defining boundaries for $s_{k,n}$ in Section 4.4.1 was easy, as $s_{k,n}$ has a physical meaning due to its equivalence to the line power of user n on tone k. This is not the case for the virtual powers $\delta_{k,n}$ in the dual MAC. Therefore, it is not trivial to see what range of values for $\delta_{k,n}$ should be included in its search grid.

On the other hand, the SINR is a variable that does have a physical meaning in both the BC and the dual MAC. Therefore, a straightforward strategy consists

of defining a search grid for $\boldsymbol{\gamma}_k$, and evaluating the Lagrangian (4.36) for each vector $\boldsymbol{\gamma}_k$ on the grid. Evaluating the Lagrangian for each $\boldsymbol{\gamma}_k$ on the grid requires finding the vector $\boldsymbol{\delta}_k$ which is mapped on to the considered vector $\boldsymbol{\gamma}_k$ by equation (4.40), i.e. finding $\boldsymbol{\delta}_k$ which satisfies the following expression.

$$\boldsymbol{\delta}_k \overset{(4.40)}{\longrightarrow} \boldsymbol{\gamma}_k \tag{4.42}$$

This vector $\boldsymbol{\delta}_k$ can be found using the following fixed point iteration

$$\delta_{k,n}(i+1) = \frac{\gamma_{k,n}}{\boldsymbol{h}_{k,n}^{\mathcal{H}} \boldsymbol{\Psi}_{k,n}^{-1}(i) \boldsymbol{h}_{k,n}}, \quad \forall n \in \mathcal{N} \tag{4.43}$$

where $\boldsymbol{\Psi}_{k,n}(i) = \sum_{m \in \mathcal{N} \setminus \{n\}} \delta_{k,m}(i) \boldsymbol{h}_{k,m} \boldsymbol{h}_{k,m}^{\mathcal{H}} + \boldsymbol{\Lambda}$. From [160] it is known that, independent of the starting point $\boldsymbol{\delta}_k(0)$, the fixed point iteration (4.43) is guaranteed to converge to the unique $\boldsymbol{\delta}_k$ that corresponds to the $\boldsymbol{\gamma}_k$. It is noted that if non-linear precoding with a predetermined encoding order is used instead of linear precoding, $\boldsymbol{\delta}_k$ can be calculated analytically from $\boldsymbol{\gamma}_k$.

The resulting algorithm is referred to as BC-OSB with UEP (BC-OSB-UEP) and is summarized in Algorithm 5. As the subgradient algorithm, the exhaustive grid search, and the fixed point iteration of (4.43) can all be proven to converge to the global optimum of the problems they solve, BC-OSB-UEP is guaranteed to converge to the global optimum of problem (4.18).

The complexity analysis of Algorithm 5 is similar to that of Algorithm 3, the only major difference being that the fixed point iteration in line 15 requires $\boldsymbol{h}_{k,n}^{\mathcal{H}} \boldsymbol{\Psi}_{k,n}^{-1} \boldsymbol{h}_{k,n}$ to be evaluated $I_{\mathrm{FP}} \in [1, \ldots, 5]$ times. The resulting complexity of BC-OSB-UEP is $\mathcal{O}(I_{\mathrm{SG}} K \epsilon^{-N} N (I_{\mathrm{FP}} N^2 + \log|\mathcal{Q}|))$. As before, BC-OSB can be obtained from BC-OSB-UEP by deleting line 17, such that the complexity of BC-OSB is $\mathcal{O}(I_{\mathrm{SG}} K \epsilon^{-N} N^3 I_{\mathrm{FP}})$. From this analysis, it is seen that the complexity difference between BC-OSB and BC-OSB-UEP is negligible.

4.5.3 Locally optimal solution: BC-DSB-UEP

Due to its exhaustive grid search with exponential complexity in N, Algorithm 5 is not practical when $N > 5$. Therefore, this subsection derives an alternative to Algorithm 5 achieving a locally optimal solution to problem (4.18), which is based on an approximate evaluation of (4.41). Apart from this change, the resulting algorithm will be identical to Algorithm 5. In each iteration of the algorithm, an approximation of (4.41) is constructed for each user n. Making a similar argument as in Section 4.4.2, it can be shown that the sequence of solutions to these approximate problems produces a monotonically increasing objective function value that can be shown to converge to a local optimum of

Algorithm 5. BC-OSB-UEP

Determine $\mathcal{G}_q$, $\forall q \in \bigcup_{n\in\mathcal{N}} \mathcal{Q}_n$
while distance $>$ tolerance **do** ▷ Master Problem
  $\mu \leftarrow 1$
  $\boldsymbol{\lambda} \leftarrow$ best $\boldsymbol{\lambda}$ so far
  $\Delta\boldsymbol{\lambda} \leftarrow (\boldsymbol{P}_{\boldsymbol{\lambda}} - \boldsymbol{P}_{\mathrm{tot}})$
  while distance $\leq$ previousDistance **do**
    previousDistance $\leftarrow$ distance
    $\mu \leftarrow \mu \times 2$
    $[\boldsymbol{p}, \boldsymbol{s}, \mathbf{T}] \leftarrow$ exhaustiveSearch$(\boldsymbol{\lambda} + \mu\Delta\boldsymbol{\lambda})$
    $\boldsymbol{P}_{\boldsymbol{\lambda}+\mu\Delta\boldsymbol{\lambda}} \leftarrow \sum_{k\in\mathcal{K}} \boldsymbol{p}_k$
    distance $\leftarrow |\boldsymbol{P}_{\mathrm{tot}} - \boldsymbol{P}_{\boldsymbol{\lambda}+\mu\Delta\boldsymbol{\lambda}}|$

function exhaustiveSearch$(\boldsymbol{\lambda})$ ▷ Slave Problem
  for $k \in \mathcal{K}$ **do**
    for $\boldsymbol{\gamma}_k \in$ grid **do**
      Iteratively calculate $\boldsymbol{\delta}_k$ using (4.43)
      for $n \in \mathcal{N}$ **do**
        Look up $\bar{q} \in \mathcal{Q}_n$ for which $\gamma_{k,n} \in \mathcal{G}_{\bar{q}}$
        Evaluate $\omega_{\bar{q}} f_s \rho_{\bar{q}} b(\gamma_{k,n}, \Gamma_{\bar{q}})$
      Calculate $\mathcal{L}_k(\boldsymbol{\lambda}, \boldsymbol{s}_k)$, retain if best so far
    Calculate transmit matrix $\mathbf{T}_k$ using (4.39)
    Calculate BC user powers $\boldsymbol{s}_k$ using (4.37)
    Calculate BC line powers $\boldsymbol{p}_k$ using (4.8)

(4.41). The algorithm derived here is a generalization of the so-called BC-DSB algorithm for rate-adaptive spectrum management [107].

The approximation of (4.41) for user n is constructed as in Section 4.4.2: by fixing the symbol power $\delta_{k,n}$ and tone allocation $q_{k,m}$ for all users $m \neq n$, and by approximating the information bit rate $b(\gamma_{k,m}, \rho_{q_{k,m}}, \Gamma_{q_{k,m}})$ of users $m \neq n$ with a hyperplane. The resulting problem is not convex, yet easy to solve:

$$\begin{aligned} &\max_{\delta_{k,n}\geq 0} \quad \ddot{b}_n(\gamma_{k,n}) + \delta_{k,n}\,(a_{k,n} - \sigma_{k,n}) \\ &\text{with} \quad a_{k,n} = \sum_{m\in\mathcal{N}\setminus\{n\}} \omega_{q_{k,m}} f_{\mathrm{s}} \frac{\partial b(\gamma_{k,m}, \rho_{q_{k,m}}, \Gamma_{q_{k,m}})}{\partial \delta_{k,n}}, \quad \forall m,\, k \end{aligned} \tag{4.44}$$

where the calculation of the partial derivatives is analogous to (4.24). Problem (4.44) is akin to problem (4.23) in Section 4.4.2, and is again solved by calculating the optimal symbol power $\delta_{k,n}^{\mathrm{opt}}$ for every possible subconnection $q \in \mathcal{Q}_n$, and

Algorithm 6. Approximate evaluation of (4.41) for BC-DSB-UEP

1: **while** $\boldsymbol{\delta}_k$ not converged **do**
2: **for** $n \in \mathcal{N}$ **do**
3: Calculate a_k^n
4: Calculate (δ_k^n, q) using (4.45), $\forall q \in \mathcal{Q}^n$
5: Select (δ_k^n, q) that maximizes objective of (4.44)

subsequently selecting the $(\delta_{k,n}^{\mathrm{opt}}, q)$ tuple that results in the largest value for the objective function. For fixed q, the solution to (4.44) can be calculated in closed form as

$$\delta_{k,n}^{\mathrm{opt}}(q) = \left[\frac{\omega_q \rho_q / \log(2)}{\sigma_{k,n} - a_{k,n}} - \frac{\Gamma_q}{\boldsymbol{h}_{k,n}^{\mathrm{H}} \boldsymbol{\Psi}_{k,n}^{-1} \boldsymbol{h}_{k,n}} \right]^+ . \tag{4.45}$$

The resulting algorithm, referred to as BC-DSB-UEP, is identical to Algorithm 5 apart from lines 14 to 19 which are replaced by Algorithm 6. UEP functionality is added to BC-DSB by replacing the single closed form calculation of the symbol power allocation in each of the I_{MM} iterations of its inner MM algorithm with $|\mathcal{Q}_n|$ calculations of the symbol power allocation and a subconnection selection procedure. These calculations exhibit $\mathcal{O}(|\mathcal{Q}|)$ complexity. The complexity of both the BC-DSB and the BC-DSB-UEP algorithm is however dominated by the calculation of $a_{k,n}$ (line 4) which, as was determined in Section 4.4.2, has complexity $\mathcal{O}(N^3)$. The complexity of BC-DSB is therefore $\mathcal{O}(I_{\mathrm{SG}} K I_{\mathrm{MM}} N^4)$, and that of BC-DSB-UEP is $\mathcal{O}(I_{\mathrm{SG}} K I_{\mathrm{MM}} N(N^3 + |\mathcal{Q}|))$. Algorithm 6 thus adds UEP functionality to BC-DSB without severely affecting its complexity.

In [220], it is pointed out that the subgradient method, which is used to update the Lagrange multipliers, is not guaranteed to converge when $g(\boldsymbol{\lambda})$ is evaluated only approximately. As the employed minorize-maximization method of Algorithm 6 cannot be guaranteed to return the global maximizer of problem (4.41), BC-DSB-UEP is not guaranteed to converge. However, in simulations, BC-DSB-UEP has been observed to converge in every scenario for which it has been evaluated.

4.6 Joint resource allocation and Reed-Solomon code rate optimization

In Section 4.2, it was mentioned that different modulation and coding (MC) schemes i, each characterized by a set of values (ρ_i, Γ_i), can achieve the same

target $\mathbb{P}_q$. This set of MC schemes is referred to as the MC set of subconnection q, and is denoted as $\mathcal{M}_q$. As employing a large number of MC schemes in parallel adversely affects delay performance, only a single MC scheme $i \in \mathcal{M}_q$ should be used per subconnection q.

Different MC schemes result in different performance. Consider two schemes $i_1, i_2 \in \mathcal{M}_q$ with the same value for ν_i and achieving the same $\mathbb{P}_q$, but for which $\Gamma_{i_1} < \Gamma_{i_2}$ and $\kappa_{i_1} < \kappa_{i_2}$. As $\rho_{i_1} < \rho_{i_2}$, MC scheme i_1 incurs a larger multiplicative bit rate overhead than i_2. However, i_2 employs a larger SNR gap, resulting in an approximately additive overhead as compared to i_1. Therefore, it is more appealing to use i_2 when $\gamma_{k,n}$ is high on all tones $k \in \mathcal{K}_q$ and vice versa. It is seen that the optimal choice for $i \in \mathcal{M}_q$ depends on the value for the achieved SINR on all tones $k \in \mathcal{K}_q$. The MC scheme selection should therefore be optimized conjointly with $\boldsymbol{s}$, $\mathbf{T}$, and $\mathcal{T}$.

In general, jointly selecting an optimal resource allocation and MC scheme is referred to as adaptive modulation and coding (AMC). In the context of DSL networks incorporating UEP, AMC can be formulated as the following optimization problem:

$$\begin{aligned} \max_{\substack{\boldsymbol{s},\mathcal{T},\boldsymbol{i}\in\mathcal{M} \\ \text{or} \\ \boldsymbol{s},\mathbf{T},\mathcal{T},\boldsymbol{i}\in\mathcal{M}}} \quad & \sum_{n\in\mathcal{N}} \sum_{q\in\mathcal{Q}_n} \omega_q R_q \\ \text{s.t.} \quad & P_n \leq P_n^{\text{tot}}, \forall n \in \mathcal{N} \\ & \boldsymbol{s} \in \mathbb{R}_+^{N\times K} \end{aligned} \tag{4.46}$$

with $\mathcal{M} = \prod_{n\in\mathcal{N}} \prod_{q\in\mathcal{Q}_n} \mathcal{M}_q$, and where $\boldsymbol{i}$ is a vector containing an element i_q for each $q \in \bigcup_{n\in\mathcal{N}} \mathcal{Q}_n$ signifying the MC scheme employed by subconnection q. The optimal choice for i_q depends on the achieved SINR on all tones $k \in \mathcal{K}_q$. Consequently, problem (4.46) is coupled over all tones by both the total power constraints and the MC scheme selection problem. This coupling makes problem (4.46) hard to solve directly.

The proposed strategy is to formulate a relaxation of problem (4.46), the solution of which is then used to select an MC scheme for each subconnection. In addition, the solution to the relaxed problem yields an upper bound on throughput performance. After having selected an MC scheme for each subconnection, problem (4.46) reduces to problem (4.16), which is solved to obtain the final resource allocation.

Consider the relaxation of problem (4.46) obtained by abandoning the constraint that a single MC scheme is used for each subconnection. Instead, let each MC scheme $i \in \mathcal{M}_q$ for each subconnection q itself constitute a distinct subconnection with which a set of tones $\mathcal{K}_i$ is associated. In addition, define

$\hat{\mathcal{T}} = \{\mathcal{K}_i \mid i \in \bigcup_{n\in\mathcal{N}} \bigcup_{q\in\mathcal{Q}_n} \mathcal{M}_q\}$. The obtained relaxed problem will be referred to as the multiple MC relaxation (MMCR) of problem (4.46), and is formulated as

$$\begin{aligned} \max_{\substack{\boldsymbol{s},\hat{\mathcal{T}} \\ \text{or} \\ \boldsymbol{s},\mathbf{T},\hat{\mathcal{T}}}} \quad & \sum_{n\in\mathcal{N}} \sum_{q\in\mathcal{Q}_n} \omega_q \sum_{i\in\mathcal{M}_q} R_i \\ \text{s.t.} \quad & P_n \leq P_n^{\text{tot}}, \forall n \in \mathcal{N} \\ & \boldsymbol{s} \in \mathbb{R}_+^{N\times K}, \end{aligned} \tag{4.47}$$

where, as before, R_i denotes the data rate achieved by subconnection i of user n. Moreover, a system which simultaneously employs multiple MC schemes to achieve a single target $\mathbb{P}_q$ is referred to as a multiple MC (MMC) system, as opposed to a one MC (OMC) system employing only a single MC scheme for each target $\mathbb{P}_q$. From an optimization point of view, problem (4.47) is fully equivalent to problem (4.16). Consequently, the algorithms developed in Sections 4.4 and 4.5 can be applied to obtain a solution $(\boldsymbol{s},\hat{\mathcal{T}})^{\text{MMCR}}$ or $(\boldsymbol{s},\mathbf{T},\hat{\mathcal{T}})^{\text{MMCR}}$.

This solution is then used to heuristically decide which MC scheme is to be employed for each subconnection $q \in \bigcup_{n\in\mathcal{N}} \mathcal{Q}_n$ as follows. The MC scheme for subconnection q is selected as $i \in \mathcal{M}_q$ maximizing the data rate of subconnection q, i.e.

$$i_q = \arg\max_{i\in\mathcal{M}_q} R_q, \tag{4.48}$$

where it is assumed that q employs tones $\mathcal{K}_q = \bigcup_{i\in\mathcal{M}_q} \mathcal{T}_i^{\text{MMCR}}$, and where the resource allocation $\boldsymbol{s}^{\text{MMCR}}$ or $(\boldsymbol{s},\mathbf{T})^{\text{MMCR}}$ is used in calculating R_q. The resulting algorithm is referred to as the MMCR-based rate selection (MMCR-RS) algorithm. After having selected an MC scheme for each subconnection, problem (4.46) reduces to problem (4.16), which is solved to obtain the final resource allocation.

The MMC system provides an upper bound on the performance of the corresponding OMC system. More specifically, consider the aggregate data rate of all subconnections achieving $\mathbb{P}_q$ in an MMC system, calculated as $R_q^{\text{MMCR}} = \sum_{i\in\mathcal{M}_q} R_i$. For each feasible point of problem (4.46) with corresponding data rates $\check{R}_q$, there exists a feasible point of problem (4.47) with corresponding aggregate data rates $\tilde{R}_q^{\text{MMCR}}$, for which $\check{R}_q \leq \tilde{R}_q^{\text{MMCR}}$, $\forall q \in \mathcal{Q}_n$, $\forall n \in \mathcal{N}$. Therefore, the set of achievable rates in the MMC system is a superset of the set of achievable rates in the corresponding OMC system. In the simulations, this upper bound property is used to assess the performance of the MMCR-RS algorithm.

4.7 Simulation results

In this section, simulation results are shown for the algorithms presented in Sections 4.4, 4.5 and 4.6. Differences in performance between the OSB and DSB algorithms are assessed in Section 4.7.1. The performance of the MMCR-RS algorithm is assessed in Section 4.7.2.

Parameter settings for all experiments are as follows. It is assumed that the twisted pair line diameter is 0.5 mm, which corresponds to 24AWG. For G.fast, the tone spacing is $\Delta_f = 51.750\,\text{kHz}$, the symbol rate is $f_\text{s} = 48\,\text{kHz}$, the maximum line power is $P_n^\text{tot} = 4\,\text{dBm}$, and the number of tones is $K = 2047$ [96]. The values for the coding gain and noise margin are respectively set to $\Gamma_c = 3\,\text{dB}$, resulting from a 2D TCM [139], and $\Gamma_n = 6\,\text{dB}$.

4.7.1 Performance comparison OSB and DSB algorithms

The differences between the OSB and DSB algorithms are analyzed in a network containing 2 users. The twisted pair line lengths are chosen to be 200m and 110m for user 1 and user 2, respectively. Each user supports two subconnections q_1 and q_2, achieving error rates $\text{BER}_{q_1} = 10^{-7}$ and $\text{BER}_{q_2} = 10^{-3}$. RS coding is applied to neither of the subconnections. The error rates, combined Γ_n and Γ_c, result in SNR gaps $\Gamma_{q_1} = 12.6\,\text{dB}$ and $\Gamma_{q_2} = 8.2\,\text{dB}$. For each user n, the weights are chosen as $\omega_{q_1} = 1$ and $\omega_{q_2} = 0.8$.

The information bit rate and power loading resulting from MAC-OSB-UEP and MAC-DSB-UEP, as well as from BC-OSB-UEP and BC-DSB-UEP, are shown in Figure 4.1. The data rate achieved for each individual subconnection is given in Table 4.1. Both Table 4.1 and Figure 4.1 demonstrate that the solutions found by the DSB algorithms are very similar to the solutions found by the OSB algorithms. In the US channel, MAC-OSB-UEP performs even slightly worse than MAC-DSB-UEP. This is explained by the discrete grid search of MAC-OSB-UEP, which, due to its finite granularity, can result in a slightly suboptimal solution when compared to MAC-DSB-UEP.

In the power loading curves of Figure 4.1 it is seen that, even though user 1 is not using any tones above $k = 1202$, its line power $p_{k,1}$ is nonzero. It is noted that, due to the precoding operation using transmit matrix $\mathbf{T}_k$, each line power $p_{k,n}$ depends on the symbol powers $s_{k,m}$ of all users m. The nonzero line power of user 1 thus results from user 1 encoding its symbols with a transmit vector $\boldsymbol{t}_{k,2}$ containing two nonzero entries. Due to increased crosstalk at high frequencies, linear precoding increases line powers, making it highly

Table 4.1: Data rates for two user US and DS systems, in Mbit/s.

	MAC-OSB-UEP		MAC-DSB-UEP	
	user 1	user 2	user 1	user 2
q_1	363.1	706.8	361.2	702.1
q_2	130.8	155.7	134.1	161.3
WSR	1299.1		1299.6	
	BC-OSB-UEP		BC-DSB-UEP	
	user 1	user 2	user 1	user 2
q_1	260.8	490.1	259.4	486.3
q_2	112.2	231.0	109.3	224.4
WSR	1025.5		1012.7	

suboptimal. As stated in [107], this suboptimality can be alleviated using non-linear precoding techniques.

Some discontinuities can be observed in the curves in Figure 4.1, originating from a change in tone allocation. For example, the bit rate curve of user 2 in the DS system is discontinuous at tone $k = 13$, where the tone allocation changes from q_2 to q_1, and at tone $k = 1022$, where the tone allocation changes back to q_2. Differences between tones belonging to q_1 and q_2 show how UEP improves performance. Obviously, lower error protection results in an increased information bit rate. Furthermore, less power is consumed on tones with lower error protection reducing crosstalk and, in addition, providing the opportunity to use the retained power elsewhere.

4.7.2 MMCR-RS performance analysis

The performance of the MMCR-RS algorithm is analyzed for a larger DSL network. The network under consideration connects 10 users to a distribution point. The distance between users and distribution point ranges from 200m for user 1 down to 110m for user 10, decreasing with 10m for each consecutive user. DSB algorithms are employed to calculate the resource allocation.

Target byte error rates $\mathbb{P}_q$ are chosen to be representative for VoIP and HDTV applications. For VoIP, it is assumed that the G.711 audio codec is used with payload size of 240 codec bytes per IP packet, resulting in an overall average IP packet size of 381 bytes [1]. Combined with an acceptable packet loss rate of 1% [90], the allowable physical layer byte error rate is $2.62 \cdot 10^{-5}$, which is

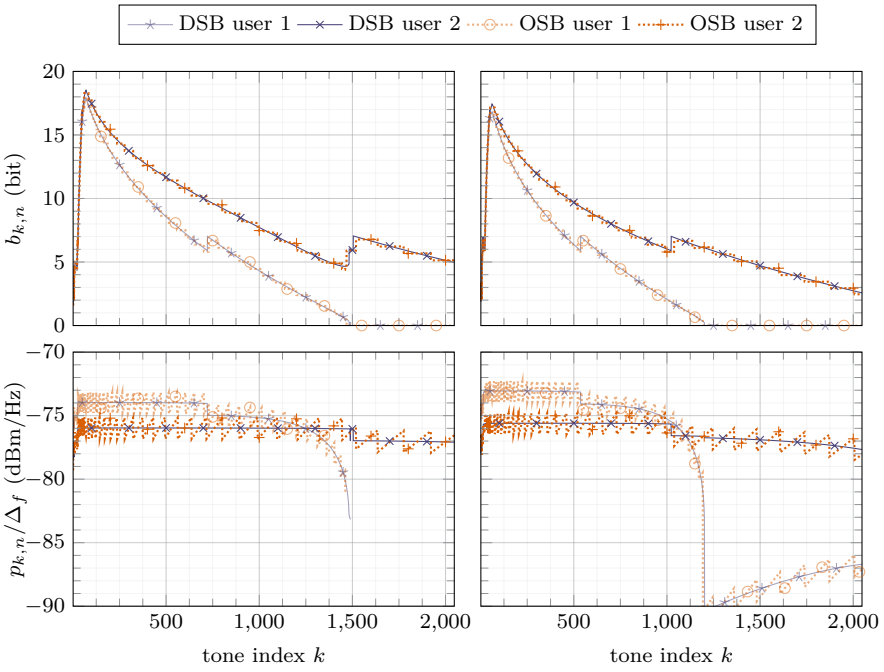


Figure 4.1: Information bit rate and transmit spectrum for two user US (left) and DS (right) G.fast systems. In the legend, OSB and DSB have been used as an abbreviation of MAC-OSB-UEP and BC-OSB-UEP, and of MAC-DSB-UEP and BC-DSB-UEP, respectively.

rounded down to $\mathbb{P}_{\text{VoIP}} = 10^{-5}$ in simulations. Likewise, the IP average packet size for MPEG-2 based HDTV is 1316 byte, and the acceptable packet loss rate is 10^{-6} [3]. This results in the requirement that $\mathbb{P}_{\text{HDTV}} \leq 7.6 \cdot 10^{-10}$, simplified to $\mathbb{P}_{\text{HDTV}} = 10^{-10}$ in simulations. The above calculations assume that each uncorrected error results in an IP packet loss.

Fixed RS codeword lengths of either $\nu = 64$ or $\nu = 255$ are employed [96]. The MC sets $\mathcal{M}_q$ of all subconnections contain an element i for each allowable number of parity symbols per RS codeword, specified in [96] as $\nu - \kappa_i = 0, 2, \ldots, 16$, such that $|\mathcal{M}_q| = 9$, $\forall q \in \mathcal{Q}_n, \forall n \in \mathcal{N}$. The value of each Γ_i can then be calculated from ν, κ_i and $\mathbb{P}_q$, as explained in Section 4.2.4.

Results for the MMCR-RS algorithm are visualized by drawing the rate region of different DSL networks, containing all achievable combinations $(\bar{R}_{\text{VoIP}}, \bar{R}_{\text{HDTV}})$ of the average data rates $\bar{R}_q = \frac{1}{N} \sum_{n \in \mathcal{N}} R_q$, which assumes that $q \in \mathcal{Q}_n$, $\forall n \in \mathcal{N}$.

Edge points of this rate region can be calculated by maximizing $\omega_{\text{VoIP}}\bar{R}_{\text{VoIP}} + \omega_{\text{HDTV}}\bar{R}_{\text{HDTV}}$ for different values for the weights ω_q [32]. Values for ω_{VoIP} range from 0.4 to 0.5, and ω_{HDTV} is set to $1 - \omega_{\text{VoIP}}$.

Figure 4.2 displays the edges of three rate regions for a set of four different DSL networks. The rate regions labeled 'UEP OMC' correspond to OMC systems employing the MMCR-RS algorithm to select an MC scheme for each subconnection, and subsequently using either MAC-DSB-UEP or BC-DSB-UEP to solve (4.16). The rate regions labeled 'UEP MMC' correspond to MMC systems employing either MAC-DSB-UEP or BC-DSB-UEP to solve (4.47), and for which R_q is calculated as the aggregate data rate of all subconnections achieving $\mathbb{P}_q$. As the UEP MMC rate region is a superset of the UEP OMC rate region, the UEP MMC rate region is an upper bound for the UEP OMC rate region. The rate regions of the OMC systems employing MMCR-RS mostly coincide with their respective MMC upper bounds, indicating that the MMCR-RS algorithm performs very well. Moreover, this result demonstrates that using a single MC scheme per subconnection has little impact on the performance of the DSL network.

The rate regions labeled 'EEP OMC' correspond to equal error protection (EEP) DSL networks achieving $\mathbb{P}_{\text{HDTV}}$ for both applications. The achievable data rates of the UEP DSL networks are clearly higher than those of the EEP DSL networks, indicating the benefit of employing UEP in DSL. It is noted that for $\nu = 255$, the gain of UEP over EEP is rather small. However, the considered EEP systems do employ MMCR-RS to decide which MC scheme to employ for each user. In other words, the developed UEP algorithms helped attaining the optimal EEP DSL performance. Therefore, even though the UEP *architecture* may lack advantages in some scenarios, the proposed UEP *algorithms* do not.

4.8 Conclusion

Four new DSM algorithms have been presented for joint signal and spectrum coordination in DSL networks providing UEP. Two OSB algorithms are provided: one for upstream and one for downstream DSL networks, both exhibiting exponential complexity in the number of users. In addition, two DSB algorithms are provided that only converge to a local optimum. However, simulations have shown that the solutions found by the DSB algorithms largely coincide with solutions found by the corresponding OSB algorithms, at only a fraction of the computation time. In addition, the MMCR-RS algorithm for MC scheme selection has been developed. Simulations have shown that MMCR-RS algorithm performs very well, and that using a single MC scheme per subconnection does

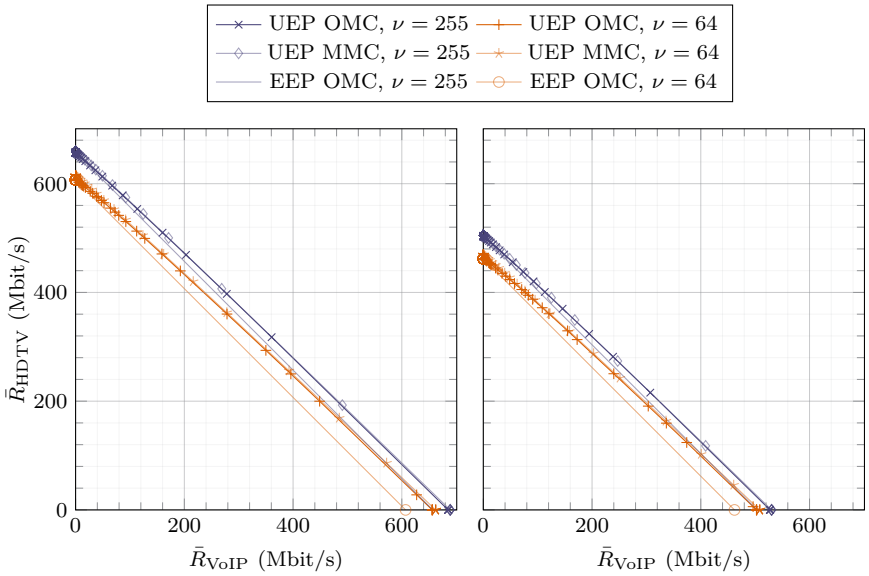


Figure 4.2: Achievable rate region of 10 user US (left) and DS (right) G.fast systems using RS codewords either of length $\nu = 64$, or of length $\nu = 255$. For each scenario, three rate region are drawn: one for an OMC UEP system, one for the corresponding MMC UEP system, and one for an OMC EEP system servicing a single subconnection achieving $\mathbb{P}_{\text{HDTV}}$.

not have a large impact on the performance of the DSL network. Results have also shown the benefit of UEP, as compared to EEP, as it is able to achieve moderate performance gains.

Chapter 5

Full-Duplex DSM

Optimal Dynamic Spectrum Management Algorithms for Multi-User Full-Duplex DSL

Jeroen Verdyck, Wouter Lanneer, Paschalis Tsiaflakis, Werner Coomans, Panagiotis Patrinos, and Marc Moonen

Published in *IEEE Access*, Vol. 7, pp. 106600 - 106616, July 2019, DOI: 10.1109/ACCESS.2019.2926616.

© 2019 IEEE. Reprinted, with permission, from:
Jeroen Verdyck, Wouter Lanneer, Paschalis Tsiaflakis, Werner Coomans, Panagiotis Patrinos, and Marc Moonen, "Optimal Dynamic Spectrum Management Algorithms for Multi-User Full-Duplex DSL," *IEEE Access*, Vol. 7, pp. 106600 - 106616, July 2019.
Changes include layout, representation, and minor editing aspects.

The candidate's contributions as first author include: co-literature study, co-development of MAC-BC duality framework, development and simulations of OSB, co-development and simulations of dual domain DSB, co-development and simulations of primal domain DSB, co-formulation of the conclusions, writing of the article.

Abstract

Driven by the exceedingly high data rates achieved in single user implementations, interest in multi-user (MU) full-duplex (FDX) transmission for digital subscriber line (DSL) networks is surging. However, near-end crosstalk (NEXT) is no longer avoided in such networks, hence appropriate dynamic spectrum management (DSM) techniques are needed. This chapter therefore proposes three novel DSM algorithms for the MU FDX DSL network. First, an optimal spectrum balancing (OSB) algorithm is derived which calculates the globally optimal resource allocation, but does so at an exceedingly high computational cost. Key in this algorithm is the use of a novel MAC-BC duality for the specific case of perfect NEXT cancellation at the distribution point unit. Two low-complexity distributed spectrum balancing (DSB) algorithms are then proposed, for which simulations show that their performance is very close to what is achieved by the OSB algorithm. Therefore, these DSB algorithms can be used to estimate the achievable performance of an MU FDX DSL network. Such performance estimations show that FDX transmission can indeed lead to significant gains in MU DSL networks as well.

5.1 Introduction

With the potential of doubling the spectral efficiency, full-duplex (FDX) transmission for digital subscriber line (DSL) networks is receiving increased attention. In early stages of lab testing, single-user FDX has exceeded expectations. In XG-FAST trials at Nokia Bell Labs in Antwerp, for instance, aggregate data rates of 8.8 Gbit/s have been achieved on a single 30 m copper line [49]. When combined with multi-line bonding, FDX promises aggregate data rates even exceeding 20 Gbit/s. Consequently, FDX transmission will be part of G.mgfast, the upcoming ITU-T recommendation for DSL.

This chapter studies FDX transmission in *multi-user* (MU) DSL networks, with a topology as illustrated in Figure 5.1. The core network of the Internet service provider (ISP) is connected to the distribution point unit (DPU) through an optical fiber cable. In turn, the DPU is connected to N network terminations (NTs), one for each user, where each connection is established by means of a single twisted pair cable. At the DPU side, these twisted pair cables are bundled together in a cable binder. The dense packing of twisted pair cables in the cable binder results in an electromagnetic coupling, giving rise to interference or crosstalk. If not addressed appropriately, crosstalk can severely deteriorate the DSL network's performance.

A distinction is often made between near-end crosstalk (NEXT), i.e. interference generated by DPU (respectively NT) transmitters into neighboring DPU (NT) receivers, and far-end crosstalk (FEXT), i.e. interference generated by DPU (respectively NT) transmitters into NT (DPU) receivers at the other side of the DSL network. In previous DSL technologies, the effects of NEXT and FEXT have been managed in a dissimilar fashion.

FEXT is typically dealt with by dynamic spectrum management (DSM) techniques. These techniques are often classified into two categories: spectrum coordination and signal coordination. Spectrum coordination involves jointly managing the transmit powers of different users, and signal coordination or vectoring comprises coordinating multiple users on a signal level [42]. Signal coordination techniques require the modems of different users to be co-located, thus introducing a difference between vectoring for upstream (US) transmission, i.e. NT to DPU, and for downstream (DS) transmission, i.e. DPU to NT.

In previous DSL technologies, the influence of NEXT has mostly[1] been avoided by dividing resources between US and DS transmission using FDD [91–94] or TDD [96]. This chapter however considers FDX transmission, in which US and DS transmissions occur at the same time and in the same frequency band. In this FDX setting, NEXT is no longer avoided and should be dealt with using DSM techniques. At the DPU, interfering DS transmitters and victim US receivers are co-located. Therefore, the effects of NEXT can be reduced with signal coordination techniques such as NEXT cancellation. For the DSL setting, the DPU-side NEXT is typically not much stronger than the received signal, such that it is reasonable to assume perfect NEXT cancellation at the DPU, such that US receivers indeed experience no NEXT. At the NTs however, interfering US transmitters and victim DS receivers are *not* co-located, such that only spectrum coordination techniques are available to mitigate the NEXT impact. Remarkably, the assumption of perfect DPU-side NEXT cancellation admits a more favorable problem structure which is hence exploited in this chapter to derive an optimal DSM algorithm for MU FDX networks.

The considered MU FDX DSL networks thus use joint vectoring and spectrum coordination to deal with FEXT, spectrum coordination to deal with NT-side NEXT, and echo cancellation to deal with DPU-side NEXT. The DSM algorithms developed in this chapter determine optimal US and DS transmit powers for all users, as well as optimal receive filter and precoding vectors. Similar DSM algorithms have been considered in [62, 177]. In [62], DSM algorithms have been derived for FDX DSL networks with imperfect DPU-side NEXT cancellation, yielding a problem statement that is more general then

[1] ADSL and ADSL2 did support FDX transmission, but referred to it as 'echo canceling mode' [91, 92].

what is considered in this chapter. The derived algorithms are however not able to find the globally optimal DSM strategy. In [177] perfect DPU-side NEXT cancellation has been considered, but the derived zero-forcing precoders and receive filters are suboptimal. Moreover, in [191] a practical frame structure is proposed for MU FDX DSL networks, by means of alternating between two FDX operating points which can be provided by any DSM algorithm.

DSM algorithms for MU FDX networks have hitherto mostly been studied in the context of wireless systems. Relevant approaches include the WMMSE-based methods from [48, 114, 135], the successive convex approximation (SCA)-based methods from [82, 83, 143], and methods relying on a simplifying precoding/receive filter design [141, 142, 215]. In wireless systems however, the self-interference[2] (SI) power is orders of magnitude stronger than the received signal power, such that it cannot be assumed that all SI is canceled. The emphasis in [48, 82, 83, 114, 141–143, 215] is therefore strongly on residual SI modeling and mitigation.

Main contributions This chapter introduces three novel DSM algorithms for MU FDX DSL networks. A first algorithm extends previously developed optimal spectrum balancing (OSB) algorithms for US and DS transmission [32, 111, 195] to an OSB algorithm for FDX transmission. Key is that the developed MAC-BC duality theory[3] yields a novel full-duplex optimal spectrum balancing (FDX-OSB) algorithm, which is able to compute the globally optimal resource allocation. This optimality result is in contrast with the OSB-type algorithm developed in [62], which does not exploit perfect DPU-side NEXT cancellation and, as such, cannot guarantee global optimality.

The resulting FDX-OSB algorithm however exhibits an exponential complexity in the number of users, such that it becomes impractical for larger DSL networks. To overcome this problem, algorithms with a polynomial complexity in the number of users are presented. Both algorithms are based on previously developed distributed spectrum balancing (DSB) algorithms [188, 193]. The first algorithm, referred to as full-duplex dual domain distributed spectrum balancing (FDX-DD-DSB), is obtained by replacing the most demanding operation of FDX-OSB by an inexact low-complexity procedure. As FDX-DD-DSB is very similar to FDX-OSB, the performance of the two algorithms is anticipated to be comparable as well. The second algorithm, referred to as full-duplex primal domain distributed spectrum balancing (FDX-PD-DSB), is an SCA-based method that is not founded on the newly developed MAC-BC duality theory. As such, FDX-PD-DSB does not require perfect DPU-side NEXT cancellation, and

[2] In wireless networks, DPU-side NEXT is referred to as self-interference.

[3] MAC and BC respectively abbreviate *multiple access channel* and *broadcast channel*.

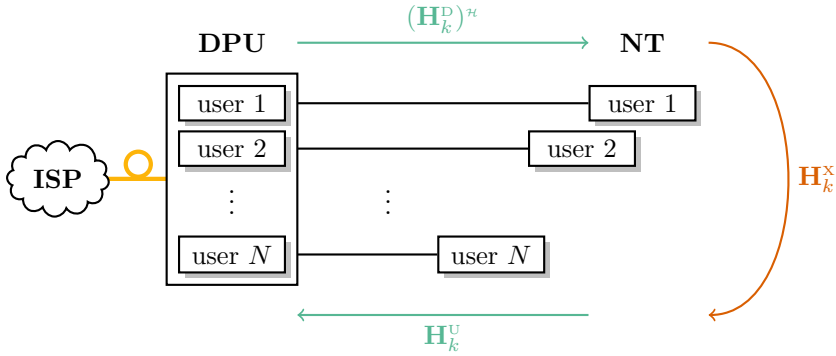


Figure 5.1: DSL network topology. The ISP core network is connected to the DPU through an optical fiber cable. In turn, the DPU is connected to N NTs, where each connection is established by means of a single twisted pair cable.

can be applied to the resource allocation problems from [48, 82, 83, 114, 143] as well. FDX-PD-DSB yields sub-problems that can be solved efficiently without relying on a solver as in [82, 83, 143]. Moreover, simulations demonstrate that FDX-PD-DSB exhibits better convergence characteristics than the WMMSE algorithms as in [48, 114]. In simulations, it is demonstrated that the low-complexity FDX-DSB algorithms achieve a similar performance as FDX-OSB at only a fraction of its computational cost. Finally, simulations demonstrate that FDX as such can indeed lead to significant performance gains in MU DSL networks.

5.2 System model

DSL employs discrete multi-tone modulation (DMT) to split the available spectrum into a set of K orthogonal sub-carriers, often referred to as tones in DSL literature. It is assumed that no inter-carrier interference (ICI) is present, such that transmission can be modeled on each tone independently. Per tone channel models are presented for US and DS transmission in Sections 5.2.1 and 5.2.2. Performance metrics for the DSL network are presented in Section 5.2.3.

5.2.1 Upstream channel

US transmission in an N-user FDX DSL network with no ICI and with perfect DPU-side NEXT cancellation can be modeled on each tone as a multiple access

channel (MAC), i.e.

$$\boldsymbol{y}_k^{\mathrm{U}} = \mathbf{H}_k^{\mathrm{U}} \boldsymbol{x}_k^{\mathrm{U}} + \boldsymbol{z}_k^{\mathrm{U}} \quad \forall k. \tag{5.1}$$

In the channel equation, the superscript 'U' indicates that a US variable is considered. Furthermore, the vector $\boldsymbol{x}_k^{\mathrm{U}} = \left[x_{k,1}^{\mathrm{U}}, \ldots, x_{k,N}^{\mathrm{U}}\right]^{\mathrm{T}}$ contains the transmitted signals of all the users on tone k. Vectors $\boldsymbol{z}_k^{\mathrm{U}}$ and $\boldsymbol{y}_k^{\mathrm{U}}$ denote the additive Gaussian noise and received signal, and have the same size as $\boldsymbol{x}_k^{\mathrm{U}}$. Moreover, $\mathbf{H}_k^{\mathrm{U}}$ denotes the $N \times N$ US channel matrix, with $\left[\mathbf{H}_k^{\mathrm{U}}\right]_{nm} = (h_k^{nm})^{\mathrm{U}}$ the transfer function between transmitter m and receiver n evaluated at tone k.

The average symbol power of user n on tone k is defined as $s_{k,n}^{\mathrm{U}} = \Delta_f \, \mathbb{E}\left\{|x_{k,n}^{\mathrm{U}}|^2\right\}$, with Δ_f the tone spacing. For each user n, the total US transmit power is then given by

$$P_n^{\mathrm{U}} = \sum_k s_{k,n}^{\mathrm{U}}. \tag{5.2}$$

In the above equation, $\sum_k$ is a shorthand notation for the summation over all elements $k \in \{1, \ldots, K\}$. Similarly, $\sum_n$ and $\prod_n$ respectively denote the summation and (Cartesian) product over all elements $n \in \mathcal{N} = \{1, \ldots, N\}$, and $\sum_{m \neq n}$ denotes the summation over all elements $m \in \mathcal{N} \setminus \{n\}$. Furthermore, $\mathbf{\Sigma}_k^{\mathrm{U}} = \Delta_f \, \mathbb{E}\left\{\boldsymbol{z}_k^{\mathrm{U}} (\boldsymbol{z}_k^{\mathrm{U}})^{\mathrm{H}}\right\}$ denotes the US additive noise covariance matrix.

In US transmission, signal coordination is possible at the DPU. The non-linear general decision feedback equalizer (GDFE) receiver structure is assumed, i.e. transmitted symbols are iteratively estimated from the received signal as

$$\hat{x}_{k,n}^{\mathrm{U}} = (\boldsymbol{r}_{k,n}^{\mathrm{U}})^{\mathrm{H}} \Big(\boldsymbol{y}_k^{\mathrm{U}} - \sum_{m<n} \boldsymbol{h}_{k,m}^{\mathrm{U}} \dot{x}_{k,m}^{\mathrm{U}} \Big), \tag{5.3a}$$

$$\dot{x}_{k,n}^{\mathrm{U}} = \mathrm{decide}(\hat{x}_{k,n}^{\mathrm{U}}). \tag{5.3b}$$

In the above equation, it is assumed that the decoding order is determined beforehand and w.l.o.g. given by the user index order. Moreover, $\mathbf{R}_k^{\mathrm{U}}$ is the tone k receive filter matrix with $\boldsymbol{r}_{k,n}^{\mathrm{U}}$ its n-th column. Likewise, $\boldsymbol{h}_{k,n}^{\mathrm{U}}$ denotes the n-th column of $\mathbf{H}_k^{\mathrm{U}}$. The resulting signal-to-interference-plus-noise ratio (SINR) for user n on tone k is given by

$$\gamma_{k,n}^{\mathrm{U}}(\boldsymbol{s}_k^{\mathrm{U}}, \boldsymbol{r}_{k,n}^{\mathrm{U}}, \mathbf{\Sigma}_k^{\mathrm{U}}) = \frac{s_{k,n}^{\mathrm{U}} |(\boldsymbol{r}_{k,n}^{\mathrm{U}})^{\mathrm{H}} \boldsymbol{h}_{k,n}^{\mathrm{U}}|^2}{\sum_{m>n} s_{k,m}^{\mathrm{U}} |(\boldsymbol{r}_{k,n}^{\mathrm{U}})^{\mathrm{H}} \boldsymbol{h}_{k,m}^{\mathrm{U}}|^2 + (\boldsymbol{r}_{k,n}^{\mathrm{U}})^{\mathrm{H}} \mathbf{\Sigma}_k^{\mathrm{U}} \boldsymbol{r}_{k,n}^{\mathrm{U}}} \tag{5.4}$$

with $\boldsymbol{s}_k^{\mathrm{U}} = [\boldsymbol{s}_{k,1}^{\mathrm{U}}, \ldots, \boldsymbol{s}_{k,N}^{\mathrm{U}}]^{\mathrm{T}}$. In this chapter, dependencies will always be explicitly mentioned for the SINR, as well as for bit loading variables later on. Finally, it is noted that when a linear receiver structure is considered, the feedback term is to be removed from (5.3) and the summation in the denominator of (5.4) should be over $\mathcal{N} \setminus \{n\}$ instead of $m > n$.

In (5.4), it is seen that only the SINR of user n depends on $\boldsymbol{r}_{k,n}^{\mathrm{U}}$. The minimum mean square error (MMSE) receiver is therefore optimal—as it maximizes the SINR of user n—and is given by (5.5) where $\boldsymbol{\Psi}_{k,n}^{\mathrm{U}} = \sum_{m>n} s_{k,m}^{\mathrm{U}} \boldsymbol{h}_{k,m}^{\mathrm{U}} (\boldsymbol{h}_{k,m}^{\mathrm{U}})^{\mathcal{H}} + \boldsymbol{\Sigma}_k^{\mathrm{U}}$ is user n's received interference-plus-noise covariance matrix on tone k. Substituting (5.5) into (5.4), $\mathbf{R}_k^{\mathrm{U}}$ can be eliminated from the US SINR expression, yielding (5.6). In case a linear receiver structure is considered, the summation in the definition of $\boldsymbol{\Psi}_{k,n}^{\mathrm{U}}$ should be over $\mathcal{N} \setminus \{n\}$ instead of $m > n$, and then (5.5) and (5.6) still apply.

$$\boldsymbol{r}_{k,n}^{\mathrm{U}} = \left(\boldsymbol{\Psi}_{k,n}^{\mathrm{U}}\right)^{-1} \boldsymbol{h}_{k,n}^{\mathrm{U}} \tag{5.5}$$

$$\gamma_{k,n}^{\mathrm{U}}(\boldsymbol{s}_k^{\mathrm{U}}, \boldsymbol{\Sigma}_k^{\mathrm{U}}) = s_{k,n}^{\mathrm{U}} (\boldsymbol{h}_{k,n}^{\mathrm{U}})^{\mathcal{H}} \left(\boldsymbol{\Psi}_{k,n}^{\mathrm{U}}\right)^{-1} \boldsymbol{h}_{k,n}^{\mathrm{U}} \tag{5.6}$$

5.2.2 Downstream channel

DS transmission in an N-user FDX DSL network with no ICI can be modeled on each tone independently as a broadcast channel (BC) with an additional term for the NEXT caused by the NTs.

$$\boldsymbol{y}_k^{\mathrm{D}} = (\mathbf{H}_k^{\mathrm{D}})^{\mathcal{H}} \tilde{\boldsymbol{x}}_k^{\mathrm{D}} + (\mathbf{H}_k^{\mathrm{X}})^{\mathcal{H}} \boldsymbol{x}_k^{\mathrm{U}} + \boldsymbol{z}_k^{\mathrm{D}} \tag{5.7}$$

In the channel equation, the superscript 'D' indicates that DS variables are considered. Vectors $\tilde{\boldsymbol{x}}_k^{\mathrm{D}}$, $\boldsymbol{y}_k^{\mathrm{D}}$, and $\boldsymbol{z}_k^{\mathrm{D}}$ have the same size as $\boldsymbol{x}_k^{\mathrm{U}}$ and denote the transmitted signal, received signal, and additive Gaussian noise. Moreover, $\mathbf{H}_k^{\mathrm{D}}$ and $\mathbf{H}_k^{\mathrm{X}}$ denote the Hermitian transpose of the $N \times N$ DS channel matrix and the $N \times N$ NT-side NEXT channel matrix, with $\left[\mathbf{H}_k^{\mathrm{D}}\right]_{mn} = ((h_k^{nm})^{\mathrm{D}})^*$ and $\left[\mathbf{H}_k^{\mathrm{X}}\right]_{mn} = ((h_k^{nm})^{\mathrm{X}})^*$ the complex conjugate of the transfer function between transmitter m and receiver n evaluated on tone k. The Hermitian transpose of the channel matrices are used in (5.7) to simplify notation later on.

In DS transmission, signal coordination is possible at the transmitter. Transmitted signals are generated as

$$\tilde{\boldsymbol{x}}_k^{\mathrm{D}} = \mathbf{T}_k^{\mathrm{D}} \boldsymbol{x}_k^{\mathrm{D}} \tag{5.8}$$

where $\mathbf{T}_k^{\mathrm{D}}$ is the precoding matrix. Furthermore, the average symbol power of user n on tone k is defined as $s_{k,n}^{\mathrm{D}} = \Delta_f \, \mathbb{E}\left\{|x_{k,n}^{\mathrm{D}}|^2\right\}$. For each line, the total DS transmit power is then given by

$$P_n^{\mathrm{D}} = \sum_k \left[\mathbf{T}_k^{\mathrm{D}} \mathbf{S}_k^{\mathrm{D}} (\mathbf{T}_k^{\mathrm{D}})^{\mathcal{H}}\right]_{nn} \tag{5.9}$$

where $\mathbf{S}_k^{\mathrm{D}} = \mathrm{diag}(\boldsymbol{s}_k^{\mathrm{D}})$ with $\boldsymbol{s}_k^{\mathrm{D}} = [s_{k,1}^{\mathrm{D}}, \ldots, s_{k,N}^{\mathrm{D}}]^{\mathrm{T}}$. The received noise power for user n on tone k is $\sigma_{k,n}^{\mathrm{D}} = \Delta_f \, \mathbb{E}\left\{|z_{k,n}^{\mathrm{D}}|^2\right\}$.

A non-linear transmitter structure implementing dirty paper coding (DPC) is assumed [26], such as the Tomlinson-Harashima precoder. DPC-based transmitters successively encode the symbols of different users, treating interference generated by previously encoded users as side information and treating the interference generated by other users as noise [207]. According to the original DPC results by Costa [50], considering the interference generated by previously encoded users to be side information allows one to obtain the same performance as when this interference were not present. The resulting SINR of user n on tone k is given as

$$\gamma^{\mathrm{D}}_{k,n}(\boldsymbol{s}^{\mathrm{U}}_k, \boldsymbol{s}^{\mathrm{D}}_k, \mathbf{T}^{\mathrm{D}}_k, \boldsymbol{\sigma}^{\mathrm{D}}_k) = \frac{s^{\mathrm{D}}_{k,n}|(\boldsymbol{h}^{\mathrm{D}}_{k,n})^{\mathrm{H}}\boldsymbol{t}^{\mathrm{D}}_{k,n}|^2}{\sum\limits_{m<n} s^{\mathrm{D}}_{k,m}|(\boldsymbol{h}^{\mathrm{D}}_{k,n})^{\mathrm{H}}\boldsymbol{t}^{\mathrm{D}}_{k,m}|^2 + (\boldsymbol{h}^{\mathrm{XX}}_{k,n})^{\mathrm{T}}\boldsymbol{s}^{\mathrm{U}}_k + \sigma^{\mathrm{D}}_{k,n}} \tag{5.10}$$

where $\boldsymbol{h}^{\mathrm{XX}}_{k,n}$ is the n-th column of the power transfer matrix of the NEXT channel on tone k, which is defined as $[\mathbf{H}^{\mathrm{XX}}_k]_{nm} = |(h^{nm}_k)^{\mathrm{X}}|^2$. In equation (5.10), it has been assumed that the user encoding order is fixed beforehand and w.l.o.g. given by the reversed user index order. Finally, note that when a linear transmitter structure is considered, all interference terms are treated as noise and the summation in the denominator of (5.10) should be over $\mathcal{N} \setminus \{n\}$ instead of $m < n$.

5.2.3 Performance metrics

When the number of users N in a DSL network is large, the interference-plus-noise received by each user is well approximated by a Gaussian distribution. Under this assumption, the relation between the SINR γ and the achievable bit loading b, which is assumed to be a continuous variable, is accurately modeled by (5.11) where $\log_2(\cdot)$ is the binary logarithm and where the SNR-gap to capacity Γ accounts for the difference in performance between ideal Gaussian signaling and the practical modulation and coding scheme in use. The Γ is additionally determined by the employed noise margin and by the target bit error rate. Typical values for Γ lie between 9.5 dB and 10.5 dB. The data rate of user n is calculated using (5.12) where f_{s} is the symbol rate.

$$b(\gamma) = \log_2\left(1 + \Gamma^{-1}\gamma\right) \tag{5.11}$$

$$R_n = f_{\mathrm{s}} \sum_k b(\gamma_{k,n}) \tag{5.12}$$

5.3 Full-duplex dynamic spectrum management

The so-called rate-adaptive DSM problem is considered, which optimizes the network's performance by selecting the resource allocation $\boldsymbol{s}_k^{\mathrm{U}}, \boldsymbol{s}_k^{\mathrm{D}}, \mathbf{T}_k^{\mathrm{D}}$ for all tones k that solves the weighted sum rate (WSR) maximization problem, i.e.

$$\underset{\substack{\boldsymbol{s}_k^{\mathrm{U}},\, \boldsymbol{s}_k^{\mathrm{D}} \in \mathbb{R}_+^N \,\forall k \\ \mathbf{T}_k^{\mathrm{D}} \,\forall k}}{\text{maximize}} \qquad \sum_n \omega_n^{\mathrm{U}} \sum_k b(\gamma_{k,n}^{\mathrm{U}}) + \sum_n \omega_n^{\mathrm{D}} \sum_k b(\gamma_{k,n}^{\mathrm{D}}) \tag{5.13a}$$

$$\text{subject to} \qquad P_n^{\mathrm{U}} \leq P_{\mathrm{tot}}^{\mathrm{U}},\, \forall n \quad \text{and} \quad P_n^{\mathrm{D}} \leq P_{\mathrm{tot}}^{\mathrm{D}},\, \forall n. \tag{5.13b}$$

In (5.13a), the factor f_{s} has been omitted for brevity, and $\mathbb{R}_+^N \triangleq \{\boldsymbol{s} \in \mathbb{R}^N \mid s_n \geq 0,\, \forall n\}$. By adjusting the real positive weights ω in the objective function (5.13a), all Pareto-optimal resource allocations can be obtained [32].

The considered WSR maximization problem (5.13) is subject to US an DS total per line power constraints (5.13b), and to positivity constraints. Spectral mask and bit cap constraints are not explicitly accounted for in the formulation of problem (5.13). Although it is possible to add these constraints to the WSR maximization problem, their absence allows for a notation that is not too unwieldy in Section 5.4 and Section 5.5. Moreover, yet another version of problem (5.13) can be obtained by abandoning the assumption of perfect DPU-side NEXT cancellation. It will be indicated after the derivation of each algorithm which modifications have to be made to adapt the algorithms to these modified problem statements.

5.4 Optimal spectrum balancing

In this section, the FDX-OSB algorithm is developed, which finds the globally optimal DSM strategy for an MU FDX DSL network. Contrary to the OSB-type algorithm developed in [62], the favorable structure of the problem considered here enables the development of a novel MAC-BC duality theory that, in turn, allows finding the globally optimal resource allocation. The FDX-OSB algorithm contains the MAC-OSB algorithm [195] and BC-OSB algorithm [111] as special cases, and relies on dual decomposition, MAC-BC duality, and an exhaustive grid search. Each of these components is now addressed individually.

5.4.1 Dual decomposition

The idea of dual decomposition is to solve the Lagrange dual problem associated with problem (5.13), as defined in (5.14). Problem (5.14) is often referred to as the master problem, and minimizes the Lagrange dual function $q(\boldsymbol{\lambda}^{\mathrm{U}}, \boldsymbol{\lambda}^{\mathrm{D}})$ with respect to the US and DS Lagrange multipliers $\boldsymbol{\lambda}^{\mathrm{U}}$ and $\boldsymbol{\lambda}^{\mathrm{D}}$. In turn, the Lagrange dual function is defined as the maximum of the Lagrangian over all possible resource allocations, as defined in (5.15), which is referred to as the slave problem.

$$\underset{\boldsymbol{\lambda}^{\mathrm{U}}, \boldsymbol{\lambda}^{\mathrm{D}} \in \mathbb{R}_{+}^{N}}{\text{minimize}} \quad q(\boldsymbol{\lambda}^{\mathrm{U}}, \boldsymbol{\lambda}^{\mathrm{D}}) \tag{5.14}$$

$$q(\boldsymbol{\lambda}^{\mathrm{U}}, \boldsymbol{\lambda}^{\mathrm{D}}) = \max_{\substack{\boldsymbol{s}_k^{\mathrm{U}},\, \boldsymbol{s}_k^{\mathrm{D}} \in \mathbb{R}_{+}^{N}\ \forall k \\ \mathbf{T}_k^{\mathrm{D}}\ \forall k}} \left\{ \mathcal{L} \right\} \tag{5.15}$$

It is noted that in (5.15), the resource allocations are no longer subject to total per line power constraints. These constraints are incorporated into the Lagrangian, which is defined as

$$\mathcal{L} = \sum_{k} \left(\mathcal{L}_k^{\mathrm{U}} + \mathcal{L}_k^{\mathrm{D}} \right) + \sum_{n} \left(\lambda_n^{\mathrm{U}} P_{\mathrm{tot}}^{\mathrm{U}} + \lambda_n^{\mathrm{D}} P_{\mathrm{tot}}^{\mathrm{D}} \right) \tag{5.16a}$$

$$\mathcal{L}_k^{\mathrm{U}} = \sum_{n} \omega_n^{\mathrm{U}} b\big(\gamma_{k,n}^{\mathrm{U}}(\boldsymbol{s}_k^{\mathrm{U}}, \boldsymbol{\Sigma}_k^{\mathrm{U}})\big) - (\boldsymbol{\lambda}^{\mathrm{U}})^{\mathrm{T}} \boldsymbol{s}_k^{\mathrm{U}} \tag{5.16b}$$

$$\mathcal{L}_k^{\mathrm{D}} = \sum_{n} \omega_n^{\mathrm{D}} b\big(\gamma_{k,n}^{\mathrm{D}}(\boldsymbol{s}_k^{\mathrm{U}}, \boldsymbol{s}_k^{\mathrm{D}}, \mathbf{T}_{k,n}^{\mathrm{D}}, \boldsymbol{\sigma}_k^{\mathrm{D}})\big) - \sum_{n} s_{k,n}^{\mathrm{D}} (\boldsymbol{t}_{k,n}^{\mathrm{D}})^{\mathcal{H}} \boldsymbol{\Lambda}^{\mathrm{D}} \boldsymbol{t}_{k,n}^{\mathrm{D}}, \tag{5.16c}$$

with $\boldsymbol{\Lambda}^{\mathrm{D}} = \mathrm{diag}(\boldsymbol{\lambda}^{\mathrm{D}})$. Assuming the number of tones K is large, the time sharing property of [220] holds such that the duality gap [20] between problem (5.13) and problem (5.15) is zero. The master problem in (5.14) is convex but non-smooth, and can therefore be solved using a subgradient-based scheme such as the subgradient method or the ellipsoid method. Subgradients are calculated as

$$\begin{aligned} \boldsymbol{g}^{\mathrm{U}} &= \boldsymbol{P}^{\mathrm{U}} - \mathbf{1}_{N \times 1} P_{\mathrm{tot}}^{\mathrm{U}}, \\ \boldsymbol{g}^{\mathrm{D}} &= \boldsymbol{P}^{\mathrm{D}} - \mathbf{1}_{N \times 1} P_{\mathrm{tot}}^{\mathrm{D}}. \end{aligned} \tag{5.17}$$

For each new value of the Lagrange multipliers $\boldsymbol{\lambda}^{\mathrm{U}}$ and $\boldsymbol{\lambda}^{\mathrm{D}}$, the slave problem (5.15) is solved to obtain $\boldsymbol{P}^{\mathrm{U}}$ and $\boldsymbol{P}^{\mathrm{D}}$. Each term $\mathcal{L}_k^{\mathrm{U}} + \mathcal{L}_k^{\mathrm{D}}$ in (5.15) depends on tone k resource allocation variables only. The slave problem is therefore separable across tones, such that the Lagrange dual function can be evaluated

by solving K decoupled per tone slave problems of the following form.

$$\underset{\substack{\boldsymbol{s}_k^{\mathrm{U}},\, \boldsymbol{s}_k^{\mathrm{D}} \in \mathbb{R}_+^N \\ \mathbf{T}_k^{\mathrm{D}}}}{\text{maximize}} \quad \mathcal{L}_k^{\mathrm{U}} + \mathcal{L}_k^{\mathrm{D}} \tag{5.18}$$

Section 5.4.2 and Section 5.4.3 elaborate on how the global optimum of each per tone slave problem can be obtained.

5.4.2 MAC-BC duality for FDX DSL

Whereas $\mathbf{R}_k^{\mathrm{U}}$ is effectively removed from the optimization problem due to the favorable structure of $\gamma_{k,n}^{\mathrm{U}}$ in (5.6), the same does not go for $\mathbf{T}_k^{\mathrm{D}}$. Therefore, a new MAC-BC duality theory for FDX networks is now developed, which allows transforming $\mathcal{L}_k^{\mathrm{D}}$ into an equivalent dual US Lagrangian plus a coupling bilinear term. The proposed theory is based on [87, 111, 219]. Using the duality theory, $\mathbf{T}_k^{\mathrm{D}}$ can then be eliminated from $\gamma_{k,n}^{\mathrm{D}}$ in the same way as $\mathbf{R}_k^{\mathrm{U}}$ is removed from $\gamma_{k,n}^{\mathrm{U}}$.

The dual US Lagrangian is defined in (5.19), with the expression for the dual upstream SINR given by (5.20).

$$\mathcal{L}_k^{\mathrm{dU}} = \sum_n \omega_n^{\mathrm{D}} b\big(\gamma_{k,n}^{\mathrm{dU}}(\boldsymbol{s}_k^{\mathrm{dU}}, \boldsymbol{t}_{k,n}^{\mathrm{D}}, \boldsymbol{\Lambda}^{\mathrm{D}})\big) - (\boldsymbol{\sigma}_k^{\mathrm{D}})^{\mathrm{T}} \boldsymbol{s}_k^{\mathrm{dU}} \tag{5.19}$$

$$\gamma_{k,n}^{\mathrm{dU}}(\boldsymbol{s}_k^{\mathrm{dU}}, \boldsymbol{t}_{k,n}^{\mathrm{D}}, \boldsymbol{\Lambda}^{\mathrm{D}}) = \frac{s_{k,n}^{\mathrm{dU}} |(\boldsymbol{t}_{k,n}^{\mathrm{D}})^{\mathrm{H}} \boldsymbol{h}_{k,n}^{\mathrm{D}}|^2}{\sum_{m>n} s_{k,m}^{\mathrm{dU}} |(\boldsymbol{t}_{k,n}^{\mathrm{D}})^{\mathrm{H}} \boldsymbol{h}_{k,m}^{\mathrm{D}}|^2 + (\boldsymbol{t}_{k,n}^{\mathrm{D}})^{\mathrm{H}} \boldsymbol{\Lambda}^{\mathrm{D}} \boldsymbol{t}_{k,n}^{\mathrm{D}}} \tag{5.20}$$

The superscript dU indicates that a variable of the dual upstream channel is considered. By comparing (5.20) to (5.4), and (5.19) to (5.16b), it is seen that this dual US Lagrangian corresponds to a MAC system with channel matrix $\mathbf{H}_k^{\mathrm{D}}$, receive filter matrix $\mathbf{T}_k^{\mathrm{D}}$, noise covariance matrix $\boldsymbol{\Lambda}^{\mathrm{D}}$, Lagrange multiplier values $\boldsymbol{\sigma}_k^{\mathrm{D}}$, and a decoding order that is the reversed encoding order of the original DS system. Duality between $\mathcal{L}_k^{\mathrm{dU}}$ and $\mathcal{L}_k^{\mathrm{D}}$ is established in the following proposition.

Proposition 5.1 (MAC-BC duality for FDX DSL)**.** *Let $\boldsymbol{s}_k^{U} \in \mathbb{R}_+^N$ and $\mathbf{T}_k^{D}$ such that $\boldsymbol{t}_{k,n}^{D} \neq \mathbf{0}_{N\times 1}$ $\forall n$. Furthermore, assume that both $\boldsymbol{\lambda}^{D}$ and $\boldsymbol{\sigma}_k^{D}$ are strictly positive. The following statements then hold true.*

- ***P.1*** *For each dual symbol power vector $\boldsymbol{s}_k^{dU} \in \mathbb{R}_+^N$, a symbol power vector $\boldsymbol{s}_k^{D} \in \mathbb{R}_+^N$ exists such that equalities* (5.21) *and* (5.22) *are satisfied.*
- ***P.2*** *The converse is also true, i.e. for each symbol power vector $\boldsymbol{s}_k^{D} \in \mathbb{R}_+^N$, a dual symbol power vector $\boldsymbol{s}_k^{dU} \in \mathbb{R}_+^N$ exists such that equalities* (5.21) *and* (5.22) *are satisfied.*

$$\gamma_{k,n}^{D}(\boldsymbol{s}_k^{U}, \boldsymbol{s}_k^{D}, \mathbf{T}_k^{D}, \boldsymbol{\sigma}_k^{D}) = \gamma_{k,n}^{dU}(\boldsymbol{s}_k^{dU}, \boldsymbol{t}_{k,n}^{D}, \boldsymbol{\Lambda}^{D}),\ \forall n \tag{5.21}$$

$$\mathcal{L}_k^{D} = \mathcal{L}_k^{dU} - (\boldsymbol{s}_k^{U})^{T}\mathbf{H}_k^{XX}\boldsymbol{s}_k^{dU} \tag{5.22}$$

Proof. Following the reasoning in [87], the validity of **P.1** is confirmed by construction of $\boldsymbol{s}_k^{\mathrm{D}}$ from $\boldsymbol{s}_k^{\mathrm{dU}}$. **P.2** can then be proven analogously.

The symbol power vector $\boldsymbol{s}_k^{\mathrm{D}}$ corresponding to a given $\boldsymbol{s}_k^{\mathrm{dU}}$ is found by solving the following system of equations, which is constructed from and equivalent to the equalities in (5.21).

$$\mathbf{Z}_k^{\mathrm{dU}}\boldsymbol{s}_k^{\mathrm{D}} = \left((\mathbf{H}_k^{\mathrm{XX}})^{\mathrm{T}}\boldsymbol{s}_k^{\mathrm{U}} + \boldsymbol{\sigma}_k^{\mathrm{D}}\right) \circ \boldsymbol{s}_k^{\mathrm{dU}} \tag{5.23}$$

$$[\mathbf{Z}_k^{\mathrm{dU}}]_{nm} = \begin{cases} -(\boldsymbol{t}_{k,m}^{\mathrm{D}})^{\mathcal{H}}\left(s_{k,n}^{\mathrm{dU}}\boldsymbol{h}_{k,n}^{\mathrm{D}}(\boldsymbol{h}_{k,n}^{\mathrm{D}})^{\mathcal{H}}\right)\boldsymbol{t}_{k,m}^{\mathrm{D}} & \text{if } n < m \\ (\boldsymbol{t}_{k,m}^{\mathrm{D}})^{\mathcal{H}}\boldsymbol{\Psi}_{k,m}^{\mathrm{dU}}\boldsymbol{t}_{k,m}^{\mathrm{D}} & \text{if } n = m \\ 0 & \text{if } n > m \end{cases}$$

In (5.23), $\boldsymbol{\Psi}_{k,n}^{\mathrm{dU}} = \sum_{m>n} s_{k,m}^{\mathrm{dU}}\boldsymbol{h}_{k,m}^{\mathrm{U}}(\boldsymbol{h}_{k,m}^{\mathrm{D}})^{\mathcal{H}} + \boldsymbol{\Lambda}^{\mathrm{D}}$ is the dual interference-plus-noise covariance matrix of user n. Positivity of $\boldsymbol{s}_k^{\mathrm{D}}$ follows from $\mathbf{Z}_k^{\mathrm{dU}}$ being an M-matrix, such that its inverse contains only non-negative elements [87, 156]. Furthermore, summing the rows of (5.23) yields

$$\sum_n s_{k,n}^{\mathrm{D}}(\boldsymbol{t}_{k,n}^{\mathrm{D}})^{\mathcal{H}}\boldsymbol{\Lambda}^{\mathrm{D}}\boldsymbol{t}_{k,n}^{\mathrm{D}} = (\boldsymbol{\sigma}_k^{\mathrm{D}})^{\mathrm{T}}\boldsymbol{s}_k^{\mathrm{dU}} + (\boldsymbol{s}_k^{\mathrm{U}})^{\mathrm{T}}\mathbf{H}_k^{\mathrm{XX}}\boldsymbol{s}_k^{\mathrm{dU}}, \tag{5.24}$$

confirming that the equality in (5.22) holds. □

In order to adapt this duality result to a linear receiver structure, the summation in the denominator of (5.20), as well as the summation in the definition of $\boldsymbol{\Psi}_{k,n}^{\mathrm{dU}}$, should be over $\mathcal{N} \setminus \{n\}$ instead of $m < n$. Furthermore, the lower triangular elements of $\mathbf{Z}_k^{\mathrm{dU}}$ should be defined similarly to the upper triangular elements.

Corollary 5.2. ***P.2*** *also holds when* $\boldsymbol{t}_{k,n}^{D} = \mathbf{0}_{N\times 1}$ *for any* n.

Proof. If $\boldsymbol{t}_{k,n}^{\mathrm{D}} = \mathbf{0}_{N\times 1}$, then an equivalent DS resource allocation can be obtained that achieves the same values for $\mathcal{L}_k^{\mathrm{D}}$ and $\gamma_{k,n}^{\mathrm{D}}(\boldsymbol{s}_k^{\mathrm{U}}, \boldsymbol{s}_k^{\mathrm{D}}, \mathbf{T}_k^{\mathrm{D}}, \boldsymbol{\sigma}_k^{\mathrm{D}})\ \forall n$, by setting $\boldsymbol{t}_{k,n}^{\mathrm{D}} \neq \mathbf{0}_{N\times 1}$ and $s_{k,n}^{\mathrm{D}} = 0$. This equivalent resource allocation satisfies the assumptions of Proposition 5.1. □

Corollary 5.3 (Dual MAC optimality)**.** *The solution to*

$$\underset{\boldsymbol{s}_k^{U},\, \boldsymbol{s}_k^{dU}\in\mathbb{R}_+^{N},\, \mathbf{T}_k^{D}}{\text{maximize}} \quad \mathcal{L}_k^{U} + \mathcal{L}_k^{dU} - (\boldsymbol{s}_k^{U})^{T}\mathbf{H}_k^{XX}\boldsymbol{s}_k^{dU}, \tag{5.25}$$

when transformed to the DS domain using (5.23)*, is the solution to the original per tone slave problem in* (5.18)*.*

Proof. The Corollary is proven by contradiction. Assume w.l.o.g. that a solution to problem (5.25) exists with $\boldsymbol{t}_{k,n}^{\mathrm{D}} \neq \mathbf{0}_{N\times 1}\ \forall n$. If Corollary 5.3 were false, a solution to problem (5.18) would exist achieving a higher value for $\mathcal{L}_k^{\mathrm{U}} + \mathcal{L}_k^{\mathrm{D}}$ than the transformed solution of (5.25). Corollary 5.2 would then imply that a dual MAC domain resource allocation exists achieving a value for $\mathcal{L}_k^{\mathrm{U}} + \mathcal{L}_k^{\mathrm{dU}} - (\boldsymbol{s}_k^{\mathrm{U}})^{\mathrm{T}}\mathbf{H}_k^{\mathrm{XX}}\boldsymbol{s}_k^{\mathrm{dU}}$ that is higher than the value achieved by the solution to (5.25), which is a contradiction. □

In problem (5.25), $\mathbf{T}_k^{\mathrm{D}}$ can now be eliminated from $\gamma_{k,n}^{\mathrm{dU}}$ in the same way as $\mathbf{R}_k^{\mathrm{U}}$ has been eliminated from $\gamma_{k,n}^{\mathrm{U}}$ in (5.4). The optimal dual domain receive filter vector $\boldsymbol{t}_{k,n}^{\mathrm{D}}$ is given by (5.26), and substituting this expression into (5.20) yields the expression for the SINR in (5.27).

$$\boldsymbol{t}_{k,n}^{\mathrm{D}} = \left(\boldsymbol{\Psi}_{k,n}^{\mathrm{dU}}\right)^{-1}\boldsymbol{h}_{k,n}^{\mathrm{D}} \tag{5.26}$$

$$\gamma_{k,n}^{\mathrm{dU}}(\boldsymbol{s}_k^{\mathrm{dU}}, \boldsymbol{\Lambda}^{\mathrm{D}}) = s_{k,n}^{\mathrm{dU}}(\boldsymbol{h}_{k,n}^{\mathrm{D}})^{\mathcal{H}}\left(\boldsymbol{\Psi}_{k,n}^{\mathrm{dU}}\right)^{-1}\boldsymbol{h}_{k,n}^{\mathrm{D}} \tag{5.27}$$

5.4.3 Exhaustive grid search

After applying MAC-BC duality and eliminating both $\boldsymbol{R}_k^{\mathrm{U}}$ and $\boldsymbol{T}_k^{\mathrm{D}}$, the following simplified per tone slave problem is obtained.

$$\underset{\boldsymbol{s}_k^{\mathrm{U}}, \boldsymbol{s}_k^{\mathrm{dU}} \in \mathbb{R}_+^N}{\text{maximize}} \quad \mathcal{L}_k^{\mathrm{U}} + \mathcal{L}_k^{\mathrm{dU}} - (\boldsymbol{s}_k^{\mathrm{U}})^{\mathrm{T}}\mathbf{H}_k^{\mathrm{XX}}\boldsymbol{s}_k^{\mathrm{dU}} \tag{5.28}$$

In problem (5.28), $\mathcal{L}_k^{\mathrm{U}}$ depends only on $\boldsymbol{s}_k^{\mathrm{U}}$, whereas $\mathcal{L}_k^{\mathrm{dU}}$ depends only on $\boldsymbol{s}_k^{\mathrm{dU}}$. This non-convex problem is solved by performing an exhaustive search over a grid of possible bit loading combinations $\prod_n \mathcal{B} \times \prod_n \mathcal{B}$, with $\mathcal{B}$ the set of possible bit loading values (assumed to be the same in US and DS). As the number of points in the grid is $|\mathcal{B}|^{2N}$, the complexity of this exhaustive search is exponential in $2N$.

For each vector $[(\boldsymbol{b}_k^{\mathrm{U}})^{\mathrm{T}}(\boldsymbol{b}_k^{\mathrm{D}})^{\mathrm{T}}]^{\mathrm{T}}$ in the search grid, the corresponding US and DS symbol powers $\boldsymbol{s}_k^{\mathrm{U}}$ and $\boldsymbol{s}_k^{\mathrm{dU}}$ are calculated, and then the objective function of (5.28) is evaluated. It is noted that $\boldsymbol{b}_k^{\mathrm{U}}$ (respectively $\boldsymbol{b}_k^{\mathrm{D}}$) solely depends on $\boldsymbol{s}_k^{\mathrm{U}}$ ($\boldsymbol{s}_k^{\mathrm{dU}}$), not on $\boldsymbol{s}_k^{\mathrm{dU}}$ ($\boldsymbol{s}_k^{\mathrm{U}}$), such that $\boldsymbol{s}_k^{\mathrm{U}}$ and $\mathcal{L}_k^{\mathrm{U}}$ ($\boldsymbol{s}_k^{\mathrm{dU}}$ and $\mathcal{L}_k^{\mathrm{dU}}$) can be calculated from $\boldsymbol{b}_k^{\mathrm{U}}$ ($\boldsymbol{b}_k^{\mathrm{dU}}$) independently of $\boldsymbol{b}_k^{\mathrm{dU}}$ ($\boldsymbol{b}_k^{\mathrm{U}}$). By calculating $\boldsymbol{s}_k^{\mathrm{U}}$ and $\mathcal{L}_k^{\mathrm{U}}$ (respectively $\mathbf{H}_k^{\mathrm{XX}}\boldsymbol{s}_k^{\mathrm{dU}}$ and $\mathcal{L}_k^{\mathrm{dU}}$) for each $\boldsymbol{b} \in \prod_n \mathcal{B}$ beforehand, storing the obtained values in a set $\mathcal{A}^{\mathrm{U}}$ ($\mathcal{A}^{\mathrm{D}}$), the complexity of evaluating the objective function of (5.28) for each $[(\boldsymbol{b}_k^{\mathrm{U}})^{\mathrm{T}}(\boldsymbol{b}_k^{\mathrm{D}})^{\mathrm{T}}]^{\mathrm{T}} \in \prod_n \mathcal{B} \times \prod_n \mathcal{B}$ is kept to a minimum.

The symbol power vector $\boldsymbol{s}_k^{\mathrm{U}}$ is obtained from $\boldsymbol{b}_k^{\mathrm{U}}$ by first calculating each $\gamma_{k,n}^{\mathrm{U}}$ using (5.11), and by subsequently inverting (5.27). When $s_{k,m}^{\mathrm{U}}$ is known for all

Algorithm 7. FDX-OSB

1: Choose $\mu > 0$, $\boldsymbol{\lambda}^{\mathrm{U}} \in \mathbb{R}_+^N$, $\boldsymbol{\lambda}^{\mathrm{D}} \in \mathbb{R}_+^N$, $\mathcal{B} \subset \mathbb{N}$, and $\epsilon > 0$
2: **while** $(|P_n^{\mathrm{U}} - P_{\mathrm{tot}}^{\mathrm{U}}| > \delta_{\mathrm{P}}$ & $\lambda_n^{\mathrm{U}} > \delta_\lambda$ for any $n)$
3: or $(|P_n^{\mathrm{D}} - P_{\mathrm{tot}}^{\mathrm{D}}| > \delta_{\mathrm{P}}$ & $\lambda_n^{\mathrm{D}} > \delta_\lambda$ for any $n)$ **do**
4: **for** $k \in \mathcal{K}$ **do**
5: $\{\boldsymbol{s}_k^{\mathrm{U}}, \mathbf{R}_k^{\mathrm{U}}, \boldsymbol{s}_k^{\mathrm{D}}, \mathbf{T}_k^{\mathrm{D}}\} \leftarrow$ ExhSearch$(\boldsymbol{\lambda}^{\mathrm{U}}, \boldsymbol{\lambda}^{\mathrm{D}}, k)$
6: Calculate P_n^{U}, P_n^{D} $\forall n$ using (5.2), (5.9)
7: Update $\boldsymbol{\lambda}^{\mathrm{U}}$, $\boldsymbol{\lambda}^{\mathrm{D}}$ using (5.17)
8: **function** ExhSearch$(\boldsymbol{\lambda}^{\mathrm{U}}, \boldsymbol{\lambda}^{\mathrm{D}}, k)$
9: Initialize $\mathcal{A}^{\mathrm{U}} \leftarrow \emptyset$, $\mathcal{A}^{\mathrm{dU}} \leftarrow \emptyset$, $\mathcal{L}_k{}^\star \leftarrow -\inf$
10: **for all** $\boldsymbol{b} \in \prod_n \mathcal{B}$ **do**
11: Calculate $\boldsymbol{s}_k^{\mathrm{U}}$, $\boldsymbol{s}_k^{\mathrm{dU}}$ from $\boldsymbol{b}$ by inverting (5.6), (5.27)
12: Calculate $\mathcal{L}_k^{\mathrm{U}}$, $\mathcal{L}_k^{\mathrm{dU}}$ using (5.16b), (5.19)
13: Add $\left(\boldsymbol{s}_k^{\mathrm{U}}, \mathcal{L}_k^{\mathrm{U}}\right)$ to $\mathcal{A}^{\mathrm{U}}$, $\left(\mathbf{H}_k^{\mathrm{XX}} \boldsymbol{s}_k^{\mathrm{dU}}, \mathcal{L}_k^{\mathrm{dU}}\right)$ to $\mathcal{A}^{\mathrm{dU}}$
14: **for all** $(\boldsymbol{s}_k^{\mathrm{U}}, \mathcal{L}_k^{\mathrm{U}}, \boldsymbol{s}_k^{\mathrm{dU}}, \mathcal{L}_k^{\mathrm{dU}}) \in \mathcal{A}^{\mathrm{U}} \times \mathcal{A}^{\mathrm{dU}}$ **do**
15: Set $\mathcal{L}_k \leftarrow \mathcal{L}_k^{\mathrm{U}} + \mathcal{L}_k^{\mathrm{dU}} - (\boldsymbol{s}_k^{\mathrm{U}})^{\mathrm{T}} \mathbf{H}_k^{\mathrm{XX}} \boldsymbol{s}_k^{\mathrm{dU}}$
16: **if** $\mathcal{L}_k{}^\star < \mathcal{L}_k$ **then**
17: Set $\mathcal{L}_k{}^\star \leftarrow \mathcal{L}_k$, $\boldsymbol{s}_k^{\mathrm{U}\star} \leftarrow \boldsymbol{s}_k^{\mathrm{U}}$, $\boldsymbol{s}_k^{\mathrm{dU}\star} \leftarrow \boldsymbol{s}_k^{\mathrm{dU}}$
18: Calculate $\boldsymbol{R}_k^{\mathrm{U}\star}$, $\boldsymbol{T}_k^{\mathrm{D}\star}$ from $\boldsymbol{s}_k^{\mathrm{U}\star}$, $\boldsymbol{s}_k^{\mathrm{dU}\star}$ using (5.5), (5.26)
19: Calculate BC user powers $\boldsymbol{s}_k^{\mathrm{D}\star}$ by solving (5.23)

users $m > n$, $s_{k,n}^{\mathrm{U}}$ can be calculated in closed form as

$$s_{k,n}^{\mathrm{U}} = \frac{\gamma_{k,n}}{(\boldsymbol{h}_{k,n}^{\mathrm{U}})^{\mathrm{H}} (\boldsymbol{\Psi}_{k,n}^{\mathrm{U}})^{-1} \boldsymbol{h}_{k,n}^{\mathrm{U}}}. \tag{5.29}$$

Therefore, $s_{k,n}^{\mathrm{U}}$ is evaluated sequentially starting from user N and ending with user 1. The dual symbol power vector $\boldsymbol{s}_k^{\mathrm{dU}}$ can similarly be obtained from $\boldsymbol{b}_k^{\mathrm{D}}$. In case a linear transceiver structure is considered, $\boldsymbol{s}_k^{\mathrm{U}}$ ($\boldsymbol{s}_k^{\mathrm{dU}}$) can be obtained from $\boldsymbol{b}_k^{\mathrm{U}}$ ($\boldsymbol{b}_k^{\mathrm{D}}$) using an iterative calculation, as in [204].

The resulting algorithm is summarized in Algorithm 7, and is referred to as full-duplex optimal spectrum balancing (FDX-OSB). To the best of the authors' knowledge, FDX-OSB is the first algorithm that is guaranteed to find the globally optimal solution of a MU FDX resource allocation problem as in (5.13). The complexity of FDX-OSB mainly stems from line 15, requiring N multiplications and $N + 1$ additions in each iteration. The overall complexity of Algorithm 7 is therefore $\mathcal{O}(I_{\mathrm{SG}} K |\mathcal{B}|^{2N} N)$, with I_{SG} the number of iterations required by the subgradient algorithm to converge.

In the above derivation of FDX-OSB, it has been indicated how to adapt the formulas used in Algorithm 7 when a linear transceiver structure is considered.

While Algorithm 7 applies to DSM problem (5.13), other versions of FDX-OSB are obtained by including bit cap and/or spectral mask constraints. Bit cap constraints are easily enforced by appropriately designing the bit loading set $\mathcal{B}$. US spectral mask constraints are easily enforced by discarding $\left(\boldsymbol{s}_k^{\mathrm{U}}, \mathcal{L}_k^{\mathrm{U}}\right)$-tuples that do not satisfy these constraints in line 13 of Algorithm 7. DS spectral mask constraints however are tougher to enforce. A possible method has been proposed in [108], consisting of dualizing the DS spectral mask constraints when formulating the Lagrange dual problem (5.14). Finally, problem (5.13) can be altered by relaxing the assumption of perfect DPU-side NEXT cancellation. In this case however, the solution strategy employed by FDX-OSB cannot be adopted to find the global optimum, as the proposed MAC-BC duality transformation is not able to eliminate $\boldsymbol{s}_k^{\mathrm{D}}$ from the resulting US Lagrangian $\mathcal{L}_k^{\mathrm{U}}$, and hence one should resort to suboptimal algorithms as in [62].

5.5 Distributed spectrum balancing

With FDX-OSB, finding the global optimum of problem (5.13) comes at the price of an exceedingly high complexity. In this section, two algorithms are presented that exhibit a lower complexity, but are only able to find a local optimum of problem (5.13). The algorithms are FDX adaptations of the distributed spectrum balancing (DSB) algorithm that has previously been developed for both the spectrum coordination problem [188], and for the US and DS joint signal and spectrum coordination problem [108, 193, 204]. A brief introduction to the DSB algorithm structure is given first, and then the two DSB algorithms are presented for the FDX channel.

5.5.1 DSB algorithm

The DSB algorithm [188, 193] comprises an iterative procedure to solve optimization problems of the following form.

$$\underset{\mathbf{X}}{\text{maximize}} \quad \sum_{i=1}^{i_{\max}} f_i(\mathbf{X}) \tag{5.30a}$$

$$\text{subject to} \quad \mathbf{X}_i \in \mathcal{X}_i, \, \forall i \tag{5.30b}$$

In problem (5.30), the decision variable $\mathbf{X}$ is comprised of multiple coordinate blocks $\mathbf{X}_i$, i.e. $\mathbf{X} = \left[\mathbf{X}_1^{\mathrm{T}}, \ldots, \mathbf{X}_{i_{\max}}^{\mathrm{T}}\right]^{\mathrm{T}}$. Each function f_i has a (possibly empty) coordinate block $\mathbf{X}_i$ associated with it, in which f_i is concave. Moreover, f_i is convex in each $\mathbf{X}_j$ with $j \in \{1, \ldots, i_{\max}\} \setminus \{i\}$. In each iteration of the DSB

algorithm, the objective function of (5.30) is replaced by the sum of surrogate functions $\tilde{f}_i$, each depending only on a single coordinate block $\mathbf{X}_i$. The resulting surrogate problem has the following form.

$$\underset{\mathbf{X}}{\text{maximize}} \quad \sum_{i=1}^{i_{\max}} \tilde{f}_i(\mathbf{X}_i; \bar{\mathbf{X}}) \tag{5.31a}$$

$$\text{subject to} \quad \mathbf{X}_i \in \mathcal{X}_i, \, \forall i \tag{5.31b}$$

In (5.31), $\bar{\mathbf{X}}$ denotes the current value of $\mathbf{X}$. The surrogate functions $\tilde{f}_i$ are defined as

$$\tilde{f}_i(\mathbf{X}_i; \bar{\mathbf{X}}) \triangleq f_i\big([\bar{\mathbf{X}}_1^{\mathrm{T}}, \ldots, \mathbf{X}_i^{\mathrm{T}}, \ldots, \bar{\mathbf{X}}_{i_{\max}}^{\mathrm{T}}]^{\mathrm{T}}\big) - \mathrm{tr}(\mathbf{A}_i^{\mathrm{H}} \mathbf{X}_i) \tag{5.32}$$

with $\mathbf{A}_i = -\nabla_{\mathbf{X}_i^*}\big(\sum_{j \neq i} f_j(\mathbf{X})\big)\big|_{\mathbf{X}=\bar{\mathbf{X}}}$ the negative conjugate cogradient of $\sum_{j \neq i} f_j(\mathbf{X})$, and where $\mathbf{A}_i^{\mathrm{H}} \mathbf{X}_i$ is assumed to be Hermitian such that its trace is real. By iteratively solving surrogate problems (5.31), which are separable across coordinate blocks $\mathbf{X}_i$, the DSB algorithm can find a stationary point of the original problem as in (5.30).

It is noted that the acronym 'DSB' is adopted from [188, 193], but that the same algorithmic structure is also known as successive convex approximation (SCA). SCA algorithms that have DSB as a special case and for which theoretical convergence results are available include BSUM, SJBR, and FLEXA. Convergence results have first been established for the 'block successive upper-bound minimization' (BSUM) algorithm [154], which updates only a single coordinate block $\mathbf{X}_i$ after solving (5.31). This sequential mode of operation is referred to as Gauss-Seidel updating. More recently, convergence results have been established for Algorithm 7 from [162], hereafter referred to as SJBR, which updates all coordinate blocks by taking a step in the direction of the solution to (5.31). The parallel mode of operation employed by SJBR is referred to as Jacobi updating. It is noted that convergence of SJBR requires each $\tilde{f}_i$ to be strongly convex, guaranteeing that all subproblems as in (5.31) have a unique solution. Finally, convergence has been established for the 'inexact flexible parallel algorithm' (FLEXA) [56], which is similar to SJBR but can also be applied to non-smooth problems.[4]

[4] Even though the results in [56, 154, 162] are derived for real variables, it is argued in [55] that these results are also valid for problems with complex variables. Any complex problem can straightforwardly be transformed to a real problem by using separate variables for the real and imaginary parts of the complex variables. As is suggested in [55] however, one can equivalently work directly with complex variables by means of 'Wirtinger derivatives'. For more information on optimization of real functions in complex variables, the reader is referred to [172].

5.5.2 FDX dual domain DSB algorithm (FDX-DD-DSB)

The first FDX DSB algorithm is obtained by applying the DSB algorithm to problem (5.28). Three different types of functions f_i are identified.

$$f_n^{\mathrm{U}}(\boldsymbol{s}_k^{\mathrm{U}}) = \omega_n^{\mathrm{U}} b\big(\gamma_{k,n}^{\mathrm{U}}(\boldsymbol{s}_k^{\mathrm{U}}, \boldsymbol{\Sigma}_k^{\mathrm{U}})\big) - \lambda_n^{\mathrm{U}} s_{k,n}^{\mathrm{U}} \tag{5.33a}$$

$$f_n^{\mathrm{dU}}(\boldsymbol{s}_k^{\mathrm{dU}}) = \omega_n^{\mathrm{D}} b\big(\gamma_{k,n}^{\mathrm{dU}}(\boldsymbol{s}_k^{\mathrm{dU}}, \boldsymbol{\Lambda}^{\mathrm{D}})\big) - \sigma_{k,n}^{\mathrm{D}} s_{k,n}^{\mathrm{dU}} \tag{5.33b}$$

$$f^{\mathrm{X}}(\boldsymbol{s}_k^{\mathrm{U}}, \boldsymbol{s}_k^{\mathrm{dU}}) = -(\boldsymbol{s}_k^{\mathrm{U}})^{\mathrm{T}} \mathbf{H}_k^{\mathrm{XX}} \boldsymbol{s}_k^{\mathrm{dU}} \tag{5.33c}$$

The coordinate block associated with f_n^{U} is $s_{k,n}^{\mathrm{U}}$, and the coordinate block associated with f_n^{dU} is $s_{k,n}^{\mathrm{dU}}$. An empty coordinate block is associated with f^{X}. Functions f_n^{U}, f_n^{dU}, and f^{X} are concave in their associated coordinate blocks, and convex in the other coordinate blocks. The gradients $\mathbf{A}_i$ in the corresponding surrogate functions are real scalars and calculated as

$$a_{k,n}^{\mathrm{U}} = \sum_{m<n} (\boldsymbol{h}_{k,n}^{\mathrm{U}})^{\mathcal{H}} \bar{\boldsymbol{\Phi}}_{k,m}^{\mathrm{U}} \boldsymbol{h}_{k,n}^{\mathrm{U}} + [\mathbf{H}_k^{\mathrm{XX}}]_{\mathrm{row}\ m} \bar{\boldsymbol{s}}_k^{\mathrm{dU}} \tag{5.34a}$$

$$a_{k,n}^{\mathrm{dU}} = \sum_{m<n} (\boldsymbol{h}_{k,n}^{\mathrm{D}})^{\mathcal{H}} \bar{\boldsymbol{\Phi}}_{k,m}^{\mathrm{dU}} \boldsymbol{h}_{k,n}^{\mathrm{D}} + (\boldsymbol{h}_{k,n}^{\mathrm{XX}})^{\mathrm{T}} \bar{\boldsymbol{s}}_k^{\mathrm{U}}, \tag{5.34b}$$

where $\boldsymbol{\Phi}_{k,m}^{\mathrm{U}}$ (respectively $\boldsymbol{\Phi}_{k,m}^{\mathrm{dU}}$) expresses the sensitivity of user m's weighted bit loading to changes in its (dual) interference-plus-noise covariance matrix $\boldsymbol{\Psi}_{k,m}^{\mathrm{U}}$ ($\boldsymbol{\Psi}_{k,m}^{\mathrm{dU}}$).

$$\boldsymbol{\Phi}_{k,n}^{\mathrm{U}} = \log(2)^{-1} \omega_n^{\mathrm{U}} \frac{s_{k,n}^{\mathrm{U}} (\boldsymbol{\Psi}_{k,n}^{\mathrm{U}})^{-1} \boldsymbol{h}_{k,n}^{\mathrm{U}} (\boldsymbol{h}_{k,n}^{\mathrm{U}})^{\mathcal{H}} (\boldsymbol{\Psi}_{k,n}^{\mathrm{U}})^{-1}}{\Gamma + s_{k,n}^{\mathrm{U}} (\boldsymbol{h}_{k,n}^{\mathrm{U}})^{\mathcal{H}} (\boldsymbol{\Psi}_{k,n}^{\mathrm{U}})^{-1} \boldsymbol{h}_{k,n}^{\mathrm{U}}} \tag{5.35a}$$

$$\boldsymbol{\Phi}_{k,n}^{\mathrm{dU}} = \log(2)^{-1} \omega_n^{\mathrm{D}} \frac{s_{k,n}^{\mathrm{dU}} (\boldsymbol{\Psi}_{k,n}^{\mathrm{dU}})^{-1} \boldsymbol{h}_{k,n}^{\mathrm{D}} (\boldsymbol{h}_{k,n}^{\mathrm{D}})^{\mathcal{H}} (\boldsymbol{\Psi}_{k,n}^{\mathrm{dU}})^{-1}}{\Gamma + s_{k,n}^{\mathrm{dU}} (\boldsymbol{h}_{k,n}^{\mathrm{D}})^{\mathcal{H}} (\boldsymbol{\Psi}_{k,n}^{\mathrm{dU}})^{-1} \boldsymbol{h}_{k,n}^{\mathrm{D}}} \tag{5.35b}$$

When a linear transceiver structure is considered, the summations in (5.34) should be over $\mathcal{N} \setminus \{n\}$ instead of $m < n$.

The resulting surrogate problem is separable across all variables, and can therefore be solved independently for each user. From the KKT conditions of the surrogate problem, a closed form solution for $s_{k,n}^{\mathrm{U}}$ and $s_{k,n}^{\mathrm{dU}}$ is obtained,

Algorithm 8. Approximate evaluation of (5.28) for FDX-DD-DSB

1: **function** DSBSEARCH($\boldsymbol{\lambda}^{\mathrm{U}}$, $\boldsymbol{\lambda}^{\mathrm{D}}$, k)
2: Choose $\bar{\boldsymbol{s}}_k^{\mathrm{U}} \in \mathbb{R}_+^N$, $\bar{\boldsymbol{s}}_k^{\mathrm{dU}} \in \mathbb{R}_+^N$, $\epsilon_\tau \in (0,1)$, set $\tau \leftarrow 1$
3: **while** $\mathcal{L}_k^{\mathrm{U}} + \mathcal{L}_k^{\mathrm{dU}} - (\boldsymbol{s}_k^{\mathrm{U}})^{\mathrm{T}} \mathbf{H}_k^{\mathrm{XX}} \boldsymbol{s}_k^{\mathrm{dU}}$ not converged **do**
4: Calculate $a_{k,n}^{\mathrm{U}}$ and $a_{k,n}^{\mathrm{dU}}$ $\forall n$ using (5.34)
5: Calculate $s_{k,n}^{\mathrm{U}}$ and $s_{k,n}^{\mathrm{dU}}$ $\forall n$ using (5.36)
6: Set $\bar{\boldsymbol{s}}_k^{\mathrm{U}} \leftarrow (1-\tau)\bar{\boldsymbol{s}}_k^{\mathrm{U}} + \tau \boldsymbol{s}_k^{\mathrm{U}}$
7: Set $\bar{\boldsymbol{s}}_k^{\mathrm{dU}} \leftarrow (1-\tau)\bar{\boldsymbol{s}}_k^{\mathrm{dU}} + \tau \boldsymbol{s}_k^{\mathrm{dU}}$
8: Set $\tau \leftarrow \tau(1-\tau\epsilon_\tau)$
9: Calculate $\boldsymbol{R}_k^{\mathrm{U}}$, $\boldsymbol{T}_k^{\mathrm{D}}$ from $\boldsymbol{s}_k^{\mathrm{U}}$, $\boldsymbol{s}_k^{\mathrm{dU}}$ using (5.5), (5.26)
10: Calculate $\boldsymbol{s}_k^{\mathrm{D}}$ by solving (5.23)

given by

$$s_{k,n}^{\mathrm{U}} = \left[\frac{\log(2)^{-1}\omega_n^{\mathrm{U}}}{\lambda_n^{\mathrm{U}} + a_{k,n}^{\mathrm{U}}} - \frac{\Gamma}{(\boldsymbol{h}_{k,m}^{\mathrm{U}})^{\mathcal{H}} (\bar{\boldsymbol{\Psi}}_{k,m}^{\mathrm{U}})^{-1} \boldsymbol{h}_{k,m}^{\mathrm{U}}} \right]^+, \tag{5.36a}$$

$$s_{k,n}^{\mathrm{dU}} = \left[\frac{\log(2)^{-1}\omega_n^{\mathrm{D}}}{\sigma_{k,n}^{\mathrm{D}} + a_{k,n}^{\mathrm{dU}}} - \frac{\Gamma}{(\boldsymbol{h}_{k,m}^{\mathrm{D}})^{\mathcal{H}} (\bar{\boldsymbol{\Psi}}_{k,m}^{\mathrm{dU}})^{-1} \boldsymbol{h}_{k,m}^{\mathrm{D}}} \right]^+, \tag{5.36b}$$

where $[\cdot]^+ \triangleq \max\{\cdot, 0\}$.

The resulting algorithm, referred to as full-duplex dual domain distributed spectrum balancing (FDX-DD-DSB), is obtained from Algorithm 7 by replacing the exhaustive search function by Algorithm 8. The complexity of Algorithm 8 is determined by the calculation of $(\bar{\boldsymbol{\Psi}}_{k,n}^{\mathrm{U}})^{-1}$ and $(\bar{\boldsymbol{\Psi}}_{k,n}^{\mathrm{dU}})^{-1}$ in line 4, where the calculation of a single matrix inverse results in a complexity of $\mathcal{O}(N^3)$. However, by using the Sherman-Morrison identity [148], $(\bar{\boldsymbol{\Psi}}_{k,n}^{\mathrm{U}})^{-1}$ can be obtained from $(\bar{\boldsymbol{\Psi}}_{k,n+1}^{\mathrm{U}})^{-1}$ with a complexity of only $\mathcal{O}(N^2)$. All other calculations in lines 4-8 of Algorithm 8 have a per user complexity of at most $\mathcal{O}(N^2)$. Each iteration of Algorithm 8 therefore has a complexity of $\mathcal{O}(N^3)$. With I_{DSB} the number of iterations required by the DSB algorithm to converge, this results in a total complexity of $\mathcal{O}(I_{\mathrm{SG}} K I_{\mathrm{DSB}} N^3)$ for FDX-DD-DSB.

Algorithm 8 adopts the SJBR step size rule for updating the symbol power variables in lines 6-8. As such, FDX-DD-DSB is a special case of the SJBR algorithm [162], such that it inherits SJBR's convergence properties. SJBR converges to a stationary point of problem (5.30), provided that the following convergence conditions are satisfied [162]:

C.1 each $\mathcal{X}_i$ is closed and convex;

C.2 each f_i is continuously differentiable;

C.3 the gradient of each f_i is Lipschitz continuous;

C.4 $\sum_{i=1}^{i_{\max}} f_i$ is coercive with respect to $\prod_i \mathcal{X}_i$;

C.5 each surrogate $\tilde{f}_i$ is uniformly strongly convex for all $\bar{\mathbf{X}}$.

Convergence conditions **C.1** and **C.2** are trivially satisfied. Moreover, **C.3** follows from $\boldsymbol{\Phi}_{k,n}^{\mathrm{U}}$ and $\boldsymbol{\Phi}_{k,n}^{\mathrm{dU}}$ being continuously differentiable. Finally, assuming $\lambda_n^{\mathrm{U}} > 0$ for all n, **C.4** and **C.5** are satisfied as the set of possible solutions to (5.36a) and (5.36b) is upper bounded by $(\lambda_n^{\mathrm{U}} \log(2))^{-1}\omega_n^{\mathrm{U}}$ and $(\sigma_n^{\mathrm{D}} \log(2))^{-1}\omega_n^{\mathrm{D}}$ [162]. In case $\lambda_n^{\mathrm{U}} = 0$ for any n, **C.4**-**C.5** are possibly not satisfied, and one should resort to Gauss-Seidel iterations with $\epsilon_\tau = 0$. The resulting algorithm is then a special case of the BSUM algorithm, which has more lenient convergence conditions.

In [204, 220], it has been pointed out that the subgradient method, which FDX-DD-DSB uses to update $\boldsymbol{\lambda}^{\mathrm{U}}$ and $\boldsymbol{\lambda}^{\mathrm{D}}$, is not guaranteed to converge when $q(\boldsymbol{\lambda}^{\mathrm{U}}, \boldsymbol{\lambda}^{\mathrm{D}})$ is evaluated only approximately. As Algorithm 8 does not necessarily return the global maximizer of problem (5.28), FDX-DD-DSB is not guaranteed to converge. FDX-DD-DSB has however been observed to converge in every scenario for which it has been executed.

In the derivation of FDX-DD-DSB, it has already been indicated how to adapt Algorithm 8 when a linear transceiver structure is considered. Other versions of FDX-DD-DSB can be obtained by including bit cap or spectral mask constraints. Bit cap constraints are readily enforced by using the following augmented bit loading function $b_{\mathrm{cap}}(\gamma) = \max\{b(\gamma), b_{\max}\}$ or, equivalently, by upper bounding $s_{k,n}^{\mathrm{U}}$ (or $s_{k,n}^{\mathrm{dU}}$) as in [108]. Convergence of the Gauss-Seidel version of FDX-DD-DSB is still guaranteed in this case, be it not to a stationary point. US spectral mask constraints are easily enforced by replacing $[\cdot]^+$ in (5.36a) with $[\cdot]_0^{s_k^{\mathrm{mask}}} = \max\{\min\{\cdot, s_k^{\mathrm{mask}}\}, 0\}$. This constraint enforces **C.4** and **C.5**, guaranteeing that Algorithm 8 converges to a stationary point. DS spectral mask constraints however are tougher to enforce. A possible method has been proposed in [108], consisting of dualizing the DS spectral mask constraints when formulating the Lagrange dual problem. In this case however, the time sharing property cannot be invoked to warrant a zero duality gap leading, in some cases, to problematic convergence behavior. Finally, problem (5.13) can be altered by relaxing the assumption of perfect DPU-side NEXT cancellation. In this case however, as for FDX-OSB, the employed solution strategy cannot be adopted here, as the MAC-BC duality transformation is not able to eliminate $\boldsymbol{s}_k^{\mathrm{D}}$ from the resulting US Lagrangian $\mathcal{L}_k^{\mathrm{U}}$.

5.5.3 FDX primal domain DSB algorithm (FDX-PD-DSB)

A second FDX DSB algorithm is obtained by applying the DSB algorithm to a reformulated version of the original optimization problem (5.13), similar to [102,162]. This reformulation is obtained by introducing DS transmit covariance matrices $\mathbf{Q}_{k,n}^{\mathrm{D}} = s_{k,n}^{\mathrm{D}} \boldsymbol{t}_{k,n}^{\mathrm{D}} (\boldsymbol{t}_{k,n}^{\mathrm{D}})^{\mathcal{H}}$. It is seen that any transmit covariance matrix must be positive semidefinite ($\mathbf{Q}_{k,n}^{\mathrm{D}} \succeq 0$), Hermitian ($(\mathbf{Q}_{k,n}^{\mathrm{D}})^{\mathcal{H}} = \mathbf{Q}_{k,n}^{\mathrm{D}}$), and rank one. Employing $\mathbf{Q}_{k,n}^{\mathrm{D}}$, the SINR for user n can be expressed as

$$\gamma_{k,n}^{\mathrm{D}}(\boldsymbol{s}_k^{\mathrm{U}}, \mathbf{Q}_k^{\mathrm{D}}, \sigma_{k,n}^{\mathrm{D}}) = (\psi_{k,n}^{\mathrm{D}})^{-1} (\boldsymbol{h}_{k,n}^{\mathrm{D}})^{\mathcal{H}} \mathbf{Q}_{k,n}^{\mathrm{D}} \boldsymbol{h}_{k,n}^{\mathrm{D}}, \tag{5.37}$$

with $\psi_{k,n}^{\mathrm{D}} = \sum_{m<n} (\boldsymbol{h}_{k,n}^{\mathrm{D}})^{\mathcal{H}} \mathbf{Q}_{k,m}^{\mathrm{D}} \boldsymbol{h}_{k,n}^{\mathrm{D}} + (\boldsymbol{h}_{k,n}^{\mathrm{XX}})^{\mathcal{H}} \boldsymbol{s}_k^{\mathrm{U}} + \sigma_{k,n}^{\mathrm{D}}$ the received interference-plus-noise power, and with $\mathbf{Q}_k^{\mathrm{D}} = [(\mathbf{Q}_{k,1}^{\mathrm{D}})^{\mathrm{T}}, \ldots, (\mathbf{Q}_{k,N}^{\mathrm{D}})^{\mathrm{T}}]^{\mathrm{T}}$. Moreover, the total DS transmit power for line n is given by

$$P_n^{\mathrm{D}} = \sum_k \sum_m \left[\mathbf{Q}_{k,m}^{\mathrm{D}}\right]_{nn}. \tag{5.38}$$

Using (5.37) and (5.38), $\boldsymbol{t}_{k,n}^{\mathrm{D}}$ and $s_{k,n}^{\mathrm{D}}$ can be fully eliminated from (5.13) which then becomes a function of $\mathbf{Q}_{k,n}^{\mathrm{D}}$ instead. It is noted that, even though the reformulated optimization problem will not explicitly assert that $\mathbf{Q}_{k,n}^{\mathrm{D}}$ should be rank one, any $\mathbf{Q}_{k,n}^{\mathrm{D}}$ yielded by FDX-PD-DSB does indeed satisfy this condition (see Appendix B, proof Lemma B.1). When a linear transceiver structure is considered, the summation in the definition of $\psi_{k,n}^{\mathrm{D}}$ should be over $\mathcal{N} \setminus \{n\}$ instead of $m < n$.

In the reformulated optimization problem, two different types of functions f_i are identified.

$$f_n^{\mathrm{U}}(\boldsymbol{s}_1^{\mathrm{U}}, \ldots, \boldsymbol{s}_K^{\mathrm{U}}) = \omega_n^{\mathrm{U}} \sum_k b\big(\gamma_{k,n}^{\mathrm{U}}(\boldsymbol{s}_k^{\mathrm{U}}, \boldsymbol{\Sigma}_k^{\mathrm{U}})\big) \tag{5.39a}$$

$$f_n^{\mathrm{D}}(\boldsymbol{s}_1^{\mathrm{U}}, \mathbf{Q}_1^{\mathrm{D}}, \ldots, \boldsymbol{s}_K^{\mathrm{U}}, \mathbf{Q}_K^{\mathrm{D}}) = \omega_n^{\mathrm{D}} \sum_k b\big(\gamma_{k,n}^{\mathrm{D}}(\boldsymbol{s}_k^{\mathrm{U}}, \mathbf{Q}_k^{\mathrm{D}}, \sigma_{k,n}^{\mathrm{D}})\big) \tag{5.39b}$$

The coordinate block associated with f_n^{U} is $[s_{1,n}^{\mathrm{U}}, \ldots, s_{K,n}^{\mathrm{U}}]^{\mathrm{T}}$, and the one associated with f_n^{D} is $[(\mathbf{Q}_{1,n}^{\mathrm{D}})^{\mathrm{T}}, \ldots, (\mathbf{Q}_{K,n}^{\mathrm{D}})^{\mathrm{T}}]^{\mathrm{T}}$. For ease of notation, also define $f_{k,n}^{\mathrm{U}}(\boldsymbol{s}_k^{\mathrm{U}}) = \omega_n^{\mathrm{U}} b\big(\gamma_{k,n}^{\mathrm{U}}(\boldsymbol{s}_k^{\mathrm{U}}, \boldsymbol{\Sigma}_k^{\mathrm{U}})\big)$ and $f_{k,n}^{\mathrm{D}}(\boldsymbol{s}_k^{\mathrm{U}}, \mathbf{Q}_k^{\mathrm{D}}) = \omega_n^{\mathrm{D}} b\big(\gamma_{k,n}^{\mathrm{D}}(\boldsymbol{s}_k^{\mathrm{U}}, \mathbf{Q}_k^{\mathrm{D}}, \sigma_{k,n}^{\mathrm{D}})\big)$, as well as the corresponding surrogate functions $\tilde{f}_{k,n}^{\mathrm{U}}(s_{k,n}^{\mathrm{U}}; \bar{\boldsymbol{s}}_{k,n}^{\mathrm{U}}, \bar{\mathbf{Q}}_k^{\mathrm{D}})$ and $\tilde{f}_{k,n}^{\mathrm{D}}(\mathbf{Q}_{k,n}^{\mathrm{D}}; \bar{\boldsymbol{s}}_{k,n}^{\mathrm{D}}, \bar{\mathbf{Q}}_k^{\mathrm{D}})$. From [102] it is known that functions f_n^{U} and f_n^{D} are concave in their associated coordinate blocks, and convex in the other coordinate blocks. The gradients in the resulting surrogate functions are given by

$(\boldsymbol{a}_n^{\mathrm{U}})^{\mathrm{T}} = [a_{1,n}^{\mathrm{U}}, \ldots, a_{K,n}^{\mathrm{U}}]$ and $(\mathbf{A}_n^{\mathrm{D}})^{\mathrm{T}} = [(\mathbf{A}_{1,n}^{\mathrm{D}})^{\mathrm{T}}, \ldots, (\mathbf{A}_{K,n}^{\mathrm{D}})^{\mathrm{T}}]$ with

$$a_{k,n}^{\mathrm{U}} = \sum_{m<n} (\boldsymbol{h}_{k,n}^{\mathrm{U}})^{\mathcal{H}} \boldsymbol{\Phi}_{k,m}^{\mathrm{U}} \boldsymbol{h}_{k,n}^{\mathrm{U}} + \sum_{m} \phi_{k,m}^{\mathrm{D}} (h_k^{mn})^{\mathrm{XX}} \tag{5.40a}$$

$$\mathbf{A}_{k,n}^{\mathrm{D}} = \sum_{m>n} \phi_{k,m}^{\mathrm{D}} \boldsymbol{h}_{k,m}^{\mathrm{D}} (\boldsymbol{h}_{k,m}^{\mathrm{D}})^{\mathcal{H}}, \tag{5.40b}$$

where $\boldsymbol{\Phi}_{k,m}^{\mathrm{U}}$ is defined as in (5.35a), and where $\phi_{k,m}^{\mathrm{D}}$ expresses the sensitivity of the weighted bit loading for user m to changes in its interference-plus-noise power $\psi_{k,m}^{\mathrm{D}}$.

$$\phi_{k,n}^{\mathrm{D}} = \log(2)^{-1} \omega_n^{\mathrm{D}} \frac{(\boldsymbol{h}_{k,n}^{\mathrm{D}})^{\mathcal{H}} \bar{\mathbf{Q}}_{k,n}^{\mathrm{D}} \boldsymbol{h}_{k,n}^{\mathrm{D}}}{\bar{\psi}_{k,n}^{\mathrm{D}} (\Gamma \bar{\psi}_{k,n}^{\mathrm{D}} + (\boldsymbol{h}_{k,n}^{\mathrm{D}})^{\mathcal{H}} \bar{\mathbf{Q}}_{k,n}^{\mathrm{D}} \boldsymbol{h}_{k,n}^{\mathrm{D}})} \tag{5.41}$$

When a linear transceiver structure is considered, the summations in (5.40) should be over $\mathcal{N} \setminus \{n\}$, instead of $m < n$ or $m > n$.

When functions f_i are identified as in (5.39), the WSR maximization problem (5.13) does not fit the DSB problem structure from (5.30) due to the feasible space of the DS transmit covariance matrices being non-separable. As a result, the convergence results from [56, 154, 162] no longer apply. Nevertheless, convergence results for the non-separable case have recently become available [55, 161] and, more importantly, the DSB algorithm still leads to a simple solution strategy.

Despite the surrogate problem being non-separable across DS users, it is still separable across US users, i.e. the surrogate problem can be independently solved for each US user. Moreover, the per user US surrogate problems can be further decoupled over tones by dual decomposition. The resulting US Lagrange dual problem

$$\underset{\lambda_n^{\mathrm{U}} \in \mathbb{R}_+}{\text{minimize}} \; q_n^{\mathrm{U}}(\lambda_n^{\mathrm{U}}) \tag{5.42}$$

is one-dimensional and convex, such that a simple bisection search algorithm can be used. As the US surrogate problem is convex and a primal feasible point exists, the duality gap between the surrogate problem and (5.42) is zero [20, Section 5.2.3], removing the necessity of invoking the time sharing property to have a zero duality gap. The Lagrange dual function is defined as

$$q_n^{\mathrm{U}}(\lambda_n^{\mathrm{U}}) = \sum_k \max_{s_{k,n}^{\mathrm{U}}} \left\{ \tilde{f}_{k,n}^{\mathrm{U}}(s_{k,n}^{\mathrm{U}}; \bar{\boldsymbol{s}}_k^{\mathrm{U}}, \bar{\mathbf{Q}}_k^{\mathrm{D}}) - \lambda_n^{\mathrm{U}} s_{k,n}^{\mathrm{U}} \right\} + \sum_n \lambda_n^{\mathrm{U}} P_{\mathrm{tot}}^{\mathrm{U}}, \tag{5.43}$$

The optimal $s_{k,n}^{\mathrm{U}}$ is given by (5.36a) with $a_{k,n}^{\mathrm{U}}$ calculated as in (5.40a) instead of (5.34a) [193]. As the duality gap is zero, the solution to the US surrogate

problem is given by the unique maximizer in (5.43) for the optimal $\boldsymbol{\lambda}^{\mathrm{U}}$ from (5.42) [20, Section 5.5.5].

The surrogate problem is non-separable across DS users. However, the Lagrange dual decomposition decouples the problem not only across tones, but also across users. The DS Lagrange dual problem is given by

$$\underset{\boldsymbol{\lambda}^{\mathrm{D}} \in \mathbb{R}_{+}^{N}}{\text{minimize}} \; q^{\mathrm{D}}(\boldsymbol{\lambda}^{\mathrm{D}}), \tag{5.44}$$

where the Lagrange dual function $q^{\mathrm{D}}(\boldsymbol{\lambda}^{\mathrm{D}})$ is defined as

$$\sum_{k} \sum_{n} \max_{\substack{\mathbf{Q}_{k,n}^{\mathrm{D}} \succeq 0 \\ \text{Hermitian}}} \left\{ \tilde{f}_{k,n}^{\mathrm{D}}(\mathbf{Q}_{k,n}^{\mathrm{D}}; \bar{\boldsymbol{s}}_{k}^{\mathrm{D}}, \bar{\mathbf{Q}}_{k}^{\mathrm{D}}) - \mathrm{tr}(\boldsymbol{\Lambda}^{\mathrm{D}} \mathbf{Q}_{k,n}^{\mathrm{D}}) \right\} + \mathbf{1}_{N \times 1}^{\mathrm{T}} \boldsymbol{\lambda}^{\mathrm{D}} P_{\mathrm{tot}}^{\mathrm{D}}. \tag{5.45}$$

As before, a closed form expression for the per tone per user maximizer in (5.45) is available [102], i.e.

$$\boldsymbol{t}_{k,n}^{\mathrm{D}} = (\mathbf{A}_{k,n}^{\mathrm{D}} + \boldsymbol{\Lambda}^{\mathrm{D}})^{-1} \boldsymbol{h}_{k,n}^{\mathrm{D}} \tag{5.46a}$$

$$s_{k,n}^{\mathrm{D}} = \left[\frac{\omega_{n}^{\mathrm{D}} \log(2)^{-1} - \Gamma \bar{\psi}_{k,n}^{\mathrm{D}} ((\boldsymbol{h}_{k,n}^{\mathrm{D}})^{\mathrm{H}} \boldsymbol{t}_{k,n}^{\mathrm{D}})^{-1}}{(\boldsymbol{h}_{k,n}^{\mathrm{D}})^{\mathrm{H}} \boldsymbol{t}_{k,n}^{\mathrm{D}}} \right]^{+} \tag{5.46b}$$

$$\mathbf{Q}_{k,n}^{\mathrm{D}} = s_{k,n}^{\mathrm{D}} \boldsymbol{t}_{k,n}^{\mathrm{D}} (\boldsymbol{t}_{k,n}^{\mathrm{D}})^{\mathrm{H}}. \tag{5.46c}$$

What remains is to solve the dual problem (5.44). As before, one possibility is to use a subgradient scheme. The dual function $q^{\mathrm{D}}(\boldsymbol{\lambda}^{\mathrm{D}})$ is however not only convex, but also continuously differentiable on its domain (see Appendix B, Proposition B.2). More efficient gradient descent schemes can therefore be employed, constituting a vast improvement over the subgradient method.

The DS dual problem can be further simplified by removing the positivity constraint on $\boldsymbol{\lambda}^{\mathrm{D}}$, which is justified by observing that any solution of the DS surrogate problem must satisfy the total power constraints with equality. Indeed, for any DS resource allocation with $P_{n}^{\mathrm{D}} < P_{\mathrm{tot}}^{\mathrm{D}}$, the objective function value of the surrogate problem can be increased by adding $\xi \boldsymbol{e}_{n} \boldsymbol{e}_{n}^{\mathrm{H}}$ to $\mathbf{Q}_{k,N}^{\mathrm{D}}$, with $\xi > 0$ and $\boldsymbol{e}_{n}$ the n-th vector in the standard basis of $\mathbb{R}^{N}$.[5] The inequality constraints in the DS surrogate problem can thus be replaced with equality constraints, resulting in an unconstrained dual problem. As such, methods for unconstrained optimization can be used. We opt for a simple gradient descent algorithm with

[5] This argument assumes $(h_{k}^{nN})^{\mathrm{D}} \neq 0$. If there does not exist any tone k for which this is true, the same argument can be repeated for user $N-1$, as $(h_{k}^{nN})^{\mathrm{D}} = 0$ and (5.40b) imply $\boldsymbol{e}_{n} \in \mathrm{null}(\mathbf{A}_{k,N-1}^{\mathrm{D}})$.

Algorithm 9. FDX-PD-DSB

1: Choose $\bar{\boldsymbol{s}}_k^{\mathrm{U}} \in \mathbb{R}_+^N$, $\bar{\boldsymbol{s}}_k^{\mathrm{D}} \in \mathbb{R}_+^N$, and set $\bar{\boldsymbol{T}}_k^{\mathrm{D}} \leftarrow (\mathbf{H}_k^{\mathrm{D}})^{-\mathrm{H}}\ \forall k$
2: Set $\bar{\mathbf{Q}}_{k,n}^{\mathrm{D}} \leftarrow \bar{s}_{k,n}^{\mathrm{D}} \bar{\boldsymbol{t}}_{k,n}^{\mathrm{D}} (\bar{\boldsymbol{t}}_{k,n}^{\mathrm{D}})^{\mathrm{H}}\ \forall k, n$
3: Choose $\epsilon_\tau \in (0,1)$, and set $\tau^+ \leftarrow 1$, $\tau^- \leftarrow 1 - \tau^+$
4: **while** $\sum_n \omega_n^{\mathrm{U}} R_n^{\mathrm{U}} + \sum_n \omega_n^{\mathrm{D}} R_n^{\mathrm{D}}$ not converged **do**
5: Calculate $a_{k,n}^{\mathrm{U}}$ and $\mathbf{A}_{k,n}^{\mathrm{D}}\ \forall k, n$ using (5.40)
6: $\boldsymbol{s}_n^{\mathrm{U}} \leftarrow \mathrm{mUS}(\boldsymbol{a}_n^{\mathrm{U}}, \bar{\boldsymbol{\Psi}}_n^{\mathrm{U}})\ \forall n$
7: $\{\mathbf{Q}_1^{\mathrm{D}}, \ldots, \mathbf{Q}_N^{\mathrm{D}}\} \leftarrow \mathrm{mDS}(\mathbf{A}_1^{\mathrm{D}}, \ldots, \mathbf{A}_N^{\mathrm{D}}, \bar{\boldsymbol{\psi}}_1^{\mathrm{D}}, \ldots, \bar{\boldsymbol{\psi}}_N^{\mathrm{D}})$
8: Decompose $\mathbf{Q}_{k,n}^{\mathrm{D}}$ into $s_{k,n}^{\mathrm{D}}$ and $\boldsymbol{t}_{k,n}^{\mathrm{D}}\ \forall k, n$
9: Set $\bar{\boldsymbol{s}}_n^{\mathrm{U}} \leftarrow \tau^- \bar{\boldsymbol{s}}_n^{\mathrm{U}} + \tau^+ \boldsymbol{s}_n^{\mathrm{U}}$, $\bar{\boldsymbol{s}}_n^{\mathrm{D}} \leftarrow \tau^- \bar{\boldsymbol{s}}_n^{\mathrm{D}} + \tau^+ \boldsymbol{s}_n^{\mathrm{D}}\ \forall n$
10: Set $\bar{\boldsymbol{t}}_{k,n}^{\mathrm{D}} \leftarrow \tau^- \bar{\boldsymbol{t}}_{k,n}^{\mathrm{D}} + \tau^+ \boldsymbol{t}_{k,n}^{\mathrm{D}}\ \forall k, n$
11: Set $\tau^+ \leftarrow \tau^+(1 - \tau^+ \epsilon_\tau)$, $\tau^- \leftarrow 1 - \tau^+$
12: **function** $\mathrm{mUS}(\boldsymbol{a}_n^{\mathrm{U}}, \bar{\boldsymbol{\Psi}}_n^{\mathrm{U}})$
13: Choose search interval $[\lambda_{\min}^{\mathrm{U}}, \lambda_{\max}^{\mathrm{U}}] \subset \mathbb{R}_+$
14: **while** $|\sum_k s_{k,n}^{\mathrm{U}} - P_{\mathrm{tot}}^{\mathrm{U}}| > \delta_{\mathrm{P}}$ & $\lambda_n^{\mathrm{U}} > \delta_\lambda$ **do**
15: Set $\lambda^{\mathrm{U}} \leftarrow (\lambda_{\min}^{\mathrm{U}} + \lambda_{\max}^{\mathrm{U}})/2$
16: Calculate $s_{k,n}^{\mathrm{U}}\ \forall k$ for λ^{U} using (5.36a)
17: **if** $P_n^{\mathrm{U}} > P_{\mathrm{tot}}^{\mathrm{U}}$ **then** $\lambda_{\min}^{\mathrm{U}} \leftarrow \lambda^{\mathrm{U}}$ **else** $\lambda_{\max}^{\mathrm{U}} \leftarrow \lambda^{\mathrm{U}}$
18: **function** $\mathrm{mDS}(\mathbf{A}_1^{\mathrm{D}}, \ldots, \mathbf{A}_N^{\mathrm{D}}, \bar{\boldsymbol{\psi}}_1^{\mathrm{D}}, \ldots, \bar{\boldsymbol{\psi}}_N^{\mathrm{D}})$
19: Choose $[\boldsymbol{g}_{\mathrm{prev}}]_n > \delta_{\mathrm{P}}\ \forall n$, $\boldsymbol{\lambda}^{\mathrm{D}} \in \mathbb{R}_+^N$, $\mu_{\max} \gg 0$
20: Set $q_{\mathrm{prev}} \leftarrow q^{\mathrm{D}}(\boldsymbol{\lambda}^{\mathrm{D}})$ using (5.45), $\mathbf{Q}_{k,n}^{\mathrm{D}}\ \forall k, n$ from (5.46)
21: **while** $|[\boldsymbol{g}_{\mathrm{prev}}]_n| > \delta_{\mathrm{P}}$ for any n **do**
22: Set $\boldsymbol{g}_{\mathrm{prev}} \leftarrow P_{\mathrm{tot}}^{\mathrm{D}} \mathbf{1}_N - \sum_k \sum_n \mathrm{diag}\{\mathbf{Q}_{k,n}^{\mathrm{D}}\}$
23: Set $\mu^{\mathrm{D}} \leftarrow \mu_{\max}$, $q_{\mathrm{new}} \leftarrow q_{\mathrm{prev}}$
24: **while** $q_{\mathrm{new}} > q_{\mathrm{prev}} - \mu_{\mathrm{Armijo}} \mu^{\mathrm{D}} |\boldsymbol{g}_{\mathrm{prev}}|^2$ **do**
25: Set $\mu^{\mathrm{D}} \leftarrow \mu^{\mathrm{D}}/2$ and $\Delta\boldsymbol{\lambda}^{\mathrm{D}} \leftarrow -\mu^{\mathrm{D}} \boldsymbol{g}_{\mathrm{prev}}$
26: Set $q_{\mathrm{new}} \leftarrow q^{\mathrm{D}}(\boldsymbol{\lambda}^{\mathrm{D}} + \Delta\boldsymbol{\lambda}^{\mathrm{D}})$ using (5.45), $\mathbf{Q}_{k,n}^{\mathrm{D}}\ \forall k, n$ from (5.46)
27: Set $q_{\mathrm{prev}} \leftarrow q_{\mathrm{new}}$, $\boldsymbol{\lambda}^{\mathrm{D}} \leftarrow \boldsymbol{\lambda}^{\mathrm{D}} + \Delta\boldsymbol{\lambda}^{\mathrm{D}}$

Armijo backtracking, which, assuming the starting point $\boldsymbol{\lambda}^{\mathrm{D}}$ is dual feasible and given the fact that $q(\boldsymbol{\lambda}^{\mathrm{D}})$ is continuously differentiable on its domain, is guaranteed to converge to the global optimum of (5.44) [24].

The resulting algorithm, referred to as full-duplex primal domain distributed spectrum balancing (FDX-PD-DSB), is summarized in Algorithm 9. The complexity of Algorithm 9 is determined by the calculation of $\mathbf{Q}_{k,n}^{\mathrm{D}}\ \forall k, n$ in line 26, which involves determining a matrix inverse (5.46a) resulting in a complexity of $\mathcal{O}(N^3)$ for each $\mathbf{Q}_{k,n}^{\mathrm{D}}$. However, by using the Sherman-Morrison identity [148], $(\mathbf{A}_{k,n-1}^{\mathrm{D}} + \boldsymbol{\Lambda}^{\mathrm{D}})^{-1}$ can be obtained from $(\mathbf{A}_{k,n}^{\mathrm{D}} + \boldsymbol{\Lambda}^{\mathrm{D}})^{-1}$ with a complexity of

only $\mathcal{O}(N^2)$. All other calculations involved in line 26 have a per user per tone complexity of at most $\mathcal{O}(N^2)$. Each iteration of line 26 therefore results in a complexity of $\mathcal{O}(KN^3)$. With I_{DSB} the number of iterations required by the DSB algorithm to converge and I_{GD} the number of iterations required by the gradient descent algorithm to converge, the resulting total complexity of FDX-PD-DSB is $\mathcal{O}(I_{\text{DSB}}I_{\text{GD}}KN^3)$.

In order to establish convergence guarantees for the algorithms of [55, 161], assumptions are made that are similar to **C.1**-**C.5**. The surrogates of FDX-PD-DSB do however not satisfy **C.5**, such that the results in [55, 161] do not warrant convergence of the primal variables $s_{k,n}^{\text{U}}$ and $\mathbf{Q}_{k,n}^{\text{D}}$.[6] All simulations have however shown monotonically increasing WSR values that converge after only a few iterations.

In the derivation of FDX-PD-DSB, it has already been indicated how to adapt Algorithm 9 when a linear transceiver structure is considered. Other versions of FDX-PD-DSB can be obtained by including bit cap or spectral mask constraints. Bit cap constraints are readily enforced by using the augmented bit loading function of Section 5.5.2. Spectral mask constraints can be enforced as for FDX-DD-DSB, i.e. by replacing $[\cdot]^+$ in (5.36a) with $[\cdot]_0^{s_k^{\text{mask}}}$ in US, and by dualizing the spectral mask constraints in DS. It is noted that, due to the convexity of the surrogate problems, the duality gap for DS will still be zero, such that dualizing the DS spectral mask constraints will not lead to problematic convergence behavior. Finally, problem (5.13) can be altered by relaxing the assumption of perfect DPU-side NEXT cancellation. One can readily adapt FDX-PD-DSB to networks with imperfect DPU-side NEXT cancellation by adding a term to (5.40b) modeling the DPU-side NEXT influence. As such, FDX-PD-DSB can be applied to the resource allocation problems of wireless FDX systems [48, 82, 83, 114, 143] as well. It is noted that this is in contrast with FDX-OSB and FDX-DD-DSB, which were both founded on the MAC-BC duality theory from Section 5.4 that required perfect DPU-side NEXT cancellation.

Another important property of FDX-PD-DSB is that after each outer iteration, a new feasible resource allocation is provided. Therefore, FDX-PD-DSB is a so-called real-time DSM algorithm, as defined in [190]. Moreover, from FDX-PD-DSB, other low complexity real-time DSM algorithms for FDX DSL networks can be derived. For example, an iterative waterfilling (IWF) type algorithm [221] can be obtained by setting $a_{k,n}^{\text{U}}$ and $\mathbf{A}_{k,n}^{\text{D}}$ to 0. Moreover, constant offset autonomous spectrum balancing (CO-ASB) type algorithms [30, 84] can be obtained by setting $a_{k,n}^{\text{U}}$ and $\mathbf{A}_{k,n}^{\text{D}}$ to a predetermined constant value.

[6] Even though strong convexity cannot be established, the results in Appendix B do imply that the surrogate problems have unique solution.

Finally, an important difference between the proposed SCA method, and the state-of-the-art (SoA) SCA methods in [82, 83, 143] is highlighted. Assuming the multi-carrier extensions of the SCA algorithms in [82, 83, 143] also entail solving the Lagrange dual of their respective surrogate problems, the SoA SCA methods rely on iterative solvers to deal with the evaluation of their respective Lagrange dual functions. This is in stark contrast with the evaluation the Lagrange dual function in FDX-PD-DSB, which can be done analytically and has a computational complexity that is mainly determined by a single matrix inversion in (5.46a).

5.6 Simulation results

In this section, the performance of the proposed DSM algorithms, as well as that of FDX transmission itself, is analyzed for the two DSL networks illustrated in Figure 5.2. Each network consists of a fiber-to-the-building (FTTB) scenario with $N = 10$. Such FTTB scenarios are considered to be the main use case for G.mgfast. The channel matrices for these scenarios are modeled based on lab measurements. The main difference between the considered scenarios is the separation length, i.e. the length of the copper line separating two NTs (e.g. the separation length of user 1 and user 2 in Figure 5.2a is 10 m). Due to the larger separation length in scenario (a), the NEXT signals travel a longer distance before the copper lines meet, such that more attenuation has taken place when interference sets in.

As ITU-T recommendations for G.mgfast are not yet publicly available, the employed system model parameters are chosen conform G.fast recommendations [95, 96]. The maximum total per line power is $P_{\text{tot}}^{\text{U}} = P_{\text{tot}}^{\text{D}} = 4\,\text{dBm}$, and spectral mask constraints range from $-65\,\text{dBm/Hz}$ to $-79\,\text{dBm/Hz}$. The tone spacing, symbol rate, and SNR-gap are $\Delta_f = 51.75\,\text{kHz}$, $f_{\text{s}} = 48\,\text{kHz}$, and $\Gamma = 10\,\text{dB}$. A bit cap of $b_{\max} = 15$ is assumed. The number of tones is $K = 4096$, corresponding to a bandwidth of up to 212 MHz. In addition to perfect DPU-side echo cancellation, perfect per user NT-side echo cancellation is assumed.

5.6.1 DSB optimality gap

The performance differences between the OSB and DSB algorithms are analyzed for a network consisting of the first three users of Figure 5.2b. All weights are chosen as $\omega_n^{\text{U}} = \omega_n^{\text{D}} = 1$, and no bit cap or spectral mask constraints are taken into account. Moreover, a linear transceiver structure is considered, which in

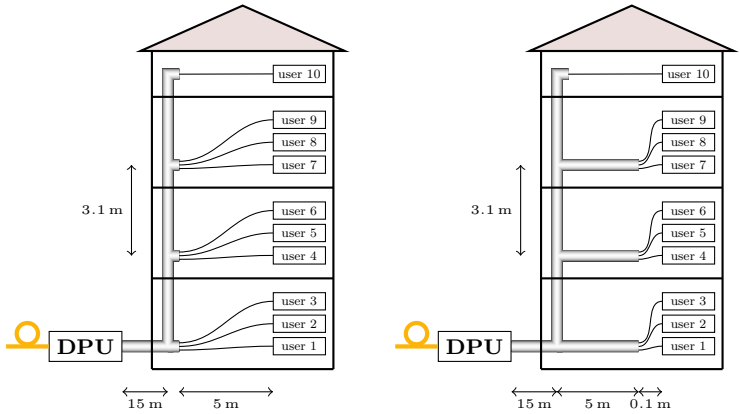


Figure 5.2: A DSL network in a 10-user fiber-to-the-building scenario, which is considered to be the main use case for G.mgfast.

simulations is often seen to result in the existence of multiple stationary points in the objective function. A system with a linear transceiver structure is therefore more adversarial for the DSB algorithms then one using a non-linear transceiver structure, and hence will highlight the performance difference between the OSB and DSB algorithms.

Executing FDX-OSB for a 3-user FDX DSL network is no easy feat. To achieve convergence in an acceptable amount of time, the dual function (5.15) is evaluated using 7 parallel computational threads, each employing GPU acceleration to evaluate line 15 of Algorithm 7. Using this setup, a single evaluation of the dual function (5.15) takes about 3 min.

The bit loading resulting from FDX-OSB, FDX-DD-DSB, and FDX-PD-DSB are shown in Figure 5.3, and the achieved per user data rates are given in Table 5.1. Both Figure 5.3 and Table 5.1 demonstrate that the solutions found by the DSB algorithms are very similar to the solution found by the OSB algorithm. The WSR obtained from the DSB algorithms is even slightly higher than the WSR obtained from the OSB algorithm. This is explained by the discrete grid search of FDX-OSB, which, due to its finite granularity, can result in a slightly suboptimal solution when compared to the DSB algorithms.

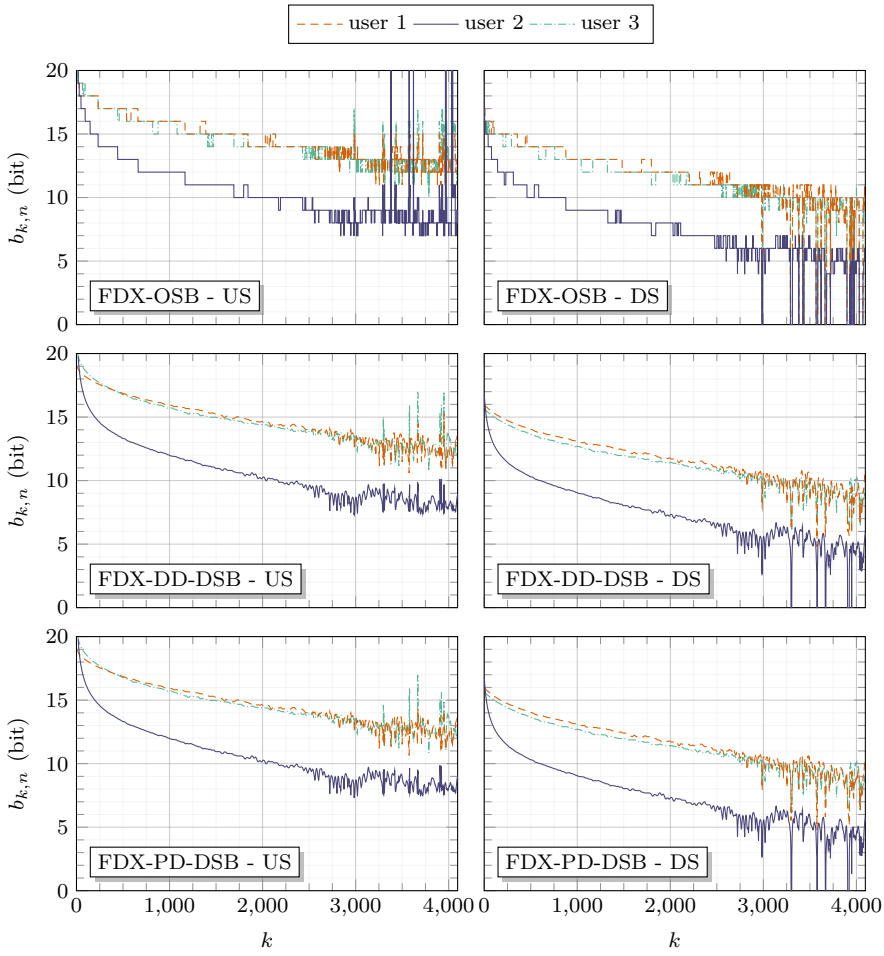


Figure 5.3: Illustration of the optimality of DSB algorithms. It is seen that the solution obtained by DSB algorithms closely resembles the one obtained by the OSB algorithm.

5.6.2 Convergence of the DSB algorithms

The convergence of the proposed DSB algorithms is analyzed for the 10-user FTTB network of Figure 5.2a. Spectral mask and bit cap constraints are considered to be inactive. For various DS weights (with $\omega_n^{\mathrm{U}} = 1 - \omega_n^{\mathrm{D}}$), the total number of iterations I and the final WSR value are shown in Figure 5.4. For FDX-PD-DSB, I equals the number of outer DSB updates times the number

Table 5.1: Data rate and WSR for a three user FDX DSL network (Gbit/s).

	FDX-OSB		
	user 1	user 2	user 3
US	2.87	2.08	2.85
DS	2.27	1.49	2.21
WSR	13.78		

	FDX-DD-DSB			FDX-PD-DSB		
	user 1	user 2	user 3	user 1	user 2	user 3
US	2.89	2.09	2.87	2.89	2.09	2.88
DS	2.30	1.47	2.24	2.29	1.47	2.23
WSR	13.78			13.86		

of gradient updates, i.e. $I = I_{\mathrm{DSB}} I_{\mathrm{GD}}$, while for FDX-DD-DSB it equals the number of subgradient updates times the average number of inner DSB iterations i.e. $I = I_{\mathrm{SG}} I_{\mathrm{DSB}}$. In the stop criteria of the Lagrange multiplier searches, the power constraints should be satisfied with an accuracy of $\delta_{\mathrm{P}} = 10^{-3} P_{\mathrm{tot}}^{\mathrm{U}} = 10^{-3} P_{\mathrm{tot}}^{\mathrm{D}}$. Moreover, the DSB algorithms are stopped when the relative objective function increase between two consecutive iterations drops below 10^{-3}. FDX-PD-DSB is initialized with non-linear QRD-based zero-forcing precoder matrices and a flat spectrum satisfying all power constraints, and FDX-DD-DSB is initialized by setting all symbol powers equal to zero.

The total number of iterations and final WSR values are given in Figure 5.4. For each DSB algorithm, three modes of operation are considered, which differ in the way the DSB algorithm updates its coordinate blocks in each iteration. The following update rules are considered.

- Data points labeled $\mathrm{DD}_{\mathrm{Jacobi}}$ and $\mathrm{PD}_{\mathrm{Jacobi}}$ are obtained by executing FDX-DD-DSB and FDX-PD-DSB with full Jacobi-style updates, as described in Algorithm 8 and Algorithm 9, with $\epsilon_\tau = 0$.
- Data points labeled $\mathrm{DD}_{\text{part. Jacobi}}$ and $\mathrm{PD}_{\text{part. Jacobi}}$ are obtained by letting FDX-DD-DSB and FDX-PD-DSB alternate between updating all US and all DS variables, with $\epsilon_\tau = 0$.
- Data points labeled $\mathrm{DD}_{\mathrm{GS}}$ are obtained by updating the power variable of only a single user after each iteration of the DSB algorithm, with $\epsilon_\tau = 0$.

- Data points labeled $\text{PD}_{\epsilon_\tau = .1}$ are obtained by executing FDX-PD-DSB with full Jacobi-style updates, as described in Algorithm 9, with $\epsilon_\tau = 0.1$.

In Figure 5.4, a single iteration of the DSB algorithm, as counted in I, consists of updating the resource allocation variables of all users exactly once.

Figure 5.4 shows that the final WSR obtained from FDX-DD-DSB and FDX-PD-DSB are very similar. The number of iterations required for convergence can however differ quite significantly. It should however be noted that, even though the per iteration complexity of the different algorithms is the same[7], I is not a perfect indicator for the actual number of additions and multiplications that are executed by each algorithm. Indeed, in practical implementations, the execution time of FDX-PD-DSB is often seen to be in the order of tens of seconds, while executing FDX-DD-DSB usually requires several minutes.

It is seen that for $\omega^{\text{D}} > 0.5$, FDX-PD-DSB requires more iterations to converge than for $\omega^{\text{D}} < 0.5$. In these cases, it takes more iterations of the DSB algorithm to make the resource allocation converge on some of the tones. However, as each DSB iteration in FDX-PD-DSB updates all resource allocation variables, this increased number of DSB iterations has a significant impact on the execution time. By contrast, each DSB iteration in FDX-DD-DSB updates only the resource allocation of a single tone, such that slower convergence on some of the tones does not significantly affect the execution time of the entire algorithm.

Additional simulations have shown that FDX-PD-DSB on average requires far fewer iterations to solve a single dual problem than FDX-DD-DSB due to the employed gradient descent algorithm. Moreover, an advantage of the gradient descent algorithm with backtracking is that it requires no parameter tuning. Indeed, convergence of the subgradient method is quite sensitive to its parameters, especially to the choice of the step size μ, and finding good values for them requires some experience.

The convergence of FDX-PD-DSB is also compared to that of the WMMSE algorithm. For this purpose, the WMMSE algorithm from [114] is adapted such that it can be applied to multi-carrier systems by using techniques from [135]. As the system model in [114] includes neither an SNR-gap nor non-linear transceivers, simulations will be executed for $\Gamma = 0\,\text{dB}$ and linear transceiver structures. The complexity of WMMSE is dominated by solving the Lagrange dual problem of the downstream precoding matrix optimization, where the most expensive operation in each iteration is a matrix inversion. As such, an outer iteration of WMMSE has the same asymptotic complexity as an outer iteration of FDX-PD-DSB.

[7] This is not true for FDX-DD-DSB with Gauss Seidel updating, which has a per iteration complexity of $\mathcal{O}(N^4)$.

The convergence experiments are performed for the 10-user FTTB network of Figure 5.2a. FDX-PD-DSB is executed with $\epsilon_\tau = 0.01$. Both FDX-PD-DSB and WMMSE are initialized with linear ZF precoders and with the same randomly generated transmit powers. For various DS weights (with $\omega_n^{\mathrm{U}} = 1 - \omega_n^{\mathrm{D}}$), the obtained normalized[8] WSR values are given in the left plot of Figure 5.5. It is observed that FDX-PD-DSB has converged after 50 iterations, whereas WMMSE has not yet converged after 200 iterations. Moreover, a significant performance gap between the two algorithms is observed, especially for larger values of ω_n^{D}: after 200 iterations, FDX-PD-DSB outperforms WMMSE by 2% to 30%. These observations can be explained by the high SINR values at the optimum, a condition under which WMMSE is seen to suffer from a very slow convergence. When the SINR values are artificially decreased by raising the noise floor from $-140\,\mathrm{dBm/Hz}$ to $-110\,\mathrm{dBm/Hz}$, as has been done to obtain convergence results in the right plot of Figure 5.5, WMMSE is observed to converge faster. However, also in this setting that is more favorable for WMMSE, FDX-PD-DSB requires far fewer iterations to obtain a high WSR.

5.6.3 Performance of MU FDX DSL networks

Finally, this section evaluates the FDX performance of DSL networks in the scenarios of Figure 5.2. Both spectral mask and bit cap constraints are considered to be active. Figure 5.6 shows the obtained results, consisting of the average achievable US and DS rates of FDX transmission, relative to the maximum achievable TDD rates.

The simulation reveals significant performance gains of FDX transmission over standard TDD transmission. In the 10-user networks of Figure 5.2, for instance, at an average US rate of 50%, FDX transmission achieves a DS rate of 77.5% and 89% in scenarios (a) and (b) respectively, instead of the 50% rate achieved by TDD. The slightly higher gain in scenario (a) is due to the larger separation length between the NTs on each floor, resulting in more attenuated NT-side NEXT signals. Moreover, scenario (a) with only one active user per floor, i.e. $N = 4$, results in weaker overall NEXT, yielding even larger FDX gains (see Fig. 5.6). The extreme case with only 2 active users even almost results in a doubled performance, close to the theoretical optimum. These results demonstrate that the level of NEXT interference at the NTs is *the* performance determining factor for MU FDX transmission in G.mgfast networks.

[8]The normalization is such the best normalized WSR value found by either WMMSE or FDX-PD-DSB is equal to 1.

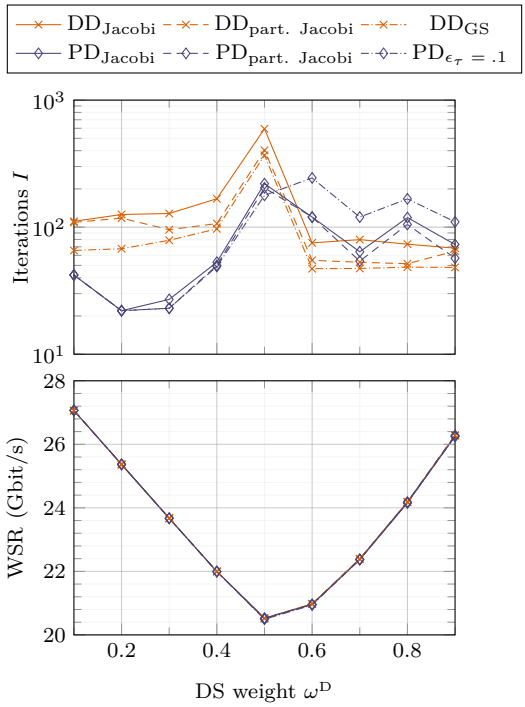


Figure 5.4: Number of iterations required for convergence and final weighted sum rate value, obtained by executing FDX-DD-DSB and FDX-PD-DSB for the network of Figure 5.2a.

5.7 Conclusion

Three novel DSM algorithms have been presented for the MU FDX DSL network. First, an OSB algorithm has been derived which calculates the globally optimal resource allocation, but does so at an exceedingly high computational cost. Two low-complexity DSB algorithms have then been proposed, for which simulations have shown that their performance is very close to what is achieved by the OSB algorithm. These DSB algorithms have then been used in performance simulations, which show that FDX transmission can indeed lead to significant performance gains in MU DSL networks.

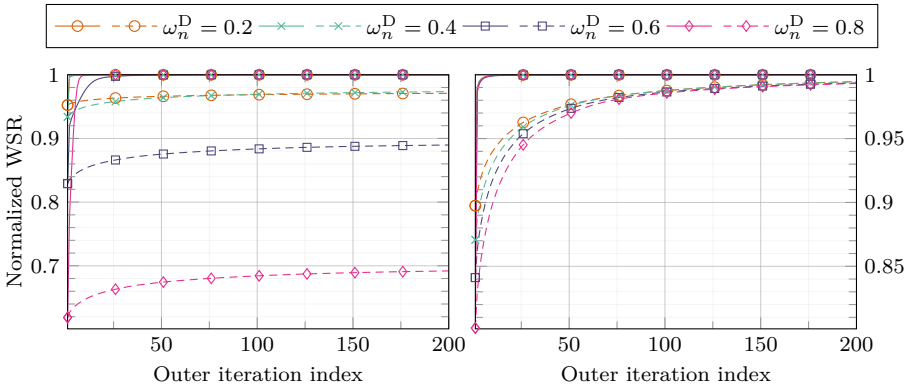


Figure 5.5: Convergence of the WMMSE and FDX-PD-DSB algorithms. Dashed curves correspond to WMMSE, solid curves to FDX-PD-DSB. Both algorithms are executed for the 10-user FTTB network of Figure 5.2a. Both plots consider the same G.fast network, but are obtained using different values for the noise floor: $\sigma_{k,n} = -140\,\mathrm{dBm/Hz}$ for the left plot, and $\sigma_{k,n} = -110\,\mathrm{dBm/Hz}$ for the right plot.

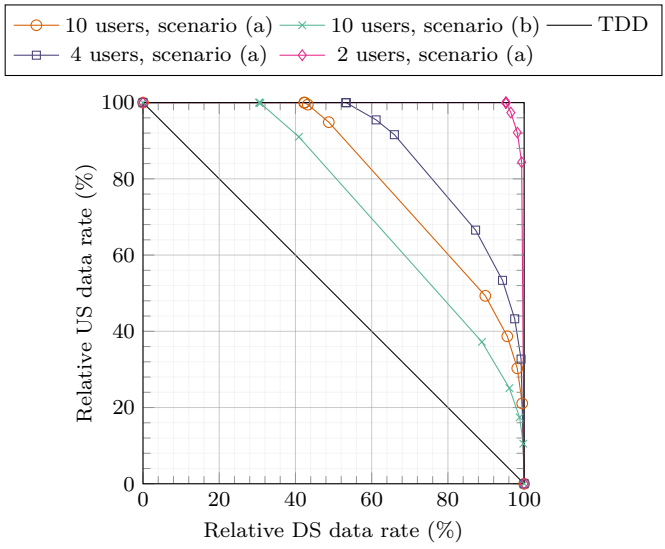


Figure 5.6: Average achievable US and DS rates of FDX transmission in the DSL networks of Figure 5.2, relative to maximum achievable TDD rates.

Chapter 6

DSM and Channel Shortening

Per-Tone Precoding and Per-Tone Equalization for OFDM and DMT Transmission Systems: Duality, Filter Optimization, and Resource Allocation

Jeroen Verdyck, Yannick Lefevre, Paschalis Tsiaflakis, and Marc Moonen

Published in *IEEE Open Journal of Signal Processing*, Vol. 1, pp. 257-273, November 2020, DOI: 10.1109/OJSP.2020.3035060.

© 2020 IEEE. Reprinted, with permission, from:
Jeroen Verdyck, Yannick Lefevre, Paschalis Tsiaflakis, and Marc Moonen, "Per-Tone Precoding and Per-Tone Equalization for OFDM and DMT Transmission Systems: Duality, Filter Optimization, and Resource Allocation," *IEEE Open Journal of Signal Processing*, Vol. 1, pp. 257-273, November 2020.
Changes include layout, representation, and minor editing aspects.

The candidate's contributions as first author include: all performed research and writing of the article under guidance of the co-authors.

Abstract

OFDM and DMT transmission systems add a cyclic prefix (CP) or zero pad (ZP) to the transmitted signal. Interference-free transmission requires this CP/ZP to be similarly long as the channel impulse response (CIR), reducing the achievable data rate in highly dispersive channels. A first strategy for dealing with long CIRs without increasing the CP/ZP overhead consists of applying a *channel shortening* filter to the received signal. A second strategy consists of spectral *resource allocation*, i.e. bit and power allocation to reduce interference. As little effort has been made towards joint channel shortening and resource allocation, a new algorithm to simultaneously optimize the channel shortening per-tone equalization (PTEQ) filters and the resource allocation is presented.

In addition, transmitter-side channel shortening filters are considered, more specifically so-called per-tone precoding (PTPC) filters which apply the channel shortening filter before the IDFT modulation of the ODFM/DMT transmitter. At first glance, the FIR filter optimization for PTPC seems much more involved than the relatively straightforward FIR filter optimization for PTEQ. However, it will be demonstrated that any OFDM/DMT system with PTPC is—after time-reversing the CIR—equivalent to an OFDM/DMT system employing PTEQ. With this result in hand, systems with PTPC can take full advantage of the straightforward FIR filter optimization in systems with PTEQ, as well as of the aforementioned resource allocation algorithm. Simulation results show that the performance obtained for systems with PTPC is nearly indistinguishable from that obtained for systems with PTEQ, making PTPC an interesting alternative channel shortening strategy.

6.1 Introduction

In OFDM and DMT systems, a cyclic prefix (CP) or zero pad (ZP) is added to the transmitted signal. This CP/ZP serves two purposes: it prevents inter-symbol interference (ISI) between successive symbols, and it suppresses inter-carrier interference (ICI) between subcarriers (a.k.a. tones) of the same symbol. If the CP/ZP is longer than the channel impulse response (CIR), ISI/ICI-free transmission can effectively be achieved. In highly dispersive channels—i.e. channels with a long CIR—ISI/ICI-free transmission will however require a long CP/ZP, reducing the achievable data rate.

In the context of DSL systems specifically, an extension of the G.fast standard [95, 96] has recently been proposed that aims to enable G.fast on lines with a length in excess of 400 m [52, 77, 128, 180, 181]. Enabling G.fast on such long

lines—which can currently only be operated by legacy DSL technologies—will facilitate convergence to a single DSL standard, thereby eliminating co-existence problems between different DSL generations. Key enabling factors for this long-reach (LR) extension of G.fast will be larger constellation sizes [77], a higher maximum aggregate transmit power [77, 181], the application of a looser spectral mask at low frequencies [181], and a longer CP to support longer lines [181]. In the case of G.fast systems however, where the same CP length is applied across all users in both upstream and downstream [96], using a longer CP to support longer lines will inevitably reduce the data rate on shorter lines. Based on this observation, interest in techniques dealing with long CIRs without increasing the CP overhead has recently resurfaced.[1]

A first strategy to mitigate the effects of ISI/ICI in highly dispersive channels without employing an excessively long CP/ZP consists of channel shortening. Chow *et al.* [38] have proposed the use of a finite impulse response (FIR) time-domain equalization (TEQ) filter to shorten the CIR. Van Acker *et al.* [6] have proposed moving this TEQ filter into the frequency domain—i.e. to after the DFT demodulation of the OFDM/DMT receiver—and allowing a different FIR filter for each subcarrier, which can be implemented without increasing the run-time complexity as compared to TEQ. The resulting channel shortening strategy is referred to as per-tone equalization (PTEQ). While PTEQ indeed requires more memory than TEQ due to the increased number of FIR filter coefficients, the main advantages are that 1) maximizing the SNR on each subcarrier individually leads to a straightforward FIR filter optimization, and 2) PTEQ is a generalization of TEQ, i.e. any specific TEQ filter can be equivalently implemented as a PTEQ filter whereas the reverse is not true. As such, PTEQ provides an upper bound on the performance of TEQ.

A second method to mitigate the effects of ISI/ICI without employing an excessively long prefix consists of spectral resource allocation, i.e. bit and power allocation [212], which exploits the fact that not all subcarriers are equally susceptible to ISI/ICI [76]. Algorithms for resource allocation have been considered in [210, 212] for ISI/ICI due to an insufficiently long prefix, and in [30, 33, 217] for ISI/ICI due to asynchronous transmissions.

While both aforementioned ISI/ICI mitigation methods have received significant attention in literature, it is remarkable that little effort has been made towards a joint channel shortening and resource allocation. To the best of the authors' knowledge, only [146] has addressed the issue by considering sparse PTEQ filter coefficient optimization combined with a power allocation method. However, the proposed method in [146] ignores the ICI while executing an exhaustive

[1] Even though the current interest in this subject is mainly coming from the DSL community, the theoretical and algorithmic developments in this chapter will be kept general such that these can be applied to other OFDM or DMT-based systems as well.

search over a discrete set of power levels to obtain a power allocation, which can lead to poor performance in the presence of ISI/ICI [33]. It is deemed that *optimal* power allocation algorithms would be more appropriate to guide the design of power allocation heuristics towards enhanced performance. In this chapter, a new algorithm to simultaneously optimize the PTEQ filter and the resource allocation is therefore presented.

In addition, transmitter-side channel shortening is considered. Time-domain precoding (TPC) filters were first considered in [169]. Similar to PTEQ, one can move the TPC filter into the frequency domain—i.e. to before the IDFT modulation of the OFDM/DMT transmitter—without a significant impact on run-time complexity, yielding a channel shortening algorithm that will be referred to as per-tone precoding (PTPC).[2]

At first glance, the FIR filter optimization for PTPC seems much more involved than the relatively straightforward FIR filter optimization for PTEQ. In addition, the more involved PTPC filter optimization complicates the resource allocation problem. However, it is demonstrated in this chapter that any OFDM/DMT system with (P)TPC is—after time-reversing the CIR—equivalent to an OFDM/DMT system employing (P)TEQ. The obtained equivalence result is rooted in MAC-BC duality theory [87, 111, 219], and will be referred to as PTEQ-PTPC duality. With this duality result in hand, PTPC systems can take full advantage of the straightforward FIR filter optimization in PTEQ systems, as well as of the developed resource allocation algorithm.

Contributions

A joint PTEQ filter optimization and resource allocation algorithm is proposed for OFDM/DMT systems with PTEQ, which provably converges to a stationary point of the considered rate maximization problem and obtains a sufficient accuracy after only a few iterations. Moreover, the use of an iterative water filling (IWF) algorithm is proposed as a resource allocation heuristic for PTEQ systems. Simulation results show that IWF achieves good performance when the ISI/ICI is sufficiently suppressed by the PTEQ filter.

In addition, the use of a transmitter-side channel shortening per-tone precoder (PTPC) is proposed. A duality result is proven between the proposed PTPC filter and the well-studied PTEQ filter. A joint PTPC filter optimization and resource allocation algorithm is developed by using this duality result. Simulation results show that the performance obtained for OFDM/DMT systems with PTPC

[2] The considered PTPC has actually first been introduced in the context of per-tone spectral shaping [35], but its use for channel shortening has not been considered before.

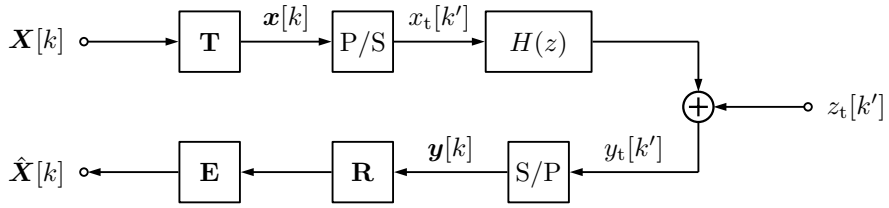


Figure 6.1: A general OFDM/DMT transceiver model.

is nearly indistinguishable from that obtained for OFDM/DMT systems with PTEQ.

Notation

Throughout the chapter, zero-based indexing will be used when addressing vector and matrix elements, i.e. for any $N \times M$ matrix $\mathbf{A}$ we have the following

$$\mathbf{A}^{\mathrm{T}} = [(\mathrm{row}_0(\mathbf{A}))^{\mathrm{T}}, \ldots, (\mathrm{row}_{N-1}(\mathbf{A}))^{\mathrm{T}}]\,;$$

$$\mathbf{A} = [\mathrm{col}_0(\mathbf{A}), \ldots, \mathrm{col}_{M-1}(\mathbf{A})]\,;$$

$$[\mathbf{A}]_{n,m} = \mathrm{row}_n\big(\mathrm{col}_m(\mathbf{A})\big).$$

The dimension subscripts in $\mathbf{I}_N$ and $\mathbf{0}_{N\times M}$ will be omitted when they can be derived from the context.

6.2 System model

Figure 6.1 depicts a general OFDM system model consisting of an encoder $\mathbf{T}$, a decoder $\mathbf{R}$, a serial-to-parallel (S/P) and parallel-to-serial (P/S) converter, and a frequency-selective channel that is modeled as an FIR filter $H(z) = \sum_{k'=0}^{L} z^{-k'} h[k']$. It is noted that a different sample index k' is used between the P/S converter and the S/P converter, as they respectively execute an upsampling and a downsampling operation. The noise samples $z_{\mathrm{t}}[k']$ are assumed to be i.i.d. and Gaussian,[3] with an average power given by $\mathbb{E}\left\{|z_{\mathrm{t}}[k']|^2\right\} = \sigma_{\mathrm{t}}^2$. The complex

[3]While certainly possible, extending the models and algorithms in this chapter to include colored noise would further obfuscate the derivations, and is therefore considered to be out-of-scope.

vectors $\boldsymbol{X}[k] \triangleq [X_0[k], \ldots, X_{N-1}[k]]^{\mathrm{T}}$ and $\hat{\boldsymbol{X}}[k] \triangleq [\hat{X}_0[k], \ldots, \hat{X}_{N-1}[k]]^{\mathrm{T}}$ respectively denote the frequency-domain input and output symbol, where N is the employed DFT size (cf. infra). The covariance matrix of $\boldsymbol{X}[k]$ is

$$\mathbb{E}\left\{\boldsymbol{X}[k]\boldsymbol{X}[l]^{\mathrm{H}}\right\} = \begin{cases} \mathrm{diag}\{\boldsymbol{S}\} & \text{when } k = l \\ \mathbf{0}_N & \text{when } k \neq l \end{cases} \tag{6.1}$$

with $\boldsymbol{S} \triangleq [S_0, \ldots, S_{N-1}]^{\mathrm{T}} \in \mathbb{R}_+^N$ the power allocation vector.

In Section 6.2.1 and Section 6.2.2, two OFDM flavors are reviewed, namely Cyclic Prefix (CP) OFDM and Zero-Padded (ZP) OFDM. In Section 6.2.3 and Section 6.2.4, PTEQ and PTPC are introduced.

Discrete multi-tone

When appropriate, it is indicated how to adapt the presented OFDM system model, algorithms and results to DMT systems. DMT systems operate at baseband, resulting in the requirement that the transmitted signal $x_{\mathrm{t}}[k']$ be real. As will be evident from the definitions of $\mathbf{T}$ in Sections 6.2.1, 6.2.2 and 6.2.4, this requirement is satisfied if and only if $\boldsymbol{X}[k]$ admits the following Hermitian symmetric structure:

$$X_{n^*}[k] = (X_n[k])^*, \forall n,$$

where—with a slight abuse of notation—n^* is the index of the subcarrier that is the Hermitian symmetric of n, i.e. where $n^* \triangleq (N-n) \mod N$. Note that only even DFT sizes N will be considered in the context of DMT systems. Assuming that the real and imaginary part of $X_n[k]$ are i.i.d. $\forall n \in \{1, \ldots, N/2-1\}$, it is readily seen that $\mathbb{E}\{X_{n^*}[k](X_n[k])^*\} = 0\ \forall n \in \{0, \ldots, N/2\}$. The covariance matrix of $\boldsymbol{X}[k]$ therefore still follows (6.1). The power vector $\boldsymbol{S}$ will however admit the same Hermitian symmetric structure as $\boldsymbol{X}[k]$, i.e. $S_n = S_{n^*}$.

6.2.1 Cyclic prefix OFDM (CP-OFDM)

The CP-OFDM transmitter transforms the input symbols $\boldsymbol{X}[k]$ to the time domain by application of the IDFT, and adds a cyclic prefix (CP) to the result. The k-th transmitted time-domain symbol is thus

$$\boldsymbol{x}[k] = \mathbf{T}^{\mathrm{CP}}\boldsymbol{X}[k] = \left[\begin{array}{c|c} \mathbf{0} & \mathbf{I}_\nu \\ \hline & \mathbf{I}_N \end{array}\right] \mathbf{F}_N^{-1}\boldsymbol{X}[k], \tag{6.2}$$

with ν the cyclic prefix length, and $\mathbf{F}_N^{-1}$ the N-point IDFT matrix. The following definition is used for the corresponding N-point DFT matrix $\mathbf{F}_N$.

$$[\mathbf{F}_N]_{n,m} \triangleq \alpha^{-nm} \qquad \alpha \triangleq e^{2\pi j/N} \tag{6.3}$$

The time-domain symbol length is denoted as $s = N + \nu$. At the receiver, the cyclic prefix is removed from the k-th received signal $\boldsymbol{y}[k] = \left[y_0[k], \ldots, y_{s-1}[k]\right]^{\mathrm{T}}$ before application of the DFT and frequency-domain equalization (FEQ). As such, the output symbol $\hat{\boldsymbol{X}}[k]$ can be expressed as

$$\hat{\boldsymbol{X}}[k] = \mathbf{E}\mathbf{R}^{\mathrm{CP}}\boldsymbol{y}[k] = \mathbf{E}\mathbf{F}_N \left[\begin{array}{cc} \mathbf{0}_{N\times\nu} & \mathbf{I}_N \end{array}\right] \boldsymbol{y}[k], \tag{6.4}$$

with $\mathbf{E}$ the diagonal FEQ matrix. Assuming perfect synchronization between the transmitter-side P/S converter and receiver-side S/P converter, each $\hat{X}_n[k]$ will be free of ISI/ICI if $\nu \geq L$.

6.2.2 Zero-padded OFDM (ZP-OFDM)

The ZP-OFDM transmitter adds a zero pad instead of a cyclic prefix. The k-th time-domain symbol is thus

$$\boldsymbol{x}[k] = \mathbf{T}^{\mathrm{ZP}}\boldsymbol{X}[k] = \left[\begin{array}{c} \mathbf{I}_N \\ \mathbf{0}_{\nu\times N} \end{array}\right] \mathbf{F}_N^{-1}\boldsymbol{X}[k], \tag{6.5}$$

with ν the pad length. A ZP-OFDM-OLA receiver is assumed here, which adds the first ν samples of the received signal $\boldsymbol{y}[k]$ to the last samples of $\boldsymbol{y}[k]$ before application of the DFT and FEQ [138]:

$$\hat{\boldsymbol{X}}[k] = \mathbf{E}\mathbf{R}^{\mathrm{ZP}}\boldsymbol{y}[k] = \mathbf{E}\mathbf{F}_N \left[\begin{array}{c|c} \mathbf{0} & \\ \mathbf{I}_\nu & \mathbf{I}_N \end{array}\right] \boldsymbol{y}[k]. \tag{6.6}$$

Assuming perfect synchronization between the P/S and S/P blocks, each $\hat{X}_n[k]$ will again be free of ISI/ICI if $\nu \geq L$.[4]

6.2.3 Per-tone equalization

PTEQ [6] is described here by first introducing TEQ in the receiver, and then deriving the PTEQ from this TEQ. The idea of TEQ is to apply a filter $W(z) = \sum_{k'=0}^{T} z^{-k'} w[k']$ to $y_{\mathrm{t}}[k']$ in order to shorten the CIR, thereby reducing the required ν for ISI/ICI-free transmission and hence the corresponding data rate overhead. The receiver with TEQ thus executes the following operation:

$$\hat{\boldsymbol{X}}[k] = \mathbf{E}\mathbf{R} \begin{bmatrix} \boxed{\boldsymbol{w}^{\mathrm{T}}} & 0 & \cdots \\ 0 & \ddots & \ddots \\ \vdots & \ddots & \boxed{\boldsymbol{w}^{\mathrm{T}}} \end{bmatrix} \tilde{\boldsymbol{y}}[k], \tag{6.7}$$

[4] The ZP-OFDM-OLA receiver from [138] adds the last ν samples of $\boldsymbol{y}[k]$ to the first samples of $\boldsymbol{y}[k]$, as opposed to what is done in (6.6). The two are however equivalent up to a phase shift of the elements of $\mathbf{E}$ due to the DFT shift theorem [9, Eq. 3.2-4].

where $\tilde{\boldsymbol{y}}[k] \triangleq \left[y_{s-T}[k-1], \ldots, y_{s-1}[k-1], (\boldsymbol{y}[k])^{\mathrm{T}}\right]^{\mathrm{T}}$ is the extended received signal, where $\boldsymbol{w}^{\mathrm{T}} \triangleq \left[w[T], \ldots, w[0]\right]$ contains the TEQ filter coefficients, and where $\mathbf{R}$ can be either $\mathbf{R}^{\mathrm{CP}}$ or $\mathbf{R}^{\mathrm{ZP}}$. From here on, it will not be specified explicitly whether $\mathbf{R}$, $\mathbf{T}$, or their derived variables correspond to a CP-OFDM or to a ZP-OFDM system in equations that are valid for both.

PTEQ is based on transferring the TEQ to the frequency domain—i.e. to after the DFT operation [6]—which can be done based on the following reformulation of equation (6.7), where $E_n \triangleq \left[\mathbf{E}\right]_{n,n}$.

$$\hat{X}_n[k] = E_n \boldsymbol{w}^{\mathrm{T}} \underbrace{\begin{bmatrix} \boxed{\mathrm{row}_n(\mathbf{R})} & 0 & \cdots \\ 0 & \ddots & \ddots \\ \vdots & \ddots & \boxed{\mathrm{row}_n(\mathbf{R})} \end{bmatrix}}_{\triangleq \mathbf{R}_n} \tilde{\boldsymbol{y}}[k] \tag{6.8}$$

The receiver with PTEQ is then obtained by effectively allowing each subcarrier to have its own TEQ—implemented as a T-th order FEQ filter with filter coefficients $\boldsymbol{w}_n^{\mathrm{H}} \triangleq \left[w_n[T], \ldots, w_n[0]\right]$—by removing the constraint that $\forall n : \boldsymbol{w}_n^{\mathrm{H}} = E_n \boldsymbol{w}^{\mathrm{T}}$ for one overall TEQ filter $\boldsymbol{w}$. The output symbol on the n-th subcarrier of a receiver with PTEQ is thus given as

$$\hat{X}_n[k] = \boldsymbol{w}_n^{\mathrm{H}} \mathbf{R}_n \tilde{\boldsymbol{y}}[k]. \tag{6.9}$$

From (6.9), it may appear that PTEQ brings a significant complexity increase w.r.t. TEQ as it seems to require $T+1$ DFT operations (whereas TEQ demands only a single DFT). Fortunately, when $\mathbf{R}_n$ corresponds to the CP-OFDM decoder of Section 6.2.1 or the ZP-OFDM decoder of Section 6.2.2, one can reduce the $T+1$ DFT operations back to one by decomposing $\mathbf{R}_n$ into a lower triangular matrix and a sparse matrix as in [6, 35], i.e.

$$\mathbf{R}_n^{\mathrm{ZP}} = \underbrace{\begin{bmatrix} \alpha^{0n} & \cdots & 0 \\ \vdots & \ddots & \vdots \\ \alpha^{Tn} & \cdots & \alpha^{0n} \end{bmatrix}}_{\triangleq \mathbf{L}_n} \underbrace{\left[\begin{array}{cc|c} \multicolumn{2}{c|}{\boxed{\mathrm{row}_n(\mathbf{R}^{\mathrm{ZP}})}} & \mathbf{0} \\ -\alpha^{(\nu+1)n}\mathbf{I}_T & \mathbf{0} & \alpha^n \mathbf{I}_T \end{array}\right]}_{\triangleq \mathbf{R}_n^{\mathrm{ZP}}} \tag{6.10a}$$

for ZP-OFDM and

$$\mathbf{R}_n^{\mathrm{CP}} = \begin{bmatrix} \alpha^{0n} & \cdots & 0 \\ \vdots & \ddots & \vdots \\ \alpha^{Tn} & \cdots & \alpha^{0n} \end{bmatrix} \underbrace{\left[\begin{array}{cc|c} \multicolumn{2}{c|}{\boxed{\mathrm{row}_n(\mathbf{R}^{\mathrm{CP}})}} & \mathbf{0} \\ \mathbf{0}_{T\times\nu} & -\alpha^n \mathbf{I}_T & \mathbf{0} \quad \alpha^n \mathbf{I}_T \end{array}\right]}_{\triangleq \mathbf{R}_n^{\mathrm{CP}}} \tag{6.10b}$$

for CP-OFDM where $\underline{\mathbf{R}}_n$ corresponds to a single DFT together with the usage of T so-called difference terms. With this decomposition, equation (6.9) becomes

$$\hat{X}_n[k] = \boldsymbol{v}_n^{\mathcal{H}} \underline{\mathbf{R}}_n \tilde{\boldsymbol{y}}[k], \tag{6.11}$$

where $\boldsymbol{v}_n \triangleq \mathbf{L}_n^{\mathcal{H}} \boldsymbol{w}_n$. An in-depth run-time complexity analysis of PTEQ is provided in [6].

Finally, an expression for the signal-to-interference-plus-noise ratio (SINR) on each subcarrier is established. The starting point for this expression is the complete input-output equation as in (6.12) on page 134,[5] where $\boldsymbol{h} \triangleq \big[h[L], \ldots, h[0]\big]$.

[5] In this equation, the PTEQ receiver as in (6.11) has been employed because it enables an efficient implementation of the SINR calculation, as well as of the resource allocation algorithm from Section 6.3. This choice has no bearing on the derivations in Sections 6.3 and 6.4, i.e. employing the PTEQ as in (6.9) would yield equivalent theories, algorithms, and results.

$$\hat{X}_n[k] = \boldsymbol{v}_n^{\mathcal{H}} \underline{\mathbf{R}}_n \underbrace{\left[\begin{array}{c|ccc|c} \mathbf{O}_1 & \boxed{\boldsymbol{h}} & 0 & \cdots & \mathbf{O}_2 \\ & 0 & \ddots & \ddots & \\ & \vdots & \ddots & \boxed{\boldsymbol{h}} & \end{array}\right]}_{\triangleq \mathbf{H}_\delta} \left[\begin{array}{ccc} \mathbf{T} & & \\ & \mathbf{T} & \\ & & \mathbf{T} \end{array}\right] \left[\begin{array}{c} \boldsymbol{X}[k-1] \\ \boldsymbol{X}[k] \\ \boldsymbol{X}[k+1] \end{array}\right] + \boldsymbol{v}_n^{\mathcal{H}} \underline{\mathbf{R}}_n \tilde{\boldsymbol{z}}[k] \tag{6.12}$$

$$\hat{\boldsymbol{X}}[k] = \mathbf{E}\mathbf{R} \underbrace{\left[\begin{array}{c|ccc|c} \mathbf{O}_3 & \boxed{\boldsymbol{h}} & 0 & \cdots & \mathbf{O}_4 \\ & 0 & \ddots & \ddots & \\ & \vdots & \ddots & \boxed{\boldsymbol{h}} & \end{array}\right]}_{\triangleq \bar{\mathbf{H}}_\delta} \left[\begin{array}{ccc} \boxed{\mathbf{P}} & \mathbf{0}_{s\times N} & \mathbf{0}_{s\times N} \\ \mathbf{0}_{s\times N} & \boxed{\mathbf{P}} & \mathbf{0}_{s\times N} \\ \mathbf{0}_{s\times N} & \mathbf{0}_{s\times N} & \boxed{\mathbf{P}} \end{array}\right] \left[\begin{array}{c} \boldsymbol{X}[k-1] \\ \boldsymbol{X}[k] \\ \boldsymbol{X}[k+1] \end{array}\right] + \mathbf{E}\mathbf{R}\boldsymbol{z}[k] \tag{6.13}$$

$$\hat{X}_n[k] = \bar{\boldsymbol{v}}_n^{\mathcal{H}} \underline{\mathbf{T}}_n^{\mathcal{H}} \left[\begin{array}{c|ccc|c} \mathbf{O}_5 & \boxed{\boldsymbol{h}^* \mathbf{J}_{L+1}} & 0 & \cdots & \mathbf{O}_6 \\ & 0 & \ddots & \ddots & \\ & \vdots & \ddots & \boxed{\boldsymbol{h}^* \mathbf{J}_{L+1}} & \end{array}\right] \left[\begin{array}{ccc} \mathbf{R}^{\mathcal{H}} & & \\ & \mathbf{R}^{\mathcal{H}} & \\ & & \mathbf{R}^{\mathcal{H}} \end{array}\right] \left[\begin{array}{c} \boldsymbol{X}[k-1] \\ \boldsymbol{X}[k] \\ \boldsymbol{X}[k+1] \end{array}\right] + N \bar{\boldsymbol{v}}_n^{\mathcal{H}} \underline{\mathbf{T}}_n^{\mathcal{H}} \tilde{\boldsymbol{z}}[k] \tag{6.14}$$

$$\hat{X}_n[k] = \bar{\boldsymbol{v}}_n^{\mathcal{H}} \underline{\mathbf{R}}_n^{\mathrm{DE}} \left[\begin{array}{c|ccc|c} \mathbf{O}_7 & \boxed{\boldsymbol{h}^* \mathbf{J}_{L+1}} & 0 & \cdots & \mathbf{O}_8 \\ & 0 & \ddots & \ddots & \\ & \vdots & \ddots & \boxed{\boldsymbol{h}^* \mathbf{J}_{L+1}} & \end{array}\right] \left[\begin{array}{ccc} \mathbf{T}^{\mathrm{DE}} & & \\ & \mathbf{T}^{\mathrm{DE}} & \\ & & \mathbf{T}^{\mathrm{DE}} \end{array}\right] \left[\begin{array}{c} \boldsymbol{X}[k-1] \\ \boldsymbol{X}[k] \\ \boldsymbol{X}[k+1] \end{array}\right] + \bar{\boldsymbol{v}}_n^{\mathcal{H}} \underline{\mathbf{R}}_n^{\mathrm{DE}} \tilde{\boldsymbol{z}}[k] \tag{6.15}$$

With $\boldsymbol{X}[k]$ the symbol of interest and $\boldsymbol{X}[k-1]$,$\boldsymbol{X}[k+1]$ its neighboring symbols, this equation accurately models the ICI, as well as all the ISI originating from the neighboring symbols. When L is very large, more neighboring symbols can be included in the equation [125]. Letting δ denote the so-called synchronization delay, the dimensions of $\mathbf{O}_1$ and $\mathbf{O}_2$ become $(s+T)\times(s-L-T+\delta)$ and $(s+T)\times(s-\delta)$, respectively. When $\delta=0$, this choice for the dimensions of $\mathbf{O}_1$ and $\mathbf{O}_2$ ensures that $y_0[k]$ is the first sample that has a contribution from $\boldsymbol{X}[k]$. By separating the Toeplitz matrix $\mathbf{H}_\delta$, which has dimensions $(s+T)\times(3s)$, into three $(s+T)\times s$ matrices $\{\mathbf{H}_\delta[l]\}_{l=\{-1,0,1\}}$, equation (6.12) can be rewritten as

$$\hat{X}_n[k] = \boldsymbol{v}_n^{\mathcal{H}}\underline{\mathbf{R}}_n \sum_{l=-1}^{1} \mathbf{H}_\delta[l]\mathbf{T}\boldsymbol{X}[k+l] + \boldsymbol{v}_n^{\mathcal{H}}\underline{\mathbf{R}}_n\tilde{\boldsymbol{z}}[k]. \tag{6.16}$$

Moreover, by defining the $(T+1)\times 1$ residual channel vectors $\boldsymbol{h}_{nm}[l]$ and residual channel matrices $\mathbb{H}_{nm}$ as

$$\boldsymbol{h}_{nm}[l] \triangleq \underline{\mathbf{R}}_n\mathbf{H}_\delta[l]\,\mathrm{col}_m(\mathbf{T}), \tag{6.17a}$$

$$\mathbb{H}_{nm} \triangleq \begin{cases} \left[\ \boldsymbol{h}_{nm}[-1]\ \middle|\ \boldsymbol{h}_{nm}[0]\ \middle|\ \boldsymbol{h}_{nm}[1]\ \right] & \text{when } n\neq m \\ \left[\ \boldsymbol{h}_{nn}[-1]\ \middle|\ \boldsymbol{h}_{nn}[1]\ \right] & \text{when } n=m \end{cases}, \tag{6.17b}$$

and introducing $\boldsymbol{h}_n \triangleq \boldsymbol{h}_{nn}[0]$—with $\mathbb{E}\left\{|z_{\mathrm{t}}[k']|^2\right\} = \sigma_{\mathrm{t}}^2$ and $\mathbb{E}\left\{\boldsymbol{X}[k]\boldsymbol{X}[l]^{\mathcal{H}}\right\}$ conforming to (6.1)—the following SINR expression is straightforwardly obtained for subcarrier n:

$$\gamma_n(\boldsymbol{S},\boldsymbol{v}_n) = \frac{S_n\left|\boldsymbol{v}_n^{\mathcal{H}}\boldsymbol{h}_n\right|^2}{\sum_{m=0}^{N-1} S_m\left|\boldsymbol{v}_n^{\mathcal{H}}\mathbb{H}_{nm}\right|^2 + \sigma_{\mathrm{t}}^2\left|\boldsymbol{v}_n^{\mathcal{H}}\underline{\mathbf{R}}_n\right|^2}. \tag{6.18}$$

6.2.4 Per-tone precoding

PTPC is described here by first introducing TPC in the transmitter, and then deriving the PTPC from this TPC. The signal flow graph of a transmitter (represented as a synthesis filter bank) with TPC is given in Figure 6.2. The filters $F_n(z)$ in Figure 6.2 realize (6.2) or (6.5), and are described by

$$F_n(z) = \left[1, z^{-1}, \ldots, z^{-(s-1)}\right]\mathrm{col}_n(\mathbf{T}). \tag{6.19}$$

The TPC filter $W(z) = \sum_{k'=0}^{T} z^{-k'}w[k']$ in Figure 6.2 is, analogous to the TEQ in Section 6.2.3, aimed at shortening the CIR. The TPC transmitter applies the

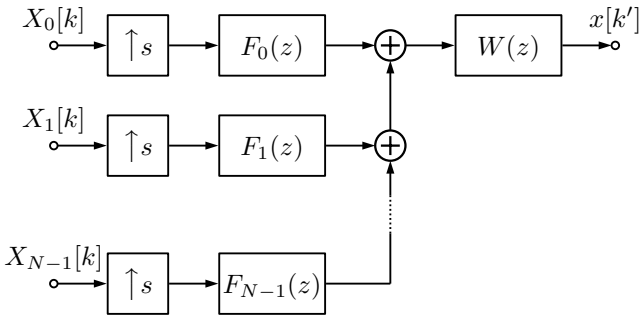


Figure 6.2: Synthesis filter bank representation of an OFDM transmitter (including P/S converter), concatenated with a Time-domain PreCoding (TPC) filter $W(z)$.

following filter to each expanded (upsampled) input symbol stream $[X_n[k]]_{\uparrow s}$:

$$P_n(z) = \left[1, z^{-1}, \ldots, z^{-(s+T-1)}\right] \underbrace{\begin{bmatrix} \boxed{\mathrm{col}_n(\mathbf{T})} & 0 & \cdots \\ & \ddots & \\ 0 & & \boxed{\mathrm{col}_n(\mathbf{T})} \\ \vdots & \ddots & \end{bmatrix}}_{\triangleq \mathbf{T}_n} \bar{\boldsymbol{w}}, \tag{6.20}$$

with $\bar{\boldsymbol{w}} \triangleq \left[w[0], \ldots, w[T]\right]^{\mathrm{T}}$. The overbar in $\bar{\boldsymbol{w}}$ indicates that PTPC filter coefficients are considered. The same overbar-notation will be used to indicate PTPC channel matrices, SINRs, and symbol powers. The transmitter with PTPC is then obtained by allowing a different, possibly complex $\bar{\boldsymbol{w}}_n$ on each subcarrier n. The transmitter with PTPC thus applies the following filter to each expanded input symbol stream $[X_n[k]]_{\uparrow s}$.

$$P_n(z) = \left[1, z^{-1}, \ldots, z^{-(s+T-1)}\right] \mathbf{T}_n \bar{\boldsymbol{w}}_n \tag{6.21}$$

A low-complexity implementation of the resulting filter structure is proposed in [35], albeit in the context of per-subcarrier spectral shaping.[6] This low

[6]Spectral shaping is usually implemented as a time-domain windowing operation. The windowing operation in OFDM-based systems, e.g. as described in [93, 96], is equivalent to applying frequency-shifted versions of a single short prototype filter $W_0(z)$ to the output of each filter $F_n(z)$ in Figure 6.2 [115]. In this context, the authors of [35] proposed to use per-subcarrier spectral shaping filters to improve on the performance of time-domain windowing.

complexity implementation is based on the decomposition of $\mathbf{T}_n$ into a sparse matrix and an upper triangular matrix [6, 35]:

$$\mathbf{T}_n^{\mathrm{ZP}} = \underbrace{\left[\begin{array}{c|c} \boxed{\mathrm{col}_n(\mathbf{T}^{\mathrm{ZP}})} & \begin{array}{c} -N^{-1}\alpha^{-n}\mathbf{I}_T \\ \mathbf{0}_{(N-T)\times T} \\ N^{-1}\alpha^{-n}\mathbf{I}_T \\ \mathbf{0}_{(\nu-T)\times T} \end{array} \\ \hline \mathbf{0}_{T\times 1} & \mathbf{0}_T \end{array}\right]}_{\triangleq \underline{\mathbf{T}}_n^{\mathrm{ZP}}} \underbrace{\begin{bmatrix} \alpha^{-0n} & \cdots & \alpha^{-Tn} \\ \vdots & \ddots & \vdots \\ 0 & \cdots & \alpha^{-0n} \end{bmatrix}}_{\triangleq \mathbf{U}_n} \tag{6.22a}$$

for ZP-OFDM and

$$\mathbf{T}_n^{\mathrm{CP}} = \underbrace{\left[\begin{array}{c|c} \boxed{\mathrm{col}_n(\mathbf{T}^{\mathrm{CP}})} & -N^{-1}\alpha^{-(\nu+1)n}\mathbf{I}_T \\ & \mathbf{0} \\ \hline \mathbf{0} & N^{-1}\alpha^{-n}\mathbf{I}_T \end{array}\right]}_{\triangleq \underline{\mathbf{T}}_n^{\mathrm{CP}}} \begin{bmatrix} \alpha^{-0n} & \cdots & \alpha^{-Tn} \\ \vdots & \ddots & \vdots \\ 0 & \cdots & \alpha^{-0n} \end{bmatrix} \tag{6.22b}$$

for CP-OFDM. Using this decomposition, (6.21) can be rewritten as

$$P_n(z) = \left[1, z^{-1}, \ldots, z^{-(s+T-1)}\right] \underline{\mathbf{T}}_n \bar{\boldsymbol{v}}_n. \tag{6.23}$$

where $\bar{\boldsymbol{v}}_n \triangleq \mathbf{U}_n \bar{\boldsymbol{w}}_n$ now contains the PTPC filter coefficients.

Finally, an expression for the SINR on each subcarrier is established. The starting point for this expression is the input-output equation as in (6.13) on page 134, where $\mathbf{P}$ is defined as

$$\mathrm{col}_n(\mathbf{P}) \triangleq \underline{\mathbf{T}}_n \bar{\boldsymbol{v}}_n. \tag{6.24}$$

The dimensions of $\mathbf{O}_3$ and $\mathbf{O}_4$ are chosen as $s \times (s + T - L + \delta)$ and $s \times (s - \delta)$, respectively. With $\delta = 0$, this choice ensures that $y_0[k]$ is the $(T+1)$-th sample that has a contribution from $\boldsymbol{X}[k]$. By separating the Toeplitz matrix $\bar{\mathbf{H}}_\delta$, which has dimensions $s \times (3s + T)$, into three overlapping $s \times (s + T)$ matrices $\left\{\bar{\mathbf{H}}_\delta[l]\right\}_{l=\{-1,0,1\}}$,[7] the channel model in (6.13) can equivalently be written as

$$\hat{\boldsymbol{X}}[k] = \mathbf{E}\mathbf{R} \sum_{l=-1}^{1} \bar{\mathbf{H}}_\delta[l] \mathbf{P} \boldsymbol{X}[k+l] + \mathbf{E}\mathbf{R}\boldsymbol{z}[k]. \tag{6.25}$$

[7] Each pair of matrices $\{\bar{\mathbf{H}}_\delta[-1], \bar{\mathbf{H}}_\delta[0]\}$ and $\{\bar{\mathbf{H}}_\delta[0], \bar{\mathbf{H}}_\delta[1]\}$ has T columns in common.

By defining the $(T+1)\times 1$ residual channel vectors $\bar{\boldsymbol{h}}_{nm}[l]$ and residual channel matrices $\bar{\mathbb{H}}_{nm}$ as

$$\bar{\boldsymbol{h}}_{nm}[l] \triangleq \underline{\mathbf{T}}_m^{\mathcal{H}} \big(\bar{\mathbf{H}}_\delta[l]\big)^{\mathcal{H}} \big(\operatorname{row}_n(\mathbf{R})\big)^{\mathcal{H}}, \tag{6.26a}$$

$$\bar{\mathbb{H}}_{nm} \triangleq \begin{cases} \left[\begin{array}{c|c|c} \bar{\boldsymbol{h}}_{nm}[-1] & \bar{\boldsymbol{h}}_{nm}[0] & \bar{\boldsymbol{h}}_{nm}[1] \end{array}\right] & \text{when } i \neq j \\ \left[\begin{array}{c|c} \bar{\boldsymbol{h}}_{nn}[-1] & \bar{\boldsymbol{h}}_{nn}[1] \end{array}\right] & \text{when } i = j \end{cases}, \tag{6.26b}$$

and introducing $\bar{\boldsymbol{h}}_n \triangleq \bar{\boldsymbol{h}}_{nn}[0]$—with $\mathbb{E}\{|z_{\mathrm{t}}[k']|^2\} = \sigma_{\mathrm{t}}^2$ and $\mathbb{E}\{\boldsymbol{X}[k]\boldsymbol{X}[l]^{\mathcal{H}}\}$ conforming to (6.1)—the following SINR expression is straightforwardly obtained for subcarrier n:

$$\bar{\gamma}_n(\bar{\boldsymbol{S}}, \bar{\boldsymbol{v}}_0, \ldots, \bar{\boldsymbol{v}}_{N-1}) = \frac{\bar{S}_n \left|\bar{\boldsymbol{v}}_n^{\mathcal{H}} \bar{\boldsymbol{h}}_n\right|^2}{\sum_{m=0}^{N-1} \bar{S}_m \left|\bar{\boldsymbol{v}}_m^{\mathcal{H}} \bar{\mathbb{H}}_{nm}\right|^2 + \sigma_{\mathrm{t}}^2 |\operatorname{row}_n(\mathbf{R})|^2}, \tag{6.27}$$

where for PTPC, the power allocation vector and its elements are denoted as $\bar{\boldsymbol{S}} \triangleq [\bar{S}_0, \ldots, \bar{S}_{N-1}]^{\mathrm{T}}$.

Discrete multi-tone

DMT systems with PTPC should enforce $\bar{\boldsymbol{w}}_{n^*} = \bar{\boldsymbol{w}}_n^*$ or $\bar{\boldsymbol{v}}_{n^*} = \bar{\boldsymbol{v}}_n^*$ to guarantee that $x_{\mathrm{t}}[k'] \in \mathbb{R}$.

6.2.5 Performance metrics

The achievable bit loading b, which is assumed here to be a continuous variable, will be modeled as a function of the SINR γ as

$$b(\gamma) = \log_2\big(1 + \Gamma^{-1}\gamma\big), \tag{6.28}$$

where $\log_2(\cdot)$ is the binary logarithm and Γ is the so-called SNR-gap to capacity—the inclusion of which results in a more accurate model of the relation between the constellation size and the SINR required to achieve a target bit error rate (BER) for practical modulation and coding schemes [39, 57, 182]. Letting f_{s} denote the sample rate, the data rate of an OFDM system with PTEQ is

$$R(\gamma_0, \ldots, \gamma_{N-1}) = \frac{f_{\mathrm{s}}}{N+\nu} \sum_{n=0}^{N-1} b(\gamma_n). \tag{6.29a}$$

The data rate equation for an OFDM system with PTPC is equivalent, but with $\bar{\gamma}_n$ instead of γ_n.

Discrete multi-tone

The data rate of a DMT system with PTEQ is

$$R(\gamma_0,\ldots,\gamma_{N/2}) = \frac{f_\mathrm{s}}{N+\nu}\left(\frac{1}{2}\sum_{n=0}^{1} b(\gamma_{nN/2}) + \sum_{n=1}^{N/2-1} b(\gamma_n)\right). \tag{6.29b}$$

The data rate equation for a DMT system with PTPC is equivalent, but with $\bar{\gamma}_n$ instead of γ_n. It is noted that a different value for Γ may be required on the DC ($n=0$) and Nyquist ($n=\frac{N}{2}$) subcarrier, as their transmitted and received symbols are real. Throughout the chapter, it is however assumed w.l.o.g. that Γ is equal on all subcarriers.

6.3 PTEQ filter optimization & resource allocation

In a system with PTEQ, the power allocation vector $\boldsymbol{S}$ and the PTEQ filter vectors $\{\boldsymbol{v}_0,\ldots,\boldsymbol{v}_{N-1}\}$ can be optimized jointly based on the following rate maximization problem[8]

$$\underset{\substack{\boldsymbol{S}\in\mathbb{R}_+^N \\ \{\boldsymbol{v}_0,\ldots,\boldsymbol{v}_{N-1}\}}}{\text{maximize}} \quad \sum_{n=0}^{N-1} \log_2\left(1+\Gamma^{-1}\gamma_n(\boldsymbol{S},\boldsymbol{v}_n)\right) \tag{6.30a}$$

$$\text{s.t.} \quad \mathbb{E}\left\{|x_\mathrm{t}[k']|^2\right\} \leq P_\mathrm{sample}. \tag{6.30b}$$

The expected sample power can be calculated as

$$\mathbb{E}\left\{|x_\mathrm{t}[k']|^2\right\} = \frac{1}{s}\sum_{n=0}^{N-1} S_n \left|\mathrm{col}_n\,\mathbf{T}\right|^2, \tag{6.31}$$

where $\left|\mathrm{col}_n\,\mathbf{T}^{\mathrm{CP}}\right|^2 = \frac{s}{N^2}$ for CP-OFDM, and $\left|\mathrm{col}_n\,\mathbf{T}^{\mathrm{ZP}}\right|^2 = \frac{1}{N}$ for ZP-OFDM. All formulas in the rest of this Section will be valid for both CP-OFDM and ZP-OFDM systems with PTEQ.

Discrete multi-tone

Returning to (6.29b), it is seen that (6.30a) does not necessarily model the data rate in DMT systems accurately. However, if $S_{n^*} = S_n$, $\forall n$ and $\boldsymbol{h}\in\mathbb{R}^{L+1}$—as

[8] Some constants have been dropped in order to simplify notation.

should be the case in DMT systems—then $\gamma_n(\boldsymbol{S}, \boldsymbol{v}_n) = \gamma_{n^*}(\boldsymbol{S}, \boldsymbol{v}_n^*)$.[9] Therefore, if constraints enforcing $S_{n^*} = S_n$ and $\boldsymbol{v}_{n^*} = \boldsymbol{v}_n^*$, $\forall n$ are added to the optimization problem in (6.30), then the objective function in (6.30a) is indeed proportional to the DMT data rate such that the optimization problem in (6.30) aptly describes the resource allocation problem in a DMT system with PTEQ as well. At the end of Section 6.3.3, it will be highlighted that even without enforcing $S_{n^*} = S_n$ and $\boldsymbol{v}_{n^*} = \boldsymbol{v}_n^*$ explicitly, these constraints will be satisfied automatically with the proposed algorithm.

6.3.1 Problem reformulation

As the SINR of subcarrier n only depends on the PTEQ filter of subcarrier n (i.e. not on the PTEQ filter of other subcarriers), and as $\log_2(1 + \bullet)$ is a monotonically increasing function, it is seen that the optimal PTEQ filter $\boldsymbol{v}_n^\star$ should maximize the SINR γ_n for a given $\boldsymbol{S}$, i.e.

$$\boldsymbol{v}_n^\star = \arg\max_{\boldsymbol{v}_n} \{\gamma_n(\boldsymbol{S}, \boldsymbol{v}_n)\}. \tag{6.32}$$

The optimal PTEQ filter $\boldsymbol{v}_n^\star$ can be calculated in closed form as

$$\boldsymbol{v}_n^\star = \boldsymbol{\Psi}_n(\boldsymbol{S})^{-1}\boldsymbol{h}_n. \tag{6.33}$$

with interference-plus-noise covariance matrix $\boldsymbol{\Psi}_n$ defined as

$$\boldsymbol{\Psi}_n(\boldsymbol{S}) \triangleq \sum_{m=0}^{N-1} S_m \mathbb{H}_{nm}\mathbb{H}_{nm}^{\text{H}} + \sigma_{\text{t}}^2 \underline{\mathbf{R}}_n \underline{\mathbf{R}}_n^{\text{H}}. \tag{6.34}$$

The same choice for $\boldsymbol{v}_n$ (up to scaling) also minimizes $\mathbb{E}\left\{|X_n[k] - \hat{X}_n[k]|^2\right\}$ [6]. Moreover, by plugging (6.33) back into (6.18), an expression for the achieved SINR is obtained that is only a function of the transmit power vector $\boldsymbol{S}$:

$$\gamma_n(\boldsymbol{S}) \triangleq \gamma_n(\boldsymbol{S}, \boldsymbol{v}_n^\star) = S_n \boldsymbol{h}_n^{\text{H}} \boldsymbol{\Psi}_n(\boldsymbol{S})^{-1}\boldsymbol{h}_n. \tag{6.35}$$

As such, $\boldsymbol{v}_n$ can effectively be removed from problem (6.30) leading to the reformulated rate maximization problem

$$\underset{\boldsymbol{S}\in\mathbb{R}_+^N}{\text{maximize}} \quad \sum_{n=0}^{N-1} \log_2\left(1 + \Gamma^{-1}\gamma_n(\boldsymbol{S})\right) \tag{6.36a}$$

$$\text{s.t.} \quad \mathbb{E}\left\{|x_{\text{t}}[k']|^2\right\} \leq P_{\text{sample}}. \tag{6.36b}$$

[9] From $\underline{\mathbf{R}}_{n^*} = \underline{\mathbf{R}}_n^*$ and $\text{col}_{n^*}(\mathbf{T}) = (\text{col}_n(\mathbf{T}))^*$, it follows that $\boldsymbol{h}_{n^*m^*}[k] = (\boldsymbol{h}_{nm}[k])^*$ and, by extension, $|(\boldsymbol{v}_n^*)^{\text{H}}\boldsymbol{h}_{n^*m^*}[k]| = |\boldsymbol{v}_n^{\text{H}}\boldsymbol{h}_{nm}[k]|$.

Algorithm 10. Successive Convex Approximation Framework

1: Choose $\boldsymbol{S}[0] \in \mathcal{S}$
2: **for** $t = 0, 1, \ldots$ **do**
3: Construct the surrogate objective function $\tilde{F}(\bullet|\boldsymbol{S}[t])$
4: Solve surrogate problem (6.38), yielding $\hat{\boldsymbol{S}}$
5: Update $\boldsymbol{S}[t+1] \leftarrow (1-\theta[t]) \cdot \boldsymbol{S}[t] + \theta[t] \cdot \hat{\boldsymbol{S}}$

6.3.2 Successive convex approximation algorithm

Even though problem (6.36) is significantly simplified with respect to problem (6.30), it is still non-convex and closely related to the NP-hard SISO IC sum-rate maximization problem considered in [118].[10] The subsequently developed algorithm will therefore seek to find a stationary point of problem (6.36), rather than its global optimum. A successive convex approximation (SCA) algorithm is proposed which, instead of directly tackling the considered non-convex problem

$$\underset{\boldsymbol{S}\in\mathcal{S}}{\text{maximize}}\ F(\boldsymbol{S}), \tag{6.37}$$

solves a sequence of more tractable surrogate problems

$$\underset{\boldsymbol{S}\in\mathcal{S}}{\text{maximize}}\ \tilde{F}(\boldsymbol{S}|\tilde{\boldsymbol{S}}) \tag{6.38}$$

wherein the original non-concave objective function is replaced by simpler concave one. A formal description of the considered SCA algorithm is given as Algorithm 10. Proposition 6.1 provides theoretical convergence conditions.

Proposition 6.1 (SCA Convergence)**.** *If assumptions* ***P6.1.a*****-*****P6.1.h*** *are satisfied,*[11] *and if in addition the step size* $\theta[t]$ *satisfies*

$$\theta[t] \in (0,1] \qquad \textstyle\sum_t \theta[t] = +\infty \qquad \sum_t \theta[t]^2 < +\infty$$

then either Algorithm 10 converges to a stationary point of problem (6.37) *in a finite number of iterations, or every limit point of the sequence* $\{\boldsymbol{S}[t]\}$ *(at least one such point exists) is a stationary point of problem* (6.37)*.*

[10] If $T = 0$ and box constraints of the form $0 \leq S_n \leq S_n^{\max}$ are added to problem (6.36), then the SISO IC sum-rate maximization problem of [118] is obtained. Even then however, (6.36) need not be NP-hard as the set of all possible SISO IC power channel coefficients $|\mathbb{H}_{ij}|^2$ may be a strict subset of $\mathbb{R}_+^{N\times N}$ that yields no NP-hard sum-rate maximization problems.

[11] In [56], it is additionally assumed that F is *coercive*, i.e. that $F(\boldsymbol{x}) \to -\infty$ as $\|\boldsymbol{x}\| \to +\infty$, such that the iterates produced by Algorithm 10 are bounded. In the context of problem (6.36), boundedness of the iterates directly follows from boundedness of the feasible set $\left\{\boldsymbol{S} \in \mathbb{R}_+^N \mid \sum_{n=0}^{N-1} S_n \left|\mathrm{col}_n\, \mathbf{T}\right|^2 \leq sP_{\text{sample}}\right\}$.

P6.1.a *$\mathcal{S}$ is non-empty, closed, and convex;*

P6.1.b *$F \in C^1$ on an open set $\mathcal{V} \supset \mathcal{S}$;*

P6.1.c *∇F is Lipschitz continuous on $\mathcal{S}$;*

P6.1.d *F is bounded from above on $\mathcal{S}$;*

P6.1.e *$\tilde{F}(\bullet|\tilde{\boldsymbol{S}}) \in C^1$ on an open set $\mathcal{V} \supset \mathcal{S}$, $\forall \tilde{\boldsymbol{S}} \in \mathcal{S}$;*

P6.1.f *$\tilde{F}(\bullet|\tilde{\boldsymbol{S}})$ is uniformly strongly concave, $\forall \tilde{\boldsymbol{S}} \in \mathcal{S}$;*

P6.1.g *$\nabla F(\tilde{\boldsymbol{S}}) = \nabla \tilde{F}(\bullet|\tilde{\boldsymbol{S}})\big|_{\boldsymbol{S}=\tilde{\boldsymbol{S}}}$, $\forall \tilde{\boldsymbol{S}} \in \mathcal{S}$;*

P6.1.h *$\nabla \tilde{F}(\boldsymbol{S}|\bullet)$ is Lipschitz continuous on $\mathcal{S}$ for all $\boldsymbol{S} \in \mathcal{S}$.*

Proof. See proof of Theorem 1 in [56]. □

Note that line search methods can be used to relax the convergence conditions from Proposition 6.1 [214]. However, experience has shown that if the surrogate problem is chosen as a suitable approximant of the original optimization problem, an SCA algorithm converges to a sufficiently accurate solution in only a few iterations [27, 56, 162, 202]. As will be demonstrated in Section 6.5, the same convergence behavior characterizes Algorithm 10 when applied to problem (6.36) with a surrogate problem that is as proposed in the ensuing paragraph.

As a surrogate to (6.36), the following problem is proposed:

$$\underset{\boldsymbol{S}\in\mathbb{R}_+^N}{\text{maximize}} \quad \sum_{n=0}^{N-1} \left(\log_2 \left(1 + \Gamma^{-1} S_n \psi_n(\tilde{\boldsymbol{S}})\right) - S_n a_n(\tilde{\boldsymbol{S}}) \right) \tag{6.39a}$$

$$\text{s.t.} \quad \mathbb{E}\left\{|x_{\mathrm{t}}[k']|^2\right\} \leq P_{\text{sample}} \tag{6.39b}$$

where the functions ψ_n and a_n are defined as

$$\psi_n(\tilde{\boldsymbol{S}}) \triangleq \boldsymbol{h}_n^{\scriptscriptstyle\mathcal{H}} \boldsymbol{\Psi}_n(\tilde{\boldsymbol{S}})^{-1} \boldsymbol{h}_n, \tag{6.40a}$$

$$a_n(\tilde{\boldsymbol{S}}) \triangleq \sum_{m=0}^{N-1} \frac{\tilde{S}_m / \log(2)}{\Gamma + \gamma_m(\tilde{\boldsymbol{S}})} \cdot \left| \mathbb{H}_{mn}^{\scriptscriptstyle\mathcal{H}} \boldsymbol{\Psi}_m(\tilde{\boldsymbol{S}})^{-1} \boldsymbol{h}_m \right|^2. \tag{6.40b}$$

The following Proposition and its proof justify this choice for the surrogate problem.

Proposition 6.2 (SCA Framework Conformity)**.** *If* $\sigma_{\mathrm{t}}^2 \underline{\mathbf{R}}_n \underline{\mathbf{R}}_n^{\mathcal{H}} \succ \mathbf{0}$ *and* $|\boldsymbol{h}_n|^2 > 0 \ \forall n$*, then problem* (6.36) *and its surrogate as in* (6.39) *satisfy assumptions* ***P6.1.a-P6.1.h*** *of Proposition 6.1.*

Proof. See Appendix C. □

Even though $|\boldsymbol{h}_n|^2 > 0$ is required to satisfy conditions **P6.1.a-P6.1.h**, convergence of Algorithm 10 is still guaranteed when $|\boldsymbol{h}_n|^2 = 0$ for some subcarriers. To see this, note that the optimal power allocation for any subcarrier with $|\boldsymbol{h}_n|^2 = 0$ is $S_n = 0$, which is exactly the value yielded for $\hat{S}_n$ on line 4 of Algorithm 10. By excluding subcarriers n for which $|\boldsymbol{h}_n|^2 = 0$ from the objective of (6.36) before applying the above convergence analysis, the convergence result can be straightforwardly extended to the case where $|\boldsymbol{h}_n|^2 > 0$ for at least one subcarrier. Moreover, the definition of $\underline{\mathbf{R}}_n$ in (6.9) implies that condition $\sigma_{\mathrm{t}}^2 \underline{\mathbf{R}}_n \underline{\mathbf{R}}_n^{\mathcal{H}} \succ \mathbf{0}$ is satisfied for both CP-OFDM and ZP-OFDM systems with PTEQ when $\sigma_{\mathrm{t}}^2 > 0$. It can therefore be concluded that if $|\boldsymbol{h}_n|^2 > 0$ for at least one subcarrier n and $\sigma_{\mathrm{t}}^2 > 0$, any limit point of Algorithm 10, with the surrogate problem defined as in (6.39), is a stationary point of problem (6.36).

6.3.3 Solving the surrogate problem

The surrogate problem in (6.39) can be solved by dual decomposition, i.e. by solving the Lagrange dual problem

$$\underset{\lambda \in \mathbb{R}_+}{\text{minimize}} \quad q(\lambda) \triangleq \lambda s P_{\text{sample}} + \sum_{n=0}^{N-1} \max_{S_n \in \mathbb{R}_+} \mathcal{L}_n(S_n, \lambda), \tag{6.41}$$

where the per-subcarrier Lagrangian $\mathcal{L}_n(\lambda, S_n)$ is defined as

$$\mathcal{L}_n(S_n, \lambda) \triangleq \log_2\left(1 + \Gamma^{-1} S_n \psi_n(\tilde{\boldsymbol{S}})\right) - S_n\left(a_n(\tilde{\boldsymbol{S}}) + \lambda \left|\mathrm{col}_n\, \mathbf{T}\right|^2\right). \tag{6.42}$$

The Lagrange dual problem in (6.41) is one-dimensional and convex, such that the optimal Lagrange multiplier $\lambda^\star$ can be obtained using a bisection algorithm. Moreover, strong concavity of $\mathcal{L}_n$ for fixed λ—which follows from strong concavity of the surrogate problem, as proven in Proposition 6.2—implies that the solution to problem (6.39) is given by the maximizer of $\mathcal{L}_n$ at the optimal Lagrange multiplier $\lambda^\star$, and can be calculated analytically as

$$S_i^\star = \left[\frac{1/\log(2)}{a_n(\tilde{\boldsymbol{S}}) + \lambda^\star \left|\mathrm{col}_n\, \mathbf{T}\right|^2} - \Gamma \psi_n(\tilde{\boldsymbol{S}})^{-1}\right]^+. \tag{6.43}$$

The asymptotic complexity of the above method solving problem (6.39) is $\mathcal{O}(I_{\text{bct}}N)$, where I_{bct} is the expected number of bisection iterations. Constructing the surrogate problem however, which entails evaluating a_n and ψ_n for each $n \in \{0, \ldots, N-1\}$, requires executing $\mathcal{O}\left(NT^2(N+T)\right)$ flops. As N can be large—e.g. $N = 4096$ for the 106b-profile of G.fast [96]—the complexity of the above method is dominated by the complexity of constructing the surrogate problem.

From the proposed SCA algorithm, other low complexity power allocation algorithms can be derived. For example, an iterative water filling (IWF) algorithm [221] can be obtained by defining $a_n(\tilde{\boldsymbol{S}}) = 0$. In addition, a constant offset autonomous spectrum balancing (CO-ASB) algorithm [30, 84] can be obtained by setting $a_n(\tilde{\boldsymbol{S}})$ to a predetermined constant value. Both IWF and CO-ASB can be implemented rather easily by, in each iteration, estimating $\psi_n(\boldsymbol{S})\ \forall n$, solving the resulting surrogate problem, and applying the resulting $\boldsymbol{S}$ during transmission. The convergence analysis of Algorithm 10 does not apply to IWF and CO-ASB. In Section 6.5, it will however be shown that the IWF algorithm achieves close-to-optimal performance when ISI/ICI is sufficiently suppressed by the PTEQ filter.

Discrete multi-tone

Finally, a comment is due highlighting that the proposed algorithm automatically satisfies $S_{n^*} = S_n$ and $\boldsymbol{w}_{n^*} = \boldsymbol{w}_n^*$ when considering DMT systems. When $\boldsymbol{S}$ is Hermitian symmetric and $\boldsymbol{h}$ is real, it follows from (6.33) and (6.34) that $\boldsymbol{w}_{n^*}^\star = (\boldsymbol{w}_n^\star)^*$. Therefore it remains to show that the final $\boldsymbol{S}[k]$ yielded by Algorithm 10 is Hermitian symmetric. When $\boldsymbol{S}$ is Hermitian symmetric and $\boldsymbol{h}$ is real, it additionally follows from (6.40a) and (6.40b) that $\psi_{n^*}(\boldsymbol{S}) = \psi_n(\boldsymbol{S})$ and $a_{n^*}(\boldsymbol{S}) = a_n(\boldsymbol{S})$. Consequently, (6.43) will yield a Hermitian symmetric solution $\boldsymbol{S}^\star$. By using an induction argument, it can then be proven that—provided that $\boldsymbol{S}[0]$ in Algorithm 10 is Hermitian symmetric and $\boldsymbol{h}$ is real—each iterate $\boldsymbol{S}[t]$ produced by Algorithm 10 will be Hermitian symmetric as well.

6.4 PTPC filter optimization & resource allocation

In an OFDM system with PTPC, the power allocation vector $\boldsymbol{S}$ and the PTPC filter vectors $\{\bar{\boldsymbol{v}}_0, \ldots, \bar{\boldsymbol{v}}_N\}$ can be optimized jointly based on the following rate

optimization problem.

$$\underset{\substack{\bar{\boldsymbol{S}}\in\mathbb{R}_+^N \\ \{\bar{\boldsymbol{v}}_0,\ldots,\bar{\boldsymbol{v}}_{N-1}\}}}{\text{maximize}} \quad \sum_{i=0}^{N-1} \log_2\left(1+\Gamma^{-1}\bar{\gamma}_n(\bar{\boldsymbol{S}},\bar{\boldsymbol{v}}_1,\ldots,\bar{\boldsymbol{v}}_N)\right) \tag{6.44a}$$

$$\text{s.t.} \quad \mathbb{E}\left\{|x_{\mathrm{t}}[k']|^2\right\} \leq P_{\text{sample}} \tag{6.44b}$$

In (6.44b), the expected sample power is

$$\mathbb{E}\left\{|x_{\mathrm{t}}[k']|^2\right\} = \frac{1}{s}\sum_{n=0}^{N-1} \bar{S}_n \left|\underline{\mathbf{T}}_n \bar{\boldsymbol{v}}_n\right|^2. \tag{6.45}$$

At first glance, the optimization problem in (6.44) seems more involved than the one in (6.30). In particular, eliminating $\bar{\boldsymbol{v}}_n$—as was done for the PTEQ problem in Section 6.3—is not straightforward because the SINR of subcarrier n now depends on the PTPC filter of all subcarriers (i.e. not only the PTPC filter of subcarrier n). Nonetheless, Sections 6.4.1 to 6.4.3 will demonstrate that problem (6.30) and problem (6.44) are equivalent.

6.4.1 Dual system with PTEQ

The duality result will be established between the system with PTPC, as described by (6.13), and its dual system, which is characterized by the following input-output equation:

$$\hat{X}_n[k] = \bar{\boldsymbol{v}}_n^{\mathcal{H}} \underline{\mathbf{T}}_n^{\mathcal{H}} \sum_{l=-1}^{1} (\bar{\mathbf{H}}_\delta[-l])^{\mathcal{H}} \mathbf{R}^{\mathcal{H}} \boldsymbol{X}[k+l] + N\bar{\boldsymbol{v}}_n^{\mathcal{H}} \underline{\mathbf{T}}_n^{\mathcal{H}} \tilde{\boldsymbol{z}}[k]. \tag{6.46}$$

The channel matrix in (6.46), when written as

$$\left[\ (\bar{\mathbf{H}}_\delta[1])^{\mathcal{H}} \ \middle|\ (\bar{\mathbf{H}}_\delta[0])^{\mathcal{H}} \ \middle|\ (\bar{\mathbf{H}}_\delta[-1])^{\mathcal{H}} \ \right], \tag{6.47}$$

is seen to have a Toeplitz structure as well. This Toeplitz structure allows the channel model in (6.46) to be rewritten as in (6.14) on page 134, where $\mathbf{O}_5$ has dimensions $(s+T)\times(s-T-\delta)$, $\mathbf{O}_6$ has dimensions $(s+T)\times(s-L+\delta)$, and $\mathbf{J}_{L+1}$ is an $(L+1)\times(L+1)$ exchange matrix with $[\mathbf{J}_{L+1}]_{n,m} = 1$ for $m = L+1-n$ and $[\mathbf{J}_{L+1}]_{n,m} = 0$ otherwise. Before stating the duality result that connects the system described by (6.46) and (6.14) to the OFDM system with PTPC, it will be established that the system characterized by input-output equations (6.46) and (6.14) correspond to an OFDM system with PTEQ.

Dual of the CP-OFDM system with PTPC

First, the case is considered where the transmit and receive matrices in (6.46) and (6.14) correspond to a CP-OFDM system. The identity $N\mathbf{F}_N^{-1} = \mathbf{F}_N^{\mathcal{H}}$ implies that the following hold:

$$\begin{bmatrix} (\mathbf{R}^{\text{CP}})^{\mathcal{H}} & & \\ & (\mathbf{R}^{\text{CP}})^{\mathcal{H}} & \\ & & (\mathbf{R}^{\text{CP}})^{\mathcal{H}} \end{bmatrix} = N\boldsymbol{\Theta}_{3s}^{\nu} \begin{bmatrix} \mathbf{T}^{\text{ZP}} & & \\ & \mathbf{T}^{\text{ZP}} & \\ & & \mathbf{T}^{\text{ZP}} \end{bmatrix} \tag{6.48a}$$

$$(\underline{\mathbf{T}}_n^{\text{CP}})^{\mathcal{H}} = \frac{1}{N}\underline{\mathbf{R}}_n^{\text{ZP}} \tag{6.48b}$$

where $\boldsymbol{\Theta}_a^b$ shifts the rows of $\mathbf{T}^{\text{ZP}}$ down by ν positions, and is defined as

$$\boldsymbol{\Theta}_a^b \triangleq \left[\begin{array}{c|c} \mathbf{0} & \\ \mathbf{I}_{a-b} & \mathbf{0}_{b\times a} \end{array}\right]. \tag{6.49}$$

After substituting (6.48) into (6.14), the Toeplitz channel matrix from (6.14) is right multiplied by $\boldsymbol{\Theta}_{3s}^{\nu}$ which shifts its columns to the left by ν positions. As the last ν rows of $\mathbf{T}^{\text{ZP}}$ contain only zeros, the last ν columns of the shifted channel matrix can be freely modified such that the result is again a Toeplitz matrix. This yields the input-output equation in (6.15) on page 134 where the dimensions of $\mathbf{O}_7$ and $\mathbf{O}_8$ are respectively $(s+T)\times(s-T-\nu-\delta)$ and $(s+T)\times(s-L+\nu+\delta)$. It is noted that, similarly to how (6.15) was obtained from (6.14), (6.14) can also be obtained from (6.15). Moreover, the superscript "DE"—which stands for "dual symbol extension"—indicates that the transmit and receive matrices in (6.15) correspond to a ZP-OFDM system, whereas the transmit and receive matrices in (6.46) corresponded to a CP-OFDM system.

The channel model in (6.46) thus describes a ZP-OFDM system with PTEQ as in (6.12), but with a time-reversed CIR and where $\delta = L - \nu$ aligns all signals such that $y_0[k]$ is the first sample that has a contribution from $\boldsymbol{X}[k]$. Also, it is noted that the PTEQ filters in the system corresponding to (6.46) have their coefficients in reversed order when compared to the PTPC filters in the original system from (6.13). For a CP-OFDM system with PTPC, the system characterized by (6.46) will be referred to as the *dual ZP-OFDM system with PTEQ*.

Dual of the ZP-OFDM system with PTPC

Second, the case is considered where the transmit and receive matrices in (6.46) and (6.14) correspond to a ZP-OFDM system. The identity $N\mathbf{F}_N^{-1} = \mathbf{F}_N^{\mathcal{H}}$

implies that the following hold.

$$\begin{bmatrix} (\mathbf{R}^{\mathrm{ZP}})^{\varkappa} & & \\ & (\mathbf{R}^{\mathrm{ZP}})^{\varkappa} & \\ & & (\mathbf{R}^{\mathrm{ZP}})^{\varkappa} \end{bmatrix} = N \begin{bmatrix} \mathbf{T}^{\mathrm{CP}} & & \\ & \mathbf{T}^{\mathrm{CP}} & \\ & & \mathbf{T}^{\mathrm{CP}} \end{bmatrix} \tag{6.50a}$$

$$(\underline{\mathbf{T}}_n^{\mathrm{ZP}})^{\varkappa} = \frac{1}{N} \mathbf{R}_n^{\mathrm{CP}} \boldsymbol{\Theta}_{s+T}^{\nu} \tag{6.50b}$$

After substituting (6.50) into (6.14), the Toeplitz channel matrix from (6.14) is left multiplied by $\boldsymbol{\Theta}_{s+T}^{\nu}$ which shifts its rows down by ν positions. As the first ν columns of $\mathbf{R}^{\mathrm{CP}}$ contain only zeros, the first ν rows of the shifted channel matrix can be freely modified such that the result is again a Toeplitz matrix. This yields the input-output equation in (6.15), where the dimensions of $\mathbf{O}_7$ and $\mathbf{O}_8$ are the same as before. It is noted that, similarly to how (6.15) was obtained from (6.14), (6.14) can also be obtained from (6.15). Moreover, the superscript "DE" indicates that the transmit and receive matrices in (6.15) correspond to a CP-OFDM, whereas the transmit and receive matrices in (6.46) corresponded to a ZP-OFDM system.

The channel model in (6.46) thus describes a CP-OFDM system with PTEQ as in (6.12), but with a time-reversed CIR and where $\delta = L - \nu$ aligns all signals such that $y_0[k]$ is the first sample that has a contribution from $\boldsymbol{X}[k]$. As before, it is noted that the PTEQ filters in the system corresponding to (6.46) have their coefficients in reversed order when compared to the PTPC filters in the original system from (6.13). For a ZP-OFDM system with PTPC, the system characterized by (6.46) will be referred to as the *dual CP-OFDM system with PTEQ*.

6.4.2 PTEQ-PTPC duality

As a final step before deriving the duality result, an SINR expression is established for the dual system with PTEQ. It is noted that the SINR expression from (6.18) is still valid—provided that the correct channel matrix is employed. However, a slightly different SINR expression will be derived here, which will yield a clearer exposition of the duality result in the ensuing paragraphs. It is once more assumed that $\mathbb{E}\left\{|z_{\mathrm{t}}[k']|^2\right\} = \sigma_{\mathrm{t}}^2$, and that $\mathbb{E}\left\{\boldsymbol{X}[k]\boldsymbol{X}[l]^{\varkappa}\right\}$ conforms to (6.1). Then, using the definitions of the residual channel vectors $\bar{\boldsymbol{h}}_{ij}[k]$ and matrices $\bar{\mathbb{H}}_{ij}$ as in (6.26), the following SINR expression is obtained for subcarrier n of the dual system with PTEQ:

$$\bar{\bar{\gamma}}_n(\boldsymbol{S}, \bar{\boldsymbol{v}}_n) = \frac{S_n \left|\bar{\boldsymbol{v}}_n^{\varkappa} \bar{\boldsymbol{h}}_n\right|^2}{\sum_{m=0}^{N-1} S_m \left|\bar{\boldsymbol{v}}_n^{\varkappa} \bar{\mathbb{H}}_{mn}\right|^2 + N^2 \sigma_{\mathrm{t}}^2 \left|\underline{\mathbf{T}}_n \bar{\boldsymbol{v}}_n\right|^2}. \tag{6.51}$$

$$\bar{S}_n \cancel{\left|\bar{\boldsymbol{v}}_n^{\mathcal{H}} \bar{\boldsymbol{h}}_n\right|^2} \left(\cancel{S_n \left|\bar{\boldsymbol{v}}_n^{\mathcal{H}} \bar{\mathbb{H}}_{nn}\right|^2} + \sum_{\substack{m=0 \\ m \neq n}}^{N-1} S_m \left|\bar{\boldsymbol{v}}_n^{\mathcal{H}} \bar{\mathbb{H}}_{mn}\right|^2 + N^2 \sigma_{\mathrm{t}}^2 \left|\underline{\mathbf{T}}_n \bar{\boldsymbol{v}}_n\right|^2 \right)$$

$$= S_n \cancel{\left|\bar{\boldsymbol{v}}_n^{\mathcal{H}} \bar{\boldsymbol{h}}_n\right|^2} \left(\cancel{\bar{S}_n \left|\bar{\boldsymbol{v}}_n^{\mathcal{H}} \bar{\mathbb{H}}_{nn}\right|^2} + \sum_{\substack{m=0 \\ m \neq n}}^{N-1} \bar{S}_m \left|\bar{\boldsymbol{v}}_m^{\mathcal{H}} \bar{\mathbb{H}}_{nm}\right|^2 + \sigma_{\mathrm{t}}^2 \left|\mathrm{row}_n \mathbf{R}\right|^2 \right) \quad (6.53)$$

A duality result will now be established between the system with PTPC, which is characterized by (6.13), and the dual system with PTEQ characterized by (6.46). The duality statement and its derivation are based on [87,111,202,219].

Proposition 6.3 (PTEQ-PTPC duality)**.** *Choose any set of PTPC vectors* $[\bar{\boldsymbol{v}}_0, \ldots, \bar{\boldsymbol{v}}_{N-1}] \in \mathbb{C}^{(T+1)\times N}$*. If* $0 < \sigma_{\mathrm{t}}^2$ *and* $\bar{\boldsymbol{v}}_n \neq \mathbf{0}_{(T+1)\times 1}$ $\forall n$*, then the following statements hold.*

P6.3.a *For each dual power vector* $\boldsymbol{S} \in \mathbb{R}_+^N$*, a corresponding power vector* $\bar{\boldsymbol{S}} \in \mathbb{R}_+^N$ *exists such that equalities* (6.52a) *and* (6.52b) *are satisfied.*

P6.3.b *The converse is also true, i.e. for each power vector* $\bar{\boldsymbol{S}} \in \mathbb{R}_+^N$*, a dual power vector* $\boldsymbol{S} \in \mathbb{R}_+^N$ *exists such that equalities* (6.52a) *and* (6.52b) *are satisfied.*

$$\bar{\gamma}_n(\bar{\boldsymbol{S}}, \bar{\boldsymbol{v}}_0, \ldots, \bar{\boldsymbol{v}}_{N-1}) = \bar{\bar{\gamma}}_n\big(\boldsymbol{S}, \bar{\boldsymbol{v}}_n\big), \quad \forall n \quad (6.52a)$$

$$\frac{1}{s}\sum_{n=0}^{N-1} \bar{S}_n \left|\underline{\mathbf{T}}_n \bar{\boldsymbol{v}}_n\right|^2 = \frac{1}{s}\sum_{n=0}^{N-1} S_n \left|\mathrm{col}_n \mathbf{T}^{DE}\right|^2 \quad (6.52b)$$

Proof. Only **P6.3.a** will be proven explicitly; the proof of **P6.3.b** is analogous.

Following the reasoning in [87], the proof of **P6.3.a** is by construction of $\bar{\boldsymbol{S}}$ from $\boldsymbol{S}$. Equation (6.53) at the top of this page reveals that the following system of equations can be obtained from and—given that $0 < \sigma_{\mathrm{t}}^2$ and $0 < \left|\underline{\mathbf{T}}_n \bar{\boldsymbol{v}}_n\right|^2$ $\forall n$—is equivalent to (6.52a):

$$\mathbf{Z}\bar{\boldsymbol{S}} = \sigma_{\mathrm{t}}^2 \begin{bmatrix} \left|\mathrm{row}_0 \mathbf{R}\right|^2 \\ \vdots \\ \left|\mathrm{row}_{N-1} \mathbf{R}\right|^2 \end{bmatrix} \circ \boldsymbol{S} \quad (6.54a)$$

where

$$[\mathbf{Z}]_{n,m} \triangleq \begin{cases} \sum_{\substack{o=0 \\ o\neq n}}^{N-1} S_o \left|\bar{\boldsymbol{v}}_n^{\mathcal{H}} \bar{\mathbb{H}}_{on}\right|^2 + N^2 \sigma_{\mathrm{t}}^2 \left|\underline{\mathbf{T}}_n \bar{\boldsymbol{v}}_n\right|^2 & \text{if } n = m \\ -S_n \left|\bar{\boldsymbol{v}}_m^{\mathcal{H}} \bar{\mathbb{H}}_{nm}\right|^2 & \text{if } n \neq m \end{cases} . \tag{6.54b}$$

The matrix $\mathbf{Z}$ is real-valued, has positive diagonal elements and non-positive off-diagonal elements, and is column diagonally dominant. Therefore, $\mathbf{Z}$ is an M-matrix [87]. As M-matrices are inverse positive, it is concluded that for each $\boldsymbol{S} \in \mathbb{R}_+^N$, solving (6.54) yields an $\bar{\boldsymbol{S}} \in \mathbb{R}_+^N$ for which (6.52a) is satisfied. By summing all rows of (6.54), the following equality is obtained.

$$\sum_{n=0}^{N-1} N^2 \bar{S}_n \left|\underline{\mathbf{T}}_n \bar{\boldsymbol{v}}_n\right|^2 = \sum_{n=0}^{N-1} S_n \left|\mathrm{row}_n \mathbf{R}\right|^2$$

After substitution of $\left|\mathrm{row}_n \mathbf{R}\right|^2$ with $N^2 \left|\mathrm{col}_n \mathbf{T}^{\mathrm{DE}}\right|^2$, it is seen that the obtained $\bar{\boldsymbol{S}}$ satisfies (6.52b) as well. □

Proposition 6.3 shows that—if the PTPC vectors $\bar{\boldsymbol{v}}_n$ satisfy some assumption—any feasible resource allocation for the dual ZP/CP-OFDM system with PTEQ that is described by (6.15) has a corresponding feasible resource allocation for the CP/ZP-OFDM system with PTPC that achieves the same SINR on all subcarriers as well as the same time-domain sample power $\mathbb{E}\left\{|x_{\mathrm{t}}[k']|^2\right\}$, and vice versa. The following Corollary relaxes the assumptions on the PTPC vectors a bit further, and will be required to prove Proposition 6.6 in Section 6.4.3.

Corollary 6.4. ***P6.3.b*** *also holds when* $\bar{\boldsymbol{v}}_n = \mathbf{0}_{(T+1)\times 1}$ *for any* n.

Proof. See proof of Corollary 2 in [202]. □

Discrete multi-tone

When a DMT system is considered rather than an OFDM system, one should additionally assert that a feasible DMT PTEQ resource allocation always has a corresponding feasible DMT PTPC resource allocation and vice versa. The required result is provided by Proposition 6.5.

Proposition 6.5 (PTEQ-PTPC duality—DMT)**.** *If* $\bar{\boldsymbol{v}}_{n^*} = \bar{\boldsymbol{v}}_n^* \ \forall n$ *and* $\boldsymbol{h} \in \mathbb{R}^{L+1}$*, then Proposition 6.3 also holds when both* $\bar{\boldsymbol{S}}$ *and* $\boldsymbol{S}$ *are confined to the set* $\{\boldsymbol{S} \in \mathbb{R}_+^N \mid S_{n^*} = S_n, \forall n\}$.

Proof. As before, only **P6.3.a** will be proven explicitly. The proof of **P6.3.b** is analogous.

Proposition 6.5 is proven by showing that, if its assumptions are satisfied and in addition $\boldsymbol{S}$ is Hermitian symmetric, solving (6.54) yields a Hermitian symmetric $\bar{\boldsymbol{S}}$. The definitions of $\mathbf{R}^{\mathrm{CP}}$, $\mathbf{R}^{\mathrm{ZP}}$, $\underline{\mathbf{T}}_n^{\mathrm{CP}}$ and $\underline{\mathbf{T}}_n^{\mathrm{ZP}}$ imply that $\mathrm{row}_{n^*}(\mathbf{R}) = (\mathrm{row}_n(\mathbf{R}))^*$ and $\underline{\mathbf{T}}_{n^*} = \underline{\mathbf{T}}_n^*$. As $\boldsymbol{h} \in \mathbb{R}^{L+1}$, it follows that $\bar{\mathbb{H}}_{n^*m^*} = (\bar{\mathbb{H}}_{nm})^*$. Keeping in mind that both $S_n = S_{n^*}$ and $\bar{\boldsymbol{v}}_{n^*} = \bar{\boldsymbol{v}}_n^*$, it is then seen that $\mathbf{Z}$ in (6.54) satisfies $[\mathbf{Z}]_{n,m} = [\mathbf{Z}]_{n^*,m^*}\ \forall i,j$. This fact can also be expressed as

$$\mathbf{Z} = \boldsymbol{\Pi}\mathbf{Z}\boldsymbol{\Pi}, \tag{6.55}$$

where $\boldsymbol{\Pi} \triangleq \left[\boldsymbol{e}_{0^*}, \ldots, \boldsymbol{e}_{(N-1)^*}\right]$ is a permutation matrix, with $\boldsymbol{e}_n$ the $(n+1)$-th vector in the standard basis of $\mathbb{R}^N$. As $\boldsymbol{\Pi} = \boldsymbol{\Pi}^{-1}$, the solution to (6.54) satisfies

$$\bar{\boldsymbol{S}} \propto \mathbf{Z}^{-1}\boldsymbol{S} = \boldsymbol{\Pi}\mathbf{Z}^{-1}\boldsymbol{\Pi}\boldsymbol{S}. \tag{6.56}$$

Hermitian symmetry of $\bar{\boldsymbol{S}}$ then directly follows from the Hermitian symmetry of $\boldsymbol{S}$, i.e. from the fact that $\boldsymbol{S} = \boldsymbol{\Pi}\boldsymbol{S}$. □

6.4.3 PTPC filter optimization & resource allocation based on PTEQ-PTPC duality

Finally, the results from Section 6.4.2 can be used to show that problem (6.30) and problem (6.44) are equivalent.

Proposition 6.6 (PTEQ-PTPC equivalence)**.** *Consider the resource allocation problem for the dual system with PTEQ as in* (6.46)*, which is defined as*

$$\underset{\substack{\boldsymbol{S}\in\mathbb{R}_+^N \\ \{\bar{\boldsymbol{v}}_0,\ldots,\bar{\boldsymbol{v}}_{N-1}\}}}{\text{maximize}} \quad \sum_{n=0}^{N-1} \log_2\left(1 + \Gamma^{-1}\bar{\bar{\gamma}}_n(\boldsymbol{S}, \bar{\boldsymbol{v}}_n)\right) \tag{6.57a}$$

$$\text{s.t.} \quad \mathbb{E}\left\{|x_{\mathrm{t}}[k']|^2\right\} \leq P_{\mathrm{sample}}. \tag{6.57b}$$

The solution to problem (6.57)*, when transformed to the PTPC domain by solving* (6.54)*, is the solution to the PTPC problem as in* (6.44)*.*

Proof. The Proposition is proven by contradiction. Assume w.l.o.g. that a solution to problem (6.57) exists with $\bar{\boldsymbol{v}}_n \neq \mathbf{0}_{(T+1)\times 1}\ \forall n$. If Proposition 6.6 were false, a solution to problem (6.44) would exist achieving a higher objective function value than the transformed solution of (6.57). Corollary 6.4 would then

imply that a PTEQ resource allocation exists achieving a value for the objective function in (6.57) that is higher than the value achieved by the solution to (6.57), which is a contradiction. □

Proposition 6.6 thus yields a method for PTPC resource allocation: find a stationary point of problem (6.57) using the PTEQ resource allocation algorithm described in Section 6.3, and transform the obtained solution to the PTPC domain by solving the system of equations in (6.54). Even if the PTEQ resource allocation algorithm is unable to find the globally optimal solution to problem (6.57), Proposition 6.3 implies that the transformed solution will always be a feasible PTPC resource allocation.

Finally, it is observed that the results in Section 6.4.2 also establish a duality between ZP/CP-OFDM systems with TEQ and CP/ZP-OFDM system with TPC. This is true as the subset of dual PTEQ filters that can be implemented as a dual TEQ filter is equivalent to the subset of PTPC filters that can be implemented as a TPC filter. The duality result in Section 6.4.2 can thus also be employed to design a TPC filter from a TEQ filter.

6.5 Simulation results

The resource allocation algorithms are assessed in the context of single-user long-reach G.fast systems. As G.fast employs CP-DMT only, this section evaluates the performance of both a CP-DMT system with PTEQ and a CP-DMT system with PTPC. Three long-reach DSL scenarios are considered, with CIRs—which are given in Figure 6.3—corresponding to twisted pair cables of length 600 m. This line length is justified by the fact that the purpose of the LR extension of G.fast [52, 77, 128, 180, 181] is to enable the use of G.fast on lines that have lengths well in excess of the currently imposed 300 m limit. Two CIRs are derived from measured frequency responses, the other is synthesized using the KM1 model [5]. Both measured IRs are artificially extended to 600 m using the following equation:

$$H_1(f) = (H_0(f))^{\frac{l_1}{l_0}}, \tag{6.58}$$

where l_0 is the original length and l_1 is the target length.

The simulation parameters are chosen conform with the 106b-profile of the G.fast standard [96], and can be found in Table 6.1. The G.fast aggregate

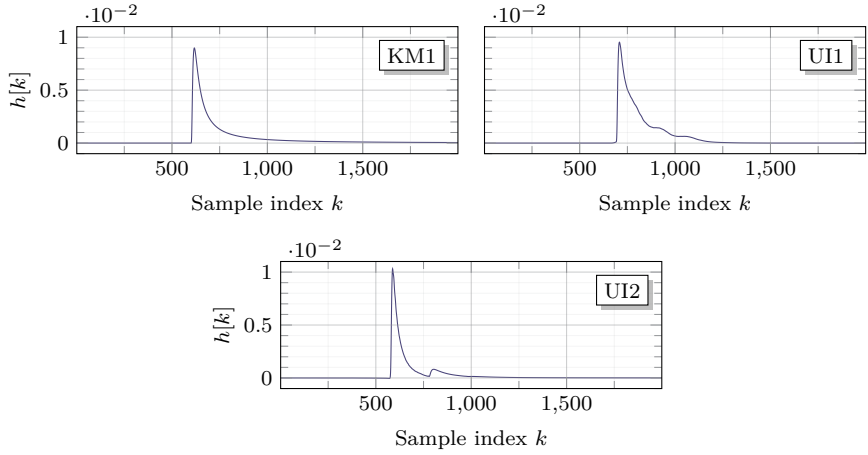


Figure 6.3: The three impulse responses (IRs) that are considered in the simulations. The IR labeled "KM1" was synthesized using the KM1 model with k-parameters corresponding to a homogeneous and perfectly terminated Cat5 cable [5, Table II]. The IRs labeled "UI1" and "UI2" were obtained by measurement of the transfer function of twisted-pair cables belonging to two different undisclosed Internet service providers. Both measured IRs were artificially extended to 600 m.

Table 6.1: Simulation parameters.

Parameter	Value	Parameter	Value
P_{tot}	8 dBm	f_{s}	212 MHz
N	4096	Γ	9.45 dB
σ_{f}^2	-145 dBm/Hz		

transmit power (ATP) constraint is often formulated as

$$\frac{f_{\text{s}}}{N} \sum_{n=1}^{N/2-1} S_n \leq P_{\text{tot}}. \tag{6.59}$$

G.fast employs CP-DMT, with subcarriers corresponding to the DC ($n = 0$) and Nyquist ($n = \frac{N}{2}$) frequencies carrying no information. As such, it is seen from (6.30b) and (6.31) that the ATP constraint as in (6.59) can equivalently be enforced in a CP-OFDM system by choosing the maximum sample power as

$$P_{\text{sample}} = \frac{2P_{\text{tot}}}{Nf_{\text{s}}}. \tag{6.60}$$

The value of P_{sample} is calculated as in (6.60) for the CP-DMT system both with PTEQ and with PTPC. As such, the average power in the time domain is equal in both systems. Care should also be taken when selecting the time-domain noise power σ_{t}^2, as one would typically only define the frequency-domain noise power σ_{f}^2 in DSL simulations. With the DFT operation in the DMT demodulation defined as in (6.3), the relation between the two is as follows.

$$\sigma_{\text{f}}^2 = N\sigma_{\text{t}}^2 \tag{6.61}$$

As the LR extension of G.fast is expected to not use the first 18 subcarriers, these are considered to be inactive—i.e. $S_n = 0\ \forall n \in \{0, \ldots, 17\}$.[12] No spectral mask constraints are considered, as enforcing them in the CP-DMT system with PTPC is not straightforward when the PTPC filter and resource allocation are optimized based on the developed PTEQ-PTPC duality.

6.5.1 PTEQ and PTPC performance

Figure 6.4 presents the data rate achieved by the considered CP-DMT systems with PTEQ and PTPC for delays δ ranging from $\delta_0 - 200$ to $\delta_0 + 100$, where the delay sweep is executed with a 10 sample granularity. Delays are relative to a reference delay δ_0, which is chosen by maximizing the energy in $\left[h[\delta_0], \ldots, h[\delta_0 + \nu]\right]$ as in [6]. The considered CP length is $\nu = 320$, and PTEQ/PTPC filter order is chosen from $T \in \{0, 1, 7\}$. The resource allocation is executed either with the IWF algorithm, or with the SCA algorithm. Both algorithms are stopped after 10 iterations.

In addition, Figure 6.4 also presents the data rate achieved by CP-DMT systems with TEQ and TPC filters. Results are given for the same δ-range, T-values and CP length as were considered for the CP-DMT systems with PTEQ and PTPC. The TEQ filter coefficients are determined using the method described in [10]. After determining the TEQ filter coefficients, the power allocation vector is optimized using an adapted version of either the SCA or the IWF method from Section 6.3. Three adaptations are needed in these methods in order to make them compatible with an additional TEQ filter: 1) the PTEQ filter order is set to $T = 0$, regardless of the TEQ filter order; 2) the CIR are convolved with the TEQ-filter; and 3) the time-domain noise covariance matrix is adapted such that it accounts for the effect of the TEQ. The TPC system is designed by applying the same procedure to the dual ZP-DMT system, and by subsequently

[12] It is readily shown that the duality result in Proposition 6.3 also holds when both $\bar{\boldsymbol{S}}$ and $\boldsymbol{S}$ are confined to the set $\{\boldsymbol{S} \in \mathbb{R}_+^N \mid S_n = 0, \forall n \in \mathcal{N}\}$ where $\mathcal{N} \subseteq \{0, \ldots, N-1\}$. In the system with PTPC, one can thus enforce the inactivity constraint by enforcing it in the dual system with PTEQ.

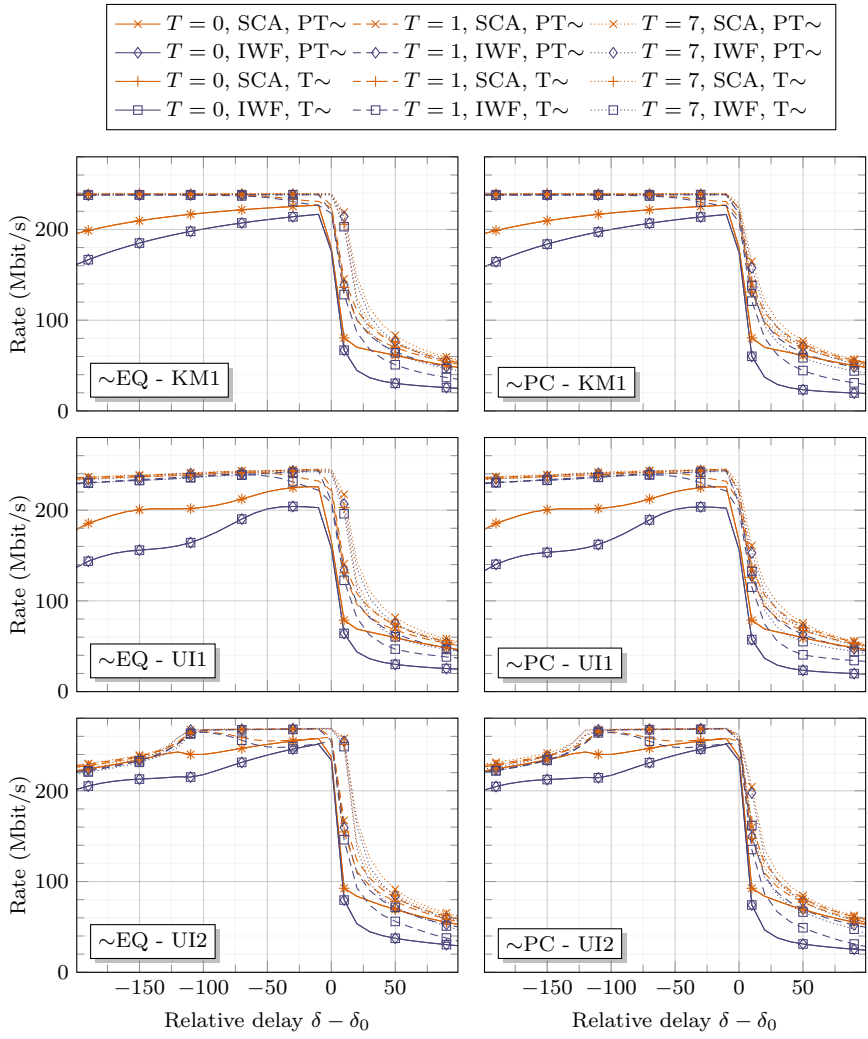


Figure 6.4: Data rate achieved by the considered CP-DMT systems with TEQ, PTEQ, TPC, and PTPC after 10 iterations of either the SCA or the IWF algorithm. Delays are relative to a reference delay δ_0, which is chosen by maximizing the energy in $\left[h[\delta_0], \ldots, h[\delta_0 + \nu]\right]$ as in [6]. The granularity of the delay sweep is 10 samples. The considered CP length is $\nu = 320$.

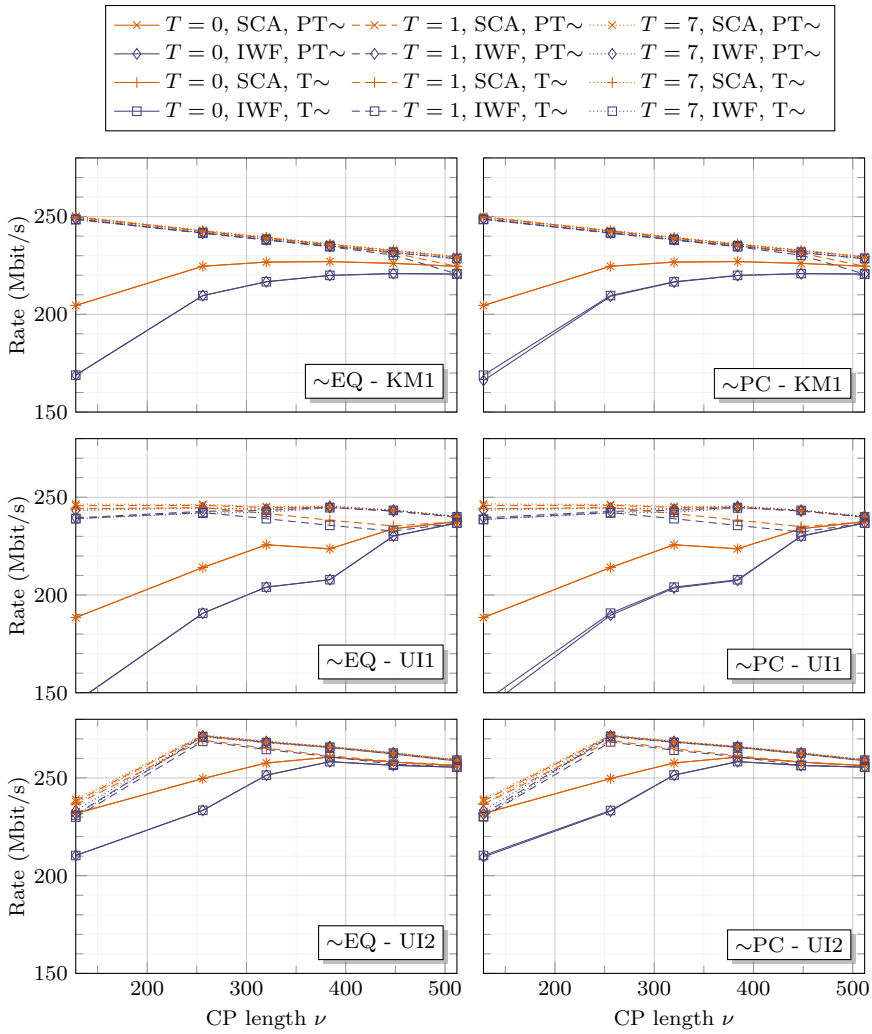


Figure 6.5: Data rate achieved by the considered CP-DMT systems with TEQ, PTEQ, TPC, and PTPC for different CP lengths. The data points correspond to the maximum data rates that are achieved when sweeping the delay δ from $\delta_0 - 200$ to $\delta_0 + 100$ with a granularity of 10 samples, as in Figure 6.4.

employing the duality result in Section 6.4.2 to obtain the corresponding TPC filter coefficients and power allocation vector.

Figure 6.5 presents the data rate achieved by the considered CP-DMT systems with TEQ, PTEQ, TPC, and PTPC for different CP lengths. For each CP length ν, the data points in Figure 6.5 correspond to the maximum data rates that are achieved for a delay sweep as presented in Figure 6.4.

A first observation that can be made from Figure 6.4 and Figure 6.5 is that, even for PTEQ/PTPC with $T = 0$ (which corresponds to merely FEQ), careful design of the transmit PSDs can lead to data rates that form an interesting middle ground between true PTEQ/PTPC with $T > 0$, and ISI/ICI-unaware resource allocation. The advantage here, of course, would be that this increase in performance is achieved without the additional system and computational complexity incurred by true PTEQ/PTPC with $T > 0$.

A second observation is that the results obtained for the CP-DMT system with TEQ or PTEQ and those obtained for the CP-DMT system with TPC or PTPC are nearly indistinguishable. As such, TPC and PTPC may be an interesting alternative channel shortening strategy in scenarios where implementing TEQ or PTEQ is either difficult or costly. For instance, in downstream DSL systems, TPC and PTPC enable the implementation of channel shortening without replacing the customer premises equipment. It is noted that this similar performance may be contingent on the assumption of i.i.d. time-domain noise, as it is expected that TEQ and PTEQ can exploit a correlation between noise samples better than TPC and PTPC. While certainly possible, extending the models and algorithms in this chapter to include colored noise would further obfuscate the derivations, and is therefore considered to be out-of-scope.

Finally, it is observed in Figure 6.5 that—even in a single user system—performance improvements can be obtained by reducing the CP length and employing a short channel shortening filter.

6.5.2 SCA convergence

Figure 6.6 illustrates the convergence behavior of the SCA algorithm. It shows the distribution of the distance to optimal rate after each iteration t, i.e. the relative difference between the data rate after iteration t and the data rate after iteration 350. The results are obtained by tracking the achieved data rate during all runs of the SCA algorithm that are used to obtain results of the systems with PTPC in Section 6.5.1.

Figure 6.6 confirms that the SCA algorithm yields no significant further data

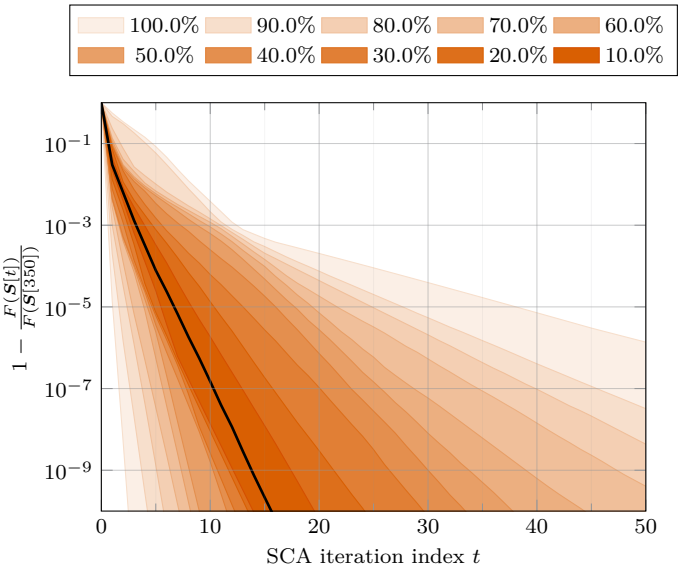


Figure 6.6: Distribution of the distance to optimal rate after each iteration t, i.e. the relative difference between the data rate after iteration t and the data rate after iteration 350. The black line shows the median distance to optimal rate, and the shaded areas show different percentiles of the distance to optimal rate distribution centered around the median.

rate improvement after the first 20 iterations. However, it does not confirm that the obtained solution is anywhere near a stationary point of problem (6.57). In order to do so, Figure 6.7 additionally illustrates the distribution of the KKT error function ϵ_t as defined in [51, Eq. 9] after each iteration. It is noted that ϵ_t does not necessarily converge to zero [51] for any sequence approaching a KKT point; its definition requires some tweaking before being applicable as a termination criterion for the SCA algorithm. However, the fact that the obtained solution after 350 iterations yields a very small KKT error—more than 10 orders of magnitude smaller than the KKT error obtained after the first iteration—implies that it lies close to a stationary point of problem (6.57) [51, Theorem 3.2]. It can thus be concluded that, for the considered systems, only 10 to 20 iterations of the SCA algorithm are needed to obtain an accurate solution to problem (6.57).

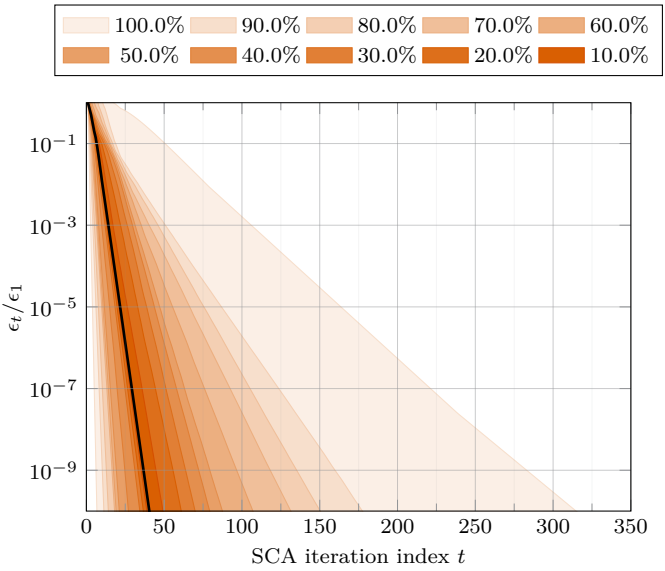


Figure 6.7: Distribution of the relative KKT error ϵ_t after each iteration t. The black line shows the median relative KKT error, and the shaded areas show different percentiles of the relative KKT error distribution centered around the median.

6.6 Conclusion & future work

In this chapter, a new algorithm to simultaneously optimize receiver-side channel shortening PTEQ filter coefficients and transmit power allocation in OFDM and DMT systems with ZP or CP has been presented. The algorithm provably converges to a stationary point of the considered rate maximization problem, and requires only few iterations to achieve sufficient accuracy. Moreover, using this resource allocation method, it has been demonstrated that iterative water filling schemes can achieve good performance when the ISI/ICI is sufficiently suppressed by the PTEQ filter. In addition, transmitter-side channel shortening PTPC has been considered. A duality result linking OFDM/DMT systems with PTPC to OFDM/DMT systems with PTEQ has been provided. With this duality result in hand, PTPC systems can take full advantage of the straightforward FIR filter optimization in PTEQ systems, as well as of the developed resource allocation algorithm. Simulation results have shown that the performance obtained for OFDM/DMT systems with PTEQ is nearly indistinguishable from that obtained for OFDM/DMT systems with PTPC, making PTPC an interesting alternative channel shortening strategy in scenarios

where implementing PTEQ is either difficult or costly.

In future work, the presented algorithms and results will be extended to multi-user systems. The joint PTEQ filter optimization and resource allocation algorithm from Section 6.3 readily extends to multi-user uplink systems—where PTEQ is thus applied at the base station—as the surrogate problem from Section 6.3.2 will be separable into subproblems that can be solved using the algorithm from Section 6.3.3. Moreover, the results from Section 6.4.2 can likely be generalized to establish a PTEQ-PTPC duality between multi-user uplink systems with PTEQ and multi-user downlink systems with PTPC, provided that a single base station-wide aggregate transmit power constraint is considered. If multi-user downlink systems with PTPC and per antenna or per line power constraints are considered—as would be customary in DSL networks [108,111,202]—PTEQ-PTPC duality can likely still be used to show an equivalence between the Lagrangian of the resulting rate maximization problem and the Lagrangian of a rate maximization problem in a multi-user uplink system with PTEQ, similar to e.g. [108, 202]. However, algorithms that are based on evaluating the Lagrange dual function by maximizing the Lagrangian of a rate maximization problem in a multi-user uplink system with PTEQ will likely exhibit a prohibitively high computational complexity, as they will require evaluating the SINR γ_n of each subcarrier n in each iteration of their inner loop. Overcoming this complexity obstacle will then represent an additional challenge.

Acknowledgment

The authors would like to thank Wouter Lanneer for proof reading the manuscript and for his constructive criticism.

Chapter 7

DSM and Widely Linear Channel Shortening

Signal Impropriety in Discrete Multi-Tone Systems and Widely Linear Per-Tone Equalization

Jeroen Verdyck, Yannick Lefevre, Paschalis Tsiaflakis, and Marc Moonen

Published in *IEEE Open Journal of the Communications Society*, Vol. 2, pp. 367-383, February 2021, DOI: 10.1109/OJCOMS.2021.3058177.

© 2021 IEEE. Reprinted, with permission, from:
Jeroen Verdyck, Yannick Lefevre, Paschalis Tsiaflakis, and Marc Moonen, "Signal Impropriety in Discrete Multi-Tone Systems and Widely Linear Per-Tone Equalization," *IEEE Open Journal of the Communications Society*, Vol. 2, pp. 367-383, February 2021.
Changes include layout, representation, and minor editing aspects.

The candidate's contributions as first author include: all performed research and writing of the article under guidance of the co-authors.

Abstract

In the context of digital subscriber line (DSL) systems, where the long-reach (LR) extension of G.fast has recently been proposed, interest in techniques dealing with long channel impulse responses (CIRs) without increasing the cyclic prefix (CP) length of the discrete multi-tone (DMT) modulation has recently resurfaced. The technique under consideration in this chapter is referred to as *channel shortening*, and applies FIR filters to the received signal to shorten the apparent CIR. Time-domain equalization (TEQ) as well optimal per-tone equalization (PTEQ) FIR filters will be considered.

When channel shortening techniques are analyzed, it is often overlooked that the received signals after DMT demodulation are generally *improper* when the CP is too short. Hence, the state-of-the-art signal-to-interference-plus-noise ratio (SINR) and bit loading expressions employed to assess system performance, which implicitly assume the received signals to be proper, misrepresent the true achievable performance. New expressions for the SINR and bit loading are therefore presented that explicitly take signal impropriety into account. Based on these expressions, it is then observed that—if the received signals are improper—the PTEQ FIR filters are no longer optimal, and that the achievable bit loading depends on a particular phase shift experienced by the transmitted signals. This chapter therefore introduces a novel widely linear PTEQ—which is again optimal when the received signals are improper—and additionally proposes to optimally rotate signals in the complex plane prior to transmission. Finally, this chapter assesses the performance increase obtainable by explicitly accounting for signal impropriety.

7.1 Introduction

G.fast is a digital subscriber line (DSL) standard [95, 96] for discrete multi-tone (DMT) based transmission over short local loops. An extension of the G.fast standard has recently been proposed, enabling its use on DSL loops with a length in excess of the originally intended 300 m limit [52,77,128,180,181]. These longer lines are currently operated with legacy DSL technologies (such as VDSL). The ability to let them be operated with G.fast would enable convergence to a single DSL standard, thereby eliminating co-existence problems between different DSL generations. Key enabling factors for this so-called long-reach (LR) extension of G.fast will be larger constellation sizes [77], a higher maximum aggregate transmit power [77, 181], the application of a looser spectral mask at low frequencies [181], and a longer cyclic prefix (CP) to support longer lines [181].

The CP—which is added to each DMT symbol prior to transmission—serves a dual purpose: 1) it eliminates inter-symbol-interference (ISI) between consecutive DMT symbols, and 2) it eliminates inter-carrier-interference (ICI) between subcarriers of the same DMT symbol. This elimination of the ISI/ICI is however contingent on the CP length plus one being at least equal to the channel impulse response (CIR) length. Supporting longer CPs as part of the LR extension of G.fast thus seems natural, as longer lines are indeed more dispersive.

However, there is an argument to be made against the use of a long CP as well. This argument relates to the fact that a G.fast system requires the same CP length to be applied across all users in the system both in upstream and in downstream [96]. When a mix of long and short lines is connected to the same distribution point unit (DPU), using a longer CP to accommodate the more dispersive long lines will inevitably reduce the data rate on shorter lines. Based on this observation, interest in techniques that can deal with long CIRs without increasing the CP length has recently resurfaced.

The technique under consideration in this chapter is referred to as channel shortening. Proposed first by Chow *et al.* [38], early channel shortening methods consisted of applying a time-domain equalization (TEQ) FIR filter to the received signal prior to DMT demodulation. The coefficients of this FIR filter were then chosen such that the channel and TEQ combined have an impulse response which is shorter than the original CIR. Optimal TEQ filter design has however proven to be challenging, leading to a plethora of design heuristics [11, 12, 38, 75, 124, 132, 166, 201]. In order to simplify the filter design, Van Acker *et al.* [6] proposed moving the TEQ filter to the frequency domain—i.e. to after the DMT demodulation. The resulting channel shortening method is referred to as per-tone equalization (PTEQ), and has two important advantages over TEQ. Firstly, PTEQ generalizes TEQ—i.e. any TEQ filter can be implemented as a PTEQ filter, while the reverse is not true—without incurring a significant complexity increase. Secondly, the PTEQ filter coefficients that maximize the data rate can be calculated analytically, whereas TEQ design is notoriously challenging.

When channel shortening performance is analyzed in the context of DMT systems [6,11,12,38,75,124,132,146,166,201,203], there is a particular aspect that is often overlooked: if the CP is too short, then the received signal after DMT demodulation (prior to a soft/hard decision operation) is generally *improper* [179, 184]. A zero-mean complex random variable Z is proper if its pseudo-variance vanishes [8]—i.e. if $\mathbb{E}\{Z^2\} = 0$—or, equivalently, if its real and imaginary part are uncorrelated and have equal variance—i.e. if $\mathbb{E}\{\Re(Z)\Im(Z)\} = 0$ and

$\mathbb{E}\{\Re(Z)^2\} = \mathbb{E}\{\Im(Z)^2\}$.[1] This definition can be extended to a random vector $\boldsymbol{Z}$, which is called proper if its pseudo-covariance matrix vanishes [8]—i.e. if $\mathbb{E}\{\boldsymbol{Z}\boldsymbol{Z}^{\mathrm{T}}\} = \mathbf{0}$. Examples of processes that produce proper random signals include the circularly symmetric complex Gaussian noise process, and randomly drawing symbols from a square 16-QAM constellation with uniform probability. An important property of propriety is that it is preserved under complex linear mappings—i.e. if $\mathbf{A} \in \mathbb{C}^{N\times M}$ and $\boldsymbol{Z}$ is a proper random vector, then $\mathbf{A}\boldsymbol{Z}$ is proper as well [73]. Consequently, a system's output will be proper if it can be written as a linear function of a proper input.

A first cause of impropriety in DMT systems with a too-short CP is that the received signal after DMT demodulation is not a linear function of the transmitted signal. Generally, it is a widely linear function of the transmitted signal, i.e. the relation between the input of the DMT system—represented by a vector $\boldsymbol{X}$—and the output after DMT demodulation—represented by a vector $\boldsymbol{Y}$—can be written as[2]

$$\boldsymbol{Y} = \mathbf{A}_1\boldsymbol{X} + \mathbf{A}_2\boldsymbol{X}^*. \tag{7.1}$$

Unlike linear mappings, widely linear mappings do not preserve propriety in general. As an example, consider the random variable $Y = X + X^* = 2\Re(X)$. This random variable is clearly improper, even if X is proper. In fact, Y in this example is said to be *maximally improper* because the support of its probability density function degenerates into a line in the complex plane [8]. Likewise in DMT systems, the transmitter's output signal is forced to be real-valued by letting some subcarriers transmit $\boldsymbol{X}$, and letting other subcarriers transmit $\boldsymbol{X}^*$. With a too-short CP, and hence ISI/ICI, this in particular will result in improper ISI/ICI and possibly a loss of orthogonality and difference in scaling between the real and imaginary parts of the transmitted signal.

A second cause of impropriety in DMT systems is the real-valued time-domain noise. If this noise is white, as is often assumed, then the noise after DMT demodulation will be proper [184]. If a TEQ filter is applied before the DMT demodulation however, then the resulting spectrally shaped time-domain noise may yield noise after the DMT demodulation that is improper [184]. A PTEQ can similarly render the noise improper, as the PTEQ output noise is a linear combination of the proper DFT output noise and multiple independent maximally improper noise contributions (see below). It can be concluded that, even if a channel shortening (P)TEQ filter is able to eliminate all

[1] The mathematical notation employed in these paragraphs is introduced at the end of Section 7.1.

[2] Equation (7.1) is intentionally kept a bit vague at this point. The purpose of this equation is to introduce the sources of signal impropriety in DMT systems, not to give a detailed system model of the considered DMT systems. A more detailed DMT system model will be provided in Section 7.2.

ISI/ICI, improper noise can still be present in the received signal after DMT demodulation.

Even though signal impropriety seems to be inherent to DMT systems with a too-short CP using either TEQ or PTEQ, its effects are not taken into account in [6, 11, 12, 38, 75, 124, 132, 146, 166, 201, 203]. As a result, the state-of-the-art signal-to-interference-plus-noise ratio (SINR) and bit loading expressions employed to assess system performance in these works—which implicitly assume that the received signal after DMT demodulation is proper—mis-represent the true achievable performance. It has also been shown in [184] that explicitly accounting for the noise impropriety can increase performance in DMT systems, even in the absence of ISI/ICI. Even though it is assumed in [184] that the CP is sufficiently long and hence ISI/ICI and channel shortening are not considered, the results in [184] suggest that explicitly accounting for signal impropriety in channel shortening filter design may also increase performance.

The objective of this chapter will therefore be twofold. The first objective is to present expressions for the SINR and bit loading that explicitly take all signal impropriety into account—i.e. the impropriety of the ISI/ICI and of the noise. These expressions will be instrumental in assessing the performance of channel shortening methods in LR G.fast systems. It is noted that an accurate performance prediction is crucial to determine the number of subscribers that can be served with a minimum data rate service, a key factor to assess the economic viability of LR G.fast. The second objective is to use these new SINR and bit loading expressions for PTEQ filter design, and to assess the performance increase that can be obtained in LR G.fast systems by explicitly accounting for signal impropriety.

Contributions & outline

In Section 7.2 and Section 7.3, the system model and problem statement will be introduced. In Section 7.4, new SINR and bit loading expressions will be presented for DMT systems with (P)TEQ that are valid when the received signal after DMT demodulation is improper. In Section 7.5, system performance—which can now be evaluated using the expressions from Section 7.4—will be optimized.

The performance optimization in Section 7.5 will be based on two observations: 1) when the SINR and bit loading expressions from Section 7.4 are employed, no analytical expression is available for the optimal PTEQ filter coefficients, and 2) if the ISI/ICI is improper, then the achievable bit loading of each subcarrier depends on a particular phase shift experienced by the transmitted signal. To address the first observation, it will be proposed in Section 7.5.1 to further

generalize the PTEQ to a widely linear (WL) PTEQ. The main advantage of WL PTEQ over PTEQ—apart from generalizing PTEQ without incurring a significant complexity increase—will also be introduced: if the SINR and bit loading expressions from Section 7.4 are employed, then the optimal WL PTEQ coefficients can indeed be calculated analytically. To tackle the second problem, it will be proposed in Section 7.5.2 to optimally rotate signals in the complex plane prior to transmission.

Finally, in Section 7.6, LR G.fast DSL simulation results will demonstrate that explicitly taking signal impropriety into account leads to an increased achievable bit loading when residual ISI/ICI is present in the system. When the employed channel shortening method is able to eliminate most of the ISI/ICI, the impact of impropriety is reduced and the gap between the state-of-the-art SINR and bit loading expressions from [6, 11, 12, 38, 75, 124, 132, 146, 166, 201, 203] and the newly developed expressions disappears.

Notation

Throughout the chapter, zero-based indexing will be used when addressing vector and matrix elements, i.e. an $N \times M$ matrix $\mathbf{A}$ is defined as follows:

$$\mathbf{A}^{\mathrm{T}} = \left[(\mathrm{row}_0(\mathbf{A}))^{\mathrm{T}}, \ldots, (\mathrm{row}_{N-1}(\mathbf{A}))^{\mathrm{T}}\right];$$

$$\mathbf{A} = \left[\mathrm{col}_0(\mathbf{A}), \ldots, \mathrm{col}_{M-1}(\mathbf{A})\right];$$

$$[\mathbf{A}]_{n,m} = \mathrm{row}_n\left(\mathrm{col}_m(\mathbf{A})\right).$$

The dimension subscripts in $\mathbf{I}_N$ and $\mathbf{0}_{N\times M}$ will be omitted when they can be derived from the context. The real and complex parts of a matrix $\mathbf{A}$ will be denoted as $\Re(\mathbf{A})$ and $\Im(\mathbf{A})$, such that $\mathbf{A} = \Re(\mathbf{A}) + j\Im(\mathbf{A})$.

7.2 DMT system model & per-tone equalization

This section introduces a general model for DMT systems with per-tone equalization (PTEQ), and presents expressions for the achieved SINR and achievable bit loading as they are commonly found in literature [6, 146, 166, 201, 203].[3]

[3] References [11, 12, 38, 75, 124, 132] have not been included here, as the SINR expressions in these works do not take part of the desired signal or ISI/ICI into account.

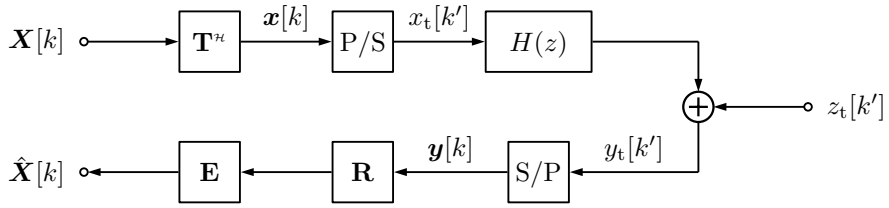


Figure 7.1: Signal flow graph of a general DMT system.

7.2.1 DMT transceiver

Figure 7.1 depicts the signal flow graph of a general DMT system consisting of an encoder $\mathbf{T}^{\varkappa}$, a decoder $\mathbf{R}$, a serial-to-parallel (S/P) and a parallel-to-serial (P/S) converter, and a frequency-selective channel that is modeled as an FIR filter with real coefficients $H(z) = \sum_{k'=0}^{L} z^{-k'} h[k']$. It is noted that L does not define the CIR length but rather the channel order. The CIR length is thus $L+1$. The complex vectors $\boldsymbol{X}[k] \triangleq [X_0[k], X_1[k], , \ldots, X_{N-1}[k]]^{\mathrm{T}}$ and $\hat{\boldsymbol{X}}[k] \triangleq [\hat{X}_0[k], \hat{X}_1[k], \ldots, \hat{X}_{N-1}[k]]^{\mathrm{T}}$ respectively denote the frequency-domain input—with each $X_n[k]$ being a quadrature amplitude modulation (QAM) symbol—and the received signal after DMT demodulation but prior to a soft/hard decision operation, where N is the employed DFT size (see below) and k is the DMT symbol index. A different sample index k' is used between the P/S converter and the S/P converter, as these respectively execute an upsampling and a downsampling operation. It will be assumed that $X_n[k]$ is proper—i.e. that $\mathbb{E}\{(X_n[k])^2\} = 0$—and that the time-domain noise $z_{\mathrm{t}}[k']$ is white. The subscript 't' is used for time-domain signals. The subcarrier power and time-domain noise power will respectively be denoted as $S_n \triangleq \mathbb{E}\{X_n[k]X_n^*[k]\}$ and $\sigma_{\mathrm{t}}^2 = \mathbb{E}\{|z_{\mathrm{t}}[k']|^2\}$.

CP-based DMT will be considered, in which the transmitter modulates the complex vector $\boldsymbol{X}[k]$ by application of an inverse discrete Fourier transform (IDFT), by adding a CP and a cyclic suffix (CS) to the IDFT output, and by windowing the result. The k-th transmitted DMT symbol is thus

$$\boldsymbol{x}[k] = \mathbf{T}^{\varkappa}\boldsymbol{X}[k] = \mathbf{C}\left[\begin{array}{c|c} \mathbf{0}_{\nu_{\mathrm{p}}\times(N-\nu_{\mathrm{p}})} & \mathbf{I}_{\nu_{\mathrm{p}}} \\ \hline \mathbf{I}_N & \\ \hline \mathbf{I}_{\nu_{\mathrm{s}}} & \mathbf{0}_{\nu_{\mathrm{s}}\times(N-\nu_{\mathrm{s}})} \end{array}\right]\mathbf{F}_N^{-1}\boldsymbol{X}[k], \tag{7.2}$$

with ν_{p} the CP length, ν_{s} the CS length, $\mathbf{C}$ the diagonal windowing matrix, and $\mathbf{F}_N^{-1}$ the N-point IDFT matrix. The following definition is used for the

N-point discrete Fourier transform (DFT) matrix $\mathbf{F}_N$.

$$[\mathbf{F}_N]_{n,m} \triangleq \alpha^{-nm} \qquad \alpha \triangleq e^{2\pi j/N} \tag{7.3}$$

It is assumed that the windowing matrix $\mathbf{C}$ satisfies

$$[\mathbf{C}]_{i,i} = 1 \qquad \text{for } \nu_\mathrm{s} \leq i \leq N + \nu_\mathrm{p} - 1, \tag{7.4a}$$

$$[\mathbf{C}]_{i,i} = 1 - [\mathbf{C}]_{j,j} \qquad \text{for } 0 \leq i \leq \nu_\mathrm{s} - 1 \text{ and } j = N + \nu_\mathrm{p} + i. \tag{7.4b}$$

The employed window is thus symmetric, and its flat part is $N + \nu_\mathrm{p} - \nu_\mathrm{s}$ samples long.[4] Prior to transmission, consecutive windowed DMT symbols $\boldsymbol{x}[k]$ are overlapped by ν_s samples and summed together to form the time-domain symbol stream $x_\mathrm{t}[k']$.[5] Taking this overlap of DMT symbols in the time domain into account, it is seen that the DMT symbol period can be denoted as $s = N + \nu_\mathrm{p}$.

At the receiver, the cyclic prefix and suffix are discarded, yielding the received signal vector $\boldsymbol{y}[k] \triangleq \big[y_\mathrm{t}[ks], y_\mathrm{t}[ks+1], \ldots, y_\mathrm{t}[ks+N-1]\big]^\mathrm{T}$. DMT demodulation further consists of the application of a DFT and a frequency-domain equalization (FEQ), such that the output $\hat{\boldsymbol{X}}[k]$ can be expressed as

$$\hat{\boldsymbol{X}}[k] = \mathbf{E}\mathbf{R}\boldsymbol{y}[k] = \mathbf{E}\mathbf{F}_N\boldsymbol{y}[k], \tag{7.5}$$

with $\mathbf{E}$ the diagonal FEQ matrix. Assuming perfect synchronization between the transmitter-side P/S converter and receiver-side S/P converter, each $\hat{X}_n[k]$ will be free of ISI/ICI if $\nu_\mathrm{p} \geq L + \nu_\mathrm{s}$.

DMT systems operate at baseband, resulting in the requirement that the DMT symbols $\boldsymbol{x}[k]$ be real-valued. In (7.2), this requirement is satisfied if and only if $\boldsymbol{X}[k]$ admits the following Hermitian symmetric structure:

$$X_{n^*}[k] = X_n^*[k], \forall n, \tag{7.6}$$

where—with a slight abuse of notation—n^* is the index of the subcarrier that is the Hermitian symmetric of subcarrier n, i.e. where $n^* \triangleq (N - n) \mod N$. The DFT size N is assumed to be even.

[4] At this point, one could also explicitly give the elements of the windowing matrix rather than defining the constraint as in (7.4). However, the G.fast standard [96] mentions that the "values of the window samples are vendor discretionary." By defining the exact values of the window matrix elements only in Section 7.6, the developed theoretical derivations in the ensuing sections are—like the G.fast standard—valid regardless of the employed transmit window.

[5] A more detailed mathematical representation of this overlap-and-sum operation is given in (7.12), see below.

7.2.2 Channel shortening - TEQ & PTEQ

PTEQ [6] is introduced here by first adding a time-domain equalization (TEQ) filter to the receiver, and then deriving PTEQ from TEQ. The idea of TEQ is to apply a T-order FIR filter $W(z) = \sum_{k'=0}^{T} z^{-k'} w[k']$ with real coefficients to $y_{\mathrm{t}}[k']$ in order to shorten the channel impulse response (CIR), thereby reducing the required ν_{p} for ISI/ICI-free transmission and hence decreasing the corresponding overhead. The DMT receiver with TEQ thus convolves the received signal $y_{\mathrm{t}}[k']$ with the filter coefficients of $W(z)$ before applying the DMT decoding and equalization matrices $\mathbf{R}$ and $\mathbf{E}$. The operation executed by the DMT receiver with TEQ can be expressed as

$$\hat{\boldsymbol{X}}[k] = \mathbf{E}\mathbf{R} \begin{bmatrix} \boxed{\boldsymbol{w}^{\mathrm{T}}} & 0 & \cdots \\ 0 & \ddots & \ddots \\ \vdots & \ddots & \boxed{\boldsymbol{w}^{\mathrm{T}}} \end{bmatrix} \bar{\boldsymbol{y}}[k], \tag{7.7}$$

where

$$\bar{\boldsymbol{y}}[k] \triangleq \big[y_{\mathrm{t}}[ks-T], y_{\mathrm{t}}[ks-T+1], \ldots, y_{\mathrm{t}}[ks+N-1]\big]^{\mathrm{T}}$$

is the extended received signal vector, and the $N \times (N+T)$ Toeplitz matrix contains N shifted copies of the TEQ filter coefficient vector $\boldsymbol{w}^{\mathrm{T}} \triangleq \big[w[T], w[T-1], \ldots, w[0]\big]$.

PTEQ is obtained from TEQ by transferring the filter $W(z)$ to the frequency domain—i.e. to after the DFT operation [6]—which can be done based on the following reformulation of equation (7.7), where $E_n \triangleq \big[\mathbf{E}\big]_{n,n}$.

$$\hat{X}_n[k] = \underbrace{(E_n \boldsymbol{w}^{\mathrm{T}})}_{\triangleq \boldsymbol{w}_n^{\mathcal{H}}} \begin{bmatrix} \boxed{\mathrm{row}_n(\mathbf{R})} & 0 & \cdots \\ 0 & \ddots & \ddots \\ \vdots & \ddots & \boxed{\mathrm{row}_n(\mathbf{R})} \end{bmatrix} \bar{\boldsymbol{y}}[k] \tag{7.8}$$

The $(T+1) \times (N+T)$ Toeplitz matrix in (7.8) contains $T+1$ shifted copies of $\mathrm{row}_n(\mathbf{R})$. Intuitively, the equivalence between (7.7) and (7.8) can be understood by interpreting the multiplication with $\mathbf{R}$ in (7.7) as applying a filter bank to the output of the TEQ—with FIR filters given as $R_n(z) = \sum_{k'=0}^{N-1} z^{-k'} \,\mathrm{col}_{N-1-k'}\,(\mathrm{row}_n(\mathbf{R}))$—followed by a downsampling operation, and considering the fact that the filters $R_n(z)$ and $W(z)$ commute. Equation (7.8) reveals that the receiver with PTEQ allows each subcarrier to have its own TEQ, which is then implemented as a T-th order FEQ filter with filter coefficients $\boldsymbol{w}_n^{\mathcal{H}} \triangleq \big[w_n[T], w_n[T-1], \ldots, w_n[0]\big]$.

It may appear that PTEQ incurs a significant run-time complexity increase w.r.t. TEQ, as the direct implementation of (7.8) would effectively require

$T+1$ DFT operations (cf. number of rows in the Toeplitz matrix) to be executed [6]. Moreover, even though the NT time-domain multiplications per received DMT symbol required by TEQ have been replaced by $\frac{N}{2}+1$ times T multiplications in the frequency domain—apparently halving the required number of multiplications—these frequency-domain multiplications are complex-valued, e.g. requiring 4 real multiplications each and further adding to the run-time complexity of PTEQ. Fortunately, it has been shown in [6] that both effects can be alleviated by decomposing the Toeplitz matrix in (7.8) into a lower triangular matrix $\mathbf{L}_n$ and a sparse matrix $\mathbf{R}_n$, i.e.

$$\begin{bmatrix} \boxed{\mathrm{row}_n(\mathbf{R})} & 0 & \cdots \\ 0 & \ddots & \ddots \\ \vdots & \ddots & \boxed{\mathrm{row}_n(\mathbf{R})} \end{bmatrix} = \mathbf{L}_n\mathbf{R}_n \tag{7.9}$$

where

$$\mathbf{L}_n \triangleq \begin{bmatrix} \alpha^{0n} & 0 & \cdots & 0 \\ \alpha^{1n} & \ddots & \ddots & \vdots \\ \vdots & \ddots & \ddots & 0 \\ \alpha^{Tn} & \cdots & \alpha^{1n} & \alpha^{0n} \end{bmatrix} \begin{bmatrix} 1 & \mathbf{0}_{1\times T} \\ \mathbf{0}_{T\times 1} & \alpha^n\mathbf{I}_T \end{bmatrix}, \tag{7.10a}$$

$$\mathbf{R}_n \triangleq \left[\begin{array}{cc|c} & \boxed{\mathrm{row}_n(\mathbf{R})} & \mathbf{0}_{1\times T} \\ -\mathbf{I}_T & \mathbf{0}_{T\times(N-T)} & \mathbf{I}_T \end{array}\right]. \tag{7.10b}$$

With this decomposition, equation (7.8) becomes

$$\hat{X}_n[k] = \boldsymbol{v}_n^{\mathrm{H}}\mathbf{R}_n\bar{\boldsymbol{y}}[k], \tag{7.11}$$

where $\boldsymbol{v}_n \triangleq \mathbf{L}_n^{\mathrm{H}}\boldsymbol{w}_n$ is merely an alternative PTEQ filter representation. In addition, $\boldsymbol{y}_n[k] \triangleq \mathbf{R}_n\bar{\boldsymbol{y}}[k]$ will denote the vector of PTEQ filter inputs on subcarrier n. The receiver with PTEQ can thus obtain $\hat{X}_n[k]$ as a linear combination of the output of a single DFT (cf. first row of $\mathbf{R}_n$) and T real-valued difference terms $y_{\mathrm{t}}[ks+N-t]-y_{\mathrm{t}}[ks-t]$ with $t\in\{1,2,\ldots,T\}$ (cf. last T rows of $\mathbf{R}_n$).

A more detailed overview of the run-time complexity of both TEQ and PTEQ is given in Table 7.1. It has been assumed that the subcarriers corresponding to the DC and Nyquist frequency are inactive, and that w.l.o.g. the first coefficient of the TEQ filter equals 1. Moreover, $n_\times$ and n_+ represent the number of real multiplications and additions that are required to execute a complex multiplication. Note that the values of $n_\times$ and n_+ are implementation-dependent.

Table 7.1: Number of floating point operations required by channel shortening and equalization a DMT receiver.

	Nb. real multiplications	Nb. real additions
TEQ	TN	TN
FEQ	$n_\times \left(\frac{N}{2}-1\right)$	$n_+ \left(\frac{N}{2}-1\right)$
T+F	$\left(\frac{N}{2}-1\right)(2T+n_\times)+2T$	$\left(\frac{N}{2}-1\right)(2T+n_+)+2T$
PTEQ	$\left(\frac{N}{2}-1\right)(2T+n_\times)$	$\left(\frac{N}{2}-1\right)(2T+n_+)+T$

The most common implementations result in $n_\times = 4$ and $n_+ = 2$ [73], or in $n_\times = 3$ and $n_+ = 5$ [103, pp. 591 & 706]. Regardless of which implementation is considered, it can be concluded from Table 7.1 that PTEQ has a complexity that is comparable to that of the combination of a TEQ and a FEQ (T+F).

7.2.3 Signal-to-interference-plus-noise ratio

An expression for the SINR in DMT systems using PTEQ can be derived as follows. The channel equation for a DMT system using PTEQ is given as

$$\bar{\boldsymbol{y}}[k] = \underbrace{\left[\begin{array}{c|ccc|c} \mathbf{O}_1 & \boldsymbol{h}^{\mathrm{T}} & 0 & \cdots & \mathbf{O}_2 \\ & 0 & \ddots & \ddots & \\ & \vdots & \ddots & \boldsymbol{h}^{\mathrm{T}} & \end{array}\right]}_{\triangleq \mathbf{H}} \left[\begin{array}{ccc} \mathbf{T}^{\mathcal{H}} & \mathbf{0}_{s\times N} & \mathbf{0}_{s\times N} \\ \mathbf{0}_{s\times N} & \mathbf{T}^{\mathcal{H}} & \mathbf{0}_{s\times N} \\ \mathbf{0}_{s\times N} & \mathbf{0}_{s\times N} & \mathbf{T}^{\mathcal{H}} \end{array}\right] \left[\begin{array}{c} \boldsymbol{X}[k-1] \\ \boldsymbol{X}[k] \\ \boldsymbol{X}[k+1] \end{array}\right] + \bar{\boldsymbol{z}}[k]. \quad (7.12a)$$

In (7.12a), the $(N+T)\times(3s+\nu_\mathrm{s})$ Toeplitz matrix $\mathbf{H}$ contains $N+T$ shifted copies of the channel vector $\boldsymbol{h}^{\mathrm{T}} \triangleq \big[h[L], h[L-1], \ldots, h[0]\big]$. Moreover, the extended noise vector is denoted as $\bar{\boldsymbol{z}}[k] \triangleq \big[z_\mathrm{t}[ks-T], z_\mathrm{t}[ks-T+1], \ldots, z_\mathrm{t}[ks+N-1]\big]^{\mathrm{T}}$. The dimensions of the all-zero matrices $\mathbf{O}_1$ and $\mathbf{O}_2$ are respectively given as $(N+T)\times(s+\nu_\mathrm{p}-L-T+\delta)$ and $(N+T)\times(s+\nu_\mathrm{s}-\delta)$, where δ denotes the so-called synchronization delay [6].[6] By partitioning the Toeplitz matrix $\mathbf{H}$ into three overlapping $(N+T)\times(s+\nu_\mathrm{s})$ matrices $\{\mathbf{H}[l]\}_{l=\{-1,0,1\}}$, equation

[6]It has implicitly been assumed that $s+\nu_\mathrm{p}+\delta \geq L+T$ and $s+\nu_\mathrm{s} \geq \delta$. The case where either condition is not satisfied can be accommodated for by extending the rows of $\mathbf{H}$ and including more interfering symbols $\boldsymbol{X}[k-a]$.

(7.12a) can be rewritten as

$$\bar{\boldsymbol{y}}[k] = \sum_{l=-1}^{1} \mathbf{H}[l] \sum_{m=0}^{N-1} \mathrm{row}_m(\mathbf{T})^{\mathcal{H}} X_m[k+l] + \bar{\boldsymbol{z}}[k]. \tag{7.12b}$$

Finally, by defining the residual channel vectors $\boldsymbol{h}_{nm}[l]$ and residual channel matrices $\mathbb{H}_{nm}$ as

$$\boldsymbol{h}_{nm}[l] \triangleq \mathbf{R}_n \mathbf{H}[l] \, \mathrm{row}_m(\mathbf{T})^{\mathcal{H}}, \tag{7.13a}$$

$$\mathbb{H}_{nm} \triangleq \begin{cases} \begin{bmatrix} \boldsymbol{h}_{nm}[-1] & \boldsymbol{h}_{nm}[0] & \boldsymbol{h}_{nm}[1] \end{bmatrix} & \text{if } m \notin \{n, n^*\} \\ \begin{bmatrix} \boldsymbol{h}_{nm}[-1] & \mathbf{0}_{(T+1)\times 1} & \boldsymbol{h}_{nm}[1] \end{bmatrix} & \text{if } m \in \{n, n^*\} \end{cases} \tag{7.13b}$$

and by introducing $\boldsymbol{h}_n \triangleq \boldsymbol{h}_{nn}[0]$, as well as $\tilde{\boldsymbol{h}}_n \triangleq \boldsymbol{h}_{nn^*}[0]$ and $\boldsymbol{X}_m[k] \triangleq [X_m[k-1], X_m[k], X_m[k+1]]^{\mathrm{T}}$, equations (7.11) and (7.12b) can be joined into the single input-output equation as follows.

$$\hat{X}_n[k] = \boldsymbol{v}_n^{\mathcal{H}} \Bigg(\underbrace{\begin{bmatrix} \boldsymbol{h}_n & \tilde{\boldsymbol{h}}_n \end{bmatrix}}_{\triangleq \mathbf{H}_n} \begin{bmatrix} X_n[k] \\ X_n^*[k] \end{bmatrix} + \underbrace{\sum_{m=0}^{N-1} \mathbb{H}_{nm} \boldsymbol{X}_m[k] + \mathbf{R}_n \bar{\boldsymbol{z}}[k]}_{\triangleq \boldsymbol{z}_n[k]} \Bigg) \tag{7.14}$$

From (7.14), the following expression for the SINR on subcarrier n can be obtained:

$$\gamma_n = \frac{\boldsymbol{v}_n^{\mathcal{H}} \left(S_n \boldsymbol{h}_n \boldsymbol{h}_n^{\mathcal{H}} \right) \boldsymbol{v}_n}{\boldsymbol{v}_n^{\mathcal{H}} \left(\boldsymbol{\Psi}_{\boldsymbol{z}_n \boldsymbol{z}_n} + S_n \tilde{\boldsymbol{h}}_n \tilde{\boldsymbol{h}}_n^{\mathcal{H}} \right) \boldsymbol{v}_n}, \tag{7.15}$$

where $\boldsymbol{\Psi}_{\boldsymbol{z}_n \boldsymbol{z}_n}$ is the interference-plus-noise covariance matrix of subcarrier n, which is defined as

$$\boldsymbol{\Psi}_{\boldsymbol{z}_n \boldsymbol{z}_n} \triangleq \mathbb{E}\{\boldsymbol{z}_n \boldsymbol{z}_n^{\mathcal{H}}\} = \sum_{m=0}^{N-1} S_m \mathbb{H}_{nm} \mathbb{H}_{nm}^{\mathcal{H}} + \sigma_{\mathrm{t}}^2 \mathbf{R}_n \mathbf{R}_n^{\mathcal{H}}. \tag{7.16}$$

Equivalent SINR expressions have been used for the design and/or performance evaluation of DMT systems in, among others, [6, 146, 166, 201, 203]. Despite this widespread adoption of the SINR expression as in (7.15), however, it seems ill-advised to model the ICI coming from subcarrier n^* as uncorrelated *noise* on subcarrier n. While the considered interfering signal—which is given as $X_n^*[k]$ due to (7.6)—is indeed uncorrelated with $X_n[k]$, it is not *independent* of $X_n[k]$ and will cause a loss of orthogonality and difference in scaling between the real and imaginary parts of $X_n[k]$ in $\hat{X}_n[k]$ rather than contributing to the total interference-plus-noise. This loss of orthogonality and difference in scaling is a manifestation of the received signals' impropriety. In the same vein, interference from both $X_m[k]$ and $X_m^*[k]$ may result in a loss of propriety for the ISI/ICI, which is not accounted for in (7.15) in general.

7.2.4 Bit loading

A relevant performance metric for DMT systems is the total achievable bit loading, where the achievable bit loading on subcarrier n is often expressed as

$$b_n = \log_2\left(1 + \Gamma^{-1}\gamma_n\right) \tag{7.17}$$

with Γ the SNR gap-to-capacity. The value of Γ depends on the target bit error rate (BER). Adjustments are often made to the SNR gap to account for a noise margin and—in case coded transmission is considered—a coding gain. Similar bit loading expressions have been used for the design and/or performance evaluation of DMT systems in, among others, [6, 11, 12, 38, 75, 124, 132, 146, 166, 201, 203].

If the PTEQ filter coefficients are chosen to maximize the bit loading, then it is readily seen that (7.15) and (7.17) yield the following expression for the optimal PTEQ filter coefficients.

$$\boldsymbol{v}_n = \left(\boldsymbol{\Psi}_{\boldsymbol{z}_n\boldsymbol{z}_n} + S_n\tilde{\boldsymbol{h}}_n\tilde{\boldsymbol{h}}_n^{\text{H}}\right)^{-1}\boldsymbol{h}_n \tag{7.18}$$

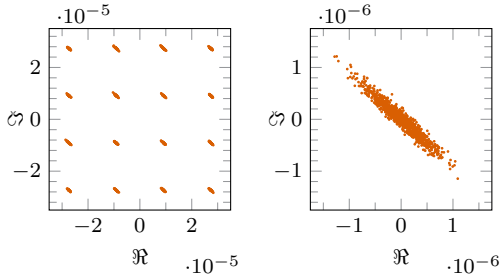
Equation (7.18) demonstrates the main advantage of PTEQ over TEQ—apart from generalizing TEQ without incurring a significant run-time complexity increase: the optimal PTEQ filter coefficients can be calculated *analytically* [6], whereas TEQ design is notoriously challenging.

7.3 Problem statement

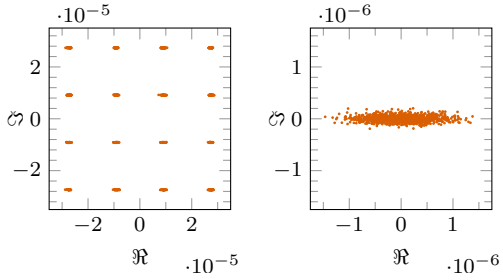
When the bit loading is calculated using (7.17), it is implicitly assumed that the received signals are proper. The fact that this assumption is not always satisfied, is illustrated in Figure 7.2 which displays a received signal after DMT demodulation in a DMT system with a too-short cyclic prefix and with PTEQ filter vectors $\boldsymbol{v} = [1, 0, \ldots, 0]^{\text{T}}$.[7] The impropriety of the interference-plus-noise in these examples is caused by the DMT symbols' Hermitian symmetric structure, which is described in (7.6). Due to this Hermitian symmetric structure, the ISI/ICI is a widely linear function of the transmitted proper QAM symbols. As widely linear mappings do not preserve propriety, the resulting ISI/ICI can be improper.

Equation (7.17) establishes a relation between the SINR and achievable bit loading for a given target BER, and is derived under the assumption that interference-plus-noise is proper and has a Gaussian distribution. The problem

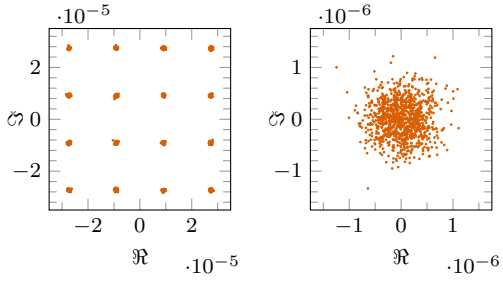
[7] A detailed description of the Monte-Carlo simulations that yielded these figures can be found in Section 7.6.1.



(a) Original signal



(b) Signal with rotated interference-plus-noise



(c) Signal with proper interference-plus-noise

Figure 7.2: Example of a received signal after DMT demodulation in a G.fast system with a 600 m loop length and $\nu_{\mathrm{p}} = 128$. In each pair of figures, the left figure depicts $[\boldsymbol{y}_n[k]]_0$ for a single subcarrier ($n = 100$), and the right figure depicts the interference-plus-noise component of the same signal. Figure 7.2a displays the received signal as obtained through the Monte-Carlo simulation of the described DMT system. It can be observed that the interference-plus-noise is improper. Figure 7.2b depicts the same received signal, but where the interference-plus-noise component has been rotated relative to the received QAM symbol (cf. Section 7.5.2). Figure 7.2c illustrates what the received signal looks like if the interference-plus-noise is proper with the same power as in Figure 7.2a and Figure 7.2b. Further details can be found in Section 7.6.1.

Table 7.2: Achieved SINR and maximum bit loading for the received signals in Figure 7.2.

Figure 7.2a: Original	$\gamma_n^{\Re}$ (dB)	$\gamma_n^{\Im}$ (dB)	b_n (bit)
(7.15) and (7.17)	35.5		8.61
(7.26) and (7.29)	35.1	35.8	8.61
Figure 7.2b: Rotated	$\gamma_n^{\Re}$ (dB)	$\gamma_n^{\Im}$ (dB)	b_n (bit)
(7.15) and (7.17)	35.5		8.61
(7.26) and (7.29)	32.5	50.9	10.68
Figure 7.2c: Proper	$\gamma_n^{\Re}$ (dB)	$\gamma_n^{\Im}$ (dB)	b_n (bit)
(7.15) and (7.17)	35.5		8.61
(7.26) and (7.29)	35.5	35.5	8.61

is not just that (7.17) is invalid when the received signals are improper, but also that (7.15) contains no information regarding the signal impropriety. This fact is reflected in the SINR values yielded by (7.15) for the three received signals in Figure 7.2—given in the first row of Table 7.2. The SINR values are all equal, even though the interference-plus-noise of Figure 7.2b will result in a higher (i.e. worse) BER than that in Figure 7.2a and Figure 7.2c.[8]

For a given constellation size and SNR, determining the achieved BER thus requires knowledge of both the interference-plus-noise variance and the pseudovariance (i.e. requires a full second order statistical characterization of the interference-plus-noise). Equivalently, if the interference-plus-noise is improper and a given target BER is to be achieved, then the maximum achievable bit loading cannot be determined given only the interference-plus-noise variance (which is expressed relatively to the direct signal power in the SINR). The motivation for why (7.15) and (7.17) cannot be considered valid, can thus also be formulated as follows: if some aspect of the interference-plus-noise distribution influences the relation between the achievable bit loading (i.e. the QAM size), the SINR, and target BER but is left un-modelled, then the highest bit loading that is guaranteed to achieve the target BER cannot be determined reliably.

Signal impropriety however need not be a source of performance degradation

[8]Provided that the QAM decision regions are constructed under the assumption that the interference-plus-noise is proper. Note that the interference-plus-noise in Figure 7.2a will lead to unexpected dependencies between error events, which can be detrimental to the BER when coded modulation is employed without taking the interference-plus-noise impropriety into account.

[184]. In order to take advantage of signal impropriety, this chapter follows [184] by decomposing each transmitted QAM symbol $X_n[k]$ into two independent pulse-amplitude modulation (PAM) symbols and by applying the PAM decoding decision independently to the real signals $\Re(X_n[k])$ and $\Im(X_n[k])$. Similar equations to (7.15) and (7.17) will be developed for PAM decoding in Section 7.4, which again establish a relation between the SINR and achievable bit loading given a target BER. These equations are derived under the assumption that the interference-plus-noise in $\Re(X_n[k])$ (or $\Im(X_n[k])$) has a 1-D Gaussian distribution. Note that these assumptions include no statement about the interference-plus-noise being proper. Contrary to what was the case for QAM, no such assumption is required here as the distribution of a zero-mean real Gaussian signal is fully determined by its variance—which, for the considered interference-plus-noise signal, is expressed relatively to the direct signal power in the SINR. Contrary to what was the case for QAM decoding, it is thus no longer possible that some un-modelled aspect of the interference-plus-noise distribution in $\Re(\hat{X}_n[k])$ (or $\Im(\hat{X}_n[k])$) influences the relation between the achievable bit loading, the SINR, and the target BER. As a result, the highest bit loading that is guaranteed to achieve the target BER can be determined reliably based solely on the SINR. In the example of Figure 7.2b, these new expressions replacing (7.15) and (7.17) will not only guarantee that the target BER is achieved: employing a different PAM constellation for the real and imaginary part of $X_n[k]$ will additionally enable a larger number of bits to be loaded in the $\Im$-direction of $X_n[k]$ than in the $\Re$-direction, thereby taking advantage of the signal impropriety and yielding a higher overall bit loading.

The increased bit loading yielded by the newly developed expressions (cf. Section 7.4) however comes at a price: maximizing the data rate of the DMT system will no longer result in analytical expressions for the optimal PTEQ filter coefficients. To tackle this issue, it will be proposed to further generalize the PTEQ to a novel *widely linear* (WL) PTEQ. Section 7.5 will demonstrate the main advantage of WL PTEQ over PTEQ—apart from generalizing PTEQ without incurring a significant complexity increase: if the new SINR and rate expressions from Section 7.4 are employed, then the optimal WL PTEQ coefficients can be calculated *analytically*.

Even when the newly developed bit loading expressions (cf. Section 7.4) and novel WL PTEQ filter (cf. Section 7.5) are employed, the interference-plus-noise affecting the received PAM symbols on tone n may still be correlated (as e.g. in Figure 7.2a). As a result, errors will not occur independently in these two PAM symbols. This dependence between the error events in the two PAM symbols in $X_n[k]$ will then complicate the design of the trellis coded modulation (TCM), the use of which is mandatory in G.fast [96]. Additionally, it will also be observed that the relative rotation of the interference-plus-noise distribution

in $\hat{X}_n[k]$ strongly impacts the achievable bit loading. To further improve the achievable bit loading, it is therefore proposed to rotate each QAM symbol $X_n[k]$ prior to transmission.[9] It will be proven that the proposed QAM symbol rotation maximizes the achievable bit loading, and that such optimal rotation effectively decorrelates the noise in the real and imaginary parts of the received signal, thereby simplifying TCM design and analysis.

7.4 Composite real channel model

This section provides expressions for the SINR of the real and imaginary part of $\hat{X}_n[k]$ and an SNR gap approximation for the achievable bit loading. The expressions for the SINR will be based on a new composite real channel model, which expresses the real signals $\Re(\hat{X}_n[k])$ and $\Im(\hat{X}_n[k])$ as linear functions of the real signals $\Re(X_m[l])$, $\Im(X_m[l])$, and $\bar{\boldsymbol{z}}[k]$. It will be assumed that $X_0[k] \equiv 0$ and $X_{\frac{N}{2}}[k] \equiv 0$ in order to simplify notation.

7.4.1 Signal-to-interference-plus-noise ratio

The starting point for the derivation of the SINR expressions for the real and imaginary part of $\hat{X}_n[k]$ will be the following *augmented complex* channel model (equivalent to (7.12b))

$$\bar{\boldsymbol{y}}[k] = \sum_{l=-1}^{1} \mathbf{H}[l] \sum_{m=1}^{N/2-1} \begin{bmatrix} \mathrm{row}_m(\mathbf{T}) \\ \mathrm{row}_m^*(\mathbf{T}) \end{bmatrix}^{\mathcal{H}} \begin{bmatrix} X_m[k+l] \\ X_m^*[k+l] \end{bmatrix} + \bar{\boldsymbol{z}}[k] \tag{7.19}$$

in conjunction with the augmented complex PTEQ filter equation (equivalent to (7.11))

$$\begin{bmatrix} \hat{X}_n[k] \\ \hat{X}_n^*[k] \end{bmatrix} = \begin{bmatrix} \boldsymbol{v}_n & \mathbf{0}_{(T+1)\times 1} \\ \mathbf{0}_{(T+1)\times 1} & \boldsymbol{v}_n^* \end{bmatrix}^{\mathcal{H}} \begin{bmatrix} \mathbf{R}_n \\ \mathbf{R}_n^* \end{bmatrix} \bar{\boldsymbol{y}}[k]. \tag{7.20}$$

In (7.19), $\mathrm{row}_n^*(\mathbf{T})$ denotes the complex conjugate of $\mathrm{row}_n(\mathbf{T})$. Equation (7.19) was obtained from (7.12b) by considering (7.6) and the relation $\mathrm{row}_n^*(\mathbf{T}) = \mathrm{row}_{n^*}(\mathbf{T})$. Similarly, equation (7.20) can be obtained from (7.11) by employing the fact that $\bar{\boldsymbol{y}}[k]$ is real-valued.

[9] This type of transmitter-side symbol rotation is compatible with the G.fast standard [96], as the standard specifies that a complex gain scaling should be applied to the transmitted symbols upon updating the vectoring matrix in order to absorb "FEQ shock".

From the augmented complex channel model as in (7.19), the following *composite real* channel model can then be obtained.

$$\bar{\boldsymbol{y}}[k] = 2\sum_{l=-1}^{1}\mathbf{H}[l]\sum_{m=1}^{N/2-1}\left(\mathrm{row}_m^{\mathbb{R}}(\mathbf{T})\right)^{\mathrm{T}}X_m^{\mathbb{R}}[k+l] + \bar{\boldsymbol{z}}[k] \tag{7.21}$$

In this equation, $\mathbf{A}^{\mathbb{R}}$ denotes the composite real representation of a complex matrix $\mathbf{A}$, which is defined as

$$\mathbf{A}^{\mathbb{R}} \triangleq \begin{bmatrix} \Re(\mathbf{A}) \\ \Im(\mathbf{A}) \end{bmatrix}.$$

In (7.21), $\mathrm{row}_m^{\mathbb{R}}(\mathbf{T})$ is thus given as

$$\mathrm{row}_m^{\mathbb{R}}(\mathbf{T}) = \begin{bmatrix} \Re(\mathrm{row}_m(\mathbf{T})) \\ \Im(\mathrm{row}_m(\mathbf{T})) \end{bmatrix}.$$

To obtain (7.21) from (7.19), the following relations are used:

$$\begin{bmatrix} \mathbf{A} \\ \mathbf{A}^* \end{bmatrix} = \boldsymbol{\Pi}\mathbf{A}^{\mathbb{R}}, \quad \mathbf{A}^{\mathbb{R}} = \tfrac{1}{2}\boldsymbol{\Pi}^{\mathcal{H}}\begin{bmatrix} \mathbf{A} \\ \mathbf{A}^* \end{bmatrix} \tag{7.22}$$

with

$$\boldsymbol{\Pi} \triangleq \begin{bmatrix} \mathbf{I} & j\mathbf{I} \\ \mathbf{I} & -j\mathbf{I} \end{bmatrix}.$$

Similarly, the following composite real PTEQ filter equation can be obtained from (7.20)

$$\hat{X}_n^{\mathbb{R}}[k] = \underbrace{\begin{bmatrix} \Re(\boldsymbol{v}_n) & -\Im(\boldsymbol{v}_n) \\ \Im(\boldsymbol{v}_n) & \Re(\boldsymbol{v}_n) \end{bmatrix}^{\mathrm{T}}}_{\triangleq\mathbf{U}_n^{\mathrm{T}}}\mathbf{R}_n^{\mathbb{R}}\bar{\boldsymbol{y}}[k]. \tag{7.23}$$

In (7.23), $\mathbf{R}_n^{\mathbb{R}}$ thus has dimensions $2(T+1)\times(N+T)$. Moreover, $\boldsymbol{y}_n^{\mathbb{R}}[k] = \mathbf{R}_n^{\mathbb{R}}\bar{\boldsymbol{y}}[k]$ will denote the composite real representation of PTEQ filter inputs $\boldsymbol{y}_n[k]$ on subcarrier n.

By defining the residual channel vectors $\boldsymbol{g}_{nm}[l]$ and residual channel matrices $\mathbb{G}_{nm}$ as

$$\boldsymbol{g}_{nm}[l] \triangleq 2\mathbf{R}_n^{\mathbb{R}}\mathbf{H}[l]\mathrm{row}_m(\mathbf{T})^{\mathrm{T}}, \tag{7.24a}$$

$$\mathbb{G}_{nm} \triangleq \begin{cases} \begin{bmatrix} \boldsymbol{g}_{nm}[-1] & \boldsymbol{g}_{nm}[0] & \boldsymbol{g}_{nm}[1] \end{bmatrix} & \text{if } m \neq n \\ \begin{bmatrix} \boldsymbol{g}_{nm}[-1] & \mathbf{0}_{2(T+1)\times 1} & \boldsymbol{g}_{nm}[1] \end{bmatrix} & \text{if } m = n \end{cases}, \tag{7.24b}$$

and by introducing $\boldsymbol{g}_n = \boldsymbol{g}_{nn}[0]$, equations (7.23) and (7.21) can be joined into the single input-output equation (equivalent to (7.14))

$$\hat{X}_n^{\mathbb{R}}[k] = \mathbf{U}_n^{\mathrm{T}} \underbrace{\begin{bmatrix} \Re(\boldsymbol{g}_n) & \Im(\boldsymbol{g}_n) \end{bmatrix}}_{\triangleq \mathbf{G}_n} X_n^{\mathbb{R}}[k] + \mathbf{U}_n^{\mathrm{T}} \Bigg(\underbrace{\sum_{m=1}^{N/2-1} \begin{bmatrix} \Re(\mathbb{G}_{nm}) & \Im(\mathbb{G}_{nm}) \end{bmatrix} \boldsymbol{X}_m^{\mathbb{R}}[k+l] + \mathbf{R}_n^{\mathbb{R}} \tilde{\boldsymbol{z}}[k]}_{\triangleq \boldsymbol{z}_n^{\mathbb{R}}[k]} \Bigg). \quad (7.25)$$

It was assumed that $X_n[k]$ is proper, such that the symbol power S_n is distributed equally over the real and imaginary component of $X_n[k]$.[10] From (7.25), the following expression for the SINR of $\Re(\hat{X}_n[k])$ can therefore be obtained:

$$\gamma_n^{\Re} = \frac{\mathrm{row}_0(\mathbf{U}_n^{\mathrm{T}}) \left(\frac{S_n}{2} \Re(\boldsymbol{g}_n) \Re(\boldsymbol{g}_n^{\mathrm{T}}) \right) \mathrm{col}_0(\mathbf{U}_n)}{\mathrm{row}_0(\mathbf{U}_n^{\mathrm{T}}) \left(\boldsymbol{\Psi}_{\boldsymbol{z}_n^{\mathbb{R}} \boldsymbol{z}_n^{\mathbb{R}}} + \frac{S_n}{2} \Im(\boldsymbol{g}_n) \Im(\boldsymbol{g}_n^{\mathrm{T}}) \right) \mathrm{col}_0(\mathbf{U}_n)}, \quad (7.26)$$

where $\boldsymbol{\Psi}_{\boldsymbol{z}_n^{\mathbb{R}} \boldsymbol{z}_n^{\mathbb{R}}} \triangleq \mathbb{E}\{\boldsymbol{z}_n^{\mathbb{R}} (\boldsymbol{z}_n^{\mathbb{R}})^{\mathrm{T}}\}$ is the composite real interference-plus-noise covariance matrix of subcarrier n, which can be calculated as

$$\boldsymbol{\Psi}_{\boldsymbol{z}_n^{\mathbb{R}} \boldsymbol{z}_n^{\mathbb{R}}} = \sum_{m=1}^{N/2-1} \frac{S_m}{2} \Re(\mathbb{G}_{nm} \mathbb{G}_{nm}^{\mathcal{H}}) + \sigma_{\mathrm{t}}^2 \mathbf{R}_n^{\mathbb{R}} (\mathbf{R}_n^{\mathbb{R}})^{\mathrm{T}}. \quad (7.27)$$

A similar expression can be obtained for $\gamma_n^{\Im}$, the SINR of $\Im(\hat{X}_n[k])$.

7.4.2 Bit loading

It is assumed that PAM symbols are transmitted on both the real and imaginary part of $X_n[k]$. The achievable bit loading for the real—or imaginary—part of $X_n[k]$ can then be expressed as

$$b = \frac{1}{2} \log_2 \left(1 + \Gamma^{-1} \gamma \right). \quad (7.28)$$

If received at the same SINR, then uncoded M^2-QAM signals that are subject to proper interference-plus-noise yield the same BER performance as uncoded

[10] The ensuing derivations can be extended to improper QAM symbols by applying a 2×2 precoding matrix $\mathbf{P}_n$ to each $X_n^{\mathbb{R}}[k]$ prior to transmission, with $\mathbf{P}_n$ the Cholesky factor of the transmitted QAM symbol's desired covariance matrix. The extension to improper QAM symbols is however considered to be out-of-scope.

M-PAM signals. As such, it is intuitively clear that—if uncoded modulation and square QAM constellations are considered—the same value of Γ will result in the same BER, regardless of whether the case is considered in which the bit loading is determined using (7.17) and all signals are proper, or the case is considered in which the bit loading is determined using (7.28) and the received signals are allowed to be improper. In order to achieve the same BER performance, the value of Γ in (7.28) should therefore be the same as in (7.17).[11] With (7.26) and (7.28), the bit loading of subcarrier n is given as

$$b_n = \frac{1}{2}\log_2(1+\Gamma^{-1}\gamma_n^{\Re}) + \frac{1}{2}\log_2(1+\Gamma^{-1}\gamma_n^{\Im}). \tag{7.29}$$

7.5 Optimizing performance: widely linear PTEQ & symbol rotation

In Table 7.2, the SINR and bit loading values corresponding to the received signals in Figure 7.2 are given. From these examples, it is already seen that taking advantage of the signal impropriety yields a higher overall bit loading. Moreover, the examples of Figure 7.2 and Table 7.2 indicate that the relative rotation between the axes of the received PAM symbols and the interference-plus-noise distribution in $\hat{X}_n[k]$ strongly impacts the achievable bit loading. In this section, it will therefore be shown that optimally rotating the symbols $X_n[k]$ in the complex plane prior to transmission can yield significant performance gains. First however, the computation of the PTEQ filter coefficients $\mathbf{U}_n$ that maximize the achievable bit loading as in (7.29) is considered.

7.5.1 Widely linear per-tone equalization

From (7.23), it is seen that—if $\hat{X}_n[k]$ is to be obtained by applying a linear filter to $\boldsymbol{y}_n[k]$ as in (7.11)—$\mathbf{U}_n$ should exhibit a block-skew-circulant structure [73], i.e. $\mathbf{U}_n$ should comply with

$$\mathbf{U}_n = \begin{bmatrix} \Re(\boldsymbol{v}_n) & -\Im(\boldsymbol{v}_n) \\ \Im(\boldsymbol{v}_n) & \Re(\boldsymbol{v}_n) \end{bmatrix} \tag{7.30}$$

[11] While intuitively clear for uncoded PAM symbols, this statement is not true for coded modulation. As the interference-plus-noise experienced by the two PAM symbols in $\hat{X}_n[k]$ may be correlated, error events in these two PAM symbols will not be statistically independent. This statistical dependence should be taken into account when designing the coded modulation. If the interference-plus-noise experienced by the two PAM symbols in $\hat{X}_n[k]$ is uncorrelated however, then the TCM encoding employed in G.fast is straightforwardly extended to the proposed scheme of composing $\hat{X}_n[k]$ of two independent PAM symbols. Further details are given in Section 7.5.2.

for some vector $\boldsymbol{v}_n \in \mathbb{C}^{T+1}$. This constraint is difficult to satisfy, as it couples the optimization of $\mathrm{col}_0(\mathbf{U}_n)$ and $\mathrm{col}_1(\mathbf{U}_n)$. Consequently, no analytical expression for the optimal $\mathbf{U}_n$ is readily available, thereby losing one of the main advantages of PTEQ over TEQ.

This problem can be circumvented by discarding the constraint specified in (7.30), and allowing $\mathbf{U}_n$ to be any matrix in $\mathbb{R}^{2(T+1)\times 2}$. The real and imaginary part of $\hat{X}_n[k]$ will then each be obtained by applying a separate linear filter to the composite real received signal $\boldsymbol{y}_n^{\mathbb{R}}[k]$, which is equivalent to applying a *widely linear* (WL) filter [150] to $\boldsymbol{y}_n[k]$. An analytical expression for the optimal $\mathbf{U}_n$, i.e. for the optimal WL PTEQ coefficients, is then readily derived.

Before presenting this analytical expression, a remark is due regarding the structure of $\mathbf{R}_n^{\mathbb{R}}$. As the last T rows of $\mathbf{R}_n$ are real-valued, the last T rows of $\mathbf{R}_n^{\mathbb{R}}$ will contain only zeros. Consequently, the interference-plus-noise covariance matrix $\boldsymbol{\Psi}_{\boldsymbol{z}_n^{\mathbb{R}}\boldsymbol{z}_n^{\mathbb{R}}} = \mathbb{E}\{\boldsymbol{z}_n^{\mathbb{R}}[k](\boldsymbol{z}_n^{\mathbb{R}}[k])^{\mathcal{H}}\}$ will be singular, causing problems when deriving the optimal WL PTEQ filter coefficients.[12] However, the all-zero rows of $\mathbf{R}_n^{\mathbb{R}}$ may readily be removed from the composite real receiver expression. To this end, $\underline{\mathbf{A}}$—which has a bar accent below the symbol—will denote the matrix that is obtained by removing the last $m-1$ rows from a $2m \times n$ matrix $\mathbf{A}$. Likewise, $\mathbf{A}^{\mathbb{R}}$ will denote the matrix that is obtained by removing the last $m-1$ rows from the composite real representation of an $m \times n$ matrix $\mathbf{A}$. Using this new notation, the last T rows of $\mathbf{U}_n$ and $\mathbf{R}_n$ in (7.23) can effectively be removed by writing the equation as

$$\hat{X}_n^{\mathbb{R}}[k] = \underline{\mathbf{U}}_n^{\mathrm{T}} \underline{\mathbf{R}}_n^{\mathbb{R}} \bar{\boldsymbol{y}}[k]. \tag{7.31}$$

Using the same notation to remove the last T rows from $\boldsymbol{g}_n$, $\boldsymbol{z}_n^{\mathbb{R}}$, and $\mathbb{G}_{nm}$, the expression for the SINR of $\Re(\hat{X}_n[k])$ can be rewritten as (equivalent to (7.26))

$$\gamma_n^{\Re} = \frac{\mathrm{row}_0(\underline{\mathbf{U}}_n^{\mathrm{T}}) \left(\frac{S_n}{2}\Re(\underline{\boldsymbol{g}}_n)\Re(\underline{\boldsymbol{g}}_n^{\mathrm{T}})\right) \mathrm{col}_0(\underline{\mathbf{U}}_n)}{\mathrm{row}_0(\underline{\mathbf{U}}_n^{\mathrm{T}}) \left(\boldsymbol{\Psi}_{\underline{\boldsymbol{z}}_n^{\mathbb{R}}\underline{\boldsymbol{z}}_n^{\mathbb{R}}} + \frac{S_n}{2}\Im(\underline{\boldsymbol{g}}_n)\Im(\underline{\boldsymbol{g}}_n^{\mathrm{T}})\right) \mathrm{col}_0(\underline{\mathbf{U}}_n)}, \tag{7.32}$$

where

$$\boldsymbol{\Psi}_{\underline{\boldsymbol{z}}_n^{\mathbb{R}}\underline{\boldsymbol{z}}_n^{\mathbb{R}}} = \sum_{m=1}^{N/2-1} \frac{S_m}{2}\Re(\underline{\mathbb{G}}_{nm}\underline{\mathbb{G}}_{nm}^{\mathcal{H}}) + \sigma_{\mathrm{t}}^2 \underline{\mathbf{R}}_n^{\mathbb{R}}(\underline{\mathbf{R}}_n^{\mathbb{R}})^{\mathrm{T}}. \tag{7.33}$$

With this equivalent expression for the SINR, the optimal WL PTEQ filter coefficients are—up to scaling—given as

$$\mathrm{col}_0(\underline{\mathbf{U}}_n) = \left(\boldsymbol{\Psi}_{\underline{\boldsymbol{z}}_n^{\mathbb{R}}\underline{\boldsymbol{z}}_n^{\mathbb{R}}} + \frac{S_n}{2}\Im(\underline{\boldsymbol{g}}_n)\Im(\underline{\boldsymbol{g}}_n^{\mathrm{T}})\right)^{-1} \Re(\underline{\boldsymbol{g}}_n). \tag{7.34}$$

[12] Compare to how, in (7.18), $\boldsymbol{\Psi}_{\boldsymbol{z}_n\boldsymbol{z}_n}$ being singular would cause problems.

Table 7.3: Number of floating point operations required by channel shortening and equalization a DMT receiver (continued).

	Nb. real mult.	Nb. real add.
WL PTEQ	$\left(\frac{N}{2}-1\right)(2T+4)$	$\left(\frac{N}{2}-1\right)(2T+2)+T$

A similar expression can be obtained for $\gamma_n^{\Re}$, the SINR of $\Im(\hat{X}_n[k])$, and for the optimal WL PTEQ filter coefficients $\text{col}_1(\underline{\mathbf{U}}_n)$.

It may appear that WL PTEQ amounts to a complexity increase w.r.t PTEQ, as the WL PTEQ—if implemented based on the composite real filter representation of (7.31)—has two $T+2$-tap filters for each subcarrier, whereas the PTEQ has only a single $T+1$-tap filter per subcarrier. However, all filter coefficients and signals in the WL PTEQ are real, such that WL PTEQ requires $2T+4$ real multiplications and $2T+2$ real additions per subcarrier. The computational complexity of WL PTQ is summarized in Table 7.3. After comparing Table 7.3 to Table 7.1, it can be concluded that the run-time complexity of WL PTEQ is exactly the same as that of PTEQ implemented with $n_\times = 4$ and $n_+ = 2$, and is comparable to that of PTEQ implemented with $n_\times = 3$ and $n_+ = 5$.

7.5.2 Transmitter-side symbol rotation

The examples of Figure 7.2 and Table 7.2 indicate that the relative rotation between the axes of the received PAM symbols and the interference-plus-noise distribution in $\hat{X}_n[k]$ strongly impacts the achievable bit loading. Indeed, the results in Table 7.2 show that a higher bit loading can be achieved if the eigenvectors of the interference-plus-noise covariance matrix $\underline{\mathbf{U}}_n^{\mathrm{T}} \boldsymbol{\Psi}_{\boldsymbol{z}_n^{\mathbb{R}} \boldsymbol{z}_n^{\mathbb{R}}} \underline{\mathbf{U}}_n$ are well aligned with the axis of the received PAM symbols in $\hat{X}_n[k]$. To further improve the achievable bit loading, it is therefore proposed to rotate the symbols $X_n[k]$ prior to transmission—i.e. to multiply the complex symbols $X_n[k]$ on each subcarrier n with a complex scalar ρ_n satisfying $|\rho_n| = 1$.[13] Here, the appropriate symbol rotation will be derived.

In the composite real channel model of (7.25), the rotation of $X_n[k]$ can be included by multiplying $X_n^{\mathbb{R}}[k]$ with an orthogonal rotation matrix $\mathbf{P}_n$, yielding

$$\hat{X}_n^{\mathbb{R}}[k] = \underline{\mathbf{U}}_n^{\mathrm{T}} \left(\underline{\mathbf{G}}_n \mathbf{P}_n X_n^{\mathbb{R}}[k] + \boldsymbol{z}_n^{\mathbb{R}}[k] \right). \tag{7.35}$$

[13] It is noted that this type of transmitter-side symbol rotation is compatible with the G.fast standard [96], as the standard specifies that a complex gain scaling should be applied to the transmitted symbols upon updating the vectoring matrix in order to absorb "FEQ shock".

It is noted that, as it was assumed that $X_n[k]$ is proper, this rotation operation has no influence on the transmitted symbol's covariance matrix.

$$\begin{aligned}\mathbb{E}\left\{\mathbf{P}_n X_n^{\mathbb{R}}[k](X_n^{\mathbb{R}}[k])^{\mathrm{T}}\mathbf{P}_n^{\mathrm{T}}\right\} &= \mathbf{P}_n\,\mathbb{E}\left\{X_n^{\mathbb{R}}[k](X_n^{\mathbb{R}}[k])^{\mathrm{T}}\right\}\mathbf{P}_n^{\mathrm{T}} \\ &= \mathbf{P}_n\frac{S_n}{2}\mathbf{I}_2\mathbf{P}_n^{\mathrm{T}} = \frac{S_n}{2}\mathbf{I}_2 = \mathbb{E}\left\{X_n^{\mathbb{R}}[k](X_n^{\mathbb{R}}[k])^{\mathrm{T}}\right\} \end{aligned} \tag{7.36}$$

Consequently, rotating the transmitted symbols $X_n[k]$ does not impact the interference-plus-noise covariance matrix $\boldsymbol{\Psi}_{\underline{\boldsymbol{z}}_m^{\mathbb{R}}\underline{\boldsymbol{z}}_m^{\mathbb{R}}}$ for any m. This independence will be exploited when calculating the optimal rotation matrix $\mathbf{P}_n$ (see below).

Next, a WL FEQ is applied to align the axes of the two received PAM symbols with the real and imaginary axis. If this WL FEQ is absorbed into the WL PTEQ, then the obtained unbiased WL PTEQ filter is given by

$$\underline{\mathbf{U}}_{n,\mathrm{ub}}^{\mathrm{T}} = (\underline{\mathbf{U}}_n^{\mathrm{T}}\underline{\mathbf{G}}_n\mathbf{P}_n)^{-1}\underline{\mathbf{U}}_n^{\mathrm{T}}. \tag{7.37}$$

In (7.37), the subscript 'ub' indicates that the resulting $\hat{X}_n^{\mathbb{R}}$ is an unbiased estimator of $X_n^{\mathbb{R}}[k]$, as is evidenced by substituting (7.37) into (7.35).

$$\hat{X}_{n,\mathrm{ub}}^{\mathbb{R}}[k] = X_n^{\mathbb{R}}[k] + \mathbf{P}_n^{\mathrm{T}}(\underline{\mathbf{U}}_n^{\mathrm{T}}\underline{\mathbf{G}}_n)^{-1}\underline{\mathbf{U}}_n^{\mathrm{T}}\underline{\boldsymbol{z}}_n^{\mathbb{R}}[k] \tag{7.38}$$

After applying the unbiased WL PTEQ, the axes of the received PAM symbols are aligned with the real and imaginary axis in $\hat{X}_{n,\mathrm{ub}}[k]$. The rotation matrix $\mathbf{P}_n$ will be chosen such that the eigenvectors of the covariance matrix of the interference-plus-noise in $\hat{X}_{n,\mathrm{ub}}^{\mathbb{R}}[k]$ are aligned with the real and imaginary axis as well. With the eigenvalue decomposition of this interference-plus-noise covariance matrix given as

$$(\underline{\mathbf{U}}_n^{\mathrm{T}}\underline{\mathbf{G}}_n)^{-1}\underline{\mathbf{U}}_n^{\mathrm{T}}\boldsymbol{\Psi}_{\underline{\boldsymbol{z}}_n^{\mathbb{R}}\underline{\boldsymbol{z}}_n^{\mathbb{R}}}\underline{\mathbf{U}}_n(\underline{\mathbf{U}}_n^{\mathrm{T}}\underline{\mathbf{G}}_n)^{-\mathrm{T}} = \mathbf{W}_n\boldsymbol{\Lambda}_n\mathbf{W}_n^{\mathrm{T}}, \tag{7.39}$$

$\mathbf{P}_n$ will thus be chosen as $\mathbf{P}_n = \mathbf{W}_n$.

With this choice for the rotation matrix $\mathbf{P}_n$, the expression for the achievable bit loading as in (7.29) can be further simplified. If $\mathbf{P}_n = \mathbf{W}_n$, then the SINRs of the real and imaginary part of $\hat{X}_{n,\mathrm{ub}}[k]$ are given by $\frac{S_n}{2}$ multiplied with the inverse of $\boldsymbol{\Lambda}_n$'s diagonal elements. Assuming w.l.o.g. that $\boldsymbol{\Lambda}_n$ is invertible, the achievable bit loading as in (7.29) becomes

$$b_n = \frac{1}{2}\log_2\det\left(\mathbf{I} + \Gamma^{-1}\frac{S_n}{2}\boldsymbol{\Lambda}_n^{-1}\right), \tag{7.40}$$

which can equivalently be expressed as

$$b_n = \frac{1}{2}\log_2\frac{\det\left(\underline{\mathbf{U}}_n^{\mathrm{T}}\left(\boldsymbol{\Psi}_{\underline{\boldsymbol{z}}_n^{\mathbb{R}}\underline{\boldsymbol{z}}_n^{\mathbb{R}}} + \Gamma^{-1}\frac{S_n}{2}\underline{\mathbf{G}}_n\underline{\mathbf{G}}_n^{\mathrm{T}}\right)\underline{\mathbf{U}}_n\right)}{\det\left(\underline{\mathbf{U}}_n^{\mathrm{T}}\boldsymbol{\Psi}_{\underline{\boldsymbol{z}}_n^{\mathbb{R}}\underline{\boldsymbol{z}}_n^{\mathbb{R}}}\underline{\mathbf{U}}_n\right)}. \tag{7.41}$$

With this expression for the achievable bit loading, the following expression for the optimal WL PTEQ filter coefficients $\underline{\mathbf{U}}_n$ can be obtained.[14]

$$\underline{\mathbf{U}}_n = \boldsymbol{\Psi}^{-1}_{\underline{\boldsymbol{z}}_n^{\mathbb{R}}\underline{\boldsymbol{z}}_n^{\mathbb{R}}} \underline{\mathbf{G}}_n \tag{7.42}$$

After plugging (7.42) back into (7.41), the following expression for the achievable bit loading is obtained.

$$b_n = \frac{1}{2}\log_2 \det\left(\mathbf{I} + \frac{S_n}{2}\Gamma^{-1}\boldsymbol{\Psi}^{-1}_{\underline{\boldsymbol{z}}_n^{\mathbb{R}}\underline{\boldsymbol{z}}_n^{\mathbb{R}}} \underline{\mathbf{G}}_n \underline{\mathbf{G}}_n^{\mathrm{T}}\right). \tag{7.43}$$

In addition to simplifying the expression for the achievable bit loading, (7.42) can also be employed to simplify the calculation of the rotation matrix $\mathbf{P}_n$. Substituting (7.42) into (7.39) yields

$$\left(\underline{\mathbf{G}}_n^{\mathrm{T}} \boldsymbol{\Psi}^{-1}_{\underline{\boldsymbol{z}}_n^{\mathbb{R}}\underline{\boldsymbol{z}}_n^{\mathbb{R}}} \underline{\mathbf{G}}_n\right)^{-1} = \mathbf{W}_n \boldsymbol{\Lambda}_n \mathbf{W}_n^{\mathrm{T}}, \tag{7.44}$$

such that $\mathbf{W}_n = \mathbf{P}_n$ can equivalently be determined from the following eigenvalue decomposition.

$$\underline{\mathbf{G}}_n^{\mathrm{T}} \boldsymbol{\Psi}^{-1}_{\underline{\boldsymbol{z}}_n^{\mathbb{R}}\underline{\boldsymbol{z}}_n^{\mathbb{R}}} \underline{\mathbf{G}}_n = \mathbf{W}_n \boldsymbol{\Lambda}_n^{-1} \mathbf{W}_n^{\mathrm{T}} \tag{7.45}$$

This expression makes clear that the receiver needs no additional information to determine the rotation matrix $\mathbf{P}_n$: the interference-plus-noise covariance matrix $\boldsymbol{\Psi}_{\underline{\boldsymbol{z}}_n^{\mathbb{R}}\underline{\boldsymbol{z}}_n^{\mathbb{R}}}$ and direct channels $\underline{\mathbf{G}}_n$ need to be determined in order to calculate the optimal WL PTEQ filter coefficients using (7.34), regardless of whether or not a symbol rotation is applied. The transmitter-side symbol rotation does require a feedback channel between receiver and transmitter, through which the desired rotation matrix $\mathbf{P}_n$ is to be communicated. The existence of such a feedback channel is however already implicitly assumed, as the transmitter should be made aware of the achieved SINR to determine the bit loading. The desired rotation matrix $\mathbf{P}_n$ can be communicated using a single real scalar θ_n per subcarrier, as any 2×2 rotation matrix can w.l.o.g. be written as

$$\mathbf{P}_n = \begin{bmatrix} \cos\theta_n & -\sin\theta_n \\ \sin\theta_n & \cos\theta_n \end{bmatrix}. \tag{7.46}$$

With the rotation matrix chosen as $\mathbf{P}_n = \mathbf{W}_n$, the interference-plus-noise in the real and imaginary part of $\hat{X}_n$ is no longer correlated. As a result, the proposed scheme of constructing the 2-D symbols X_n from two 1-D PAM symbols can be combined with the adapted version of Wei's 4-D 16-state TCM encoding

[14] The optimality of this expression is established in Section 7.5.3.

that is used in G.fast [96]. This TCM encoding requires the constellations of its constituent 2-D symbols X_n to be partitioned into four subsets that—after scaling the real and imaginary part of X_n such that they experience the same interference-plus-noise power—maximize the minimum squared distance among them [197]. It is noted that this combining of two 1-D symbols into a single 2-D symbol which is then partitioned into four subsets is similar to how, in G.fast, the 2-PAM symbols of single-bit tones are combined into 2-D symbols for TCM encoding [96].

This section is concluded with a comment regarding bit loading discretization, a subject that has not been touched upon so far. In G.fast, cross-constellations enable loading a fractional number of bits per dimension. The proposed scheme of constructing 2-D symbols X_n from two 1-D PAM symbols however requires an integer number of bits to be loaded per dimension. The discretization of the bit loading in (7.29) thus involves rounding down the bit loading of the real and imaginary part of X_n to the nearest integer separately, whereas the discretization in (7.17) involves only a single rounding down operation. As a result, the bit loading discretization loss is expected to be higher for the proposed scheme. It is however possible to scale any rectangular constellation—i.e. any 2-D constellation consisting of two orthogonal 1-D PAM constellations—such that an additional 1/2 bit can be loaded per dimension using the technique from [58, Section II.F]. The resulting family of constellations will have essentially the same properties as the original family of rectangular constellations [58, Section II.F], such that the same value for the SNR gap Γ will result in the same BER being achieved. It is noted that the technique to add an additional 1/2 bit per dimension to a rectangular constellation as in [58, Section II.F] will result in a family of constellations with the same properties only if the real and imaginary part of interference-plus-noise in $\hat{X}_n$ are uncorrelated—a condition that is satisfied when $\mathbf{P}_n = \mathbf{W}_n$.

7.5.3 Symbol rotation optimality

This section shows that the proposed choice for $\mathbf{P}_n$ and $\underline{\mathbf{U}}_n$ maximizes the bit loading on subcarrier n. It is noted that the result is trivial when $\Gamma = 0\,\text{dB}$. Indeed, for $\Gamma = 0\,\text{dB}$ equation (7.43) corresponds to the capacity of a real MIMO channel with proper $X_n^{\mathbb{R}}[k]$, an orthogonal transmit beamforming matrix $\mathbf{P}_n$, and which treats the ISI/ICI as noise [86]. As such, a higher bit loading cannot be achieved, and the proposed $\mathbf{P}_n$ and $\underline{\mathbf{U}}_n$ from Section 7.5.2 are optimal. In order to show that the proposed $\mathbf{P}_n$ and $\underline{\mathbf{U}}_n$ from Section 7.5.2 are optimal in general, it is proven here that (7.43) upper bounds the achievable bit loading when $\Gamma \geq 0\,\text{dB}$ as well. The desired result is stated in Proposition 7.1.

Proposition 7.1. *Consider the real MIMO channel which is described by*

$$\hat{\boldsymbol{X}} = \mathbf{U}^{T}\left(\mathbf{G}\mathbf{P}\boldsymbol{X} + \boldsymbol{Z}\right), \tag{7.47}$$

where $\boldsymbol{X}$ *is a real* 2×1*-vector with* $\mathbb{E}\{\boldsymbol{X}\boldsymbol{X}^{T}\} = S\mathbf{I}$*,* $\mathbf{P} = [\boldsymbol{p}_0, \boldsymbol{p}_1]$ *is an orthogonal transmit beamforming matrix,* $\mathbf{U} = [\boldsymbol{u}_0, \boldsymbol{u}_1]$ *is a receive beamforming matrix, and where* $\boldsymbol{Z}$ *is a vector of zero-mean additive Gaussian noise which has a non-singular covariance matrix* $\boldsymbol{\Psi} = \mathbb{E}\{\boldsymbol{Z}\boldsymbol{Z}^{T}\}$*. If* $\Gamma \geq 0\,\mathrm{dB}$*, then the achievable bit loading in this channel—which is considered to be given by*

$$\frac{1}{2}\sum_{i=0}^{1}\log_2\left(1+\Gamma^{-1}\frac{S\boldsymbol{u}_i^{T}\mathbf{G}\boldsymbol{p}_i\boldsymbol{p}_i^{T}\mathbf{G}^{T}\boldsymbol{u}_i}{\boldsymbol{u}_i^{T}\left(\boldsymbol{\Psi}+S\mathbf{G}\boldsymbol{p}_{-i}\boldsymbol{p}_{-i}^{T}\mathbf{G}^{T}\right)\boldsymbol{u}_i}\right) \tag{7.48}$$

— cannot exceed

$$\frac{1}{2}\log_2\det\left(\mathbf{I}+S\Gamma^{-1}\boldsymbol{\Psi}^{-1}\mathbf{G}\mathbf{G}^{T}\right) \tag{7.49}$$

for any $\mathbf{U}$ *and orthogonal* $\mathbf{P}$*.*

Proof. From (7.48), it is readily seen that the optimal $\boldsymbol{u}_i$ maximizes the following generalized Rayleigh quotient

$$r(\boldsymbol{u}_i) = \frac{S\boldsymbol{u}_i^{\mathrm{T}}\mathbf{G}\boldsymbol{p}_i\boldsymbol{p}_i^{\mathrm{T}}\mathbf{G}^{\mathrm{T}}\boldsymbol{u}_i}{\boldsymbol{u}_i^{\mathrm{T}}\left(\boldsymbol{\Psi}+S\mathbf{G}\boldsymbol{p}_{-i}\boldsymbol{p}_{-i}^{\mathrm{T}}\mathbf{G}^{\mathrm{T}}\right)\boldsymbol{u}_i}$$

and is therefore given as [225, Chapter 7.9]

$$\boldsymbol{u}_i^{\mathrm{opt}} = \left(\boldsymbol{\Psi}+S\mathbf{G}\boldsymbol{p}_{-i}\boldsymbol{p}_{-i}^{\mathrm{T}}\mathbf{G}^{\mathrm{T}}\right)^{-1}\mathbf{G}\boldsymbol{p}_i.$$

Substituting $\boldsymbol{u}_i^{\mathrm{opt}}$ back into (7.48) yields

$$\frac{1}{2}\sum_{i=0}^{1}\log_2\left(1+\Gamma^{-1}\boldsymbol{p}_i^{\mathrm{T}}\mathbf{G}^{\mathrm{T}}\left(\boldsymbol{\Psi}+S\mathbf{G}\boldsymbol{p}_{-i}\boldsymbol{p}_{-i}^{\mathrm{T}}\mathbf{G}^{\mathrm{T}}\right)^{-1}\mathbf{G}\boldsymbol{p}_i S\right)$$

which—as it is assumed that $\Gamma \geq 0\,\mathrm{dB}$—is upper bounded by

$$\frac{1}{2}\sum_{i=0}^{1}\log_2\left(1+\Gamma^{-1}\boldsymbol{p}_i^{\mathrm{T}}\mathbf{G}^{\mathrm{T}}\left(\boldsymbol{\Psi}+S\Gamma^{-1}\mathbf{G}\boldsymbol{p}_{-i}\boldsymbol{p}_{-i}^{\mathrm{T}}\mathbf{G}^{\mathrm{T}}\right)^{-1}\mathbf{G}\boldsymbol{p}_i S\right). \tag{7.50}$$

Some algebraic manipulations reveal that (7.50) is equivalent to

$$\frac{1}{2}\log_2\frac{\det\left(\mathbf{I}+S\Gamma^{-1}\boldsymbol{\Psi}^{-1}\mathbf{G}\mathbf{G}^{\mathrm{T}}\right)^2}{\prod_{i=0}^{1}\boldsymbol{p}_i^{\mathrm{T}}\left(\mathbf{I}+S\Gamma^{-1}\mathbf{G}^{\mathrm{T}}\boldsymbol{\Psi}^{-1}\mathbf{G}\right)\boldsymbol{p}_i}. \tag{7.51}$$

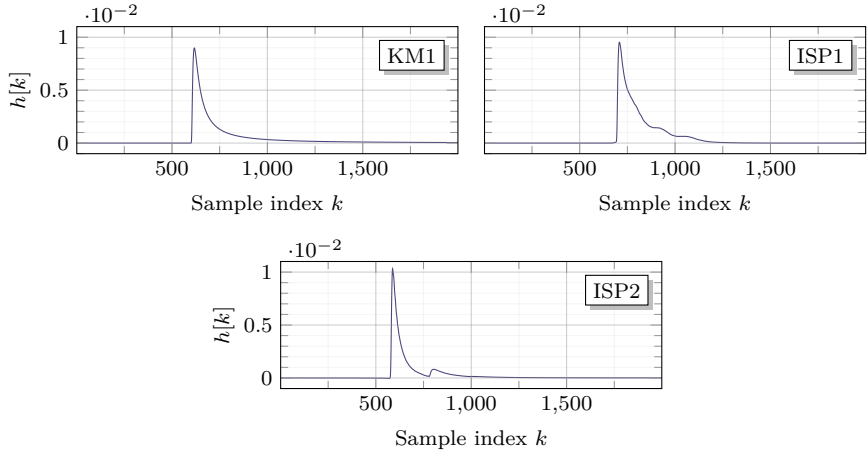


Figure 7.3: The three CIRs that are considered in the simulations. The CIR labeled "KM1" was synthesized using the KM1 model with k-parameters corresponding to a homogeneous and perfectly terminated Cat5 cable [5, Table II]. The CIRs labeled "ISP1" and "ISP2" were obtained by measurement of the transfer function of twisted-pair cables belonging to two different undisclosed Internet service providers. These measured CIRs were artificially extended to 600 m.

Applying Hadamard's inequality to the denominator in (7.51) reveals that the achieved bit loading is upper bounded by

$$\frac{1}{2}\log_2 \frac{\det\left(\mathbf{I}+S\Gamma^{-1}\boldsymbol{\Psi}^{-1}\mathbf{G}\mathbf{G}^{\mathrm{T}}\right)^2}{\det\left(\mathbf{I}+S\Gamma^{-1}\boldsymbol{\Psi}^{-1}\mathbf{G}\mathbf{G}^{\mathrm{T}}\right)}, \tag{7.52}$$

which is equivalent to (7.49). □

7.6 Simulation results

The performance gains that can be achieved by explicitly taking interference-plus-noise impropriety into account are assessed in the context of single-user long-reach G.fast systems. Three long-reach DSL scenarios are considered, with CIRs—which are given in Figure 7.3—corresponding to twisted pair cables of length 600 m. One CIR is synthesized using the KM1 model [5], while the other two are derived from measured frequency responses. These measured CIRs are

Table 7.4: Simulation parameters.

Parameter	Value	Parameter	Value
P_{tot}	8 dBm	f_{s}	212 MHz
N	4096	Γ	9.54 dB
σ_{f}^2	-145 dBm/Hz	S_n^{mask}	See [95]
ν_{s}	64		

artificially extended to 600 m using the following equation:

$$H_1(f) = (H_0(f))^{\frac{l_1}{l_0}}, \tag{7.53}$$

where l_0 is the original length and $l_1 = 600\,\text{m}$.

The simulation parameters are chosen conform the 106b-profile of G.fast [96], and can be found in Table 7.4. Note that Table 7.4 defines the frequency domain noise power σ_{f}^2 instead of the time domain noise power σ_{t}^2. With the DFT operation in the DMT demodulation defined as in (7.3), the relation between the two is as follows.

$$\sigma_{\text{t}}^2 = \frac{1}{N}\sigma_{\text{f}}^2 \tag{7.54}$$

A raised cosine window is used at the transmitter. More specifically, the diagonal elements of the windowing matrix $\mathbf{C}$ are defined as follows.

$$[\mathbf{C}]_{n,n} \triangleq \begin{cases} \sin^2\left(\frac{\pi(n+1)}{2\nu_{\text{s}}}\right) & \text{for } 0 \leq n \leq \nu_{\text{s}} - 1 \\ 1 & \text{for } \nu_{\text{s}} \leq n \leq s - 1 \\ \sin^2\left(\frac{\pi(n+1-s+\nu_{\text{s}})}{2\nu_{\text{s}}}\right) & \text{for } s \leq n \leq s + \nu_{\text{s}} - 1 \end{cases} \tag{7.55}$$

The symbol powers S_n are chosen such that the G.fast aggregate transmit power (ATP) constraint and spectral mask constraint are satisfied, which are respectively given as

$$\frac{f_{\text{s}}}{N}\sum_{n=1}^{N/2-1} S_n \leq P_{\text{tot}}, \tag{7.56a}$$

$$S_n \leq S_n^{\text{mask}}. \tag{7.56b}$$

As the LR extension of G.fast is expected to not use the first 18 subcarriers, $S_n = 0\ \forall n \in \{0, \ldots, 17\}$. The employed symbol powers S_n are determined using a known heuristic procedure. As a first step of this heuristic procedure, the

available transmit power is distributed evenly over all subcarriers by setting $S_n = \frac{P_{\text{tot}} N}{f_s(N/2-18)}$, $\forall n \in \{18, \ldots, N/2-1\}$. Then, the resulting SINR is determined for each subcarriers using (7.15).[15] Finally, the symbol power is set to $S_n = 0$ on all subcarriers after the highest subcarrier n for which $\gamma_n \geq \Gamma$, and the reclaimed transmit power is distributed evenly over the remaining subcarriers while making sure not to violate the spectral mask constraints.

In the ensuing simulations, SINR and bit loading values will be presented that are obtained with (7.15) and (7.17), as well as with (7.26) and (7.29). In all bit loading calculations—irrespective of which equation is considered—the value of the SNR gap Γ from Table 7.4 is employed. The considered value of Γ includes a coding gain for the employed TCM encoding of G.fast, as well as a noise margin. It is emphasized that, with the considered value of Γ, achieving the target error performance requires the following.

- If (7.17) is employed to determine the bit loading, then the received signal $\hat{X}_n[k]$ must be free of interference from $\hat{X}_{n^*}[k]$ and the interference-plus-noise in $\hat{X}_n[k]$ must be proper.
- If (7.29) is employed to determine the bit loading, then the interference-plus-noise in the estimators of the real and imaginary parts of $\hat{X}_n[k]$ must be uncorrelated.

Plots will show the continuous bit loading, i.e. no bit loading discretization is executed.

7.6.1 Examples Figure 7.2 and Table 7.2

The scatter plots of Figure 7.2 are obtained by Monte-Carlo simulation of a G.fast system. The transmitted symbols $X_n[k]$ are randomly drawn from a scaled 16-QAM constellation, where the scaling factor is chosen such that the symbol power on each subcarrier n corresponds to the value of S_n obtained through the previously described heuristic procedure. The number of transmitted DMT symbols is 1000. The considered CP length is $\nu_{\text{p}} = 128$, which is the lowest value allowed by the G.fast standard [96]. The delay δ is chosen by maximizing the energy in $\big[h[\delta], h[\delta+1], \ldots, h[\delta+\nu_{\text{p}}]\big]$ as in [6]. Simulations employed CIR ISP1.

Figure 7.2 consists of three subplots, each containing a left scatter plot depicting the received signal $\boldsymbol{y}_n[k]$ for a single subcarrier ($n = 100$), and a right scatter

[15] In practice, the SINR can be estimated from the training sequence transmitted during system initialization.

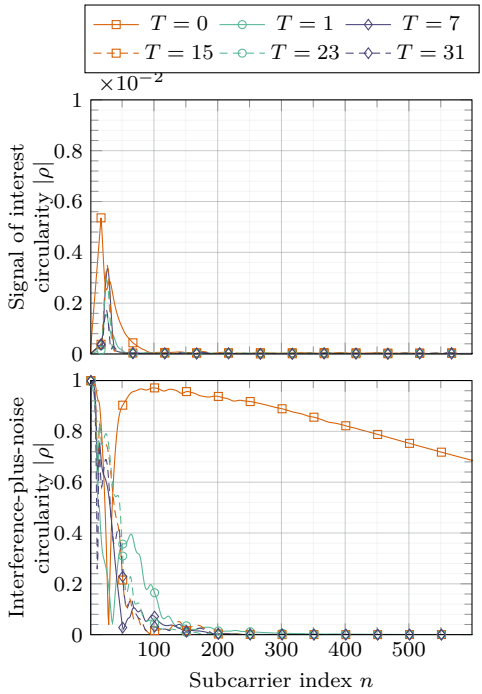


Figure 7.4: Circularity coefficients of the received direct signal (top) and the received interference-plus-noise (bottom) in a DMT receiver using PTEQ. The same system as in Section 7.6.1 is considered. The y-axes of the two plots have a different rage: the y-axis of the top plot ranges from 0 to 0.01, while the y-axis of the bottom plot ranges from 0 to 1.

plot depicting the interference-plus-noise component of the same signal. The depicted signals are rotated prior to plotting, such that the received 16-QAM symbols are aligned with the real and imaginary axes. To obtain the scatter plots in Figure 7.2b, the transmitted symbols $X_n[k]$ are rotated prior to transmission, where the rotation matrices $\mathbf{P}_n$ are chosen to be optimal for a DMT system with WL PTEQ and $T = 0$. Finally, Figure 7.2c was obtained from Figure 7.2a by subtracting the interference-plus-noise term from the received signal, and adding artificially generated circularly symmetric Gaussian noise with the same power as the previously subtracted interference-plus-noise.

7.6.2 PTEQ output impropriety

To further illustrate the need for paying attention to impropriety in DMT systems with a too-short CP, Figure 7.4 shows the circularity coefficient $|\rho|$ for the received signal of interest and for the received interference-plus-noise in a DMT system using PTEQ. The employed definition of $|\rho|$ can be found in Appendix D. The range of possible values for $|\rho|$ is $0 \leq |\rho| \leq 1$, with $\rho = 0$ when the considered signal is proper and $|\rho| = 1$ when the considered signal is maximally improper.

In the received signal of interest—i.e. in the contribution of $X_n[k]$ to $\hat{X}_n[k]$—impropriety can cause a loss of orthogonality and difference in scaling between the real and imaginary parts of $X_n[k]$. It is observed in Figure 7.4 that the circularity coefficient of the received signal of interest is rather low, meaning that signal of interest is close to being proper. This is to be expected, as the power of the interference from tone n^* is outweighed by the power of the direct signal, even if the CP is too short.

Figure 7.4 confirms that the interference-plus-noise is close to maximally improper when $T = 0$ (i.e. when no channel shortening is applied), as was already illustrated in Figure 7.2. When a channel shortening filter is then applied, i.e. when $T \geq 1$, the interference-plus-noise at higher frequencies becomes mostly proper. On subcarriers with index $n \leq 100$ however, the interference-plus-noise remains improper. On subcarriers with index $n \leq 50$, the interference-plus-noise impropriety often even seems to be increased by the PTEQ. Moreover, there seems to be no straightforward relation between the level of interference-plus-noise impropriety and the PTEQ filter order T. Such a relation is not expected to exist, as the PTEQ filter design equation in (7.18) is based on maximizing the SINR, not on minimizing the impropriety.

7.6.3 SINR and achievable bit loading

Figure 7.5 displays the achieved SINR and achievable bit loading for the system considered in Section 7.6.1. Results labeled 'CL' are obtained using (7.15) and (7.17), whereas results labeled 'WL' are obtained using (7.26) and (7.29). For DMT systems with WL PTEQ, separate SINR curves are given for the real and imaginary part of the received signal. However, the SINR curves of the real and imaginary parts of the same received signal are assigned the same line style and the same label in the legend. SINR and bit loading values are provided for a CL receiver with 0-order PTEQ ($T = 0$ - CL, Assumed Proper), for a WL receiver with 0-order WL PTEQ without transmitter-side symbol rotation ($T = 0$ - WL), for a WL receiver with both 0-order WL PTEQ and transmitter-side symbol

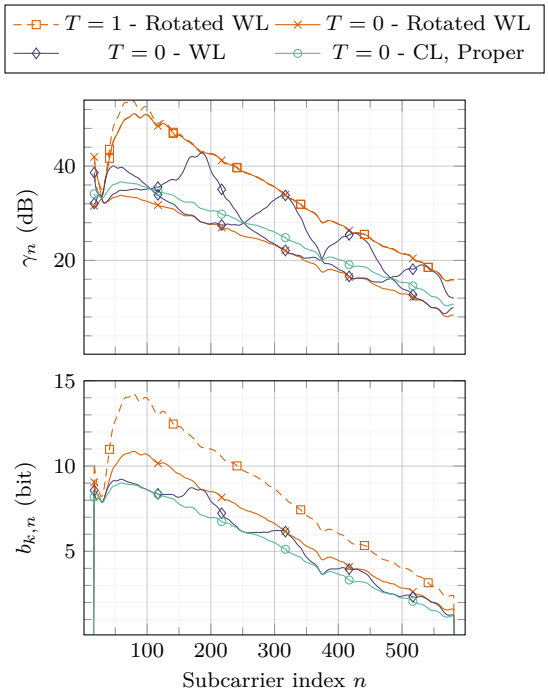


Figure 7.5: Achieved SINR (top) and achievable bit loading (bottom) for the system considered in Section 7.6.1. A line mark offset was applied to the curves labeled '$T = 1$ - Rotated WL' to make the difference between this curve and the curve labeled '$T = 0$ - Rotated WL' more clear.

rotation ($T = 0$ - Rotated WL), and for a WL receiver with both 1-st-order WL PTEQ and transmitter-side symbol rotation ($T = 1$ - Rotated WL).

A first observation is that the bit loading curve labeled '$T = 0$ - WL' has distinct peaks and troughs. At the peaks—which are located at $n = 47$, $n = 185$, $n = 315$, and $n = 530$—the axes of the received PAM symbols are well aligned with the eigenvectors of the residual interference-plus-noise covariance matrix. It is observed that no further performance increase can be obtained by rotating the symbols prior to transmission. At the troughs of the same bit loading curve—which are located at $n = 104$, $n = 252$, $n = 375$, and $n = 482$—the axes of the received PAM symbols are poorly aligned with the eigenvectors of the residual interference-plus-noise covariance matrix, and significant performance improvements can be obtained by optimally rotating the symbols prior to transmission. Note that this misalignment between the axes of the received PAM symbols and the eigenvectors of the residual interference-plus-

noise covariance matrix is also illustrated by Figure 7.2a, where the received signal of the considered system is plotted for a subcarrier that is near the trough at $n = 104$.

A second observation is that the two SINR curves labeled '$T = 1$ - Rotated WL' almost coincide with the upper SINR curve labeled '$T = 0$ - Rotated WL'. Increasing the PTEQ filter order from $T = 0$ to $T = 1$ thus improves the SINR for a single PAM signal, leaving the SINR of the other PAM signal on the same subcarrier mostly unaltered. On subcarriers $n \geq 100$, this observation indicates that the interference-plus-noise in the optimal unbiased WL PTEQ filter output is approximately proper for $T = 1$—as was the case in the PTEQ output for $T = 1$ (see Figure 7.4).

A final observation is that the bit loading curve labeled '$T = 0$, CL, Assumed proper' consistently lies below the other bit loading curves in Figure 7.5. As such, it can be concluded that —in the considered DSL system—explicitly taking the interference-plus-noise impropriety into account increases the system performance.

7.6.4 Achievable data rate

Finally, the performance increase enabled by explicitly taking the interference-plus-noise covariance into account is assessed. The metric under consideration is the achievable data rate, which is calculated as

$$R = \frac{f_{\mathrm{s}}}{N + \nu_{\mathrm{p}}} \sum_{n=0}^{N/2} b_n. \tag{7.57}$$

Figure 7.6 displays the achievable data rate as a function of the delay δ for G.fast systems using either PTEQ or WL PTEQ. The delay sweep has a granularity of 10 samples and ranges from $\delta_0 - 200$ to $\delta_0 + 100$, where δ_0 is chosen by maximizing the energy in $\left[h[\delta_0], \ldots, h[\delta_0 + \nu_{\mathrm{p}}]\right]$ as in [6]. The considered CP length is $\nu_{\mathrm{p}} = 128$. In addition, Figure 7.7 displays the maximum achievable data rate as a function of the CP length ν_{p}. Each data point in Figure 7.7 is obtained by executing a delay sweep ranging from $\delta_0 - 200$ to $\delta_0 + 100$ with a granularity of 10 samples, and determining the maximum achieved data rate over the considered values of δ.

The results in Figure 7.6 and Figure 7.7 indicate that explicitly taking the interference-plus-noise impropriety into account by using (7.26) and (7.29) yields better performance, especially for $T = 0$—which corresponds to a DMT receiver without channel shortening and with (WL) FEQ. When $T \geq 1$ however,

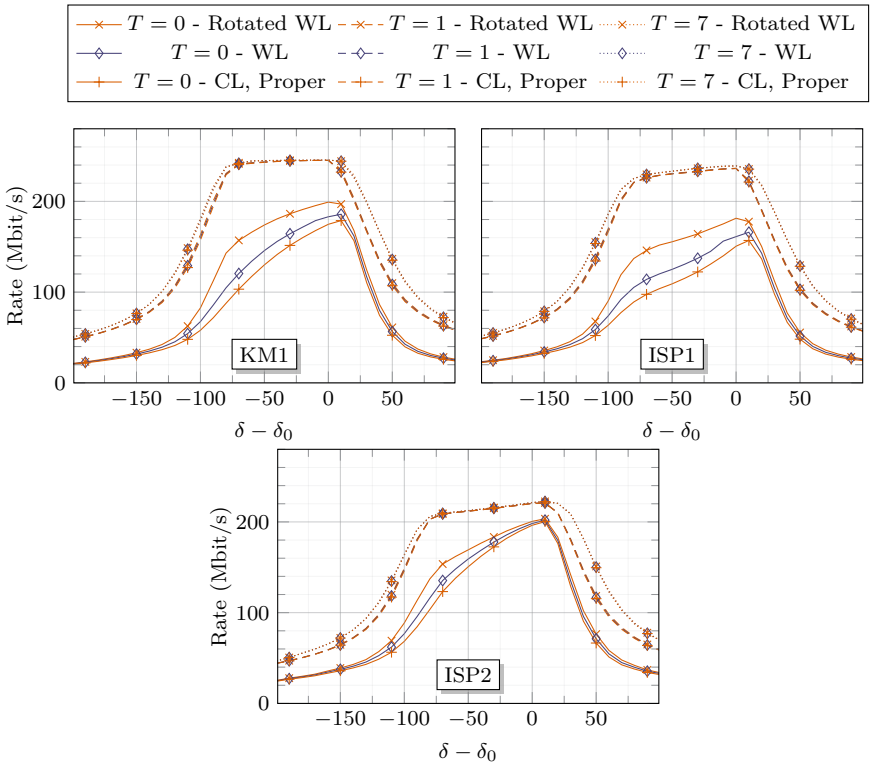


Figure 7.6: Achievable data rate as a function of the delay δ for G.fast systems using WL PTEQ with impulse responses given by Figure 7.3. Delays are relative to a reference delay δ_0, which is chosen by maximizing the energy in $\left[h[\delta_0], \ldots, h[\delta_0 + \nu_\mathrm{p}]\right]$ as in [6]. The granularity of the delay sweep is 10 samples. The considered CP length is $\nu_\mathrm{p} = 128$.

the results for DMT systems using PTEQ and WL PTEQ mostly coincide, indicating that the impact of interference-plus-noise impropriety on the data rate calculation is reduced by the PTEQ filter even without generalizing it to the WL PTEQ filter structure. It can be concluded that, when the employed channel shortening technique is able to eliminate most of the ISI/ICI, the impact of impropriety is reduced and the gap between the legacy SINR and bit loading expressions from [6, 11, 12, 38, 75, 124, 132, 146, 166, 201, 203] and the newly developed expressions disappears.

It is once more emphasized that, if regular QAM symbols are transmitted and (7.17) is used to determine the bit loading, then the target BER may not be

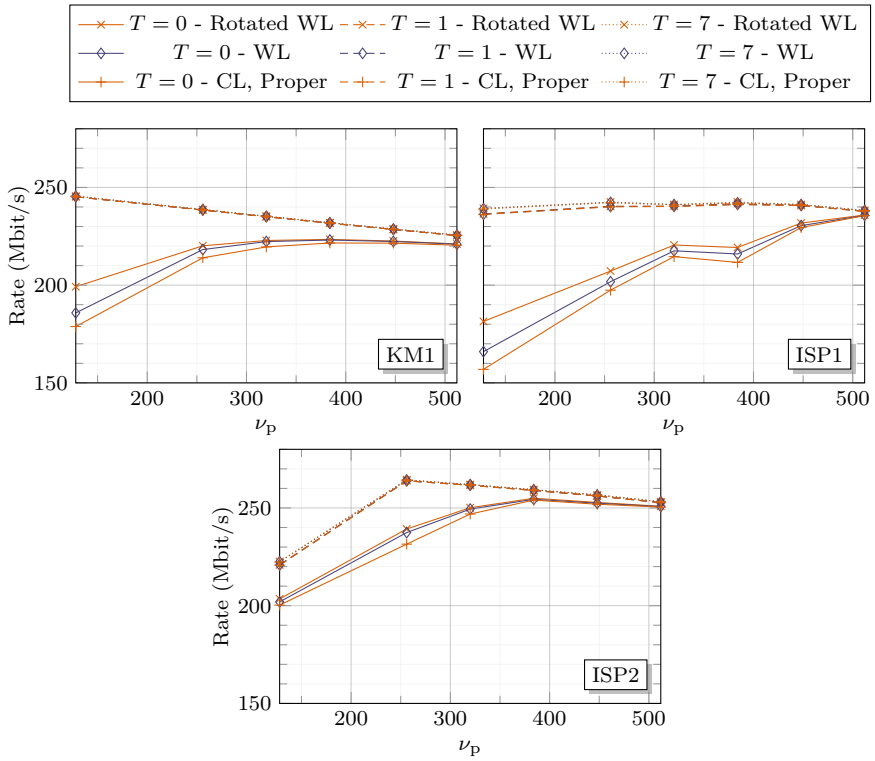


Figure 7.7: Maximum data rate achieved for different CP lengths. The data points correspond to the maximum data rates that are achieved when sweeping the delay δ from $\delta_0 - 200$ to $\delta_0 + 100$ with a granularity of 10 samples, as in Figure 7.6.

achieved by a receiver employing a PTEQ filter due to the residual impropriety at the lower frequencies (see Section 7.6.2). This failure to achieve the target BER is even more likely if the receiver is employing a 0-order PTEQ filter, as the ISI/ICI may be improper on all active subcarriers. Failing to achieve the target BER can be counteracted by reducing the bit loading, resulting in an even lower achieved data rate for 0-order PTEQ than is indicated in Figure 7.6 and Figure 7.7 ($T = 0$ - CL, Assumed Proper). Even without this further reduction in data rate for 0-order PTEQ however, it is seen that the 0-order WL PTEQ filter with double PAM symbols achieves part of the data rate increase without the more significant increase in computational complexity that is required by 1-order PTEQ. As such, 0-order WL PTEQ provides an interesting trade-off between the more complex 1-order PTEQ and the worse-performing 0-order

PTEQ.

Finally, the results in Figure 7.6 and Figure 7.7 also indicate that performance of the PTEQ saturates with a very short FIR filter (only two taps), as moving from $T = 2$ to $T = 7$ provides negligible gain. This observation suggests that the employed channel impulse responses have few poles which are readily canceled with the PTEQ. Moreover, the PTEQ clearly enables reducing ν_{p} for all considered systems without reducing the achieved data rate, and even achieves performance improvements for KM1. A notable exception however are the results for ISP2, where a significant performance drop is observed when ν_{p} is reduced from $\nu_{\mathrm{p}} = 256$ to $\nu_{\mathrm{p}} = 128$. A possible explanation is as follows. It is seen in Figure 7.3 that the CIR of ISP2 has a specific structure: the CIR looks like the sum of two impulse responses of almost identical systems characterized by only few poles, with a distance between the impulse response peeks of ca. 225 samples. The PTEQ is likely able to significantly shorten these impulse responses individually—as they are similar in shape to the CIR of KM1—but seems to struggle with reducing the length of their sum to below $\nu_{\mathrm{p}} - \nu_{\mathrm{s}}$ for smaller values of ν_{p}.

7.7 Conclusion

In this chapter, new SINR and bit loading expressions have been presented for DMT systems with (P)TEQ, which are valid when the received signals are improper. The performance of such DMT systems has been further optimized by generalizing the PTEQ to a widely linear PTEQ, and by optimally rotating the symbols $X_n[k]$ prior to transmission. Finally, simulation results have demonstrated that explicitly taking signal impropriety into account leads to an increased achievable bit loading when residual ISI/ICI is present in the system. When the employed channel shortening technique is able to eliminate most of the ISI/ICI, the impact of impropriety is reduced and the gap between the state-of-the-art SINR and bit loading expressions from [6, 11, 12, 38, 75, 124, 132, 146, 166, 201, 203] and the newly developed expressions disappears.

In future work, power loading algorithms will be developed to determine optimal symbol powers S_n. Such algorithms can be based on filter-less bit loading expressions as in (7.43), and may employ successive convex approximation (SCA) algorithms similar to those developed in [203]. Furthermore, it will be interesting to generalize the bit loading expression as in (7.43) so that it also applies to the case where the transmitted symbols are improper, as the use of improper transmitted symbols is indeed expected to yield further performance gains [73, 78, 97, 105, 223, 224]. Such a bit loading expression could then be used

to design SCA algorithms optimizing the improper symbols' transmit covariance matrices as well.

Chapter 8

Conclusions

This final chapter provides some final conclusions and perspectives for future research. In Section 8.1, the main conclusions are repeated that were already made in each individual chapter, and some additional comments and ideas for future research directions are provided. Section 8.2 then concludes the thesis with some perspectives on the future of DSL.

8.1 Conclusions and suggestions for future work

8.1.1 Cross-layer DSM

Real-time DSM

In Chapter 2, the framework of bi-coordinate ascent methods was proposed for real-time spectrum coordination. The new framework gave rise to fast derivative-based iterative power difference balancing (F-DB-IPDB), a real-time dynamic spectrum management (RT-DSM) algorithm with provable convergence properties. These provable convergence properties were contrasted with the state-of-the-art real-time spectrum coordination algorithms in [189, 190], which could not be proven to converge to a stationary point. Using simulations, F-DB-IPDB has additionally been shown to outperform the same state-of-the-art real-time spectrum coordination algorithms. Proposed further improvements to F-DB-IPDB encompass including inequality constraints by the means of 'slack tones', and deriving tone selection rules that allow for parallel execution.

Network utility maximization-based DSM

In Chapter 3, a fast algorithm has been presented for finding a local solution to the network utility maximization (NUM) problem, which is referred to as NUM-DSB, and which consists of iteratively solving sets of surrogate problems. The algorithm has been shown to be applicable in many DSL deployment scenarios, and regardless of the utility function's properties. In the context of grouped vectoring deployment scenarios, NUM-DSB leads to surrogate problems that are straightforward to solve. Moreover, empirical evidence has shown that NUM-DSB needs only few iterations to find a satisfactory solution.

As was pointed out in Chapter 1 and Chapter 3, NUM algorithms for adaptive resource allocation should be able to find an improved resource allocation under stringent time constraints in order to enable real-time adaptivity to upper layer demands. Iterative optimization algorithms, such as the one proposed in Chapter 3, may however still require too much time to be applicable in practical systems.

An alternative and computationally more efficient approach could be to exploit the time-invariance of the DSL channel by calculating a given number of Pareto-optimal resource allocations upon DSL system start-up, thereby effectively sampling the Pareto surface of the rate region. Some literature is available on selecting a representative set of DSL resource allocations in order to achieve good performance. Most notably, it has been proposed in [18,68,211] to employ multi-objective evolutionary algorithms to obtain a large set of DSL resource allocation algorithms that achieve—in some sense—a diverse set of points on the rate region.

A disadvantage of the evolutionary algorithm-based approaches in [18,68,211], is that the number of resource allocations that are required to construct a good representation of the rate region's Pareto surface is, in the worst case, exponential in the number of CPEs connected to the network. For larger networks, storing the set of resource allocations therefore results in large memory requirements. Additionally, systematically constructing a set of resource allocations that form a good representation of the rate region's Pareto surface is a non-trivial task for which, to the best of the candidate's knowledge, only heuristic approaches are available in the literature. Ideally, the design of this set of resource allocations should take the expected preference information coming from the upper layers into account.

In an effort to provide an alternative to the evolutionary algorithm-based approaches in [18, 68, 211], the candidate has contributed to [16], where a machine learning-based approach has been proposed. Rather than explicitly calculating a finite set of resource allocations, the proposed approach is to map

upper layer preference information—in the case of the work in [16] given by weights in the WSR maximization problem—to resource allocations using an artificial neural network (ANN). The ANN can be trained using either supervised or non-supervised approaches, where training samples in the supervised approach are generated by solving the WSR maximization problem for many different weight vectors using a state-of-the-art (but slow) resource allocation algorithm. The trained ANN can be thought of as implicitly and continuously sampling the rate region, which is to be contrasted with the explicit and discrete sampling of the rate region by the state-of-the-art approaches. Moreover, by choosing the weight vectors in the training set such that their distribution is equal to that of the weights yielded by the upper layer layer algorithms, the ANN is able to take into account the expected preference information coming from the upper layers. The results in [16] have demonstrated the feasibility of the proposed approach, but should be expanded upon to include more realistic—but also more challenging—DSL deployment scenarios.

8.1.2 New DSM degrees of freedom

DSM and QoS classes

In Chapter 4, four new DSM algorithms have been presented for joint signal and spectrum coordination in DSL networks providing unequal error protection (UEP). Two optimal spectrum balancing (OSB) algorithms have been provided: one for upstream and one for downstream DSL networks, both exhibiting exponential complexity in the number of users. In addition, two distributed spectrum balancing (DSB) algorithms were provided that converge to a local optimum. Providing unequal error protection functionality has not lead to an increase in computational complexity in any of the proposed algorithms. Furthermore, simulations have shown that the solutions obtained from the DSB algorithms largely coincide with solutions found by the corresponding OSB algorithms, at only a fraction of the computational cost.

In addition to the OSB and DSB algorithms, the multiple modulation and coding relaxation-based rate selection (MMCR-RS) algorithm for modulation and coding (MC) scheme selection has been proposed, which selects the MC scheme to be used for each QoS class. Simulations have shown that MMCR-RS algorithm performs well, and that using a single MC scheme per QoS class does not have a large impact on the performance of the DSL network. Results have also shown the benefit of UEP, as compared to EEP, as it is able to achieve moderate performance gains.

In the context of G.mgfast, it has been decided to employ a different mechanism to support different QoS classes, namely automatic repeat request (ARQ). G.mgfast will thus support QoS by using a different retransmission function for each class [145]. For example, in order to satisfy the QoS requirements of the ultra low-latency service (ULLS) and ultra reliable low-latency service (URLLS) classes, G.mgfast defines "proactive retransmission", which enables retransmission without waiting for an acknowledgment [145]. Tweaking the retransmission function is deemed to be more efficient than increasing the SNR of ultra-reliable low-latency services, as it provides better protection against impulse noise [145].

The availability of more efficient physical layer mechanisms for providing QoS support, combined with the fact that the performance gains of the analyzed UEP implementation are only moderate, leads the candidate to suggest that this research direction should not be pursued any further.

Full-duplex DSM

In Chapter 5, three novel DSM algorithms have been presented for the MU FDX DSL network. First however, a new MAC-BC duality theory for MU FDX networks was developed, which relies on perfect DPU-side NEXT cancellation. Based on this duality result, an OSB algorithm was derived which calculates the globally optimal resource allocation, but does so at an exceedingly high computational cost. Despite its high computational cost, the developed OSB algorithm is—to the best of the authors' knowledge—the first to establish the globally optimal solution to the considered full-duplex DSM problem that is considered in Chapter 5. In addition to the OSB algorithm, two low-complexity DSB algorithms were proposed. Simulations have shown that the performance of the low-complexity DSM algorithms is very close that achieved by the OSB algorithm. These DSB algorithms have then been used in performance simulations, which show that FDX transmission can indeed lead to significant performance gains in MU DSL networks.

It should be noted that neither of the low-complexity DSB algorithms was proven to converge. Convergence of the dual domain DSB algorithm cannot be established due to the fact that DD-DSB may incorrectly evaluate the Lagrange dual function's subgradient. Such an incorrect evaluation may then lead to convergence problems for the algorithm solving the Lagrange dual problem. Convergence of the primal domain DSB algorithm could not immediately be established due to the employed surrogate problem not being strongly convex.

Given the excellent convergence properties of the PD-DSB algorithm in practice—see e.g. the results in Figure 5.5—it would be interesting to further pursue

a theoretical analysis of the algorithm. Concretely, an effort should be made to establish theoretical convergence results for PD-DSB. If such convergence results cannot be obtained, it should be explored how to adapt the algorithm to make it provably convergent without surrendering its low complexity. As adaptations of the PD-DSB algorithm can be applied to resource allocation problems in a wide variety of network topologies, such results may be valuable in the context of both wired and wireless communications systems.

DSM and channel shortening

In Chapter 6, a new algorithm to simultaneously optimize receiver-side channel shortening PTEQ filter coefficients and transmit power allocation in OFDM and DMT systems with ZP or CP has been presented. The algorithm provably converges to a stationary point of the considered rate maximization problem, and requires only few iterations to achieve sufficient accuracy. Moreover, using this resource allocation method, it has been demonstrated that iterative water filling schemes can achieve good performance when the ISI/ICI is sufficiently suppressed by the PTEQ filter. In addition, transmitter-side channel shortening PTPC has been considered. A duality result linking OFDM/DMT systems with PTPC to OFDM/DMT systems with PTEQ has been provided. With this duality result in hand, PTPC systems can take full advantage of the straightforward FIR filter optimization in PTEQ systems, as well as of the developed resource allocation algorithm. Simulation results have shown that the performance obtained for OFDM/DMT systems with PTEQ is nearly indistinguishable from that obtained for OFDM/DMT systems with PTPC, making PTPC an interesting alternative channel shortening strategy in scenarios where implementing PTEQ is either difficult or costly.

In future work, the presented algorithms and results will be extended to multi-user systems. The joint PTEQ filter optimization and resource allocation algorithm from Section 6.3 readily extends to multi-user uplink systems—where PTEQ is thus applied at the base station—as the surrogate problem from Section 6.3.2 will be separable into subproblems that can be solved using the algorithm from Section 6.3.3. Moreover, the results from Section 6.4.2 can likely be generalized to establish a PTEQ-PTPC duality between multi-user uplink systems with PTEQ and multi-user downlink systems with PTPC, provided that a single base station-wide aggregate transmit power constraint is considered. If multi-user downlink systems with PTPC and per antenna or per line power constraints are considered—as would be customary in DSL networks [108,111,202]—PTEQ-PTPC duality can likely still be used to show an equivalence between the Lagrangian of the resulting rate maximization problem and the Lagrangian of a rate maximization problem in a multi-user uplink

system with PTEQ, similar to e.g. [108, 202]. However, algorithms that are based on evaluating the Lagrange dual function by maximizing the Lagrangian of a rate maximization problem in a multi-user uplink system with PTEQ will likely exhibit a prohibitively high computational complexity, as they will require evaluating the SINR γ_n of each subcarrier n in each iteration of their inner loop. Overcoming this complexity obstacle will then represent an additional challenge.

The multi-user systems described in the previous paragraph both locate the channel shortening filters at the base-station side. In the downlink however, it would also be interesting to place the channel shortening filter at the user equipment, thereby enabling (P)TEQ filter initialization based on estimates of the signal and interference-plus-noise covariance matrices, which are more readily available than estimates of the channel impulse response and time-domain noise power. Placing the (P)TEQ filter at the user equipment would however result in a more involved precoding matrix design problem. A straightforward approach could consist of alternating between updating the PTEQ filter coefficients and optimizing the precoding matrix with an adapted version of the PD-DSB algorithm from Chapter 5. However, the more interesting challenge here would be the joint optimization of the precoding matrix and PTEQ filter coefficients.

DSM and widely linear channel shortening

In Chapter 7, new SINR and bit loading expressions have been presented for DMT systems with (P)TEQ, which are valid when the received signals are improper. The performance of such DMT systems has been further optimized by generalizing the PTEQ to a widely linear PTEQ, and by optimally rotating the symbols $X_n[k]$ prior to transmission. Finally, simulation results have demonstrated that explicitly taking signal impropriety into account leads to an increased achievable bit loading when residual ISI/ICI is present in the system. When the employed channel shortening technique is able to eliminate most of the ISI/ICI, the impact of impropriety is reduced and the gap between the state-of-the-art SINR and bit loading expressions from [6, 11, 12, 38, 75, 124, 132, 146, 166, 201, 203] and the newly developed expressions disappears.

In future work, power loading algorithms will be developed to determine optimal symbol powers S_n. Such algorithms can be based on filter-less bit loading expressions as in (7.43), and may employ successive convex approximation (SCA) algorithms similar to those developed in [203]. Furthermore, it will be interesting to generalize the bit loading expression as in (7.43) so that it also applies to the case where the transmitted symbols are improper, as the use of improper transmitted symbols is indeed expected to yield further performance

gains [73, 78, 97, 105, 223, 224]. Such a bit loading expression could then be used to design SCA algorithms optimizing the improper symbols' transmit covariance matrices as well.

Furthermore, it would be interesting to analyze the performance of the proposed methods in the context of the upcoming G.mgfast standard. G.mgfast will employ full-duplex signaling which, similar to Zipper FDD [170], requires increasing the CP length—or, equivalently, adding a cyclic suffix—such that it accommodates for both the upstream and downstream CIRs, a well as for the delay difference between direct and echo signals. It is believed that the methods proposed in Chapter 6 and Chapter 7 will grow in practical relevance in the context of G.mgfast: the difference in delay between the direct signal and the echo in full duplex may result in the inability of channel shortening techniques to sufficiently shorten either channel, which in turn may result in improper residual ISI/ICI from the echo, the effects of which can be further mitigated using spectrum coordination techniques.

8.2 Future DSL technologies

The thesis will be concluded with some perspectives on the future of DSL. Two emergent research directions will be discussed, both of which have been tipped by John Cioffi as being interesting paths forward for DSL research [45, 46]. The first considered research direction is that of terabit DSL. Thereafter, cellular subscriber lines are elaborated upon.

8.2.1 Terabit digital subscriber lines

All DSL technologies considered in this thesis have transmitted signals over the twisted-pairs in "transmission-line mode" at frequencies below 848 MHz, where electrical signals are transfered as currents in the copper wire [46, 72]. In order to further increase the achievable data rates, it has been proposed to use the waveguide transmission modes of the twisted-pairs in the $100 - 300$ GHz range instead [46]. These waveguide modes support propagation of electromagnetic waves traveling through the millimeter-scale air or dielectric gaps between the metalic twisted-pair lines, as well as through the cable's plastic outer cover and the surrounding air [72, 168]. In [46], it was projected that by using these waveguide modes, data rates of 1 Tbit/s at line lengths up to 100 m could be achieved.

In ideal waveguides, signals can be transmitted independently over the different modes without any crosstalk between them [72]. However, non-idealities in practical twisted-pair lines can cause scattering of modes, resulting in crosstalk between the different waveguide modes [72]. It has therefore been proposed in [46] to model the coupling between the different waveguide modes as a MIMO channel, and to use vectoring techniques to reduce the effects of—or even take advantage of—the crosstalk between the waveguide modes.

After the initial proposal of terabit DSLs in [46], additional work has been done to validate the concept. The authors of [168] fine-tuned estimates of the achievable data rate by measuring the channel characteristics of a wire waveguide that was built to emulate a twisted-pair line in a larger cable binder. Furthermore, the authors of [72, 173] calculated the achievable data rates by determining the attenuation characteristics of different waveguide modes (through numerical simulations) of a CAT5e cable [173]—consisting of four copper twisted-pairs with a different twist rate, placed together in an aluminum shield and outer PVC cover— and of a twisted-pair line as it is used in DSL networks [72]. The results in [72, 168, 173] indicate that rates of 1 Tbit/s are only achievable on twisted-pair lines shorter than $10 - 20$ m [72, 168, 173], and that transmission over waveguide modes does not achieve a better data rate than G.mgfast on lines longer than 60 m [72].

8.2.2 Cellular subscriber lines

Providing indoor users with high bandwidth wireless connections at a low cost is one of the main challenges in the development of future mobile networks [127]. This claim is substantiated by Cisco's prediction that only 4% of mobile data is expected to be consumed "on the go" by the time 5G is deployed [4]. Most other data will be consumed indoors, in environments such as—among others—retail properties, transportation hubs, health-care environments, and education establishments [4]. Matching this increasing demand for indoor mobile service is becoming ever more challenging due to increasingly energy-efficient building standards, urbanization, and the gradual shift from laptops to smartphones [117].

Distributed antenna systems (DASs) are one possible solution to the indoor connectivity problem [117]. A DAS replaces base station antenna(s) with multiple antennas that can be distributed in space, and which share a common—often coaxial or fiber optic—connection to a remote unit [117]. Even though this technology has proven useful in the past, DAS provides too low a bandwidth per user and should therefore not be considered for improving the indoor coverage of future mobile networks [117]. Femto cells constitute another mature technology that can improve indoor coverage. Femto cells are essentially small

base stations that are—similar to WiFi modems—digitally backhauled over twisted-pair, coaxial, or fiber optic cables [65]. Synchronizing femto cells with regular base stations—which is a requirement when OFDMA is used as an access method, as well as for features like coordination, seamless mobility and interference management [117]—is difficult, leading to a need for interference avoidance between femto cells and base stations, thereby reducing the achievable performance gains of femto cells [65].

It should be noted that modern base stations already have a distributed architecture, which separates signal processing and radio frequency (RF) functionality over two entities: a base band unit (BBU) and a remote radio head (RRH) [34]. In the downlink, the BBU performs all base band signal processing tasks and sends the IQ samples-to-be-transmitted over a digital fiber-optic front-haul link to the RRH using protocols such as the common public radio interface (CPRI) [127]. The RHH then performs digital-to-analog conversion, (digital) upconversion, power amplification, and filtering [34, 98]. Optical front-haul links using CPRI, or any other protocol for streaming digitized IQ signals, however have bandwidth requirements that can easily exceed the backhaul data rate by $\times 50$ [34].

Methods for providing indoor connectivity can take advantage of the distributed architecture of modern base stations, e.g. by installing RRHs inside buildings and connecting them to a remote BBU. Additionally, one could take advantage of the presence of copper lines—which can include twisted-pair, coaxial, or power lines—and implement the front-haul connection over copper [45, 65, 117, 127, 130]. Front-hauling RRHs over copper may then again reduce installation costs, especially as copper line connections enable power delivery alongside data transmission [45, 127]. An important obstacle to overcome, however, are the data rate requirements of digital front-haul links, which exceed copper's capacity [45].

One approach to overcome this capacity problem, known as analog front-haul, consists of transmitting fully analog rather than digitized IQ signals over the copper lines [126]. Analog front-haul architectures separate RRH functionality, and put different functional blocks at either end of the copper cable.[1] A digital front-haul over fiber optic cable connects to a remote radio unit (RRU), which converts the received digital IQ signals to analog baseband IQ signals. The RRU is in turn connected to an RRH using a copper cable over which it transmits the analog baseband IQ signals. The RRH in this case only executes RF processing—i.e. analog upconversion and power amplification [65]. Architectures implementing an analog front-haul over copper cables are referred to as analog radio-over-copper (A-RoC) [126, 127]. As long as the

[1] Originally, the analog front-haul architecture was proposed as a functional split of femto cells in [65].

wireline connection supports enough bandwidth, the entire chain after the digital fronthaul link—consisting of the RRU, the analog fronthaul link, and the RRH—appear to the BBU as having the same functionality as the original RRH [45].

Several works have analyzed the feasibility of the A-RoC approach. In [81], it was demonstrated through numerical simulations that A-RoC can be used as a front-haul technique for LTE over twisted-pair lines. Coexistence with DSL was even achieved, by placing the 3GPP compliant LTE IQ signals between frequencies that are used by VDSL2 and G.fast systems [81]. Results in [81] demonstrated that LTE over twisted-pair lines can be built at a reasonable price point and deployed up to 350 m away from the street cabinet [130]. Furthermore, numerical simulations in [127] have demonstrated that A-RoC over LAN cables can achieve performance in excess of the requirements for 5G indoor networks. Finally, going beyond numerical simulations, Ericsson's radio dot system has demonstrated that A-RoC can be implemented in practice as well [117].

One challenge for A-RoC systems, is the fact that crosstalk in the twisted pair lines may result in interference between RRH signals when the BBU does not expect the RRHs to interfere with one another [127, 130]. In [130], it has therefore been proposed to implement frequency-domain precoding in the downlink by OFDM demodulating the digital IQ signal at the RRU, applying precoding in the frequency domain, and OFDM modulating the signal before digital-to-analog conversion. The resulting operation is said to be "transparent", i.e. the BBU will be unaware that the precoding is taking place. It should however be noted that the work in [130] does not provide details about the delay that the proposed precoding operation introduces between digital and analog IQ signals—a delay that would be caused by the OFDM modulation and demodulation operation. It would therefore be interesting to analyze the impact of such delay, and to examine if the crosstalk can be removed without causing such a delay.

Another challenge in the context of A-RoC over twisted-pair is posed by the long channel impulse responses (CIRs) resulting from the concatenation of a twisted-pair channel with a wireless channel. It is therefore deemed that channel shortening filters could yield improved data rates for A-RoC systems as well. Designing channel shortening filters for this use-case will pose additional interesting technical challenges, particularly due to the fact that (in the uplink) the RRU can only observe the concatenation of a time-invariant twisted-pair channel, and a constantly changing—due to multiple and possibly moving users—wireless channel. Designing the channel shortening filters such that they shorten the time-invariant twisted-pair channel will then pose an interesting challenge.

Appendix A

Appendix to Chapter 2

Convergence of Algorithm 1

The following theorem and proof are inspired by [104, 154].

Theorem 1 (Convergence of Algorithm 1)**.** *The stop criterion on line 4 is met within a finite number of iterations, provided that $f_i(t;\boldsymbol{s})$ and $f_{i_{\text{cvx}}}(t;\boldsymbol{s})$ have the following properties.*

$$f_{i,n_{\text{cvx}}}{}'(0;\boldsymbol{s}_i) = f_{i,n}{}'(0;\boldsymbol{s}_i) \tag{A.1}$$

$$f_{i,n_{\text{cvx}}}(t;\boldsymbol{s}_i) - f_{i,n_{\text{cvx}}}(0;\boldsymbol{s}_i) \leq f_{i,n}(t;\boldsymbol{s}_i) - f_{i,n}(0;\boldsymbol{s}_i), \quad \forall t \in \text{dom} f_{i,n}(t;\boldsymbol{s}_i) \tag{A.2}$$

$$f_{i,n_{\text{cvx}}}(t;\boldsymbol{s}_i) \text{ is continuous} \tag{A.3}$$

$$f_{i,n_{\text{cvx}}}(t;\boldsymbol{s}_i) \text{ is a convex function of } t \tag{A.4}$$

$$f_{i,n}{}'(0;\boldsymbol{s}_i) \text{ is a continuous function of } \boldsymbol{s}_i \tag{A.5}$$

Proof. To simplify notation, the functions $\text{WRS}(\boldsymbol{s})$ and $\text{WRS}_{-ij}(\boldsymbol{s})$ are defined as follows.

$$\text{WRS}(\boldsymbol{s}) \triangleq \sum_{k\in\mathcal{K}} \sum_{n\in\mathcal{N}} \omega_n b_{k,n}(\boldsymbol{s}_k) \tag{A.6}$$

$$\text{WRS}_{-ij}(\boldsymbol{s}) \triangleq \text{WRS}(\boldsymbol{s}) - \phi_n^{i,j}(0;\boldsymbol{s}) \tag{A.7}$$

Consider $\{\boldsymbol{s}^{(\ell)}\}$ the sequence of values for the decision variable $\boldsymbol{s}$ generated by Algorithm 1. Moreover, let $t^{(\ell)}$ denote the value calculated for t on line 7 of Algorithm 1 for the present value of ℓ. Using (A.2), and the fact that $t^{(\ell)}$ is chosen to maximize ${\phi_n^{i,j}}_{\text{cvx}}(t; \boldsymbol{s}^{(\ell)})$, the following inequalities are obtained

$$\begin{aligned}
&\text{WRS}(\boldsymbol{s}^{(\ell+1)}) - \text{WRS}_{-ij}(\boldsymbol{s}^{(\ell+1)}) \\
&= \phi_n^{i,j}(t^{(\ell)}; \boldsymbol{s}^{(\ell)}) \\
&\geq {\phi_n^{i,j}}_{\text{cvx}}(t^{(\ell)}; \boldsymbol{s}^{(\ell)}) - {\phi_n^{i,j}}_{\text{cvx}}(0; \boldsymbol{s}^{(\ell)}) + \phi_n^{i,j}(0; \boldsymbol{s}^{(\ell)}) \\
&\geq {\phi_n^{i,j}}_{\text{cvx}}(0; \boldsymbol{s}^{(\ell)}) - {\phi_n^{i,j}}_{\text{cvx}}(0; \boldsymbol{s}^{(\ell)}) + {\phi_n^{i,j}}_{\text{cvx}}(0; \boldsymbol{s}^{(\ell)}) \\
&= \phi_n^{i,j}(0; \boldsymbol{s}^{(\ell)}) \\
&= \text{WRS}(\boldsymbol{s}^{(\ell)}) - \text{WRS}_{-ij}(\boldsymbol{s}^{(\ell)})
\end{aligned} \tag{A.8}$$

As $\text{WRS}_{-ij}(\boldsymbol{s}^{(\ell+1)}) = \text{WRS}_{-ij}(\boldsymbol{s}^{(\ell)})$, it can be concluded that Algorithm 1 produces a sequence of monotonically increasing objective function values, i.e.

$$\text{WRS}(\boldsymbol{s}^{(\ell+1)}) \geq \text{WRS}(\boldsymbol{s}^{(\ell)}). \tag{A.9}$$

In what follows, Theorem 1 is proven by contradiction. Suppose that Theorem 1 is not true, i.e. Algorithm 1 will continue for an infinite number of iterations without ever satisfying the stop condition on line 4. In each of these infinite iterations, Algorithm 1 selects a donor-acceptor pair from a finite set of such pairs. This implies that at least one donor-acceptor pair, say (i', j'), is selected an infinite number of times. Let $\{\ell'_q\}_{q\in\mathbb{N}_0}$ be the sequence of iterations of Algorithm 1 in which (i', j') is the considered donor-acceptor pair, and let $\{\boldsymbol{s}^{(\ell'_q)}\}_{q\in\mathbb{N}_0}$ be the sequence of values for the decision variable $\boldsymbol{s}$ in these iterations. As the values of $\{\boldsymbol{s}^{(\ell'_q)}\}_{q\in\mathbb{N}_0}$ lie in a bounded set, the Bolzano-Weierstrass theorem dictates that there exists a sub sequence of $\{\boldsymbol{s}^{(\ell'_q)}\}_{q\in\mathbb{N}_0}$ that converges to a limit point $\bar{\boldsymbol{s}}'$. Without loss of generality, it can be assumed that $\{\boldsymbol{s}^{(\ell'_q)}\}_{q\in\mathbb{N}_0}$ itself converges to $\bar{\boldsymbol{s}}'$, i.e. that

$$\lim_{q\to\infty} \boldsymbol{s}^{(\ell'_q)} = \bar{\boldsymbol{s}}'. \tag{A.10}$$

For consecutive elements in $\{\boldsymbol{s}^{(\ell'_q)}\}_{q\in\mathbb{N}_0}$, the following inequalities then hold due to (A.2) and (A.9).

$$\begin{aligned}
&\mathrm{WRS}(\boldsymbol{s}^{(\ell'_{q+1})})\\
&\geq \mathrm{WRS}(\boldsymbol{s}^{(\ell'_q+1)})\\
&= \phi_n^{i',j'}(t^{(\ell'_q)};\boldsymbol{s}^{(\ell'_q)}) + \mathrm{WRS}_{-i'j'}(\boldsymbol{s}^{(\ell'_q)})\\
&\geq \phi_n^{i',j'}{}_{\mathrm{cvx}}(t^{(\ell'_q)};\boldsymbol{s}^{(\ell'_q)}) - \phi_n^{i',j'}{}_{\mathrm{cvx}}(0;\boldsymbol{s}^{(\ell'_q)}) + \phi_n^{i',j'}(0;\boldsymbol{s}^{(\ell'_q)}) + \mathrm{WRS}_{-i'j'}(\boldsymbol{s}^{(\ell'_q)})\\
&= \phi_n^{i',j'}{}_{\mathrm{cvx}}(t^{(\ell'_q)};\boldsymbol{s}^{(\ell'_q)}) - \phi_n^{i',j'}{}_{\mathrm{cvx}}(0;\boldsymbol{s}^{(\ell'_q)}) + \mathrm{WRS}(\boldsymbol{s}^{(\ell'_q)})\\
&\geq \phi_n^{i',j'}{}_{\mathrm{cvx}}(t;\boldsymbol{s}^{(\ell'_q)}) - \phi_n^{i',j'}{}_{\mathrm{cvx}}(0;\boldsymbol{s}^{(\ell'_q)}) + \mathrm{WRS}(\boldsymbol{s}^{(\ell'_q)}), \quad \forall t\in[t_{\min}^{(\ell'_q)}, t_{\max}^{(\ell'_q)}]
\end{aligned} \tag{A.11}$$

Equation (A.11) thus yields the following relation.

$$\begin{aligned}
&\phi_n^{i',j'}{}_{\mathrm{cvx}}(0;\boldsymbol{s}^{(\ell'_{q+1})}) + \mathrm{WRS}(\boldsymbol{s}^{(\ell'_{q+1})})\\
&\geq \phi_n^{i',j'}{}_{\mathrm{cvx}}(t;\boldsymbol{s}^{(\ell'_q)}) + \mathrm{WRS}(\boldsymbol{s}^{(\ell'_q)}), \quad \forall t\in[t_{\min}^{(\ell'_q)}, t_{\max}^{(\ell'_q)}]
\end{aligned} \tag{A.12}$$

Taking the limit $q\to\infty$—and considering (A.3)—implies

$$\phi_n^{i',j'}{}_{\mathrm{cvx}}(0;\bar{\boldsymbol{s}}') \geq \phi_n^{i',j'}{}_{\mathrm{cvx}}(t;\bar{\boldsymbol{s}}'), \quad \forall t\in[\bar{t}'_{\min}, \bar{t}'_{\max}]. \tag{A.13}$$

Owing to (A.4), one of the following must then be true.

$$\phi_n^{i',j''}{}_{\mathrm{cvx}}(0;\bar{\boldsymbol{s}}') \leq 0 \tag{A.14}$$

$$\phi_n^{i',j''}{}_{\mathrm{cvx}}(0;\bar{\boldsymbol{s}}') < 0 \quad \text{and} \quad \bar{t}'_{\min} = 0 \tag{A.15}$$

$$\phi_n^{i',j''}{}_{\mathrm{cvx}}(0;\bar{\boldsymbol{s}}') > 0 \quad \text{and} \quad \bar{t}'_{\max} = 0 \tag{A.16}$$

Due to (A.1), the same must hold for $\phi_n^{i',j''}(0;\bar{\boldsymbol{s}}')$. Two distinct possibilities arise, which both lead to a contradiction.

First, consider that either (A.14) or (A.15) is true. These conditions imply that the stop criterion of Algorithm 1 is strictly satisfied at $\bar{\boldsymbol{s}}'$, i.e. that

$$\phi_n^{i',j''}(0;\bar{\boldsymbol{s}}') = f_{i,n}{}'(0;\bar{\boldsymbol{s}}') - f_{j,n}{}'(0;\bar{\boldsymbol{s}}') \leq 0 < \tau. \tag{A.17}$$

Combined with (A.4) and (A.10), this inequality implies that there exists a finite integer N for which

$$f_{i,n}{}'(0; \boldsymbol{s}^{(\ell'_N)}) - f_{j,n}{}'(0; \boldsymbol{s}^{(\ell'_N)}) < \tau. \tag{A.18}$$

As such, the stopping condition on line 4 must be satisfied after a finite number of iterations, contradicting the assumption that Algorithm 1 will continue for an infinite number of iterations.

Second, consider that (A.16) is true. In this case, owing to the definition of $t_{\max}$ in (2.8), at least one of the following two statements must be true.

$$\bar{s}_{i',n}{}' = s_{i',n}^{\text{mask}} \text{ or } \bar{s}_{j',n}{}' = 0 \tag{A.19}$$

As such, (A.10) would then imply that there exists a finite integer M for which

$$s_{i',n}^{(\ell'_M)} \geq s_{i',n}^{\text{mask}} - \epsilon \quad \Longrightarrow \quad i' \notin \mathcal{A}_n^{\epsilon}(\boldsymbol{s}_n^{(\ell'_M)}) \tag{A.20}$$

or

$$s_{j',n}^{(\ell'_M)} \leq \epsilon \quad \Longrightarrow \quad j' \notin \mathcal{D}_n^{\epsilon}(\boldsymbol{s}_n{}^{(\ell'_M)}) \tag{A.21}$$

This is a contradiction, as the tone selection rule of (2.14) implies that $i' \in \mathcal{A}_n^{\epsilon}(\boldsymbol{s}_n^{(\ell'_M)})$ and $j' \in \mathcal{D}_n^{\epsilon}(\boldsymbol{s}_n^{(\ell'_M)})$. □

Appendix B

Appendix to Chapter 5

Differentiability of the FDX-PD-DSB surrogate's dual function

Differentiability of the dual function in (5.45) is strongly related to uniqueness of the maximizers in (5.45). It is therefore first proven that when $\boldsymbol{\Lambda}^{\mathrm{D}} \succ 0$, all maximization problems in (5.45) have a unique solution. Differentiability of $q(\boldsymbol{\lambda}^{\mathrm{D}})$ then follows from standard results in convex analysis.

Lemma B.1 (Maximizer uniqueness)**.** *Optimization problem*

$$\underset{\substack{\mathbf{Q}\succeq 0\\ \text{Hermitian}}}{\text{maximize}} \log\left(1 + \boldsymbol{h}^{\scriptscriptstyle\mathcal{H}}\mathbf{Q}\boldsymbol{h}\right) - \operatorname{tr}(\mathbf{Y}^{\scriptscriptstyle\mathcal{H}}\mathbf{Q}), \tag{B.1}$$

with $\boldsymbol{h} \neq \mathbf{0}_N$ and $\mathbf{Y}^{\scriptscriptstyle\mathcal{H}}$ positive definite Hermitian, has a unique solution, which furthermore is a rank-1 matrix.

Proof. The proof is based on the proof of [102, Proposition 1]. Let $\mathbf{L}\mathbf{L}^{\scriptscriptstyle\mathcal{H}}$ denote the Cholesky factorization of $\mathbf{Y}$. Furthermore, factorize $\mathbf{Q} = \mathbf{T}\mathbf{T}^{\scriptscriptstyle\mathcal{H}}$ where $\mathbf{T}$ is an $N \times N$ matrix. Defining $\tilde{\mathbf{T}} \triangleq \mathbf{L}^{\scriptscriptstyle\mathcal{H}}\mathbf{T}$, the following problem is equivalent to (B.1).

$$\underset{\tilde{\mathbf{T}}}{\text{maximize}} \log\left|\mathbf{I} + \tilde{\mathbf{T}}^{\scriptscriptstyle\mathcal{H}}\mathbf{L}^{-1}\boldsymbol{h}\boldsymbol{h}^{\scriptscriptstyle\mathcal{H}}\mathbf{L}^{-\scriptscriptstyle\mathcal{H}}\tilde{\mathbf{T}}\right| - \operatorname{tr}(\tilde{\mathbf{T}}\tilde{\mathbf{T}}^{\scriptscriptstyle\mathcal{H}})$$

Let $\mathbf{U}\boldsymbol{\Sigma}\mathbf{U}^{\scriptscriptstyle\mathcal{H}}$ denote the eigendecomposition of the Hermitian matrix $\mathbf{L}^{-1}\boldsymbol{h}\boldsymbol{h}^{\scriptscriptstyle\mathcal{H}}\mathbf{L}^{-\scriptscriptstyle\mathcal{H}}$. After defining $\hat{\mathbf{T}} \triangleq \mathbf{U}^{\scriptscriptstyle\mathcal{H}}\tilde{\mathbf{T}}$, the following problem is obtained, which is still

equivalent to (B.1).

$$\underset{\hat{\mathbf{T}}}{\text{maximize}} \log \left| \mathbf{I} + \hat{\mathbf{T}}^{\mathcal{H}} \boldsymbol{\Sigma} \hat{\mathbf{T}} \right| - \operatorname{tr}(\hat{\mathbf{T}} \hat{\mathbf{T}}^{\mathcal{H}})$$

As $\boldsymbol{\Sigma}$ contains only a single non-zero element $[\boldsymbol{\Sigma}]_{ii} = \sigma$, the problem (B.1) simplifies to

$$\underset{\hat{\mathbf{T}}}{\text{maximize}} \log \left(1 + \sigma \| [\hat{\mathbf{T}}]_{\text{row}i} \|_2^2 \right) - \| \hat{\mathbf{T}} \|_F^2. \tag{B.2}$$

Equation (B.2) implies that any optimal $\hat{\mathbf{T}}$ has non-zero elements only in its ith row, as any non-zero element in $\hat{\mathbf{T}}$ that is not on the i-th row decreases the objective function value of (B.2). Therefore, problem (B.2) simplifies to

$$\underset{[\hat{\mathbf{T}}]_{\text{row}i}}{\text{maximize}} \log \left(1 + \sigma \| [\hat{\mathbf{T}}]_{\text{row}i} \|_2^2 \right) - \| [\hat{\mathbf{T}}]_{\text{row}i} \|_2^2,$$

Observe that any optimal $[\hat{\mathbf{T}}]_{\text{row}i}$ must satisfy $\| [\hat{\mathbf{T}}]_{\text{row}i} \|_2^2 = [1 - \sigma^{-1}]^+$. Therefore, any optimal $\hat{\mathbf{T}}$ yields

$$\mathbf{Q} = \mathbf{L}^{-\mathcal{H}} \mathbf{U} \mathbf{D} \mathbf{U}^{\mathcal{H}} \mathbf{L}^{-1}$$

with $\mathbf{D}$ containing only a single non-zero element $[\mathbf{D}]_{ii} = [1 - \sigma^{-1}]^+$. The solution to (B.1) is thus unique and rank-1. □

Proposition B.2 (Continuous differentiability q^{D})**.** *If $\boldsymbol{h}_{k,n}^{D} \neq \mathbf{0}_N \ \forall k, n$, then the dual function $q^{D}(\boldsymbol{\lambda}^{D})$ defined by* (5.45) *is continuously differentiable on its domain.*

Proof. First, it is argued that the domain of q^{D} is given by $\{\boldsymbol{\lambda}^{\mathrm{D}} \in \mathbb{R}_+^N \mid \lambda_n^{\mathrm{D}} > 0 \, \forall n\}$. Then it is shown that on its domain, q^{D} is continuously differentiable.

If any $\lambda_n^{\mathrm{D}} \leq 0$, then the objective of the maximization in (5.45) can be made arbitrarily large by choosing $\mathbf{Q}_{k,N}^{\mathrm{D}} = \Omega \boldsymbol{e}_n \boldsymbol{e}_n^{\mathcal{H}}$, with $\Omega \to +\infty$.[1] The objective of the maximization in (5.45) is therefore unbounded such that $\boldsymbol{\lambda}^{\mathrm{D}}$ is outside domain of q^{D}. For any $\boldsymbol{\lambda}^{\mathrm{D}} \in \{\boldsymbol{\lambda}^{\mathrm{D}} \in \mathbb{R}_+^N \mid \lambda_n^{\mathrm{D}} > 0 \, \forall n\}$ however, Lemma B.1 implies that a finite maximizer exists, such that $q^{\mathrm{D}}(\boldsymbol{\lambda}^{\mathrm{D}})$ is finite also.

To prove that q^{D} is continuously differentiable on its domain, introduce

$$F_{k,n}(\mathbf{Q}_{k,n}^{\mathrm{D}}) = \begin{cases} -\tilde{f}_{k,n}^{\mathrm{D}}(\mathbf{Q}_{k,n}^{\mathrm{D}}; \bar{\boldsymbol{s}}_k^{\mathrm{D}}, \bar{\mathbf{Q}}_k^{\mathrm{D}}) & \text{if } \mathbf{Q}_{k,n}^{\mathrm{D}} \succeq 0, \text{ Hermitian} \\ +\infty & \text{otherwise} \end{cases}$$

and its conjugate function [155, Chapter 11]

$$F_{k,n}^{*}(\mathbf{Y}) \triangleq \sup_{\mathbf{Q}_{k,n}^{\mathrm{D}}} \left\{ \operatorname{tr}(\mathbf{Y}^{\mathcal{H}} \mathbf{Q}_{k,n}^{\mathrm{D}}) - F_{k,n}(\mathbf{Q}_{k,n}^{\mathrm{D}}) \right\}.$$

[1] See footnote 5 of chapter 5 on page 114.

Using this definition of $F^*_{k,n}(\mathbf{Y})$, (5.45) can be rewritten as

$$q^{\mathrm{D}}(\boldsymbol{\lambda}^{\mathrm{D}}) = \sum_k \sum_n F^*_{k,n}\big(-\operatorname{diag}(\boldsymbol{\lambda}^{\mathrm{D}})\big) + \mathbf{1}_N^{\mathrm{T}} \boldsymbol{\lambda}^{\mathrm{D}} P^{\mathrm{D}}_{\mathrm{tot}}.$$

From [155, Theorem 11.8] it is known that the subdifferential of $F^*_{k,n}(\mathbf{Y})$ is given by the solution set of the optimization problem defining the conjugate function, i.e.

$$\partial F^*_{k,n}(\mathbf{Y}) = \underset{\mathbf{Q}^{\mathrm{D}}_{k,n}}{\arg\max} \left\{ \operatorname{tr}(\mathbf{Y}^{\mathcal{H}} \mathbf{Q}^{\mathrm{D}}_{k,n}) - F_{k,n}(\mathbf{Q}^{\mathrm{D}}_{k,n}) \right\}.$$

Lemma B.1 implies that $\partial F^*_{k,n}(\mathbf{Y})$ is a singleton whenever $\mathbf{Y}$ is negative definite and Hermitian, i.e. $F^*_{k,n}(\mathbf{Y})$ is differentiable at any negative definite Hermitian $\mathbf{Y}$. Moreover, the proof of [155, Theorem 11.8] mentions that "$\partial F^*_{k,n}(\bar{\mathbf{Y}})$ is singleton if and only if $F^*_{k,n}(\mathbf{Y})$ is strictly differentiable at $\bar{\mathbf{Y}}$". $F^*_{k,n}(\mathbf{Y})$ is thus strictly differentiable on the open set of negative definite Hermitian matrices, implying that $F^*_{k,n}(\mathbf{Y})$ is continuously differentiable on the same set [155, Corollary 9.19]. It immediately follows that $q^{\mathrm{D}}(\boldsymbol{\lambda}^{\mathrm{D}})$ is continuously differentiable on its domain. □

Appendix C

Appendix to Chapter 6

Proof of Proposition 6.2

P6.1.a $\mathcal{S}$ **is non-empty, closed, convex:**
Trivially satisfied, as

$$\mathcal{S} = \left\{ \boldsymbol{S} \in \mathbb{R}_{+}^{N} \mid \sum\nolimits_{n=0}^{N-1} S_n \left|\mathrm{col}_n \, \mathbf{T}\right|^2 \leq sP_{\text{sample}} \right\}.$$

P6.1.b $F \in C^1$ **on an open set** $\mathcal{V} \supset \mathcal{S}$**:**
As the function $\log_2(1 + \Gamma^{-1}\bullet)$ is differentiable on $\mathbb{R}_{++} - \{\Gamma\}$, the result can be proven by constructing an open set $\mathcal{V} \supset \mathcal{S}$ on which $\gamma_n \in C^1$ and $\gamma_n > -\Gamma$ for each $n \in \{0, \ldots, N-1\}$. By restricting $\mathcal{V}$ to be of the form

$$\mathcal{V} = \left\{ \boldsymbol{V} \in \mathbb{R}_{++}^{N} - \{[\epsilon, \ldots, \epsilon]^{\mathrm{T}}\} \mid \sum\nolimits_{n=0}^{N-1} V_n \left|\mathrm{col}_n \, \mathbf{T}\right|^2 < 2sP_{\text{sample}} \right\},$$

the proof simplifies to finding an $\epsilon > 0$ such that on $\mathcal{V}$, both $\gamma_n \in C^1$ and $\gamma_n > -\Gamma$ for each $n \in \{0, \ldots, N-1\}$. It will be proven that if ϵ is chosen such that

$$\epsilon < \min_{n} \frac{\lambda_{\min}\left(\sigma_{\mathrm{t}}^2 \mathbf{R}_n \mathbf{R}_n^{\mathcal{H}}\right)}{\Gamma^{-1} \left|\boldsymbol{h}_n\right|^2 + \lambda_{\max}\left(\sum_{m=0}^{N-1} \mathbb{H}_{nm} \mathbb{H}_{nm}^{\mathcal{H}}\right)}, \tag{C.1}$$

where $\lambda_{\min}(\mathbf{A})$ and $\lambda_{\max}(\mathbf{A})$ denote the smallest and largest eigenvalue of $\mathbf{A}$ respectively, both conditions are satisfied.

As for the condition that $\gamma_n > -\Gamma$ on $\mathcal{V}$, from (C.1) it follows that for each $n \in \{0, \ldots, N-1\}$

$$\epsilon\Gamma^{-1} |\boldsymbol{h}_n|^2 < \lambda_{\min}\big(\sigma_{\mathrm{t}}^2 \underline{\mathbf{R}}_n \underline{\mathbf{R}}_n^{\scriptscriptstyle\mathcal{H}}\big) + \lambda_{\min}\big(-\sum_{m=0}^{N-1} \epsilon \mathbb{H}_{nm} \mathbb{H}_{nm}^{\scriptscriptstyle\mathcal{H}}\big).$$

Weyl's inequality then implies that for each $n \in \{0, \ldots, N-1\}$

$$\epsilon\Gamma^{-1} |\boldsymbol{h}_n|^2 < \lambda_{\min}\big(\boldsymbol{\Psi}_n(-[\epsilon, \ldots, \epsilon]^{\scriptscriptstyle\mathcal{T}})\big) = \inf_{\boldsymbol{V} \in \mathcal{V}} \lambda_{\min}\big(\boldsymbol{\Psi}_n(\boldsymbol{V})\big), \tag{C.2}$$

which is equivalent to

$$\epsilon\, |\boldsymbol{h}_n|^2 \sup_{\boldsymbol{V} \in \mathcal{V}} \lambda_{\max}\big(\boldsymbol{\Psi}_n(\boldsymbol{V})^{-1}\big) < \Gamma. \tag{C.3}$$

As $\boldsymbol{b}^{\scriptscriptstyle\mathcal{H}} \mathbf{A} \boldsymbol{b} \leq \lambda_{\max}(\mathbf{A}) |\boldsymbol{b}|^2$ for any invertible matrix $\mathbf{A}$ and vector $\boldsymbol{b}$, equation (C.3) yields

$$-\Gamma < -\epsilon \sup_{\boldsymbol{V} \in \mathcal{V}} \left\{ \boldsymbol{h}_n^{\scriptscriptstyle\mathcal{H}} \boldsymbol{\Psi}_n(\boldsymbol{V})^{-1} \boldsymbol{h}_n \right\}, \tag{C.4}$$

implying that for each $n \in \{0, \ldots, N-1\}$

$$-\Gamma < \inf_{\boldsymbol{V} \in \mathcal{V}} \gamma_n(\boldsymbol{V}). \tag{C.5}$$

Returning to the condition that $\gamma_n \in C^1$ on $\mathcal{V}$, as $f, g \in C^1 \implies fg \in C^1$, it suffices to establish continuous differentiability for $\boldsymbol{h}_n^{\scriptscriptstyle\mathcal{H}} \boldsymbol{\Psi}_n^{-1} \boldsymbol{h}_n$. To do so, it is noted that the inverse of any invertible matrix $\mathbf{A}$ can be written as

$$\mathbf{A}^{-1} = \frac{1}{\det \mathbf{A}} \mathbf{C} \tag{C.6}$$

with $\mathbf{C}$ the cofactor matrix of $\mathbf{A}$, the elements of which are given by the (negative) determinant of specific sub-matrices of $\mathbf{A}$. Using the fact that the determinant of any matrix is a polynomial function of the matrix elements, it can then be seen that there exists a real polynomial function $P : \mathbb{R}^N \to \mathbb{R}$ such that

$$\boldsymbol{h}_n^{\scriptscriptstyle\mathcal{H}} \boldsymbol{\Psi}_n^{-1} \boldsymbol{h}_n = \frac{P}{\det \boldsymbol{\Psi}_n}. \tag{C.7}$$

As both P and $\det \boldsymbol{\Psi}_n$ are continuously differentiable functions, and as it is known from (C.2) that $0 < \det \boldsymbol{\Psi}_n$ on $\mathcal{V}$, it can be concluded that $\boldsymbol{h}_n^{\scriptscriptstyle\mathcal{H}} \boldsymbol{\Psi}_n^{-1} \boldsymbol{h}_n$—and by extension γ_n—is continuously differentiable on $\mathcal{V}$.

P6.1.c ∇F is Lipschitz continuous on $\mathcal{S}$:
Using the same arguments as in the proof of **P6.1.b**, it can be seen that each $(n+1)$-th partial derivative of F—which is given in (C.8)—is itself continuously

$$\frac{\partial F}{\partial S_n} = -\sum_{m=0}^{N-1} \frac{S_m/\log(2)}{\Gamma + \gamma_m(\boldsymbol{S})} \left|\mathbb{H}_{mn}^{\scriptscriptstyle\mathcal{H}} \boldsymbol{\Psi}_m(\boldsymbol{S})^{-1} \boldsymbol{h}_m\right|^2 + \frac{1/\log(2)}{\Gamma + \gamma_n(\boldsymbol{S})} \boldsymbol{h}_n^{\scriptscriptstyle\mathcal{H}} \boldsymbol{\Psi}_n(\boldsymbol{S})^{-1} \boldsymbol{h}_n \tag{C.8}$$

differentiable on $\mathcal{V}$. As continuous differentiability implies Lipschitz continuity, it is concluded that ∇F is Lipschitz continuous on $\mathcal{S}$.

P6.1.d F **is bounded from above on** $\mathcal{S}$**:**
Trivially satisfied, as

$$\max_{\boldsymbol{S}\in\mathcal{S}} \gamma_n(\boldsymbol{S}) \leq \frac{sP_{\text{sample}}}{\left|\text{col}_n\, \mathbf{T}\right|^2} \boldsymbol{h}_n^{\scriptscriptstyle\mathcal{H}} (\sigma_{\text{t}}^2 \underline{\mathbf{R}}_n \underline{\mathbf{R}}_n^{\scriptscriptstyle\mathcal{H}})^{-1} \boldsymbol{h}_n, \quad \forall n. \tag{C.9}$$

P6.1.e $\tilde{F}(\bullet|\tilde{\boldsymbol{S}}) \in C^1$ **on an open set** $\mathcal{V} \supset \mathcal{S}$**,** $\forall \tilde{\boldsymbol{S}} \in \mathcal{S}$**:**
As $\sigma_{\text{t}}^2 \underline{\mathbf{R}}_n \underline{\mathbf{R}}_n^{\scriptscriptstyle\mathcal{H}} \succ 0$, it is evident from their definitions in (6.40) that both ψ_n and a_n are positive and bounded on $\mathcal{S}$. Letting $\psi_n^{\max} \in \mathbb{R}_+$ denote a finite upper bound for ψ_n on $\mathcal{S}$, it can be seen that $\tilde{F}(\bullet|\tilde{\boldsymbol{S}}) \in C^1$ on the open set

$$\mathbb{R}_{++}^N - \left\{\Gamma\left[(\psi_0^{\max})^{-1}, \ldots, (\psi_{N-1}^{\max})^{-1}\right]^{\text{T}}\right\}. \tag{C.10}$$

P6.1.f $\tilde{F}(\bullet|\tilde{\boldsymbol{S}})$ **is uniformly strongly concave,** $\forall \tilde{\boldsymbol{S}} \in \mathcal{S}$**:**
The $(n+1)$-th partial derivative of $\tilde{F}(\bullet|\tilde{\boldsymbol{S}})$ is given as

$$\frac{\partial}{\partial S_n} \tilde{F}(\bullet|\tilde{\boldsymbol{S}}) = \frac{\psi_n(\tilde{\boldsymbol{S}})/\log(2)}{\Gamma + S_n \psi_n(\tilde{\boldsymbol{S}})} - a_n(\tilde{\boldsymbol{S}}). \tag{C.11}$$

Using the same arguments as in the proof of **P6.1.e**, it is proven that $\tilde{F}(\bullet|\tilde{\boldsymbol{S}}) \in C^2$ on an open set $\mathcal{V} \supset \mathcal{S}$. The Hessian of $\tilde{F}(\bullet|\tilde{\boldsymbol{S}})$ is a diagonal matrix that is defined by

$$\frac{\partial^2}{\partial S_n^2} \tilde{F}(\bullet|\tilde{\boldsymbol{S}}) = -\frac{\psi_n(\tilde{\boldsymbol{S}})^2/\log(2)}{\left(\Gamma + S_n \psi_n(\tilde{\boldsymbol{S}})\right)^2}. \tag{C.12}$$

Strong concavity of $\tilde{F}(\bullet|\tilde{\boldsymbol{S}})$ can thus be proven by establishing an upper bound on the Hessian's diagonal elements, which in turn requires establishing a positive upper bound and a strictly positive lower bound for ψ_n on $\mathcal{S}$. An upper bound for ψ_n on $\mathcal{S}$ was already established as part of the proof for **P6.1.e**. The fact that a strictly positive lower bound for ψ_n exists on $\mathcal{S}$ is due to the eigenvalues of $\boldsymbol{\Psi}_i$ being bounded on $\mathcal{S}$.

P6.1.g $\nabla F(\tilde{\boldsymbol{S}}) = \nabla \tilde{F}(\bullet|\tilde{\boldsymbol{S}})\big|_{\boldsymbol{S}=\tilde{\boldsymbol{S}}}$**,** $\forall \tilde{\boldsymbol{S}} \in \mathcal{S}$**:**
Substituting $a_n(\tilde{\boldsymbol{S}})$ in (C.11) with its definition in (6.40b) and setting $\boldsymbol{S} = \tilde{\boldsymbol{S}}$ yields (C.8).

P6.1.h $\nabla\tilde{F}(\boldsymbol{S}|\bullet)$ is Lipschitz continuous on $\mathcal{S}$ for all $\boldsymbol{S} \in \mathcal{S}$:
Using the same arguments as in the proof of **P6.1.b**, it can be proven that each $(n+1)$-th partial derivative of $\tilde{F}(\boldsymbol{S}|\bullet)$—which is given in (C.13a)-(C.13d) on page 221— is itself continuously differentiable on $\mathcal{V}$. As continuous differentiability implies Lipschitz continuity, it is concluded that $\nabla\tilde{F}(\boldsymbol{S}|\bullet)$ is Lipschitz continuous on $\mathcal{S}$.

$$\frac{\partial}{\partial \tilde{S}_n}\tilde{F}(\boldsymbol{S}|\bullet) = -\sum_{m=0}^{N-1}\left(\frac{S_m\left|\mathbb{H}^{\mathcal{H}}_{mn}\boldsymbol{\Psi}_m(\tilde{\boldsymbol{S}})^{-1}\boldsymbol{h}_m\right|^2}{\Gamma + S_m\psi_m(\tilde{\boldsymbol{S}})} + S_m\frac{\partial a_m}{\partial \tilde{S}_n}\right) \tag{C.13a}$$

$$\frac{\partial a_m}{\partial \tilde{S}_n} = \sum_{o=0}^{N-1}\left[\left|\mathbb{H}^{\mathcal{H}}_{om}\boldsymbol{\Psi}_o(\tilde{\boldsymbol{S}})^{-1}\boldsymbol{h}_o\right|^2\frac{\partial}{\partial \tilde{S}_n}\frac{\tilde{S}_o/\log(2)}{\Gamma+\gamma_o(\tilde{\boldsymbol{S}})} + \frac{\tilde{S}_o/\log(2)}{\Gamma+\gamma_o(\tilde{\boldsymbol{S}})}\frac{\partial}{\partial \tilde{S}_n}\left|\mathbb{H}^{\mathcal{H}}_{om}\boldsymbol{\Psi}_o(\tilde{\boldsymbol{S}})^{-1}\boldsymbol{h}_o\right|^2\right] \tag{C.13b}$$

$$\frac{\partial}{\partial \tilde{S}_n}\frac{\tilde{S}_o/\log(2)}{\Gamma+\gamma_o(\tilde{\boldsymbol{S}})} = -\left(\Gamma+\gamma_o(\tilde{\boldsymbol{S}})\right)^{-2}/\log(2)\begin{cases}\tilde{S}_o\left|\mathbb{H}^{\mathcal{H}}_{on}\boldsymbol{\Psi}_o(\tilde{\boldsymbol{S}})^{-1}\boldsymbol{h}_o\right|^2 - \Gamma - \gamma_o(\tilde{\boldsymbol{S}}) & \text{when } n=o\\ \tilde{S}_o\left|\mathbb{H}^{\mathcal{H}}_{on}\boldsymbol{\Psi}_o(\tilde{\boldsymbol{S}})^{-1}\boldsymbol{h}_o\right|^2 & \text{when } n\neq o\end{cases} \tag{C.13c}$$

$$\frac{\partial}{\partial \tilde{S}_n}\left|\mathbb{H}^{\mathcal{H}}_{om}\boldsymbol{\Psi}_o(\tilde{\boldsymbol{S}})^{-1}\boldsymbol{h}_o\right|^2 = 2\Re\left\{\boldsymbol{h}_o^{\mathcal{H}}\boldsymbol{\Psi}_o(\tilde{\boldsymbol{S}})^{-1}\mathbb{H}_{on}\mathbb{H}^{\mathcal{H}}_{on}\boldsymbol{\Psi}_o(\tilde{\boldsymbol{S}})^{-1}\mathbb{H}_{om}\mathbb{H}^{\mathcal{H}}_{om}\boldsymbol{\Psi}_o(\tilde{\boldsymbol{S}})^{-1}\boldsymbol{h}_o\right\} \tag{C.13d}$$

Appendix D

Appendix to Chapter 7

The circularity coefficient

The circularity coefficient is defined as the magnitude of the complex correlation coefficient ρ [8], which in turn is defined for scalar random variables of the form $x = x_r + jx_i$ as

$$\rho = \frac{\mathbb{E}\left\{x^2\right\}}{\mathbb{E}\left\{xx^*\right\}}. \tag{D.1}$$

The range of possible values for the circularity coefficient $|\rho|$ is $0 \leq |\rho| \leq 1$. Moreover, $\rho = 0$ when x is proper, and $|\rho| = 1$ when x is maximally improper. Given $\Psi_{x_r x_r} \triangleq \mathbb{E}\{x_r x_r\}$, $\Psi_{x_i x_i} \triangleq \mathbb{E}\{x_i x_i\}$, $\Psi_{x_r x_i} \triangleq \mathbb{E}\{x_r x_i\}$, the complex correlation coefficient ρ can equivalently be calculated as [8]

$$\rho = \frac{\Psi_{x_r x_r} - \Psi_{x_i x_i}}{\Psi_{x_r x_r} + \Psi_{x_i x_i}} + j\frac{2\Psi_{x_r x_i}}{\Psi_{x_r x_r} + \Psi_{x_i x_i}}. \tag{D.2}$$

Expressions will now be given that can be used to determine the complex correlation coefficient of the interference-plus-noise, as well as for the complex correlation coefficient of the direct signals. If x in (D.2) is given by $x^{\mathbb{R}} = \underline{\mathbf{U}}_n^{\mathrm{T}} \underline{\boldsymbol{z}}_n^{\mathbb{R}}$, then it can be seen from the composite real channel model in (7.25) that $\Psi_{x_r x_r}$, $\Psi_{x_i x_i}$, and $\Psi_{x_r x_i}$ can be calculated as follows.

$$\begin{bmatrix} \Psi_{x_r x_r} & \Psi_{x_r x_i} \\ \Psi_{x_i x_r} & \Psi_{x_i x_i} \end{bmatrix} = \underline{\mathbf{U}}_n^{\mathrm{T}} \boldsymbol{\Psi}_{\boldsymbol{z}_n^{\mathbb{R}} \boldsymbol{z}_n^{\mathbb{R}}} \underline{\mathbf{U}}_n \tag{D.3}$$

If, on the other hand, x in (D.2) is given by $x^{\mathbb{R}} = \underline{\mathbf{U}}_n^{\mathrm{T}} \underline{\mathbf{G}}_n X_n^{\mathbb{R}}[k]$, then—using $\mathbb{E}\{X_n^{\mathbb{R}}[k](X_n^{\mathbb{R}}[k])^{\mathrm{T}} = \frac{S_n}{2}\mathbf{I}_2$—it can be seen that $\Psi_{x_r x_r}$, $\Psi_{x_i x_i}$, and $\Psi_{x_r x_i}$ can be

calculated as follows.

$$\begin{bmatrix} \Psi_{x_r x_r} & \Psi_{x_r x_i} \\ \Psi_{x_i x_r} & \Psi_{x_i x_i} \end{bmatrix} = \underline{\mathbf{U}}_n^{\mathrm{T}} \left(\frac{S_n}{2} \underline{\mathbf{G}}_n \underline{\mathbf{G}}_n^{\mathrm{T}} \right) \underline{\mathbf{U}}_n \tag{D.4}$$

Bibliography

[1] Cisco Voice Codec Calculator.

[2] Multitone modulation. In *Subband and Wavelet Transforms: Design and Applications*, I. Kalet, Ed., vol. 340 of *The Kluwer International Series in Engineering and Computer Science*. Springer US, Boston, MA, 1996.

[3] Triple-play services quality of experience (QoE) requirements. Tech. Rep. 126, DSL-Forum, 2006.

[4] Cisco Vision: 5G - thriving indoors, 2007. Whitepaper.

[5] Acatauassu, D., Höst, S., Lu, C., Berg, M., Klautau, A., and Börjesson, P. O. Simple and causal twisted-pair channel models for G.fast systems. In *Proc. IEEE Global Communications Conference (GLOBECOM)* (Atlanta, United States, Dec. 2013), pp. 2834–2839.

[6] Acker, K. V., Leus, G., Moonen, M., Wiel, O. v. d., and Pollet, T. Per tone equalization for DMT-based systems. *IEEE Transactions on Communications 49*, 1 (Jan. 2001), 109–119.

[7] Acker, K. V., Moonen, M., and Pollet, T. Per-tone echo cancellation for DMT-based systems. *IEEE Transactions on Communications 51*, 9 (Sept. 2003), 1582–1590.

[8] Adali, T., Schreier, P. J., and Scharf, L. L. Complex-valued signal processing: The proper way to deal with impropriety. *IEEE Transactions on Signal Processing 59*, 11 (Nov. 2011), 5101–5125.

[9] Ahmed, N. U., and Rao, K. R. *Orthogonal transforms for digital signal processing*. Springer-Verlag, Berlin, Heidelberg, 1975.

[10] Al-Dhahir, N., and Cioffi, J. Efficiently computed reduced-parameter input-aided MMSE equalizers for ML detection: a unified approach. *IEEE Transactions on Information Theory 42*, 3 (May 1996), 903–915.

[11] Al-Dhahir, N., and Cioffi, J. Optimum finite-length equalization for multicarrier transceivers. *IEEE Transactions on Communications 44*, 1 (Jan. 1996), 56–64.

[12] Arslan, G., Evans, B., and Kiaei, S. Equalization for discrete multitone transceivers to maximize bit rate. *IEEE Transactions on Signal Processing 49*, 12 (Dec. 2001), 3123–3135.

[13] Barthelme, A., Joham, M., Strobel, R., and Utschick, W. User demand based precoding for G.fast DSL systems. *arXiv:1811.05150* (Nov. 2018). arXiv: 1811.05150.

[14] Beck, A. The 2-coordinate descent method for solving double-sided simplex constrained minimization problems. *Journal of Optimization Theory and Applications 162*, 3 (Sept. 2014), 892–919.

[15] Behfarnia, M., Forouzan, A. R., and Sabahi, M. F. A fast fixed point algorithm for real-time spectrum balancing of DSL. In *Proc. International Symposium on Telecommunications (IST)* (Tehran, Iran, Dec. 2018), pp. 144–148.

[16] Behmandpoor, P., Verdyck, J., and Moonen, M. Deep learning-based cross-layer resource allocation for wired communication systems. In *Proc. IEEE International Conference on Acoustics, Speech and Signal Processing (ICASSP)* (Toronto, Canada (online), June 2021).

[17] Bertsekas, D. P. *Nonlinear Programming*, 2nd ed. Athena Scientific, Sept. 1999.

[18] Bezerra, J., Klautau, A., Monteiro, M., Pelaes, E., Medeiros, E., and Dortschy, B. An evolutionary algorithm for improved diversity in DSL spectrum balancing solutions. *EURASIP Journal on Advances in Signal Processing*, 1 (May 2010), 1–11.

[19] Bingham, J. A. C. Multicarrier modulation for data transmission: an idea whose time has come. *IEEE Communications Magazine 28*, 5 (May 1990), 5–14.

[20] Boyd, S., and Vandenberghe, L. Duality. In *Convex optimization*. Cambridge university press, 2004.

[21] Boyd, S., Xiao, L., Mutapcic, A., and Mattingley, J. Notes on decomposition methods. *Notes for EE364B, Stanford University* (2007), 1–36.

[22] Brehmer, J. *Utility Maximization in Nonconvex Wireless Systems*, vol. 5 of *Springer Foundations in Signal Processing, Communications and Networking*. Springer, Berlin, Heidelberg, 2012.

[23] Bruggen, T., and Vary, P. Unequal error protection by modulation with unequal power allocation. *IEEE Communications Letters 9*, 6 (June 2005), 484–486.

[24] Burachik, R., Drummond, L. M. G., Iusem, A. N., and Svaiter, B. F. Full convergence of the steepest descent method with inexact line searches. *Optimization 32*, 2 (Jan. 1995), 137–146.

[25] Byrd, R. H., Lu, P., Nocedal, J., and Zhu, C. A limited memory algorithm for bound constrained optimization. *SIAM Journal on Scientific Computing 16*, 5 (Sept. 1995), 1190–1208.

[26] Caire, G., and Shamai, S. On the achievable throughput of a multiantenna Gaussian broadcast channel. *IEEE Transactions on Information Theory 49*, 7 (July 2003), 1691–1706.

[27] Cannelli, L., Facchinei, F., Kungurtsev, V., and Scutari, G. Asynchronous parallel algorithms for nonconvex big-data optimization - Part II: Complexity and numerical results. *arXiv:1701.04900 [math]* (Jan. 2017). arXiv: 1701.04900.

[28] Cendrillon, R., Ginis, G., Bogaert, E. V. D., and Moonen, M. A near-optimal linear crosstalk precoder for upstream VDSL. *IEEE Transactions on Signal Processing 54*, 8 (Aug. 2006), 3136–3146. Conference Name: IEEE Transactions on Signal Processing.

[29] Cendrillon, R., Ginis, G., Van den Bogaert, E., and Moonen, M. A near-optimal linear crosstalk precoder for downstream VDSL. *IEEE Transactions on Communications 55*, 5 (May 2007), 860–863.

[30] Cendrillon, R., Huang, J., Chiang, M., and Moonen, M. Autonomous spectrum balancing for digital subscriber lines. *IEEE Transactions on Signal Processing 55*, 8 (Aug. 2007), 4241–4257.

[31] Cendrillon, R., and Moonen, M. Iterative spectrum balancing for digital subscriber lines. In *Proc. IEEE International Conference on Communications (ICC)* (Coruña, Spain, May 2005), vol. 3, pp. 1937–1941.

[32] Cendrillon, R., Yu, W., Moonen, M., Verlinden, J., and Bostoen, T. Optimal multiuser spectrum balancing for digital subscriber lines. *IEEE Transactions on Communications 54*, 5 (May 2006), 922–933.

[33] Chan, V. M. K., and Yu, W. Multiuser spectrum optimization for discrete multitone systems with asynchronous crosstalk. *IEEE Transactions on Signal Processing 55*, 11 (Nov. 2007), 5425–5435.

[34] Checko, A., Christiansen, H. L., Yan, Y., Scolari, L., Kardaras, G., Berger, M. S., and Dittmann, L. Cloud RAN for mobile networks—A technology overview. *IEEE Communications Surveys Tutorials 17*, 1 (2015), 405–426.

[35] Chen, C.-Y., and Phoong, S.-M. Per tone shaping filters for DMT transmitters. In *Proc. IEEE International Conference on Acoustics, Speech, and Signal Processing (ICASSP)* (Montreal, Canada, Apr. 2004), pp. 1061–1064.

[36] Chiang, M., Low, S. H., Calderbank, a. R., and Doyle, J. C. Layering as optimization decomposition: A mathematical theory of network architectures. *Proceedings of the IEEE 95*, 1 (Jan. 2007), 255–312.

[37] Chiang, M., Tan, C. W., Palomar, D. P., O'neill, D., and Julian, D. Power control by geometric programming. *IEEE Transactions on Wireless Communications 6*, 7 (July 2007), 2640–2651.

[38] Chow, J., Tu, J., and Cioffi, J. A discrete multitone transceiver system for HDSL applications. *IEEE Journal on Selected Areas in Communications 9*, 6 (Aug. 1991), 895–908.

[39] Chow, P., Cioffi, J., and Bingham, J. A practical discrete multitone transceiver loading algorithm for data transmission over spectrally shaped channels. *IEEE Transactions on Communications 43*, 2/3/4 (Feb. 1995), 773–775.

[40] Chung, S. T., and Goldsmith, A. Degrees of freedom in adaptive modulation: a unified view. *IEEE Transactions on Communications 49*, 9 (Sept. 2001), 1561–1571.

[41] Cioffi, J., Brady, M., Pourahmad, V., Jagannathan, S., Lee, W.-Y., Kim, Y., Chen, C., and Seong, K. Vectored DSLs with DSM : The road to ubiquitous gigabit.

[42] Cioffi, J., Jagannathan, S., and Lee, W. Digital subscriber line (DSL). *Scholarpedia 3*, 8 (Aug. 2008), 3995–3995.

[43] Cioffi, J. M. Lighting up copper: History of communications. *IEEE Communications Magazine 49*, 5 (May 2011), 30–43.

[44] Cioffi, J. M., and Forney, G. D. Generalized decision-feedback equalization for packet transmission with ISI and gaussian noise. In *Communications, Computation, Control, and Signal Processing*, A. Paulraj, V. Roychowdhury, and C. D. Schaper, Eds. Springer US, Boston, MA, 1997, pp. 79–127.

[45] Cioffi, J. M., Hwang, C.-S., Kanellakopoulos, I., Oh, J., and Kerpez, K. J. Cellular subscriber lines (CSL): A wireless-wireline physically converged architecture. *IEEE Transactions on Communications 68*, 12 (Dec. 2020), 7289–7310.

[46] Cioffi, J. M., Kerpez, K. J., Hwang, C. S., and Kanellakopoulos, I. Terabit DSLs. *IEEE Communications Magazine 56*, 11 (Nov. 2018), 152–159.

[47] Cioffi, J. M., Rhee, W., Mohseni, M., and Brady, M. H. Band preference in dynamic spectrum management. In *12th European Signal Processing Conference (EUSIPCO)* (Vienna, Austria, Sept. 2004), pp. 1205–1208.

[48] Cirik, A. C., Wang, R., Hua, Y., and Latva-aho, M. Weighted sum-rate maximization for full-duplex MIMO interference channels. *IEEE Transactions on Communications 63*, 3 (Mar. 2015), 801–815.

[49] Coomans, W., Moraes, R. B., Hooghe, K., Duque, A., Galaro, J., Timmers, M., van Wijngaarden, A. J., Guenach, M., and Maes, J. XG-fast: the 5th generation broadband. *IEEE Communications Magazine 53*, 12 (Dec. 2015), 83–88.

[50] Costa, M. Writing on dirty paper (Corresp.). *IEEE Transactions on Information Theory 29*, 3 (May 1983), 439–441.

[51] Dutta, J., Deb, K., Tulshyan, R., and Arora, R. Approximate KKT points and a proximity measure for termination. *Journal of Global Optimization 56*, 4 (Aug. 2013), 1463–1499.

[52] Effenberger, F. Future broadband access networks. *Proceedings of the IEEE 104*, 11 (Nov. 2016), 2078–2081.

[53] Ehtiati, N. *Dual domain echo cancellation for discrete multitone systems.* PhD Thesis, McGill University, Montreal, Canada, Apr. 2011.

[54] Ehtiati, N., and Champagne, B. Constrained adaptive echo cancellation for discrete multitone systems. *IEEE Transactions on Signal Processing 57*, 1 (Jan. 2009), 302–312.

[55] Facchinei, F., Lampariello, L., and Scutari, G. Feasible methods for nonconvex nonsmooth problems with applications in green communications. *Mathematical Programming 164*, 1 (July 2017), 55–90.

[56] Facchinei, F., Scutari, G., and Sagratella, S. Parallel selective algorithms for nonconvex big data aptimization. *IEEE Transactions on Signal Processing 63*, 7 (Apr. 2015), 1874–1889.

[57] Forney, G., and Eyuboglu, M. Combined equalization and coding using precoding. *IEEE Communications Magazine 29*, 12 (Dec. 1991), 25–34.

[58] Forney, G., and Wei, L.-F. Multidimensional constellations. I. Introduction, figures of merit, and generalized cross constellations. *IEEE Journal on Selected Areas in Communications 7*, 6 (Aug. 1989), 877–892.

[59] Forouzan, A. R., Moonen, M., Maes, J., and Guenach, M. Efficient calculation of the MMSE-GDFE decoding order in non-ideal DSL multiple-access channels. In *Proc. IEEE Symposium on Communications and Vehicular Technology in the Benelux (SCVT)* (Enschede, Netherlands, Nov. 2010), IEEE, pp. 1–6.

[60] Forouzan, A. R., Moonen, M., Maes, J., and Guenach, M. Joint level 2 and 3 dynamic spectrum management for upstream VDSL. *IEEE Transactions on Communications 59*, 10 (Oct. 2011), 2851–2861.

[61] Forouzan, A. R., Moonen, M., Maes, J., and Guenach, M. Joint level 2 and 3 dynamic spectrum management for downstream DSL. *IEEE Transactions on Communications 60*, 10 (Oct. 2012), 3111–3122.

[62] Forouzan, A. R., Moonen, M., Maes, J., and Guenach, M. Dynamic bandplanning for vectored DSL. *IEEE Transactions on Communications 62*, 1 (Jan. 2014), 302–315.

[63] Forouzan, A. R., and Shahtalebi, K. Price of fairness in digital subscriber line systems using dynamic spectrum management. *IEEE Transactions on Communications* (2021), 1–1.

[64] FTTH Council Europe. The cost of meeting Europe's future network needs. Tech. rep., Mar. 2017.

[65] Gambini, J., and Spagnolini, U. Radio over telephone lines in femtocell systems. In *Proc. Annual IEEE International Symposium on Personal, Indoor and Mobile Radio Communications (PIMRC)* (Istanbul, Turkey, Sept. 2010), pp. 1544–1549.

[66] Ginis, G., and Cioffi, J. A multi-user precoding scheme achieving crosstalk cancellation with application to DSL systems. In *Proc. Asilomar Conference on Signals, Systems and Computers* (Pacific Grove, United States, Oct. 2000), vol. 2, pp. 1627–1631.

[67] Ginis, G., and Cioffi, J. Vectored transmission for digital subscriber line systems. *IEEE Journal on Selected Areas in Communications 20*, 5 (June 2002), 1085–1104.

[68] Gomes, A., Monteiro, M., Dortschy, B., and Klautau, A. An hybrid evolutionary multiobjective algorithm for multiuser margin maximization in DSL. *International Journal of Communication Systems 29*, 1 (2016), 194–209.

[69] Harashima, H., and Miyakawa, H. Matched-transmission technique for channels with intersymbol interference. *IEEE Transactions on Communications 20*, 4 (Aug. 1972), 774–780.

[70] Harry S. Truman. Letter to Dr. Irvin L. Stewart on the establishment of the President's communications policy board, 1950. Online by Gerhard Peters and John T. Woolley, https://www.presidency.ucsb.edu/node/230679.

[71] Hayashi, S., and Luo, Z. Spectrum management for interference-limited multiuser communication systems. *IEEE Transactions on Information Theory 55*, 3 (Mar. 2009), 1153–1175.

[72] Hejazi, A. M., Stockman, G.-J., Lefevre, Y., Ginis, V., and Coomans, W. Calculating millimeter-wave modes of copper twisted-pair cables using transformation optics. *IEEE Access* (2021), 1–1.

[73] Hellings, C., and Utschick, W. Block-skew-circulant matrices in complex-valued signal processing. *IEEE Transactions on Signal Processing 63*, 8 (Apr. 2015), 2093–2107.

[74] Henkel, W., Hassan, K., von Deetzen, N., Sandberg, S., Sassatelli, L., and Declercq, D. UEP concepts in modulation and coding. *Advances in Multimedia 2010* (Aug. 2010), 1–14.

[75] Henkel, W., and Kessler, T. Maximizing the channel capacity of multicarrier transmission by suitable adaptation of the time-domain equalizer. *IEEE Transactions on Communications 48*, 12 (Dec. 2000), 2000–2004.

[76] Henkel, W., Taubock, G., Odling, P., Borjesson, P., and Petersson, N. The cyclic prefix of OFDM/DMT - An analysis. In *Proc. International Zurich Seminar on Broadband Communications Access - Transmission - Networking (Cat. No.02TH8599)* (Feb. 2002), pp. 22–22.

[77] Hincapie, D., Leibiger, M., and Oswald, E. Roll-out of giga-bit copper: Impact-analysis of deploying G.fast in FTTC access networks. In *Proc. 12th ITG-Symposium; Broadband Coverage in Germany* (Apr. 2018), pp. 1–6.

[78] Ho, Z. K., and Jorswieck, E. Improper Gaussian signaling on the two-user SISO interference channel. In *Proc. International Symposium on Wireless Communication Systems (ISWCS)* (Aachen, Germany, Nov. 2011), pp. 824–828.

[79] Honig, M. L., Steiglitz, K., and Gopinath, B. Multichannel signal processing for data communications in the presence of crosstalk. *IEEE Transactions on Communications 38*, 4 (Apr. 1990), 551–558.

[80] Huang, J., Tan, C. W., Chiang, M., and Cendrillon, R. Statistical multiplexing over DSL networks. In *Proc. IEEE International Conference on Computer Communications (INFOCOM)* (Anchorage, United States, May 2007), pp. 571–579.

[81] Huang, Y., Medeiros, E., Fonseca, N., Höst, S., Magesacher, T., Eriksson, P., Lu, C., Ödling, P., and Börjesson, P. O. LTE over copper — Potential and limitations. In *Proc. IEEE Annual International Symposium on Personal, Indoor, and Mobile Radio Communications (PIMRC)* (Hong Kong, Hong Kong, Aug. 2015), pp. 1339–1343.

[82] Huberman, S., and Le-Ngoc, T. Full-duplex MIMO precoding for sum-rate maximization with sequential convex programming. *IEEE Transactions on Vehicular Technology 64*, 11 (Nov. 2015), 5103–5112.

[83] Huberman, S., and Le-Ngoc, T. MIMO full-duplex precoding: A joint beamforming and self-interference cancellation structure. *IEEE Transactions on Wireless Communications 14*, 4 (Apr. 2015), 2205–2217.

[84] Huberman, S., Leung, C., and Le-Ngoc, T. Constant offset autonomous spectrum balancing using multiple reference lines for VDSL. *IEEE Transactions on Signal Processing 60*, 12 (Dec. 2012), 6719–6723.

[85] Huberman, S., Leung, C., and Le-Ngoc, T. Dynamic spectrum management (DSM) algorithms for multi-user xDSL. *IEEE Communications Surveys & Tutorials 14*, 1 (Jan. 2012), 109–130.

[86] Hunger, R., and Joham, M. A general rate duality of the MIMO multiple access channel and the MIMO broadcast channel. In *Proc. IEEE Global Telecommunications Conference (GLOBECOM)* (New Orleans, United States, Nov. 2008), pp. 1–5.

[87] Hunger, R., Joham, M., and Utschick, W. On the MSE-Duality of the broadcast channel and the multiple access channel. *IEEE Transactions on Signal Processing 57*, 2 (Feb. 2009), 698–713.

[88] Huo, Y., Hellge, C., Wiegand, T., and Hanzo, L. A tutorial and review on inter-layer FEC coded layered video streaming. *IEEE Communications Surveys & Tutorials 17*, 2 (Jan. 2015), 1166–1207.

[89] Ioannou, N., Katsianis, D., and Varoutas, D. Comparative techno-economic evaluation of LTE fixed wireless access, FTTdp G.fast and FTTC VDSL network deployment for providing 30Mbps broadband services in rural areas. *Telecommunications Policy 44*, 3 (Apr. 2020), 101875.

[90] ITU-T Study Group 12. End-user multimedia QoS categories. Tech. Rep. ITU-T G.1010, International Telecommunication Union, 2001.

[91] ITU-T Study Group 15. Asymmetric digital subscriber line (ADSL) transceivers. Tech. Rep. ITU-T G.992.1, International Telecommunication Union, 1999.

[92] ITU-T Study Group 15. Asymmetric digital subscriber line transceivers 2 (ADSL2). Tech. Rep. ITU-T G.992.3, International Telecommunication Union, 2002.

[93] ITU-T Study Group 15. Very high speed digital subscriber line transceivers. Tech. Rep. ITU-T G.993.1, International Telecommunication Union, 2004.

[94] ITU-T Study Group 15. Very high speed digital subscriber line transceivers 2 (VDSL2). Tech. Rep. ITU-T G.993.2, International Telecommunication Union, 2007.

[95] ITU-T Study Group 15. Fast access to subscriber terminals (G.fast) - Power spectral density specification. Tech. Rep. ITU-T G.9700, International Telecommunication Union, 2014.

[96] ITU-T Study Group 15. Fast access to subscriber terminals (G.fast) - Physical layer specification. Tech. Rep. ITU-T G.9701, International Telecommunication Union, 2015.

[97] Jafar, S. A., Cadambe, V., and Wang, C. Interference alignment with asymmetric complex signaling. In *Proc. Annual Allerton Conference on Communication, Control, and Computing* (Allerton, United States, Sept. 2009), pp. 991–996.

[98] Kardaras, G., and Lanzani, C. Advanced multimode radio for wireless mobile broadband communication. In *Proc. IEEE European Wireless Technology Conference (EW)* (Aalborg, Denmark, Sept. 2009), pp. 132–135.

[99] Keerthi, S., and Gilbert, E. Convergence of a generalized SMO algorithm for SVM classifier design. *Machine Learning 46*, 1/3 (2002), 351–360.

[100] Kelly, F. P., Maulloo, A. K., and Tan, D. K. H. Rate control for communication networks: shadow prices, proportional fairness and stability. *Journal of the Operational Research Society 49*, 3 (Mar. 1998), 237–252.

[101] Kim, N., Lee, Y., and Park, H. Performance analysis of MIMO system with linear MMSE receiver. *IEEE Transactions on Wireless Communications 7*, 11 (Nov. 2008), 4474–4478.

[102] Kim, S.-J., and Giannakis, G. B. Optimal resource allocation for MIMO ad hoc cognitive radio networks. *IEEE Trans. Inf. Theory 57*, 5 (May 2011), 3117–3131.

[103] Knuth, D. E. *The Art of Computer Programming, Volume 2: Seminumerical Algorithms*. Addison-Wesley Pub, Reading, Massachusetts, Jan. 1981.

[104] Konnov, I. V. A method of bi-coordinate variations with tolerances and its convergence. *Russian Mathematics 60*, 1 (Jan. 2016), 68–72.

[105] Lameiro, C., and Santamaría, I. Degrees-of-freedom for the 4-user SISO interference channel with improper signaling. In *Proc. IEEE International Conference on Communications (ICC)* (Budapest, Hungary, June 2013), pp. 3053–3057.

[106] Lamparter, O., Fang, L., Bischoff, J., Reitmann, M., Schwendener, R., Zasowski, T., and Zhang, X. Multi-gigabit over copper access networks: architectural evolution and techno-economic analysis. *IEEE Communications Magazine 57*, 8 (Aug. 2019), 22–27.

[107] Lanneer, W., Moonen, M., Tsiaflakis, P., and Maes, J. Linear and nonlinear precoding based dynamic spectrum management for downstream vectored G.fast transmission. In *Proc. IEEE Global Communications Conference (GLOBECOM)* (San Diego, United States, Dec. 2015), IEEE, pp. 1–6.

[108] Lanneer, W., Tsiaflakis, P., Maes, J., and Moonen, M. Linear and nonlinear precoding based dynamic spectrum management for downstream vectored G.fast transmission. *IEEE Transactions on Communications 65*, 3 (Mar. 2017), 1247–1259.

[109] Lanneer, W., Tsiaflakis, P., Maes, J., and Moonen, M. alpha-Fair dynamic spectrum management for QRD-based precoding with user encoding ordering in downstream G.fast transmission. *IEEE Transactions on Communications 67*, 4 (Apr. 2019), 2939–2950.

[110] Lanneer, W., Verdyck, J., Tsiaflakis, P., Maes, J., and Moonen, M. Vectoring-based dynamic spectrum management for G.fast multi-user full-duplex transmission. In *Proc. IEEE Annual International Symposium on Personal, Indoor, and Mobile Radio Communications (PIMRC)* (Montreal, QC, Canada, Oct. 2017), pp. 1–5.

[111] Le Nir, V., Moonen, M., Verlinden, J., and Guenach, M. Optimal power allocation for downstream xDSL with per-modem total power constraints: broadcast channel optimal spectrum balancing (BC-OSB). *IEEE Transactions on Signal Processing 57*, 2 (Feb. 2009), 690–697.

[112] Lechleider, J. W. High bit rate digital subscriber lines: A review of HDSL progress. *IEEE Journal on Selected Areas in Communications 9*, 6 (Aug. 1991), 769–784.

[113] Leung, C., Huberman, S., and Le-Ngoc, T. Autonomous spectrum balancing using multiple reference lines for digital subscriber lines. In *Proc. IEEE Global Telecommunications Conference (GLOBECOM)* (Miami, United States, Dec. 2010), pp. 1–6.

[114] Li, S., Murch, R. D., and Lau, V. K. N. Linear transceiver design for full-duplex multi-user MIMO system. In *IEEE International Conference on Communications (ICC)* (Sydney, Australia, June 2014), pp. 4921–4926.

[115] Lin, Y., Li, C., and Phoong, S. A filterbank approach to window designs for multicarrier systems. *IEEE Circuits and Systems Magazine 7*, 1 (2007), 19–30.

[116] Liu, Y. Dynamic spectrum management: A complete complexity characterization. *IEEE Transactions on Information Theory 63*, 1 (Jan. 2017), 392–403.

[117] Lu, C., Berg, M., Trojer, E., Eriksson, P.-E., Laraqui, K., Tidblad, O. V., and Almeida, H. Connecting the dots: Small cells shape up for high-performance indoor radio. *Ericsson Review 91* (Dec. 2014), 2–9.

[118] Luo, Z.-Q., and Zhang, S. Dynamic spectrum management: complexity and duality. *IEEE Journal of Selected Topics in Signal Processing 2*, 1 (Feb. 2008), 57–73.

[119] Madhow, U., and Honig, M. MMSE interference suppression for direct-sequence spread-spectrum CDMA. *IEEE Transactions on Communications 42*, 12 (Dec. 1994), 3178–3188.

[120] Maeda, Y., Starr, T. et. al. Wireline broadband access networks and home networking. *ITU-T Technical paper* (Dec. 2011).

[121] Maes, J., and Nuzman, C. Energy efficient discontinuous operation in vectored G.fast. In *Proc. IEEE International Conference on Communications (ICC)* (Sidney, Australia, June 2014), pp. 3854–3858.

[122] Maes, J., Nuzman, C., and Tsiaflakis, P. Sensitivity of nonlinear precoding to imperfect channel state information in G.fast. In *Proc. European Signal Processing Conference (EUSIPCO)* (Budapest, Hungary, Aug. 2016), pp. 290–294.

[123] Mariotte, H. Overview of ITU-T SG15 Q4 xDSL and G.(mg)fast, May 2017.

[124] Martin, R., Balakrishnan, J., Sethares, W., and Johnson, C. A blind adaptive TEQ for multicarrier systems. *IEEE Signal Processing Letters 9*, 11 (Nov. 2002), 341–343.

[125] Martins, W. A., Cruz–Roldán, F., Moonen, M., and Ramirez Diniz, P. S. Intersymbol and intercarrier interference in OFDM transmissions through highly dispersive channels. In *Proc. European Signal Processing Conference (EUSIPCO)* (A Coruña, Spain, Sept. 2019), pp. 1–5.

[126] Matera, A. Enhancing indoor coverage by multi-pairs copper cables: The analog MIMO radio-over-copper architecture. In *Special Topics in Information Technology*, B. Pernici, Ed., Springer Briefs in Applied Sciences and Technology. Springer International Publishing, Cham, Swiss Confederation, 2020, pp. 17–29.

[127] Matera, A., and Spagnolini, U. Analog MIMO radio-over-copper downlink with space-frequency to space-frequency multiplexing for multi-user 5G indoor deployments. *IEEE Transactions on Wireless Communications 18*, 5 (May 2019), 2813–2827.

[128] Mazzenga, F., and Giuliano, R. Analysis of zero-forcing vectoring for VDSL2 and long reach VDSL technologies. *IEEE Transactions on Communications 67*, 11 (Nov. 2019), 7811–7823.

[129] McKinley, A., and Marshall, A. An optimal multi-user, multi-service algorithm for dynamic spectrum management in DSL. In *Proc. International Conference on Telecommunications (ICT)* (June 2008), IEEE, pp. 1–5.

[130] Medeiros, E., Huang, Y., Magesacher, T., Höst, S., Eriksson, P., Lu, C., Ödling, P., and Börjesson, P. O. Crosstalk mitigation for LTE-over-copper in downlink direction. *IEEE Communications Letters 20*, 7 (July 2016), 1425–1428.

[131] Mehmood, H., Udell, M., and Cioffi, J. Revenue maximization for broadband service providers using revenue capacity. In *Proc. IEEE Global Commun. Conf. (GLOBECOM)* (San Diego, United States, Dec. 2015), pp. 1–7.

[132] Melsa, P., Younce, R., and Rohrs, C. Impulse response shortening for discrete multitone transceivers. *IEEE Transactions on Communications 44*, 12 (Dec. 1996), 1662–1672.

[133] Mestdagh, D. G., Isaksson, M. R., and Odling, P. Zipper VDSL: a solution for robust duplex communication over telephone lines. *IEEE Communications Magazine 38*, 5 (May 2000), 90–96.

[134] Moraes, R. B., Tsiaflakis, P., Maes, J., and Moonen, M. DMT MIMO IC rate maximization in DSL with combined signal and spectrum coordination. *IEEE Transactions on Signal Processing 61*, 7 (Apr. 2013), 1756–1769.

[135] Moraes, R. B., Tsiaflakis, P., Maes, J., and Moonen, M. DMT MIMO IC rate maximization in DSL with per-transceiver power constraints. *Signal Processing 101* (Aug. 2014), 87–98.

[136] Moraes, R. B., Tsiaflakis, P., and Moonen, M. Reduced complexity dynamic spectrum management based on a polar coordinates formulation. In *Proc. International Conference on Communications (ICC)* (Budapest, Hungary, June 2013), pp. 3991–3995.

[137] Moraes, R. B., Wolkerstorfer, M., Tsiaflakis, P., and Moonen, M. Dynamic spectrum management with spherical coordinates. *IEEE Transactions on Signal Processing 62*, 21 (Nov. 2014), 5589–5602.

[138] Muquet, B., Wang, Z., Giannakis, G. B., Courville, M. d., and Duhamel, P. Cyclic prefixing or zero padding for wireless multicarrier transmissions? *IEEE Transactions on Communications 50*, 12 (Dec. 2002), 2136–2148.

[139] Neckebroek, J. *Error correction, precoding and bitloading algorithms in high-speed access networks.* PhD thesis, Ghent, Belgium, 2016.

[140] Neckebroek, J., Moeneclaey, M., Guenach, M., Timmers, M., and Maes, J. Comparison of error-control schemes for high-rate communication over short DSL loops affected by impulsive noise. In *Proc. International Conference on Communications (ICC)* (Budapest, Hungary, June 2013), pp. 4014–4019.

[141] Nguyen, D., Tran, L., Pirinen, P., and Latva-aho, M. Transmission strategies for full duplex multiuser MIMO systems. In *Proc. IEEE International Conference on Communications (ICC)* (Ottawa, Canada, June 2012), pp. 6825–6829.

[142] Nguyen, D., Tran, L., Pirinen, P., and Latva-aho, M. Precoding for full duplex multiuser MIMO systems: Spectral and energy efficiency maximization. *IEEE Transactions on Signal Processing 61*, 16 (Aug. 2013), 4038–4050.

[143] Nguyen, D., Tran, L., Pirinen, P., and Latva-aho, M. On the spectral efficiency of full-duplex small cell wireless systems. *IEEE Transactions on Wireless Communications 13*, 9 (Sept. 2014), 4896–4910.

[144] Nongpiur, R. C., Shpak, D. J., and Antoniou, A. Near-end crosstalk cancellation in xDSL systems. In *Proc. Asilomar Conference on Signals, Systems and Computers* (Pacific Grove, United States, Nov. 2002), vol. 1, pp. 393–397 vol.1.

[145] Oksman, V., Strobel, R., Starr, T., Maes, J., Coomans, W., Kuipers, M., Tovim, E. B., and Wei, D. MGFAST: A new generation of copper broadband access. *IEEE Communications Magazine 57*, 8 (Aug. 2019), 14–21.

[146] Pandey, P. K., Moonen, M., and Deneire, L. Sparse approximation based resource allocation in DSL/DMT transceivers with per-tone equalization. *Signal Processing 95* (Feb. 2014), 43–48.

[147] Papandriopoulos, J., and Evans, J. S. SCALE: A low-complexity distributed protocol for spectrum balancing in multiuser DSL networks. *IEEE Transactions on Information Theory 55*, 8 (Aug. 2009), 3711–3724.

[148] Petersen, K. B., and Pedersen, M. S. *The Matrix Cookbook.* Technical University of Denmark, Nov. 2012.

[149] Phan, K. T., Vorobyov, S. A., Telambura, C., and Le-Ngoc, T. Power control for wireless cellular systems via D.C. programming. In *Proc.*

IEEE/SP Workshop on Statistical Signal Processing (SSP) (Madison, United States, Aug. 2007), pp. 507–511.

[150] Picinbono, B., and Chevalier, P. Widely linear estimation with complex data. *IEEE Transactions on Signal Processing 43*, 8 (Aug. 1995), 2030–2033.

[151] Pisoni, F., Bonaventura, M., and Cioffi, J. M. Echo cancellation in DMT modems with frame-asynchronous operation. *IEEE Transactions on Signal Processing 55*, 1 (Jan. 2007), 246–255.

[152] Point Topic. World fixed broadband statistics Q2 2020: growth recovers after recent slowdown, 2020.

[153] Rashid-Farrokhi, F., Liu, K., and Tassiulas, L. Transmit beamforming and power control for cellular wireless systems. *IEEE Journal on Selected Areas in Communications 16*, 8 (Oct. 1998), 1437–1450.

[154] Razaviyayn, M., Hong, M., and Luo, Z.-q. A unified convergence analysis of block successive minimization methods for nonsmooth optimization. *SIAM Journal on Optimization 23*, 2 (June 2013), 1126–1153.

[155] Rockafellar, R. T., and Wets, R. J.-B. *Variational Analysis*, first ed., vol. 317. Springer Science & Business Media, Berlin, Heidelberg, Germany, 2009.

[156] Saad, Y. *Iterative methods for sparse linear systems*. Society for Industrial and Applied Mathematics, Jan. 2003.

[157] Schneir, J. R., and Xiong, Y. Economic aspects of fibre to the distribution point with G.fast. *Telecommunications Policy 39*, 6 (July 2015), 450–462.

[158] Schneir, J. R., and Xiong, Y. Cost assessment of FTTdp networks with G.fast. *IEEE Communications Magazine 54*, 8 (Aug. 2016), 144–152.

[159] Schubert, M., and Boche, H. Joint 'dirty paper' pre-coding and downlink beamforming. In *Proc. IEEE International Symposium on Spread Spectrum Techniques and Applications (ISSSTA)* (Prague, Czech Republic, Sept. 2002), vol. 2, IEEE, pp. 536–540.

[160] Schubert, M., and Boche, H. A generic approach to QoS-based transceiver optimization. *IEEE Transactions on Communications 55*, 1 (Jan. 2007), 235–235.

[161] Scutari, G., Facchinei, F., and Lampariello, L. Parallel and distributed methods for constrained nonconvex optimization - Part I: theory. *IEEE Transactions on Signal Processing 65*, 8 (Apr. 2017), 1929–1944.

[162] Scutari, G., Facchinei, F., Song, P., Palomar, D. P., and Pang, J. S. Decomposition by partial linearization: Parallel optimization of multi-agent systems. *IEEE Transactions on Signal Processing 62*, 3 (Feb. 2014), 641–656.

[163] Scutari, G., Palomar, D. P., and Barbarossa, S. Asynchronous iterative water-filling for Gaussian frequency-selective interference channels. *IEEE Transactions on Information Theory 54*, 7 (July 2008), 2868–2878.

[164] Seong, K., Narasimhan, R., and Cioffi, J. M. Queue proportional scheduling via geometric programming in fading broadcast channels. *IEEE Journal on Selected Areas in Communications 24*, 8 (Aug. 2006), 1593–1602.

[165] Sharfer, I. Performance of concatenated Reed-Solomon and TCM over DMT modulation. In *Proc. Convention of Electrical and Electronics Engineers in Israel* (Tel-Aviv, Israel, Dec. 2002), pp. 308–310.

[166] Sharma, M., Moonen, M., Lefevre, Y., and Tsiaflakis, P. MIMO Time Domain Equalizer Design for Long Reach xDSL MIMO Channel Shortening. *IEEE Access 8* (2020), 203468–203477.

[167] Sharma, M., Verdyck, J., Lefevre, Y., Tsiaflakis, P., and Moonen, M. MIMO per-tone equalizer design for long reach xDSL. *submitted for publication* (Apr. 2021).

[168] Shrestha, R., Kerpez, K., Hwang, C. S., Mohseni, M., Cioffi, J. M., and Mittleman, D. M. A wire waveguide channel for terabit-per-second links. *Applied Physics Letters 116*, 13 (Mar. 2020), 131102.

[169] Singh, I., and Giridhar, K. Enhancement in spectral efficiency using transmit-side channel shortener for MISO-OFDM systems. *IEEE Signal Processing Letters 21*, 6 (June 2014), 712–716.

[170] Sjoberg, F., Isaksson, M., Nilsson, R., Odling, P., Wilson, S. K., and Borjesson, P. O. Zipper: a duplex method for VDSL based on DMT. *IEEE Transactions on Communications 47*, 8 (Aug. 1999), 1245–1252.

[171] Song, G., Li, Y., and Cimini, L. Joint channel- and queue-aware scheduling for multiuser diversity in wireless OFDMA networks. *IEEE Transactions on Communications 57*, 7 (July 2009), 2109–2121.

[172] Sorber, L., Van Barel, M., and De Lathauwer, L. Unconstrained optimization of real functions in complex variables. *SIAM Journal on Optimization 22*, 3 (Jan. 2012), 879–898.

[173] Souza, D. D., Sousa, B. P. T., Borges, G. S., Rodrigues, R. M., Cavalcante, A. M., Almeida, I. M., and Costa, J. C. W. A. Evaluation of copper cables as waveguides in next-generation wireline technologies. In *Proc. SBMO/IEEE MTT-S International Microwave and Optoelectronics Conference (IMOC)* (Aveiro, Portugal, Nov. 2019), pp. 1–3.

[174] Stanczak, S., Wiczanowski, M., and Boche, H. *Fundamentals of Resource Allocation in Wireless Networks: Theory and Algorithms*. Springer Science & Business Media, June 2009.

[175] Starr, T., Cioffi, J. M., and Silverman, P. *Understanding Digital Subscriber Line Technology*. Prentice Hall PTR, 1999.

[176] Statovci, D., Nordström, T., and Nilsson, R. The normalized-rate iterative algorithm: A practical dynamic spectrum management method for DSL. *EURASIP Journal on Advances in Signal Processing 2006* (2006), 1–18.

[177] Strobel, R. Copper transmission for multi-gigabit hybrid copper-fiber access networks. In *Proc. International Workshop on Fiber Optics in Access Networks (FOAN)* (Munich, Germany, Nov. 2017), pp. 1–6.

[178] Strobel, R. Physical layer framework for the multi-gigabit copper-fiber access networks. *Fiber and Integrated Optics 37*, 6 (Nov. 2018), 291–313.

[179] Strobel, R. *Channel Modeling and Physical Layer Optimization in Copper Line Networks*. Signals and Communication Technology. Springer International Publishing, 2019.

[180] Strobel, R., and Oksman, V. Line grouping for crosstalk avoidance, Feb. 2018.

[181] Strobel, R., and Utschick, W. Coexistence of G.fast and VDSL in FTTdp and FTTC deployments. In *Proc. European Signal Processing Conference (EUSIPCO)* (Nice, France, Aug. 2015), pp. 1103–1107.

[182] Suls, A., Verdyck, J., Moonen, M., and Moeneclaey, M. Modified SNR gap approximation for resource allocation in LDPC-coded multicarrier systems. *IEEE Access 8* (2020), 1577–1586.

[183] Sun, Y., Babu, P., and Palomar, D. P. Majorization-minimization algorithms in signal processing, communications, and machine learning. *IEEE Transactions on Signal Processing 65*, 3 (Feb. 2017), 794–816.

[184] Taubock, G. Complex noise analysis of DMT. *IEEE Transactions on Signal Processing 55*, 12 (Dec. 2007), 5739–5754.

[185] Thomas Starr. Applying G.fast technology in an age of fiber integrations, Oct. 2019.

[186] Timmers, M., Guenach, M., Nuzman, C., and Maes, J. G.fast: evolving the copper access network. *IEEE Communications Magazine 51*, 8 (Aug. 2013), 74–79.

[187] Tomlinson, M. New automatic equaliser employing modulo arithmetic. *Electronics Letters 7*, 5 (Mar. 1971), 138–139.

[188] Tsiaflakis, P., Diehl, M., and Moonen, M. Distributed spectrum management algorithms for multiuser DSL networks. *IEEE Transactions on Signal Processing 56*, 10 (Oct. 2008), 4825–4843.

[189] Tsiaflakis, P., Glineur, F., and Moonen, M. Iterative convex approximation based real-time dynamic spectrum management in multi-user multi-carrier communication systems. *IEEE Signal Processing Letters 21*, 5 (May 2014), 535–539.

[190] Tsiaflakis, P., Glineur, F., and Moonen, M. Real-time dynamic spectrum management for multi-user multi-carrier communication systems. *IEEE Transactions on Communications 62*, 3 (Mar. 2014), 1124–1137.

[191] Tsiaflakis, P., Lefevre, Y., Coomans, W., and Maes, J. Friendly full duplex: A multi-user full duplex method for MGfast in coexistence with G.fast. In *Proc. Global Communications Conference (GLOBECOM)* (Abu Dhabi, United Arab Emirates, Dec. 2018), pp. 1–6.

[192] Tsiaflakis, P., and Moonen, M. Low-complexity dynamic spectrum management algorithms for digital subscriber lines. In *Proc. IEEE International Conference on Acoustics, Speech and Signal Processing (ICASSP)* (Mar. 2008), pp. 2769–2772.

[193] Tsiaflakis, P., Moraes, R. B., and Moonen, M. A low-complexity algorithm for joint spectrum and signal coordination in upstream DSL

transmission. In *Proc. IEEE Symposium on Communications and Vehicular Technology in the Benelux (SCVT)* (Ghent, Belgium, Nov. 2011), pp. 1–6.

[194] Tsiaflakis, P., Vangorp, J., Moonen, M., and Verlinden, J. A low complexity optimal spectrum balancing algorithm for digital subscriber lines. *Signal Processing 87*, 7 (July 2007), 1735–1753.

[195] Tsiaflakis, P., Vangorp, J., Verlinden, J., and Moonen, M. Multiple access channel optimal spectrum balancing for upstream DSL transmission. *IEEE Communications Letters 11*, 4 (Apr. 2007), 398–300.

[196] Tsiaflakis, P., Yi, Y., Chiang, M., and Moonen, M. Throughput and delay performance of DSL broadband access with cross-layer dynamic spectrum management. *IEEE Transactions on Communications 60*, 9 (Sept. 2012), 2700–2711.

[197] Ungerboeck, G. Trellis-coded modulation in DSL systems. In *Fundamentals of DSL Technology*. CRC Press, Sept. 2005.

[198] Van den Bogaert, E., Bostoen, T., Verlinden, J., Cendrillon, R., and Moonen, M. ADSL transceivers applying DSM and their nonstationary noise robustness. *EURASIP Journal on Advances in Signal Processing*, 1 (May 2006), 1–9.

[199] Van Den Eynde, J., Verdyck, J., Blondia, C., and Moonen, M. Delay performance enhancement for DSL networks through cross-layer scheduling. In *Proc. WIC Symposium on Information Theory in the Benelux (SITB)* (Louvain-la-Neuve, Belgium, May 2016), pp. 1–8.

[200] Van den Eynde, J., Verdyck, J., Moonen, M., and Blondia, C. A delay-based cross-layer scheduler for adaptive DSL. In *Proc. IEEE International Conference on Communications (ICC)* (Paris, France, May 2017), pp. 1–6.

[201] Vanbleu, K., Ysebaert, G., Cuypers, G., Moonen, M., and Acker, K. V. Bitrate-maximizing time-domain equalizer design for DMT-based systems. *IEEE Transactions on Communications 52*, 6 (June 2004), 871–876.

[202] Verdyck, J., Lanneer, W., Tsiaflakis, P., Coomans, W., Patrinos, P., and Moonen, M. Optimal dynamic spectrum management algorithms for multi-user full-duplex DSL. *IEEE Access 7* (2019), 106600–106616.

[203] Verdyck, J., Lefevre, Y., Tsiaflakis, P., and Moonen, M. Per-Tone Precoding and Per-Tone Equalization for OFDM and DMT Transmission Systems: Duality, Filter Optimization, and Resource Allocation. *IEEE Open Journal of Signal Processing 1* (2020), 257–273.

[204] Verdyck, J., and Moonen, M. Dynamic spectrum management in digital subscriber line networks with unequal error protection requirements. *IEEE Access 5* (2017), 18107–18120.

[205] Verdyck, J., Tsiaflakis, P., and Moonen, M. Unequal error protection in rate adaptive spectrum management for digital subscriber line systems. In *Proc. European Signal Processing Conference (EUSIPCO)* (Nice, France, Aug. 2015), IEEE, pp. 1451–1455.

[206] Visotsky, E., and Madhow, U. Optimum beamforming using transmit antenna arrays. In *Proc. IEEE Vehicular Technology Conference (VTC)* (Houston, United States, July 1999), pp. 851–856.

[207] Viswanath, P., and Tse, D. N. C. Sum capacity of the vector Gaussian broadcast channel and uplink-downlink duality. *IEEE Transactions on Information Theory 49*, 8 (Aug. 2003), 1912–1921.

[208] Wicker, S. B. *Reed-Solomon Codes and Their Applications*. IEEE Press, Piscataway, NJ, USA, 1994.

[209] Wolkerstorfer, M., and Mecklenbrauker, C. F. Variational inequality approach to spectrum balancing in vectoring xDSL networks. In *Proc. IEEE International Conference on Communications (ICC)* (Paris, France, May 2017), pp. 1–7.

[210] Wolkerstorfer, M., Moonen, M., and Statovci, D. Multiuser spectrum balancing under inter-carrier interference. *IEEE Communications Letters 16*, 10 (Oct. 2012), 1560–1563.

[211] Wolkerstorfer, M., and Statovci, D. Fairness tradeoff analysis during VDSL2 network migration - Simulation and testbed results. In *Proc. IEEE Symposium on Computers and Communications (ISCC)* (Funchal, Portugal, June 2014), pp. 1–6.

[212] Wolkerstorfer, M., Tsiaflakis, P., Moonen, M., and Statovci, D. Joint power-loading and cyclic prefix length optimization for OFDM-based power line communication. In *Proc. IEEE International Conference on Acoustics, Speech and Signal Processing (ICASSP)* (Vancouver, Canada, May 2013), pp. 4688–4692.

[213] Xu, Y., Panigrahi, S., and Le-Ngoc, T. A concave minimization approach to dynamic spectrum management for digital subscriber lines. In *Proc. IEEE International Conference on Communications (ICC)* (Istanbul, Turkey, June 2006), pp. 84–89.

[214] Yang, Y., and Pesavento, M. A unified successive pseudoconvex approximation framework. *IEEE Transactions on Signal Processing 65*, 13 (July 2017), 3313–3328.

[215] Yin, B., Wu, M., Studer, C., Cavallaro, J. R., and Lilleberg, J. Full-duplex in large-scale wireless systems. In *Proc. Asilomar Conference on Signals, Systems and Computers* (Pacific Grove, US, Nov. 2013), pp. 1623–1627.

[216] Ysebaert, G., Vanbleu, K., Cuypers, G., Moonen, M., and Verlinden, J. Echo cancellation for discrete multitone frame-asynchronous ADSL transceivers. In *Proc. IEEE International Conference on Communications (ICC)* (Anchorage, United States, May 2003), vol. 4, pp. 2421–2425.

[217] Yu, W. Multiuser water-filling in the presence of crosstalk. In *Proc. Information Theory and Applications Workshop* (La Jolla, CA, USA, Jan. 2007), pp. 414–420.

[218] Yu, W., Ginis, G., and Cioffi, J. Distributed multiuser power control for digital subscriber lines. *IEEE Journal on Selected Areas in Communications 20*, 5 (June 2002), 1105–1115.

[219] Yu, W., and Lan, T. Transmitter optimization for the multi-antenna downlink with per-antenna power constraints. *IEEE Transactions on Signal Processing 55*, 6 (June 2007), 2646–2660.

[220] Yu, W., and Lui, R. Dual methods for nonconvex spectrum optimization of multicarrier systems. *IEEE Transactions on Communications 54*, 7 (July 2006), 1310–1322.

[221] Yu, W., Rhee, W., Boyd, S., and Cioffi, J. M. Iterative water-filling for Gaussian vector multiple-access channels. *IEEE Transactions on Information Theory 50*, 1 (Jan. 2004), 145–152.

[222] Zafaruddin, S., Bergel, I., and Leshem, A. Signal processing for gigabit-rate wireline communications: An overview of the state of the art and research challenges. *IEEE Signal Processing Magazine 34*, 5 (Sept. 2017), 141–164.

[223] Zeng, Y., Yetis, C. M., Gunawan, E., Guan, Y. L., and Zhang, R. Transmit optimization with improper gaussian signaling for interference channels. *IEEE Transactions on Signal Processing 61*, 11 (June 2013), 2899–2913.

[224] Zeng, Y., Zhang, R., Gunawan, E., and Guan, Y. L. Optimized transmission with improper gaussian signaling in the K-User MISO interference channel. *IEEE Transactions on Wireless Communications 12*, 12 (Dec. 2013), 6303–6313.

[225] Zhang, X.-D. *Matrix Analysis and Applications*. Cambridge University Press, Oct. 2017.

[226] Zhang, Y., Zhang, R., Zhang, J., Bai, T., Rawi, A. F. A., Moonen, M., and Hanzo, L. Far-end crosstalk mitigation for future wireline networks beyond G.mgfast: A survey and an outlook. *IEEE Access 8* (2020), 9998–10039.

[227] Zheng, H., and Liu, K. Power minimization for delivering integrated multimedia services over digital subscriber line. *IEEE Journal on Selected Areas in Communications 18*, 6 (June 2000), 841–849.

[228] Zhi-Quan Luo, and Shuzhong Zhang. Dynamic Spectrum Management: Complexity and Duality. *IEEE Journal of Selected Topics in Signal Processing 2*, 1 (Feb. 2008), 57–73.

Curriculum Vitae



Jeroen Verdyck was born in Turnhout, Belgium on August 27th, 1991. He received a B.Sc. degree in electrical engineering and computer science in 2012, and a M.Sc. degree in electrical engineering (magna cum laude) in 2014, both from KU Leuven, Leuven, Belgium. Since 2014, he has been a Ph.D. candidate with the Electrical Engineering Department, in the research group of STADIUS Center for Dynamical Systems, Signal Processing and Data Analytics, under the supervision of Prof. Marc Moonen. He has been involved in joint projects with Nokia Bell Labs and the University of Antwerp, Antwerp, Belgium. He received the ICC 2017 TAOS best paper award (with Jeremy Van den Eynde). His research interests include signal processing, numerical optimization, and machine learning for digital communication systems.

List of publications

International journal articles

1. Jeremy Van den Eynde, **Jeroen Verdyck**, Marc Moonen, and Chris Blondia, "Minimal Delay Violation-based Cross-layer Scheduler and Resource Allocation for DSL Networks," *IEEE Access*, Vol. 9, pp. 75905 - 75922, May 2021.

2. **Jeroen Verdyck**, Yannick Lefevre, Paschalis Tsiaflakis, and Marc Moonen, "Signal Impropriety in Discrete Multi-Tone Systems and Widely Linear Per-Tone Equalization," *IEEE Open Journal of the Communications Society*, Vol. 2, pp. 367 - 383, February 2021.

3. **Jeroen Verdyck**, Yannick Lefevre, Paschalis Tsiaflakis, and Marc Moonen, "Per-Tone Precoding and Per-Tone Equalization for OFDM and DMT Transmission Systems: Duality, Filter Optimization, and Resource Allocation," *IEEE Open Journal of Signal Processing*, Vol. 1, pp. 257 - 273, November 2020.

4. Adriaan Suls, **Jeroen Verdyck**, Marc Moonen, and Marc Moeneclaey, "Modified SNR Gap Approximation for Resource Allocation in LDPC-Coded Multicarrier Systems," *IEEE Access*, Vol. 8, pp. 1577 - 1586, December 2019.

5. **Jeroen Verdyck**, Wouter Lanneer, Paschalis Tsiaflakis, Werner Coomans, Panagiotis Patrinos, and Marc Moonen, "Optimal Dynamic Spectrum Management Algorithms for Multi-User Full-Duplex DSL," *IEEE Access*, Vol. 7, pp. 106600 - 106616, July 2019.

6. **Jeroen Verdyck**, and Marc Moonen, "Dynamic Spectrum Management in Digital Subscriber Line Networks with Unequal Error Protection Requirements," *IEEE Access*, Vol. 5, pp. 18107 - 18120, September 2017.

7. Mohit Sharma, **Jeroen Verdyck**, Yannick Lefevre, Paschalis Tsiaflakis, and Marc Moonen, "MIMO Per-Tone Equalizer Design for Long Reach xDSL," *to be submitted* (under internal review).

8. Richard P. Ketcham, **Jeroen Verdyck**, and Marc Moonen, "Joint Beamforming and Power Allocation for Multi-user MISO Broadcast Channel SWIPT Employing OFDM," *submitted to IEEE Access* (under review).

International conference proceedings

1. Pourya Behmandpoor, **Jeroen Verdyck**, and Marc Moonen, "Deep learning-based cross-layer resource allocation for wired communications systems," *Proc. of the 2021 IEEE International Conference on Acoustics, Speech and Signal Processing (ICASSP)*, Toronto, Canada, pp. 4120 - 4124, June 2021.

2. **Jeroen Verdyck**, Chris Blondia, and Marc Moonen, "Network utility maximization for adaptive resource allocation in DSL systems," *Proc. of the 2018 European Signal Processing Conference (EUSPICO)*, Rome, Italy, pp. 787–791, September 2018.

3. Wouter Lanneer, **Jeroen Verdyck**, Paschalis Tsiaflakis, Jochen Maes, and Marc Moonen, "Vectoring-based dynamic spectrum management for G.fast multi-user full-duplex transmission," in *Proc. of the 2017 IEEE 28th Annual International Symposium on Personal, Indoor, and Mobile Radio Communications (PIMRC)*, Montreal, Canada, pp. 1–5, October 2017.

4. Jeremy Van den Eynde, **Jeroen Verdyck**, Marc Moonen, and Chris Blondia, "A delay-based cross-layer scheduler for adaptive DSL," *Proc. of the 2017 IEEE International Conference on Communications (ICC)*, Paris, France, pp. 1-6, May 2017.

5. **Jeroen Verdyck**, Chris Blondia, and Marc Moonen, "A low-complexity algorithm for utility based spectrum coordination in DSL systems," *Proc. of the 2017 IEEE International Conference on Acoustics, Speech and Signal Processing (ICASSP)*, New Orleans, USA, pp. 3659-3663, March 2017.

6. **Jeroen Verdyck**, Chris Blondia, and Marc Moonen, "Derivative based real-time spectrum coordination for DSL," *Proc. of the 2016 European Signal Processing Conference (EUSPICO)*, Budapest, Hungary, pp. 305–309, August 2016.

7. **Jeroen Verdyck**, Paschalis Tsiaflakis, and Marc Moonen, “Unequal error protection in rate adaptive spectrum management for digital subscriber line systems,” *Proc. of the 2015 European Signal Processing Conference (EUSPICO)*, Nice, France, pp. 1451 - 1455, August 2015.

National conference proceedings (non peer-reviewed)

1. Jeremy Van den Eynde, **Jeroen Verdyck**, Chris Blondia, and Marc Moonen, "Delay performance enhancement for DSL networks through cross-layer scheduling", *Proc. of the 6th joint WIC/IEEE SP Symposium on Information Theory and Signal Processing in the Benelux (SITB)*, Louvain-la-Neuve, Belgium, pp. 2-9, May 2016.



FACULTY OF ENGINEERING SCIENCE
DEPARTMENT OF ELECTRICAL ENGINEERING
STADIUS CENTER FOR DYNAMICAL SYSTEMS, SIGNAL PROCESSING AND DATA ANALYTICS
Kasteelpark Arenberg 10 box 2446
B-3001 Leuven
jeroen.verdyck@esat.kuleuven.be
http://www.esat.kuleuven.be/stadius/